41st Danubia-Adria Symposium

Advances in Experimental Mechanics

September 23-26, 2025
Kragujevac, Serbia

PROCEEDINGS

Edited by:
Miroslav Živković
Vladimir Milovanović
Vladimir Dunić
Aleksandar Bodić

https://www.das2025.fin.kg.ac.rs/

41st Danubia-Adria Symposium

Advances in Experimental Mechanics

PROCEEDINGS

September 23-26, 2025
Kragujevac, Serbia

Edited by:
Miroslav Živković
Vladimir Milovanović
Vladimir Dunić
Aleksandar Bodić

41ST DANUBIA-ADRIA SYMPOSIUM ADVANCES IN EXPERIMENTAL MECHANICS

ISBN: 978-86-6335-157-8

DOI: 10.46793/41DAS2025

Edited by:	**Miroslav Živković, Vladimir Milovanović, Vladimir Dunić, Aleksandar Bodić** Faculty of Engineering University of Kragujevac
Publisher:	**Faculty of Engineering University of Kragujevac**
For the publisher:	**Slobodan Savić** Faculty of Engineering University of Kragujevac
Place and year of publication	Kragujevac, 2025
Technical editor:	**Aleksandar Bodić, Vladimir Milovanović** Faculty of Engineering University of Kragujevac
Printed by:	**Inter Print** Jurija Gagarina 12, 34000 Kragujevac, Serbia
Circulation:	100 Copies

The publication of this Proceedings was financially supported by the Ministry of Science, Technological Development and Innovation, Republic of Serbia.

Organized by:

Faculty of Engineering University of Kragujevac
Serbian Society of Mechanics (SSM)

Co-organized by:

Austrian Society of Experimental Strain Analysis (ASESA)
Croatian Society of Mechanics (HDM)
Czech Society for Mechanics (CSM)
German Society of Experimental Structural Analysis (GESA)
Greek Society of Experimental Mechanics of Materials (GSEMM)
Hungarian Scientific Society of Mechanical Engineering (GTE)
Italian Association for Stress Analysis (AIAS)
Polish Committee for Mechanics of the Polish Academy of Sciences (KMPAN)
Romanian Association of Stress Analysis and Materials Testing (ARTENS)
Slovak Society of Mechanics (SSM)
Slovenian Society of Experimental Mechanics (SSEM)

Scientific Committee:

Adrian Pascu	Lucian Blaga University of Sibiu (Romania)
Anatoly Nikonov	University of Ljubljana (Slovenia)
Attila Kossa	BME (Hungary)
Bernhard Pichler	Technische Universität Wien (Austria)
Damir Semenski	University Zagreb (Croatia)
Dan Mihai Constantinescu	University Politehnica of Bucharest (Romania)
Ermioni D. Pasiou	Hellenic Ministry of Culture (Greece)
Eva Tillová	University of Zilina (Slovakia)
Florian Grün	University of Leoben (Austria)
Francesca Cosmi	University of Trieste (Italy)
František Novy	University of Zilina (Slovakia)
Igor Emri	University of Ljubljana (Slovenia)
Josef Eberhardsteiner	Technische Universität Wien (Austria)
Karel Doubrava	Czech Technical University of Prague (Czech Republic)
Lovre Krstulović-Opara	University of Split (Croatia)
Matthias Bartholmai	BAM (Germany)
Mario Guagliano	Politecnico di Milano (Italy)
Miroslav Živković	University of Kragujevac (Serbia)
Nenad Kolarević	University of Belgrade (Serbia)
Pawel Pyrzanowski	Warsaw University of Technology (Poland)
Radim Halama	Technical University of Ostrava (Czech Republic)
Rita Kiss	BME (Hungary)
Stavros K. Kourkoulis	National Technical University of Athens (Greece)

Reviewers:

Marko Topalović	University of Kragujevac (Serbia)
Vladimir Milovanović	University of Kragujevac (Serbia)
Miroslav Zivković	University of Kragujevac (Serbia)
Snežana Vulović	University of Kragujevac (Serbia)
Vladimir Dunić	University of Kragujevac (Serbia)
Miloš Matejić	University of Kragujevac (Serbia)
Dragan Rakić	University of Kragujevac (Serbia)
Dušan Arsić	University of Kragujevac (Serbia)
Nebojša Hristov	University of Defence in Belgrade (Serbia)
Damir Jerković	University of Defence in Belgrade (Serbia)
Nenad Kolarević	University of Belgrade (Serbia)
Miroslav Milutinović	University of East Sarajevo (B & H)
Vladimir Simić	University of Kragujevac (Serbia)
Petra Bagavac	University of Split (Croatia)
Zvonimir Tomičević	University of Zagreb (Croatia)

Organising Committee:

Chair

Miroslav Živković	University of Kragujevac (Serbia)

Vice-Chair

Vladimir Milovanović	University of Kragujevac (Serbia)

Secretary

Vladimir Dunić	University of Kragujevac (Serbia)

Members

Aleksandar Bodić	University of Kragujevac (Serbia)
Miloš Pešić	University of Kragujevac (Serbia)
Anđela Perović	University of Kragujevac (Serbia)
Mirjana Piskulić	University of Kragujevac (Serbia)
Strahinja Milenković	University of Kragujevac (Serbia)

Supported by

Republic of Serbia

MINISTRY OF SCIENCE, TECHNOLOGICAL DEVELOPMENT AND INNOVATION

Sponsors

IC INŽENJERING D.O.O.
PROIZVODNO INŽENJERING PREDUZEĆE
SKLADIŠNI I TRANSPORTNI SISTEMI
www.icinzenjering.com; office @icinzenjering.com
Gornjomilanovačka 209, 34204 Divostin Kragujevac

jbr ndt

KONTROL INSPEKT

LOTRIČ METROLOGY

AXIOM TECH

MIND GROUP

VERTEX STAR
design & engineering

PREFACE:

Scientific conferences of Experimental Mechanics in Europe have here is a long tradition to cover all areas of experimental research in mechanics of materials and structures, including interactive fields. The first Danubia-Adria Symposium took place in 1984 in Stubicke-Toplice, Croatia, and further successfully continued in: 1985 – Graz, Austria, 1986 – Budapest, Hungary, 1987 – Plzen, Czech Republic, 1988 – Udine, Italy; 1989 – Mösern-Seefeld, Austria; 1990 – Pula, Croatia; 1991 – Gödöllö, Hungary; 1992 – Trieste, Italy; 1993 – Merin, Czech Republic; 1994 – Baden, Austria; 1995 – Sopron, Hungary; 1996 – Rajecké Teplice, Slovak Republic; 1997 – Porec, Croatia; 1998 – Bertinoro, Italy; 1999 – Cluj Napoca, Romania; 2000 – Prague, Czech Republic; 2001 – Steyr, Austria; 2002 – Polanica Zdroj, Poland; 2003 – Györ, Hungary; 2004 – Brijuni/Pula, Croatia; 2005 – Parma, Italy; 2006 – Zilina, Slovak Republic; 2007 – Sibiu, Romania; 2008 – Ceske Budejovice/Budweis, Czech Republic; 2009 – Leoben, Austria; 2010 – Wroclaw, Poland; 2011 – Siofok, Hungary; 2012 – Belgrade, Serbia; 2013 – Primosten, Croatia; 2014 – Kempten, Germany; 2015 – Stary Smokovec, High Tatras, Slovak Republic; 2016 – Portoroz, Slovenia; 2017 – Triest, Italy; 2018 – Sinaia, Romania; 2019 – Pilsen, Czech Republic; 2021 – Linz, Austria; 2022 – Poros, Greece, 2023 – Siofok; Hungary and 2024 – Gdansk, Poland.

The 41st Danubia-Adria Symposium in Kragujevac represent continuation to the series of fruitful meetings at the previous Danubia-Adria Symposia. The current Symposium DAS2025 is the second conference organized in Serbia. Serbia joint to Danubia-Adria Society on Experimental Methods in 2008 year and got active member in organization and participation of DAS which take place every year in one DA member country. This year Kragujevac has been chosen as the Conference venue and we are offering the hospitality for our Symposium. Serbian society for mechanics is the member of Danubia-Adria Society on Experimental Methods and University of Kragujevac, Faculty of Engineering is executive organizer of 41st Danubia-Adria Symposium in Advances in Experimental Mechanics.

The Faculty of Mechanical Engineering in Kragujevac, or today the Faculty of Engineering University of Kragujevac, was formed in October 1, 1960, as a department of the Faculty of Mechanical Engineering in Belgrade. The Faculty of Mechanical Engineering in Kragujevac became an independent faculty, within the University of Belgrade, on December 2, 1971. Since 1976, the Faculty of Mechanical Engineering has been part of the "Svetozar Marković" University in Kragujevac, today the University of Kragujevac.

The Faculty of Engineering University of Kragujevac is among the most reputable and prestigious scientific and educational institutions in the field of technical sciences. Today, it is a modern scientific and educational institution with a clearly defined mission, vision, goals and programmatic orientations.

The Danubia-Adria Symposium bring together internationally recognized experts and young researchers in an effort to exchange ideas on different topics of „Experimental Mechanics“. The conferences serve also a platform for establishing connections between different research teams and development of future scientific collaboration.

This year Danubia-Adria Symposium has received 57 accepted submissions from 10 countries (Austria-3, Croatia-3, Czech Republic-3, Germany-2, Hungary-7, Poland-4, Romania-3, Greece-1, Serbia-30, Bosnia & Herzegovina-1). The Program Committee selected 9 papers for keynote presentations and 48 papers for poster presentations.

We wish all participants a fruitful and enjoyable conference time in Kragujevac and hope that it will pave new ways for the development of Experimental Mechanics.

On behalf of the organizers, we would like to express our gratitude to all who showed their interest and actively helped us in preparing the event. It is a great pleasure to express our cordial thanks to all members of the Scientific Committee, to all members of the Local Organizing Committee, to all supporting institutions for their help.

Finally, on behalf of the Organizing Committee of the 41st Danubia-Adria Symposium in Advances in Experimental Mechanics, we wish a worm WELCOME to all participants in Kragujevac, and hope that all guests will have pleasant time in Serbia.

September, 2025
Kragujevac, Serbia

Chairman of 41st DAS 2025

Miroslav Živković

Vice-chairman of 41st DAS 2025

Vladimir P. Milovanović

TABLE OF CONTENTS:

KEYNOTE PRESENTATIONS:

POSTER AND ORAL PRESENTATIONS:

KEYNOTE PRESENTATIONS

41st Danubia-Adria Symposium Advances in Experimental Mechanics
September 23-26, 2025, Kragujevac, Serbia

Extended abstract

DOI: 10.46793/41DAS2025.003L

THE INFLUENCE OF BUILD PARAMETERS ON THE COLLAPSE BEHAVIOUR OF A HIGHLY POROUS RANDOM OPEN-CELL LATTICE 3D PRINTED IN IN718 ALLOY

Tomasz LIBURA[1], Judyta SIENKIEWICZ[2], Zdzisław NOWAK[3], Zbigniew L. KOWALEWSKI[4], Alexis RUSINEK[5], George Z. VOYIADJIS[6], Urvashi GUNPUTH[7], Paul WOOD[8]

[1] 0000-0003-0526-8973 Institute of Fundamental Technological Research, Pawińskiego 5B, 02-106 Warsaw, Poland. E-mail: tlibura@ippt.pan.pl

[2] 0000-0001-5372-1862 Faculty of Mechatronics, Armament and Aerospace, Military University of Technology, ul. Gen. S. Kaliskiego 2,00-908 Warsaw, Poland. E-mail: judyta.sienkiewicz@wat.edu.pl

[3] 0000-0003-4441-5112 Institute of Fundamental Technological Research, Pawińskiego 5B, 02-106 Warsaw, Poland. E-mail: znowak@ippt.pan.pl

[4] 0000-0002-8128-0846 Institute of Fundamental Technological Research, Pawińskiego 5B, 02-106 Warsaw, Poland. E-mail: zkowalew@ippt.pan.pl

[5] 0000-0002-8060-0844 Laboratory of Microstructure Studies and Mechanics of Materials, 7 rue Félix Savart, 57073 Metz, France, E-mail: alexis.rusinek@iniv-lorraine.fr

[6] 0000-0002-7965-6592 Affiliation, Department of Civil & Environmental Engineering, Louisiana State University, Baton Rouge, USA, E-mail: voyiadjis@eng.lsu.edu

[7] 0000-0002-8739-2427 Institute of Innovation in Sustainable Engineering (IISE), University of Derby, UK, E-mail: U.Gunputh@derby.ac.uk

[8] 0000-0002-9030-6868 Institute of Innovation in Sustainable Engineering (IISE), University of Derby, UK, E-mail: p.wood7@derby.ac.uk

1. Introduction

Nowadays, additive manufacturing (AM) is revolutionizing production, enabling the rapid fabrication of objects in various sizes and shapes, including complex designs such as metallic foam, while significantly reducing material waste. This paper examines the effect of 3D printing parameters (Set A and Set B) on the mechanical behavior of a highly porous random open-cell lattice (HPROCL) in IN718 alloy produced by selective laser melting (PBF-LM). The modified build parameters were applied to reduce manufacturing cost and time while minimizing micro porosity in ligaments by increasing exposure time through reduced laser scanning speed or higher energy density. Furthermore, the researchers investigate ligament deformation, key stages of collapse and stability, its role in impact resistance, and how microstructure influences the hardening behavior of the HPROCL across a wide range of strain rates. The SEM-EDS elemental distribution analysis carried out on the tested specimens enabled to conclude that the foam printed with modified parameters (Set B) contained a lower content of the Laves phase and a higher amount of the δ-phase, which led to an increase in both static and dynamic compressive behavior of HPROCL in IN718 alloy.

2. Materials and Methods

A Renishaw AM 250 SLM system with a Gaussian beam continuous wave (CW) laser (200 W power for set A and 175 W power for set B, 70 µm spot size, and 1070 nm wavelength) was used to manufacture the HPROCL in IN718 test pieces [1]. All test pieces were printed alongside the HPROCL. The SLM parameters to fabricate the cubic test pieces of set A (default build parameters) used an energy density of 2,2 to 5,5 (J/mm^2) for volume scanning and 0,6 to 3,1 (J/mm^2) for the surface. In turn, the energy density applied to the fabrication of set B samples (modified design parameters) was within the range from 1.9 to 4,9 (J/mm^2) while for volume scanning of the surface from 4,5 to 6,4 (J/mm^2). All test pieces were stress-relieved on the build plate. The diameter of ligaments in the lattice range in size from typically 0,4 to 1,2 mm, to give a volumetric porosity of 96% for a 25,4 x 25,4 x 25,4 cubic test piece, Fig. 1. Density measurements of samples were performed using Archimedes' method and computer X-Ray tomography (CT scan).

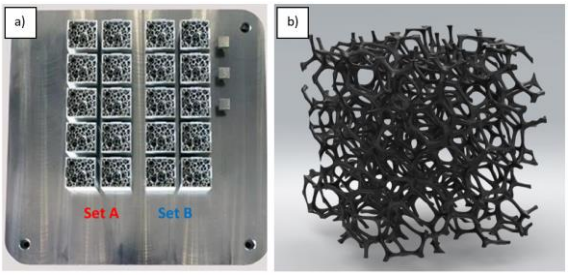

Fig. 1. SLM build record (a), HPROCL sample (b).

Testing of the lattice was performed in compression under quasi-static loading and high speed impact.

Static compression tests were carried out under displacement control. The load cell of the MTS testing machine was calibrated in the range of ±25 kN. The axial and transversal strain components were determined using two Aramis 12 M DIC systems positioned at opposite corners of the cubic test specimen. Recording frequency for image capturing was constant and equal to 2 Hz.

Dynamic compression tests were performed using the Direct Impact Hopkinson Pressure Bar (DIHPB) technique with the impact configuration which ensures large strain deformation of the specimen (up to densification in the case of cellular solids) [2], Fig. 2. The IN718 foam specimen located during each test at the front of the 6,0 m long output bar was directly impacted by the striker bar of length and mass equal to 0,6 m and 4760 g, respectively, (both made of C45). In order to record transmitted signals and determine force/stress on the loading surface of specimen, a pair of strain gauges placed 0,5 m from the front end of output bar was used. Position of strain gauges and length of output bar were chosen in such manner that enabled to avoid the wave superposition.

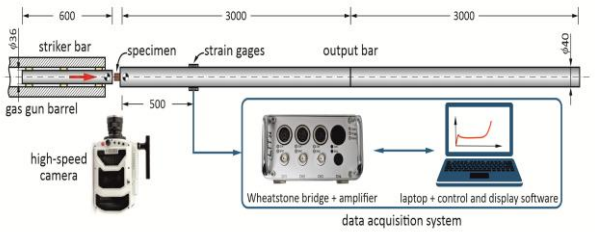

Fig. 2. DIHPB set-up.

Phantom V1612 high-speed camera was used to measure the compression rate and to identify the failure modes, as well as to confirm that the striker bar kinetic energy was sufficient to provide a nearly constant compression velocity of specimen up to the nominal strain equal to at least 0.5. High-speed video images were recorded with a resolution of 512×208 pixels and a frame rate of 110,000 fps. A crush test markers and specialized TEMA Classic software were applied to ensure high measurement accuracy based on video images. Impact velocity and deformation length history of specimens were determined by the subtraction of the displacements between the projectile and output bar. Thus, the corresponding nominal strain values can be calculated similarly to those in the quasi-static tests captured.

3. Results and Discussion

IN718 is well known for its outstanding mechanical properties due to precipitation strengthening, however, the Laves phase, that may appear in some cases (e.g. caused by shorter exposure time of laser power), often leads to deterioration of its mechanical properties, significantly [3]. Schirra et al. reported that the Laves phase observed in the grain boundary network reduces the room temperature impact and fracture toughness properties.

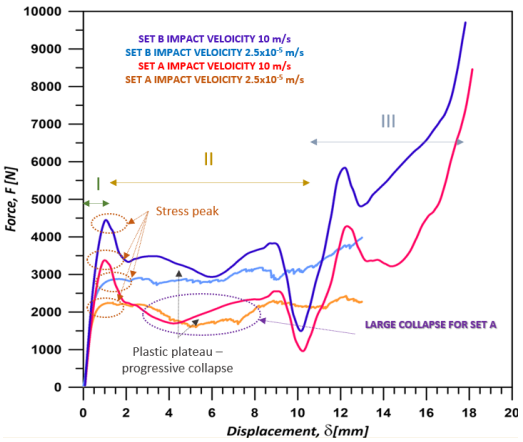

Fig. 3. Force-displacement curves for the specimens of set A and B under quasi-static and dynamic loading.

The SEM-EDS elemental distribution analysis carried out on the tested specimens enabled to conclude that the content of Laves phases in set B was much lower than that observed in set A. Moreover, set B was characterized by the higher amount of δ-phase which led to an increase in both static and dynamic compressive mechanical parameters of IN718 alloy produced by SLM with modified build parameters (set B).

Acknowledgements

The support of National Agency for Academic Exchange (NAWA, PPI/APM/2018/1/00045/U/001), Poland is greatly acknowledged.

References

[1] Wood, P., Libura, T. Kowalewski, Z.L., Williams, G., Serjouei, A. Influences of Horizontal and Vertical Build Orientations and Post-Fabrication Processes on the Fatigue Behavior of Stainless Steel 316L Produced by Selective Laser Melting. Materials, 2019, 12, 4203.

[2] Liu, J., He, S., Zhao, H., Li, G., Wang, M. Experimental investigation on the dynamic behaviour of metal foam: from yield to densification. Int J Impact Eng., 2018; 114: 69–77.

[3] Schirra, J.J., Caless, R.H., Hatala, R.W. The effect of laves phase on the mechanical properties of wrought and cast + hip inconel 718. The Minerals, Metals & Materials Society (TMS), 1991; 375-388.

41st Danubia-Adria Symposium Advances in Experimental Mechanics
September 23-26, 2025, Kragujevac, Serbia

Extended abstract DOI: 10.46793/41DAS2025.005P

INFLUENCE OF STRINGER GEOMETRY ON THE STRUCTURAL INTEGRITY OF CRACKED STIFFENED PLATES

Stefan-Dan PASTRAMA[1]

[1] 0000-0003-1099-702X, National University of Science and Technology POLITEHNICA, 313, Splaiul Independentei, Sector 6, 060042, Bucharest, Romania, E-mail: stefan.pastrama@upb.ro

1. Introduction

Aluminum stiffened panels are extensively used in aeronautical, automotive, marine industry, and in many other fields. They are light sheets reinforced by stringers in order to increase their strength and stiffness and are designed to cope with a variety of loading conditions. Usual stiffener cross-sections used in industry are rectangular, T-shaped, L-shaped, I-shaped, U-shaped, etc. They can be continuously attached to the plate or discretely attached by welding, bolting, riveting, bonding, etc.

Stiffeners improve the strength and stability of the structure and are also used to decrease or even stop the growth of cracks that can appear during the manufacturing process or in service. In order to avoid catastrophic failures, the knowledge of the crack size, stress field, material properties and the parameters used to assess the integrity of structures containing cracks should be known or calculated. Such parameters are the stress intensity factor (SIF), the J-integral or the crack tip opening displacement (CTOD). They can be obtained using analytical, numerical, or experimental methods.

In this paper, a part of a research involving the influence of different type of stringers on the structural integrity of thin aluminum plates is presented. Continuously attached stiffeners with rectangular, L and T-shaped cross-section are considered. Further, the results obtained using the finite element method (FEM) for a cracked plate with a rectangular stiffener are presented in two variants: with the stiffener broken and unbroken. The proposed numerical model is also validated by comparing the obtained results with those calculated using the compounding method, [1].

2. The studied structure and the finite element model

A thin aluminum plate continuously stiffened with a stringer having a rectangular cross section was first studied using FEM, for a constant remote stress $\sigma = 100$MPa. A crack symmetric with respect to the stiffener and having a length $2a$ was considered in two cases: broken stiffener and unbroken stiffener. The geometry of the cracked plate and stringers are shown in Fig. 1.

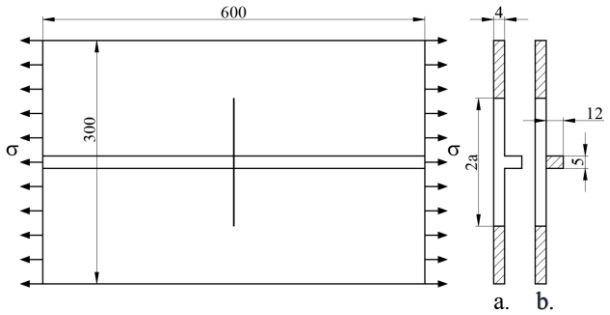

Fig. 1. The studied structure: a. Broken rectangular stiffener; b. Unbroken rectangular stiffener.

Different crack lengths were considered for the numerical analyses: $2a = 30$, 60, 90, 120, 150, 180, and 210 mm, corresponding to the ratios $2a/W$=0.1, 0.2, …, 0.7, where $W = 300$mm is the plate width.

The three-dimensional numerical analyses were undertaken using the software Ansys [2]. The elastic constants of the material of the plate and stiffener were taken as: Young's modulus E = 70GPa and Poisson ratio $\nu = 0.33$. Each model was meshed with tetrahedral elements, suitable for fracture mechanics analyses in Ansys, to obtain SIF. Depending on the crack length, the meshes contained between 82294 … 127493 nodes and 50217 … 74336 elements. A detail of the FE model for $a/W = 0.2$ (broken stiffener) with the map of von Mises stresses near the crack tips is shown in Fig. 2.

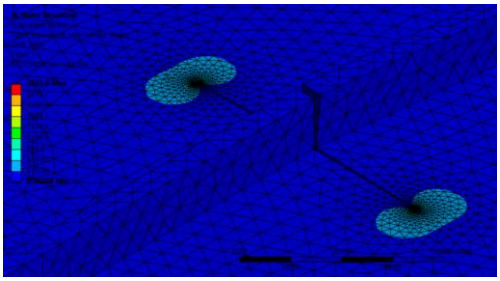

Fig. 2. Mesh in the crack tips area for 2a/W=0.2, broken stiffener

3. Results

For all studied cases, the main goal of the analyses was to obtain the stress intensity factor K_I as the fundamental parameter in linear elastic fracture mechanics, used to assess the structural integrity of a cracked structure. Results for SIF are presented in the dimensionless form $F = \frac{K_I}{\sigma\sqrt{\pi a}}$, as a function of the parameter $\lambda = \frac{2E_1 at}{AE_2}$, where E_1 and E_2 are the Young's moduli of the plate and stiffener, $A = 60$ mm^2 is the cross section area of the stiffener, and $t = 4$ mm is the thickness of the plate.

The models were validated by comparing the results with those obtained with the compounding method [1]. It is known that, even for a thin plate, SIF varies along the thickness of the plate and this variation can be emphasized if a three-dimensional analysis is performed [3]. The compounding results are obtained using equations available in the literature, and they are two-dimensional. The variation of SIF along the thickness and the value found using the compounding method for the case a/W=0.2 ($\lambda = 4$) in the case of broken and unbroken stiffener is presented in Fig. 3 as a function of the non-dimensional parameter d/t where d is the depth, measured from the stiffener side.

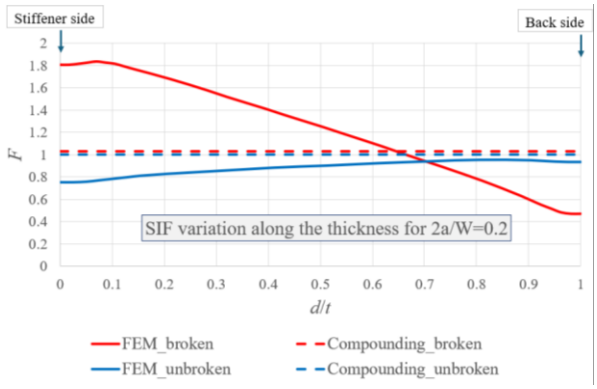

Fig. 3. SIF variation for $2a/W$=0.2.

One can notice that, in the case of a broken stiffener, the highest value of SIF occurs near the surface of the plate on the stiffener side and decreases along the thickness. The value that matches the one obtained using the compounding method occurs at a depth around 2.6 mm.

In the case of the unbroken stiffener, the variation of SIF along the thickness is opposite: the highest value occurs near the surface back to the stiffener. The compounding value underestimates the closest non-dimensional numerical SIF with about 5.2%, validating thus the numerical model. The same pattern is noticed for all studied crack lengths. A similar behavior was predicted in [2] for a cracked plate with two stiffeners.

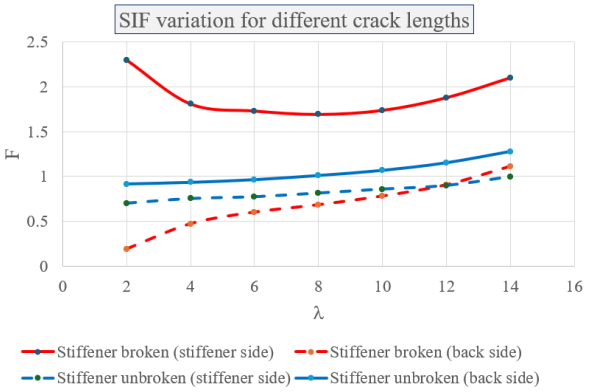

Fig. 4. Non-dimensional SIF variation for different crack lengths

Similar analyses are performed for stiffeners with L and T-shaped cross section, keeping the same area of the cross-section as for the rectangular stringer, in order to verify if the shape of the stiffener influences the values of SIF.

4. Conclusions

Extensive finite element analyses were conducted to study the structural integrity of aluminum thin stiffened plates with cracks crossing the stiffener and having different lengths. Also, different type of cross-section were considered for the stringers in order to find the influence of the stringer on the crack propagation and if the shape of the stringer influences the SIF values at the crack tips.

It can be concluded that, in the case when the stiffener is broken, the variation of SIF along the thickness is important and the results match the two-dimensional ones obtained with the compounding method close to the mid-plane of the plate, but closer to the surface opposite to the stiffener. In the case of unbroken stiffener, much smaller values of SIF are obtained. It can be emphasized also that the shape of the stiffener, keeping its cross-section area constant, is not significant.

References

[1] Cartwright, D.J. and Rooke, D.P. Approximate Stress Intensity Factors Compounded from Known Solutions, *Engng. Fracture Mech.*, 1974, 6, 563-571.

[2] Ansys® Student, Release 2025 R1, https://www.ansys.com/academic/students/ansys-student, ANSYS, Inc, 2025.

[3] Moreira, P.M.G.P., Pastrama, S.D., de Castro, P.M.S.T. Three-dimensional stress intensity factor calibration for a stiffened cracked plate, *Engng. Fracture Mech.*, 2009, 76(14), 2298-2308.

41st Danubia-Adria Symposium Advances in Experimental Mechanics
September 23-26, 2025, Kragujevac, Serbia

Extended abstract

DOI: 10.46793/41DAS2025.007H

IMPLEMENTATION AND PRACTICAL APPLICATION OF NON-EQUIVALENT BIAXIAL MEASUREMENTS FOR HYPERELASTIC MATERIALS

Kristóf HAVASI[1], Attila KOSSA[2]

[1] 0009-0009-9466-4636, Department of Applied Mechanics, Budapest University of Technology and Economics, University of Technology rkp. 3. Budapest, 1111, Hungary, E-mail: havasi@mm.bme.hu

[2] 0000-0003-3638-3237, Department of Applied Mechanics, Budapest University of Technology and Economics, University of Technology rkp. 3. Budapest, 1111, Hungary, E-mail: kossa@mm.bme.hu

1 Introduction

In the case of hyperelastic material models, it is not possible to reliably fit the parameters of the constitutive model to general load cases from a single set of uniaxial measurements. In order to obtain a more accurate model, different measurements are used, but these are very complex and difficult to perform in most cases.

The most commonly used measurement datasets for fitting are data from uniaxial and biaxial tensile tests and constrained uniaxial loading (planar tension), but due to the complexity of the measurement implementation, fitting is often done with less data. It can be seen that the stress-strain relationship obtained for the uniaxial and equibiaxial test cases envelops the case of planar tension from two sides, the application of which helps to define a better material model. Treloar's dataset also describes three different cases of experiments, in which the results of these tensile experiments were analysed [1]. However, if we perform biaxial measurements and can control the displacements along the two axes independently, we may be able to generate a new dataset that is neither uniaxial nor equibiaxial measurement data, this dataset describes an intermediate state. This way, we are also able to make other types of measurements in the same measurement setup, which can lead to a more accurate result when fitting a material model.

2 Details of work

In the present work, silicone specimens, which are capable of large elastic deformation, were used. These materials suffer negligible residual deformation even under high strain, and therefore, the mechanical behaviour can be well approximated by a hyperelastic material model [2]. For the measurements, we used an in-house developed biaxial material testing machine, which can be used to impose arbitrary independent displacements along the two axes using stepper motors, so that the specimen can be loaded to an arbitrary general biaxial stress state of our choice. A schematic illustration of the general biaxial in-plane loading case is shown in Fig. 1.

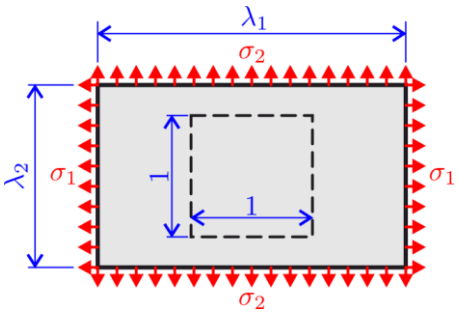

Fig. 1 Schematic representation of the general biaxial in-plane loading case.

During the measurements, the exact biaxial stress state we have prescribed is only present at the centre of the test specimen, so that the force and displacement quantities that can be easily measured physically are not sufficient for us to directly determine the numeric values we are looking for. However, knowing the load and the geometry of the specimen, it is possible to approximate the stress state using a stress distribution and a geometric factor [3,4]. A good approximation for the design and evaluation of the measurements is to assume the material to be incompressible. By imposing the strains along two perpendicular axes, we can determine the total deformation state for our load case at any instant. We can characterize a general biaxial stress case by its deformation gradient and stress tensor matrix, which can be written as

$$\boldsymbol{F} = \begin{bmatrix} \lambda_1 & 0 & 0 \\ 0 & \lambda_2 & 0 \\ 0 & 0 & \lambda_T \end{bmatrix}, \quad \boldsymbol{\sigma} = \begin{bmatrix} \sigma_1 & 0 & 0 \\ 0 & \sigma_2 & 0 \\ 0 & 0 & 0 \end{bmatrix}, \quad (1)$$

where λ_T is the transverse stretch. Note that $\lambda_1\lambda_2\lambda_T = 1$ for the incompressible case. If we impose displacement along the two axes independently, we can also align the elongations, so we are free to impose any relationship between the stretch values λ_1 and λ_2. Performing the measurements, we used a linear combination of the uniaxial and equibiaxial cases. The relationships for the principal stretches in this case are as follows:

$$\lambda_2 = (1-\alpha)\cdot\lambda_1^{-0.5} + \alpha\cdot\lambda_1. \quad (2)$$

For $\alpha = 0$, we obtain uniaxial loading, while for $\alpha = 1$, we obtain equibiaxial loading. It is important to note that in the case of planar tension loading, when using the above relationship, the stretch value in the 1-direction becomes a function of the α parameter, since for this loading mode $\lambda_2 = 1$. Solving the above equation for α yields

$$\alpha = \left(\lambda_1 + \sqrt{\lambda_1} + 1\right)^{-1}. \quad (3)$$

The resulting solution is illustrated in Fig. 2. Note that for $\lambda_1 = 1$, the value of α is 1/3, while for $\lambda_1 = 0$, it is 1.

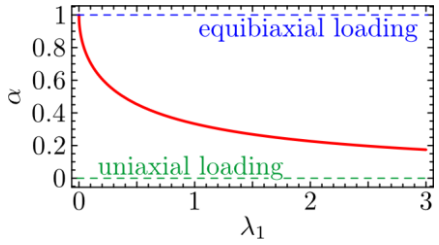

Fig. 2 Resulting values of the α parameter in the case of planar tension.

The stress solution for the general biaxial loading case can be derived analytically using the α parameter for most incompressible hyperelastic material models. This enables the parameter identification process to be carried out using closed-form expressions, facilitating the optimization task. Measurements can be performed using various values of the α parameter, thereby providing data corresponding to different loading conditions for the parameter fitting procedure.

Although the α parameter provides information about the loading mode, it does not directly indicate where the resulting stress state lies between uniaxial and equibiaxial stress conditions. To characterize the stress state, the stress triaxiality variable is a suitable choice. Stress triaxiality can be defined simply by relating the instantaneous hydrostatic stress to the instantaneous equivalent von Mises stress:

$$\eta = \frac{\sigma_h}{\sigma_{eq}^{vM}}. \quad (4)$$

This variable is widely used in damage mechanics models but can also be advantageously applied in this context.

3 Conclusions

Within the framework of this research, we have defined a general biaxial stress state, which relates two commonly used cases with continuous transitions, and given the analytical solutions for these cases in terms of strain and stress. In addition, a measurement setup suitable for the case presented previously was set up, and a series of measurements were made and evaluated, so that we were able to build a finite element model by generating useful numerical data, fitting a material model to the material, and comparing the measured results with simulations. With the newly proposed procedure, we are able to investigate the behaviour of a material in several cases without changing the experimental setup many times, which allows us to characterise the material under investigation more accurately.

Acknowledgments

This research was supported by the Hungarian National Research, Development and Innovation Office (FK 142457). This research was supported by the János Bolyai Research Scholarship of the Hungarian Academy of Sciences. The project supported by the Doctoral Excellence Fellowship Programme (DCEP) / University Research Scholarship Programme (URSP) is funded by the National Research Development and Innovation Fund of the Ministry of Culture and Innovation and the Budapest University of Technology and Economics, under a grant agreement with the National Research, Development and Innovation Office.

References

[1] Treloar, Leslie RG. Stress-strain data for vulcanised rubber under various types of deformation. *RUBBER CHEM TECHNOL*, 1944, 17.4 : 813-825.

[2] Havasi, K., Kossa, A. Development of a new hyperelastic constitutive model and implementation in a finite element software. In: *OGÉT 2023: XXXI International Conference on Mechanical Engineering*, Timisoara, 27-30 Apr., 2023.

[3] Havasi, K., Kossa, A. A novel approach to calculating the equibiaxial stress response from biaxial tests with non-homogeneous deformations *J STRAIN ANAL ENG*, 2025.

[4] Havasi, K., Kossa, A. Estimating equibiaxial stress-strain relation based on non-homogeneous biaxial measurement. *J THEOR APPL MECH*, 2025.

Extended abstract

DOI: 10.46793/41DAS2025.009D

GRP TANK LOADING INVESTIGATION USING CFS AND DFOS SENSORS

Karel DOUBRAVA[1], Nikola SCHMIDOVÁ[1], David BLAHA[1], Ctirad NOVOTNÝ[1], Zdeněk PADOVEC[1], Radek SEDLÁČEK[1], Radek KOTTNER[2], Milan RŮŽIČKA[1]

[1] 0000-0003-2975-321X, Czech Technical University in Prague, Faculty of Mechanical Engineering, Technická 4, 166 07 Praha 6, Czech Republic, E-mail: Karel.Doubrava@fs.cvut.cz
[2] 0000-0003-2606-5948, Czech Technical University in Prague, Faculty of Mechanical Engineering, Technická 4, 166 07 Praha 6, Czech Republic, E-mail: Nikola.Schmidova@fs.cvut.cz
[3] 0000-0002-6856-8116, Czech Technical University in Prague, Faculty of Mechanical Engineering, Technická 4, 166 07 Praha 6, Czech Republic, E-mail: David.Blaha@cvut.cz
[4] 0000-0002-3865-6684, Czech Technical University in Prague, Faculty of Mechanical Engineering, Technická 4, 166 07 Praha 6, Czech Republic, E-mail: Ctirad.Novotny@fs.cvut.cz
[5] 0000-0002-6094-2804, Czech Technical University in Prague, Faculty of Mechanical Engineering, Technická 4, 166 07 Praha 6, Czech Republic, E-mail: Zdenek.Padovec@fs.cvut.cz
[6] 0000-0001-8468-5921, Czech Technical University in Prague, Faculty of Mechanical Engineering, Technická 4, 166 07 Praha 6, Czech Republic, E-mail: Radek.Sedlacek@fs.cvut.cz
[7] 0000-0001-9027-1303, ACO Industries Tábor; Průmyslová 1158, Sezimovo Ústí, Czech Republic, E-mail: rkottner@aco.cz;
[8] 0000-0002-4665-1402 Czech Technical University in Prague, Faculty of Mechanical Engineering, Technická 4, 166 07 Praha 6, Czech Republic, E-mail: Milan.Ruzicka@fs.cvut.cz

1. Introduction

Surface water management is one of the main topics nowadays. The Glass Reinforced Plastic (GRP) surface water treatment tank is one of the important parts of the system chain solution. GRP tanks are placed below the surface, and during the placement process, high loads can occur on the tank structure. The possibility of monitoring loading using sensors is being investigated. Resistive and optical sensors were installed on the surface of the vessel, and verification measurements were performed during the vacuum test of the vessel. The obtained results were compared with the FEM calculation.

2. Method

The body of the investigated vessel is manufactured using the winding technology, where the bottoms and other technological inputs and outputs are subsequently manually connected to the body. Locations suitable for monitoring the load of the structure were selected based on the initial FEM calculation. The vicinity of the service input was selected for the installation of sensors. Strain Gauges (SG), Carbon Fiber Sensors (CFS), and Distributed Fiber Optic Sensing (DFOS) sensors were used for measurement.

3. Measurement

Two specimens were loaded under vacuum at four load levels. Three types of sensors were used to determine the tank loading.

3.1 Strain Gauges

HBM LY-11-6/350 strain gauges were used and were glued with cyanoacrylate adhesive and connected to the HBM QuantumX 1615B measuring unit, as well as CFS sensors. The strain gauges were installed in the tangential and radial directions on specimen 1, see Fig. 1, and in the tangential direction following the CFS sensor direction on specimen 2, see Fig. 2. Specimen 1 with installed sensors is shown in Fig. 3.

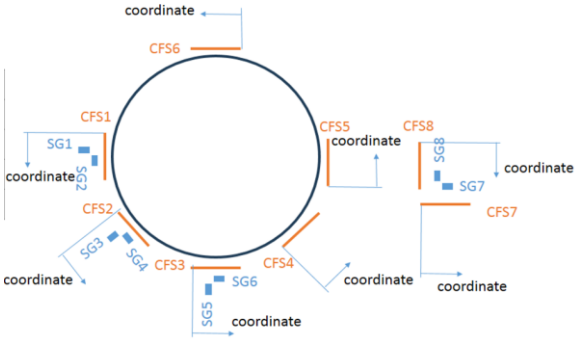

Fig. 1. Schema of sensors placement around service input -- Specimen 1.

3.2 Carbon Fiber Sensors

Carbon Fiber Sensors (CFSs) were prepared in ta length of 200 mm from carbon fiber roving T300 1000-50A. The methodology for the manufacturing of the CF sensor was described in [1], and the identical approach was implemented in this investigation. A nickel electrolyte coating was applied to the ends of each roving. Subsequently,

thin copper wire was used to establish electrical connections. Prepared CFSs were installed on the polished, clean, degreased surface of the tank. In the area near the inlet were installed 6 sensors for specimen 1 were installed according to Fig. 1. 6 CSF sensors were placed on specimen 2 as shown in Fig. 2.

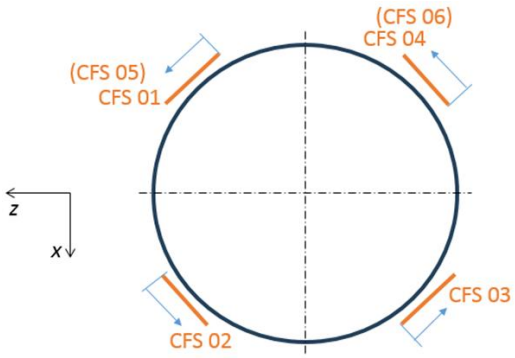

Fig. 2. Schema of sensors placement around service inputs -- Specimen 2.

3.3 Distributed fiber optic sensing sensors

A Distributed Fiber Optic Sensing (DFOS) system is used in this measurement for its unique properties – dense measurements of the strain points along the length of the fiber optic sensor. This is especially valuable in the development of new products or systems with complicated material layouts, such as composite structures. With this method, it is possible to evaluate material properties in a wider context of the larger structures. In this case, the sensor is placed along the critical spot – the neck of the water tank.

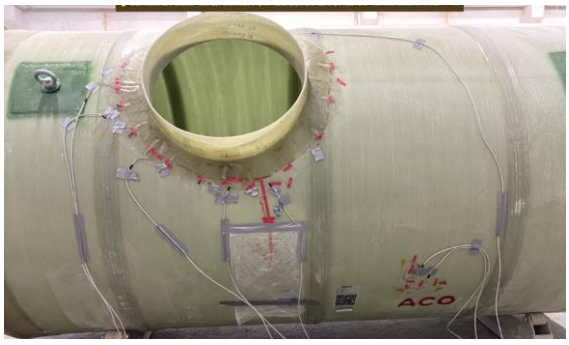

Fig. 3. Specimen 1 with installed sensors.

For the installation, the main DFOS sensor was prepared and welded for ad-hoc use at a length of 4.8 m. The DFOS sensor was installed with cyanoacrylate adhesive. CFS sensors and DFOS sensors were placed together in the prepared sections in a tangential direction along the neck of the tank. The strain from DFOS sensors was measured with the optical interrogator Luna ODISI 6100 system based on the Rayleigh backscattering principle.

4. Numerical analysis

Numerical analysis was performed in ABAQUS CAE. Continuum shell elements were used to model the vessel body. The sensors are modeled by beam elements that are connected to the tank by a Tie connection. The model allows for obtaining the strain course in the direction of the longitudinal axis of the sensor. The tank model is loaded with negative pressure, just like in the experiment. FE mesh of specimen 2 is shown in Fig. 4.

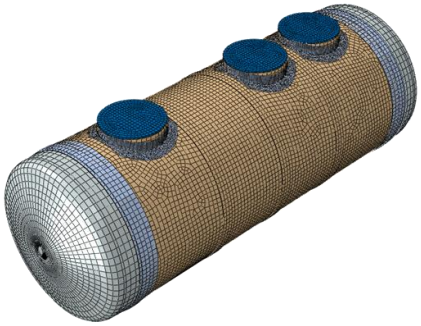

Fig. 4. FE mesh of specimen 2.

5. Conclusions

Data obtained from measurements on sample 1 showed differences with the numerical solution in some places, caused by certain differences between the numerical model and the actual design of the tank. About the level of the measured signals, measurement locations corresponding to CFS2 and CFS4 locations on sample 1 were selected for sample 2, see Fig. 2. The results obtained from the experiment on specimen 2 and the numerical solution were in good agreement in some places, while larger differences were found in others. Because signals from different sensors in given places showed similar levels of detected strains, the differences between the experiment and the numerical solution are caused by imperfections in the ideal shape of the tank. Further research should enable the potential of the mentioned sensors to be exploited for a given application, i.e., a low-cost solution for monitoring vessel stress during installation.

Acknowledgments

The work was supported by the project TN02000010 of the National Competence Centre of Mechatronics and Smart Technologies for Mechanical Engineering is co-financed from the state budget by the TACR within the National Centres of Competence Programme.

References

[1] Horoschenkoff, A., Christner, C. Carbon Fibre Sensor: Theory and Application, *Composites and Their Applications*, Hu, N. ed. InTech, 2012. https://doi.org/10.5772/50504.

41st Danubia-Adria Symposium Advances in Experimental Mechanics
September 23-26, 2025, Kragujevac, Serbia

Extended abstract DOI: 10.46793/41DAS2025.011L

IDENTIFICATION OF ENERGETIC AND DISSIPATIVE FLOW STRESS USING INFRARED THERMOGRAPHY

Nikola LALOVIĆ[1], Thomas BÖHLKE[2]

[1]0009-0002-6069-1088, Karlsruhe Institute of Technology (KIT) – Institute of Engineering Mechanics – Continuum Mechanics, Kaiserstr. 10, 76131 Karlsruhe, Germany, E-mail: nikola.lalovic@kit.edu;

[2]0000-0001-6884-0530, Karlsruhe Institute of Technology (KIT) – Institute of Engineering Mechanics – Continuum Mechanics, Kaiserstr. 10, 76131 Karlsruhe, Germany, E-mail: thomas.boehlke@kit.edu

1. Introduction

Based on own continuum-thermomechanical considerations extending [1], not only the energy stored and dissipated during plastic deformation of metals can be determined using infrared thermography (IRT), but also the flow stress can be additively separated into an energetic and dissipative component. An experimental-numerical methodology as well as some results for oxygen-free copper Cu-OF in pre-deformed and recrystallized condition are presented.

2. Materials and Methodology

To identify the energetic and dissipative components of flow stress, σ_{energ} and σ_{diss}, respectively, during plastic deformation, we combine quasi-static uniaxial tensile testing with in-situ infrared thermography (IRT). The experimental setup consists of a custom-built biaxial testing machine (based on the ZwickRoell Z150) and a high-resolution mid-wave infrared range (1.5–5.7 µm) camera (ImageIR 8340 S, InfraTec GmbH), offering high thermal sensitivity (<25 mK). Flat specimens of oxygen-free copper (Cu-OF, EN CW008A), prepared according to ISO 6892-1, were tested in both as-received (worked) and recrystallized conditions. Recrystallization was achieved by annealing at 400 °C for 30 minutes followed by water quenching.

To ensure accurate thermal measurements, the specimen surface facing the IR camera was coated black to achieve a high emissivity ($\varepsilon = 0.99$). Prior to testing, specimens were thermally equilibrated with the environment. Tests were conducted at a crosshead speed of 0.025 mm/s (initial strain rate ~9×10^{-4} s^{-1}), with mechanical and thermal data recorded at 10 Hz and 20 Hz, respectively.

Thermal data were processed using a digital image analysis routine based on the inverse solution of a simplified 2D heat conduction equation. Gaussian filtering and Laplacian-of-Gaussian smoothing were applied to mitigate noise amplification from derivative operations. A central region of interest (60×200 pixels) was extracted to avoid edge effects. The resulting pixel-wise field data enabled the quantification of internal heat sources, facilitating the separation of σ_{energ} and σ_{diss} contributions. The methodology closely follows and extends the framework proposed in [2], with recent adaptations for high-resolution IRT and advanced image processing. Key process parameters were identified through dedicated experiments and numerical optimization.

The characteristic time of heat transfer τ_{th}, which governs the rate of thermal exchange with the environment, was determined by heating a specimen uniformly and observing its cooling behavior via IRT. Assuming no internal heat generation, τ_{th} was optimized by minimizing the residual heat source field using a least-squares objective function.

The spatial smoothing parameter σ_{lap} for the Laplacian-of-Gaussian (LoG) filter was calibrated using synthetic temperature fields generated via finite element analysis (FEA) in Abaqus. These simulations modeled a constant internal heat source and fixed boundary temperatures. Gaussian white noise was added to match experimental conditions. The optimal σ_{lap} was found by minimizing the deviation between the reconstructed and simulated heat source fields. Both optimization problems were solved using the L-BFGS algorithm with multiple randomized initializations to ensure robustness. This methodology is similar to the one described in [3].

3. Results

Key parameters for thermal image analysis were identified through dedicated experiments and simulations. The characteristic time of heat transfer was determined from cooling tests on insulated specimens, yielding $\tau_{th} = 320$ s. Its sensitivity to temporal and spatial filtering parameters (σ_t, σ_{xy}) was found to be minimal. The optimal LoG filter parameter ($\sigma_{lap} = 22$ px) was identified using finite element simulations with added Gaussian noise averaging over multiple noise realizations.

Using these calibrated values, deformation-induced heat sources were reconstructed from infrared thermography data and used to decompose the flow stress into energetic and dissipative components. Mechanical testing showed minimal scatter. For worked Cu-OF, the dissipative stress component dominated the early plastic regime, while the energetic component exhibited a sharp initial drop followed by a gradual increase. This behavior might be attributed to microstructural reorientation due to the change in deformation path. In contrast, recrystallized Cu-OF showed a more balanced evolution, with the energetic stress steadily increasing and contributing up to one-third of the total flow stress at higher strains.

The Taylor-Quinney factor, defined as the ratio between dissipated heat power and mechanical work power supplied, stabilized around 0.7 for both conditions, with an initial overshoot observed in the recrystallized state. These findings can serve as a validation of the specific setup and the method's capability to resolve the thermomechanical response and provide a robust experimental basis for validating constitutive models that account for energy partitioning during plastic deformation.

4. Conclusions

A custom tensile setup, high-resolution thermal imaging, and a dedicated image processing routine enabled spatially and temporally resolved reconstruction of deformation-induced heat sources, accurate evaluation of the heat conduction equation and subsequent stress partitioning. The results show that both stress components evolve with plastic strain and are path-dependent, challenging the assumption of constant dissipative stress. The Taylor-Quinney factor derived directly from experimental data remained relatively stable during monotonic loading. Overall, the method provides a robust, non-invasive approach for quantifying internal energy storage and validating thermomechanically consistent constitutive models, offering new experimental insights into the coupling between mechanical work and thermal dissipation. The method's potential to infer microstructural evolution from macroscopic measurements represents a promising direction for future research.

References

[1] Rosakis, P., Rosakis, A.J., Ravichandran, G., Hodowany. J. A thermodynamic internal variable model for the partition of plastic work into heat and stored energy in metals. *J Mech Phys Solids*, 2000, 48(3), 581–607.

[2] Chrysochoos, A., Louche, H. An infrared image processing to analyse the calorific effects accompanying strain localisation. *Int J Eng Sci*, 2000, 38(16), 1759–88.

[3] Delpueyo D, Balandraud X, Grédiac M. Heat source reconstruction from noisy temperature fields using an optimised derivative Gaussian filter. *Infrared Phys Techn*, 2013, 60, 312–22.

Extended abstract
DOI: 10.46793/41DAS2025.013G

NOVEL TEST METHODS FOR TRIBO/MECHANICAL PROPERTIES IN THE CONTEXT OF ALTERNATIVE FUELS

Florian GRÜN[1], Peter OBERREITER[2], Philipp RENHART[3], Michael PUSTERHOFER[4]

[1] 0000-0002-6637-8140, Montanuniversität Leoben, Chair of Mechanical Engineering, Franz Josef-Straße 18, 8700 Leoben, Austria, E-mail: florian.gruen@unileoben.ac.at;

[2] 0009-0007-1607-3617, Montanuniversität Leoben, Chair of Mechanical Engineering, Franz Josef-Straße 18, 8700 Leoben, Austria, E-mail: peter.oberreiter@unileoben.ac.at;

[3] 0000-0001-8238-907X, Montanuniversität Leoben, Chair of Mechanical Engineering, Franz Josef-Straße 18, 8700 Leoben, Austria, E-mail: philipp.renhart@unileoben.ac.at;

[4] 0000-0001-7677-0392, Montanuniversität Leoben, Chair of Mechanical Engineering, Franz Josef-Straße 18, 8700 Leoben, Austria, E-mail: michael.pusterhofer@unileoben.ac.at

1. Introduction

Alternative fuels such as hydrogen, ammonia, and methanol are becoming increasingly important to meet global climate goals. However, their impact on mechanical and tribological properties is not yet fully understood. This creates a pressing need for the development of novel experimental methods to establish reliable design criteria for components exposed to these fuels. To date, hydrogen embrittlement has been the most extensively studied in this context [1].

2. Methodology and Results

To address the challenges posed by alternative fuels, the experimental methods at the Chair of Mechanical Engineering were systematically expanded. A key challenge lies in ensuring safety, as hydrogen is flammable over a wide range of concentrations, while ammonia and methanol are highly toxic. Consequently, small volumes and permanently sealed systems were prioritized in the design and implementation of the test setups.

2.1 Mechanical Properties – Hollow Specimen Technology

The hollow specimen technology offers several advantages, including small gas volumes, high pressure resistance, and the ability to conduct tests at elevated temperatures. The technology was further developed to meet the specific requirements of our laboratory as depicted in Figure 1. Recently, a new standard, ISO 7039:2024 [2], has been established for this method. The main challenges were the design of a clamping system within the test rig and the precise manufacturing of the internal bore with diameters of 2.4 mm and 3 mm. A specialized process was developed to polish the internal surface and measure its roughness using a Mahr contour measurement system. Additionally, a procedure was devised to mount and purge the specimens, ensuring the required purity inside the sample. Tests can now be performed using gas mixtures at pressures up to 1000 bar and temperatures up to 600 °C, achieved through inductive heating.

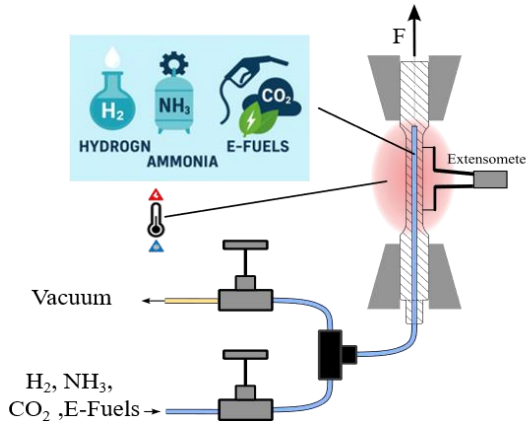

Fig. 1. Hollow specimen technology

In this study the steel 17-4 PH was used as a benchmark material as it shows a high sensitivity to hydrogen embrittlement. Tensile tests were conducted at a low strain rate of 5e-5 [1/s] (SSRT). Figure 2 presents a comparison of results for 200 bar hydrogen, 200 bar argon, and a solid specimen used as a reference. A 90% reduction in elongation at fracture was observed in hydrogen compared to argon. However, the Young's modulus, Yield strength and ultimate tensile strength did not change.

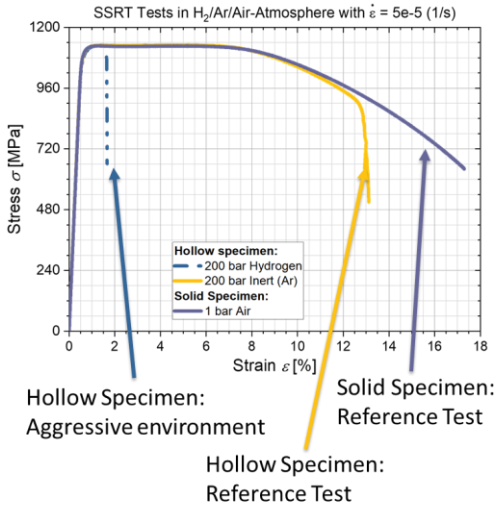

Fig. 2. Results SSRT (hollow specimen technology)

Figure 3 illustrates the effect of hydrogen on fatigue properties as low cycle fatigue tests (LCF) were performed. When plastic strain components are present, the number of cycles to failure decreases, and the scatter in results increases.

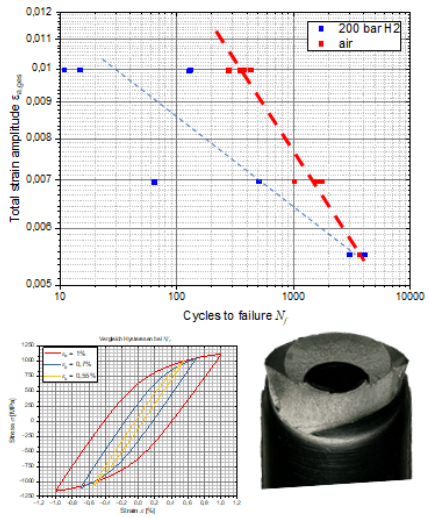

Fig. 3. Results LCF (hollow specimen technology)

2.2 Tribological properties

To investigate the effects of different atmospheres on tribological conditions, such as those in ball bearings, a novel test cell based on the ball-on-rod principle was developed. In this setup, three balls are pressed radially onto a rotating rod.

Key challenges included the implementation of a magnetic feedthrough, which eliminates the need for moving seals, and the integration of a specialized measurement system to record contact forces in-situ. The autoclave's dead volume was minimized to meet safety requirements. Figure 4 depicts the realized design.

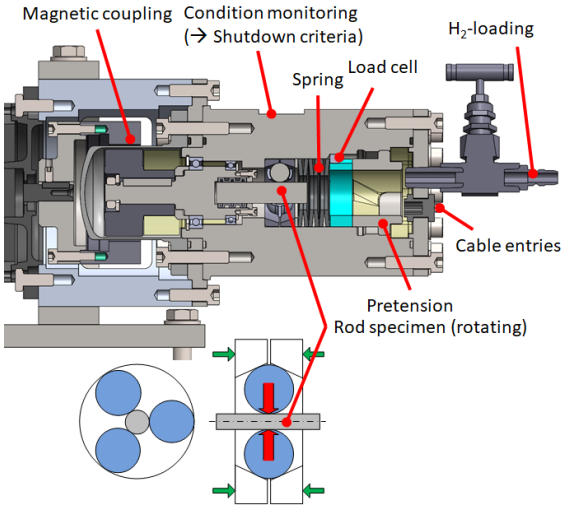

Fig. 4. Ball-on-rod test configuration

In addition, a model test configuration for Ring-on-Liner contacts was set-up enabling the testing under hydrogen and methanol atmospheres under lubricated conditions.

3. Conclusions / Outlook

The results demonstrate the feasibility of these complex test setups and their ability to simulate challenging environmental conditions safely. Future work will focus on expanding the range of testable gases and refrigerants.

Hollow Specimen Technology:

- Investigating the influence of notches, where localized plastic deformation occurs, by introducing internal notches into the specimens.
- Correlating LCF results with autoclave tests under comparable specimen conditions.

Tribological systems:

- Ball-on-Rod: Implementing an improved in-situ force measurement system for aggressive environments and enhancing the cage guidance system for better performance.
- Ring-on-Liner: Enhance towards ammonia.

References

[1] Michler, T., Ebling, F., et al., Comparison of tensile properties of X60 pipeline steel tested in high pressure gaseous hydrogen using tubular and conventional specimen, *International Journal of Hydrogen Energy*, 2022, 47 (81), 34676–34688

[2] ISO 7039:2024, Metallic materials — Tensile testing — Method for evaluating the susceptibility of materials to the effects of high-pressure gas within hollow test pieces, 2024

41st Danubia-Adria Symposium Advances in Experimental Mechanics
September 23-26, 2025, Kragujevac, Serbia

Extended abstract DOI: 10.46793/41DAS2025.015T

THE DEPENDENCE OF THE DEGREE OF NON-ADDITIVITY OF MECHANICALLY LOADED SYSTEMS ON THE LOADING RATE

Dimos TRIANTIS[1], Ilias STAVRAKAS[2], Ermioni D. PASIOU[3], Stavros K. KOURKOULIS[4]

[1] 0000-0003-4219-8687, University of West Attica, Dept. of Electrical & Electronics Engineering, Electronic Devices and Materials Lab., 250 Thivon Avenue, 122 44, Athens, Greece, E-mail: triantis@uniwa.gr;

[2] 0000-0001-8484-8751, University of West Attica, Dept. of Electrical & Electronics Engineering, Electronic Devices and Materials Lab., 250 Thivon Avenue, 122 44, Athens, Greece, E-mail: ilias@uniwa.gr;

[3] 0000-0003-1580-3415, National Technical University of Athens, School of Applied Mathematical & Physical Sciences, Dept. of Mechanics, Lab. for Testing and Materials, Zografou Campus 157 73, Athens, Greece, E-mail: epasiou@central.ntua.gr;

[4] 0000-0003-3246-9308, National Technical University of Athens, School of Applied Mathematical & Physical Sciences, Dept. of Mechanics, Lab. for Testing and Materials, Zografou Campus 157 73, Athens, Greece, E-mail: stakkour@central.ntua.gr;

1. Introduction

Considering that the phenomenon of fracture is a manifestation of the series of non-linear processes, which characterize complex dynamical systems, it is reasonable to approach the specific phenomenon using advanced statistical tools rather than traditional Statistical Mechanics [1,2], taking into account that the response of such systems (at non-equilibrium stages) is not compatible to the thermodynamic principle of additivity.

This incompatibility is attributed to the non-independent nature of the processes responsible for fracture, which, after specific load levels tend to produce well-organized and mutually interacting networks (sub-systems) of micro-cracks. In this context, Boltzmann-Gibbs (BG) Statistical Mechanics (and the respective BG entropy concept, S_{BG}) must be properly modified to cope with such phenomena, which are characterized by long-range interactions and memory effects (in other words by non-additivity), giving birth to the relatively new discipline of Non-Extensive Statistical Mechanics (NESM). Among various NESM formulations, the one most broadly used is that introduced by Tsallis [1], based on an extended definition of entropy, as:

$$S_q = k\frac{1-\sum_{i=1}^{w} P_i^q}{q-1} \quad (1)$$

where k is Boltzmann's constant, P_i the probability of the i^{th} configuration, w the number of possible configurations, and, q the entropic index, quantifying the degree of non-additivity of the system [1].

While S_{BG}, is maximized by the Gaussian (distribution), S_q is maximized at distributions denoted as q-Gaussians, described as [2]:

$$P(\chi,\beta) = A_q e_q\left(-\beta_q \chi^2\right) \quad (2)$$

In Eq.(2) A_q and β_q are numerical constants and $e_q(z)$ stands for the q-exponential function, which is defined as follows [1, 2]:

$$e_q(z) = [1+(1-q)z]^{\frac{1}{1-q}} \quad (3)$$

Within the frame of the above argumentation, an attempt is described here to explore the potential dependence of the degree of non-additivity of a mechanically loaded system (i.e., specimens made of brittle rock) on the loading rate imposed externally, by quantifying the respective values of the q-index.

2. Materials and methods

To achieve the target of this study, advantage is taken of experimental data gathered from a protocol (described thoroughly in a previous publication [3]) comprising uniaxial compression tests with prismatic specimens made of Dionysos marble (which is used for the needs of the ongoing restoration project of the Athenian Acropolis). The acoustic activity was recorded using sensors of the R6α type. The principal characteristic of that protocol is that the loading rates imposed varied within a relatively broad interval, ranging from 34 to 350 kPa/s.

The quantity used here, to explore the self-organized state of the fracture process, is the amplitude,

A, of the Acoustic Emissions, expressed in terms of the so called "*variable returns*" parameter [4, 5] (quantifying, in fact, the fluctuations of the amplitudes), defined as:

$$(\delta A)_i = A(t_{i-1}) - A(t_i) \quad (4)$$

In Eq.(4) $A(t_i)$ is the amplitude of the signal that was recorded at the instant t_i. Usually, $(\delta A)_i$ is normalized over the variance σ, as:

$$(\Delta A)_i = \frac{(\delta A)_i - \mu}{\sigma} \quad (5)$$

where μ is the respective mean value.

As a next step, the interval of the values of $(\Delta A)_i$, namely the interval $[(\Delta A)_{min}, (\Delta A)_{max}]$, is divided into a number of sub-intervals of equal width. For each sub-interval the Probability Density Function (PDF) of the distribution of $(\Delta A)_i$ is determined in terms of the mean value δ of each one of the sub-intervals. Combining Eqs.(2) and (3) the PDF reads as:

$$PDF(\delta, \beta_q) = A_q\left[1 - (1-q)\beta_q \delta^2\right]^{\frac{1}{1-q}} \quad (6)$$

3. Results, discussion and conclusions

The experimental data are then fitted by means of Eq.(6) using commercial available software. A very good correlation is revealed, as it can be clearly seen from Fig.1, in which the q-Gaussian distributions are plotted for the four classes of loading rates imposed in the specific experimental protocol, (they were equal to 34, 84, 140 and 350 kPa/s).

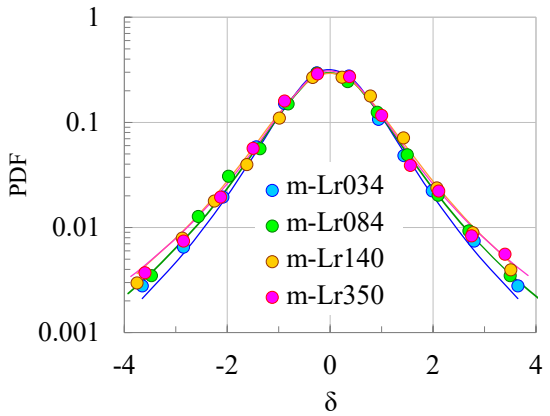

Fig. 1. The q-Gaussian distributions for the four classes of specimens.

The respective values of q, as obtained from the fitting procedure, are plotted in Fig.2, against the loading rate imposed. It is clearly seen that a monotonously increasing trend characterizes the response of q, suggesting, that the degree of non-additivity of the fracture process is an increasing function of the loading rate. The dependence of q on the loading rate seems to be governed by a power law (see Fig. 2), however additional protocols are necessary before definite conclusions are drawn.

A similar, positive correlation of the displacement rate (rather than of the loading rate) with q, was highlighted recently by Shan et al. [5], in terms of the evolution of the electric potential, for specimens made of various rocks. In that study, the potential use of q as pre-failure index was, also, suggested by the authors.

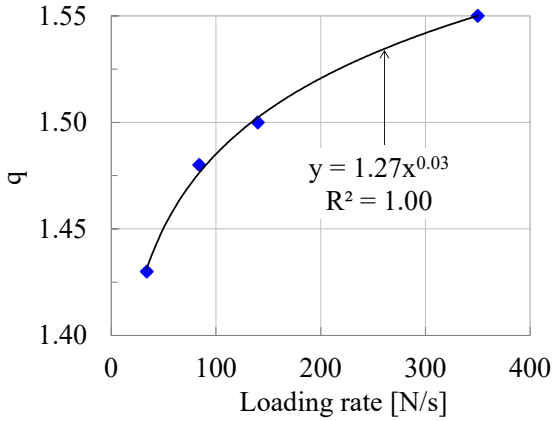

Fig. 2. The dependence of the entropic index q on the loading rate.

Concluding, it could be stated that increasing the loading/displacement rate the damage mechanisms activated within the bulk of a mechanically loaded system are intensified, leading to denser networks (subsystems) of micro-cracks, or, equivalently to further deviation of the system (and the respective processes) from additivity.

References

[1] C. Tsallis (2009). Nonadditive entropy and non-extensive statistical mechanics - An overview after 20 years, *Braz. J. Phys*., 39, 337–356.

[2] S. Umarov, C. Tsallis, S. Steinberg (2008). On a q-central limit theorem consistent with nonextensive statistical mechanics, *Milan J. Math*., 76(1), 307–328.

[3] D. Triantis, I. Stavrakas, E.D. Pasiou, S.K. Kourkoulis (2024). Exploring the acoustic activity in brittle materials in terms of the position of the acoustic sources and the power of the acoustic signals-Part II: Applications, *Forces Mech*., 15, 100265.

[4] D. Tsuji, H. Katsuragi (2015). Temporal analysis of acoustic emission from a plunged granular bed, *Phys. Rev. E*, 92, 042201.

[5] Shan T. et al. (2024). Failure evolution and disaster prediction of rock under uniaxial compression based on non-extensive statistical analysis of electric potential, *J Mining Sci. Technol*., 34, 975-993.

41st Danubia-Adria Symposium Advances in Experimental Mechanics
September 23-26, 2025, Kragujevac, Serbia

Extended abstract DOI: 10.46793/41DAS2025.017B

IMPACT VELOCITY INFLUENCE ON THE FRACTURE BEHAVIOUR OF PORCINE FEMURS UNDER DYNAMIC LOADING

Petra BAGAVAC[1], Marijo BEKIĆ[2], Lovre KRSTULOVIĆ-OPARA[3]

[1] 0000-0003-2027-3180, FESB, University of Split, R. Boškovića 21, Split, Croatia, E-mail: petra.bagavac@fesb.hr;

[2] 0000-0003-1754-6299, OB Dubrovnik, Dr. Roka Mišetića 2, Dubrovnik, Croatia, E-mail: marijob@bolnica-du.hr;

[3] 0000-0002-0823-9783, FESB, University of Split, R. Boškovića 21, Split, Croatia, E-mail: opara@fesb.hr;

1. Introduction

Bone is a complex tissue composed of inorganic, organic, and cellular components. Far from being inert, it is a metabolically active, dynamic structure that undergoes continuous remodeling throughout life. Most high-resolution imaging techniques are currently limited to ex vivo research due to radiation exposure, sample size restrictions, and long acquisition times. High-resolution computed tomography (HR-CT) and magnetic resonance imaging (HR-MR) can be performed in vivo, but have been used primarily for validating diagnostic methods and evaluating osteoporosis treatments.

A significant challenge in bone research lies in accurately classifying bone quality. Biomechanical studies on cadaveric material are needed to correlate clinically accessible parameters such as bone mineral density (BMD) with more precise histological and three-dimensional high-resolution imaging data.

This study presents experimental results on post-mortem porcine femurs, aiming to compare the mechanical response of bone under different impact velocities. The working hypothesis is that loading rate influences fracture mechanics: at lower velocities, fractures are expected to be ductile, while higher velocities are expected to produce brittle or even comminuted fractures.

2. Materials and Methods

Dynamic impact tests were conducted at the Structural Mechanics Laboratory, Faculty of Electrical Engineering, Mechanical Engineering and Naval Architecture, using an INSTRON Drop Tower 9450 (capacity: 222 kN). Adjustable test parameters included impact velocity (1–24 m/s), drop height (0.5–40 m), striker mass (up to 70 kg), impact energy (up to 1800 J), and striker geometry (wedge, spherical, or flat). For this study, impact energy was kept constant across tests (360 J), while impact velocity was varied. Two test series were performed: one at an impact velocity of 5 m/s and another at 10 m/s. Each series included four healthy femurs, resulting in a total of eight specimens tested.

Force–time data were recorded at up to 4 MHz and processed to determine absorbed energy, displacement, and velocity during impact. The fracture mechanism was assessed using the ductility index, calculated from the ratio of post-peak to peak absorbed energy. A ductility index below 30% indicates purely brittle fracture, while values above 60% correspond to purely ductile fracture:

$$Ductility\ index\ [\%] = \frac{(Energy\ at\ Total) - (Energy\ at\ Peak)}{Energy\ at\ Peak}. \quad (1)$$

Characteristic Ponits are shown in Fig 1.

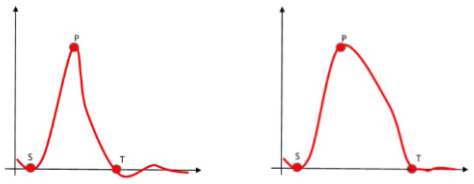

Fig. 1. Characteristic force–time diagram for a) ductile fracture, b) brittle fracture.

Fresh porcine femurs were obtained from animals of similar size, age, and sex, with comparable living conditions. Weight, volume, and length were measured for each specimen. Bones were tested fresh, within 48 hours post-mortem, to avoid dehydration.

3. Results

Bar charts compare the average values obtained from the two test series. It is evident that both the

maximum impact force and the fracture force are higher for impacts conducted at higher velocities (Figs. 2 and 3).

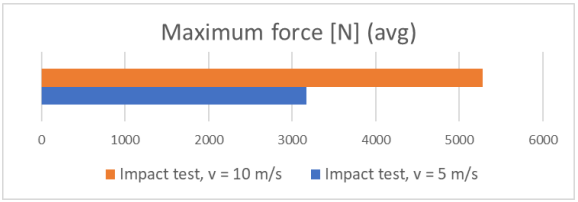

Fig. 2. Maximum (average) force.

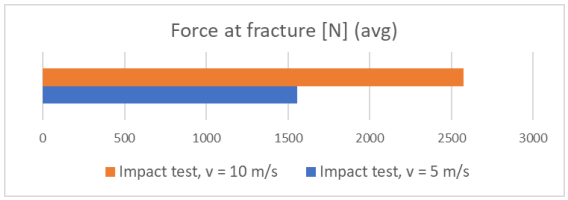

Fig. 3. (Average) force at fracture.

Conversely, displacements at maximum force and at fracture are greater for the lower-velocity impacts (Fig 4).

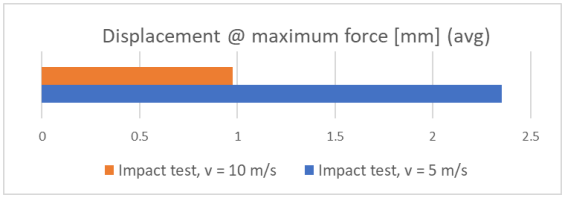

Fig. 4. (Average) displacement at fracture.

In Figs. 5 and 6 femur bones after impact tests are shown.

Fig. 5. Femur after dynamic testing at an impact velocity of 5 m/s

Fig. 6. Femur after dynamic testing at an impact velocity of 10 m/s

Of particular interest is the comparison of total absorbed energy during impact. The absorbed energy at lower impact velocity was clearly higher than that recorded at higher velocity, Fig. 7. This can be attributed to the fact that, at lower velocity, the bone had more time to undergo gradual plastic deformation and dissipate energy progressively, which supports the hypothesis that lower-velocity impacts promote more ductile fracture behavior. In contrast, higher-velocity impacts are predominantly characterized by brittle fracture mechanisms.

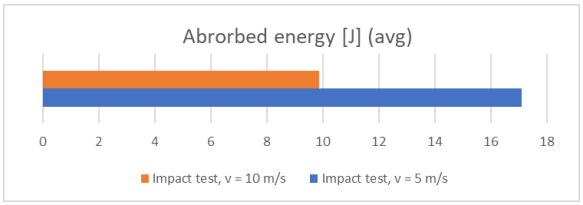

Fig. 7. (Average) absorbed energy during impact.

This study demonstrates that the fracture behavior of porcine femurs under dynamic loading is strongly dependent on impact velocity, Fig. 8.

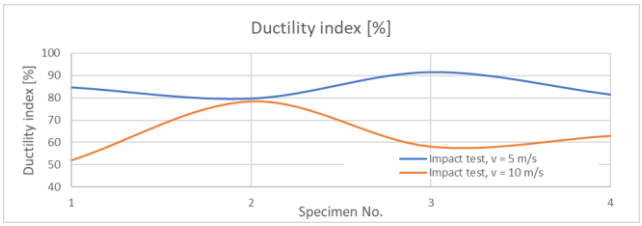

Fig.8. Comparison of ductility indices for fractures resulting from impacts at 5 m/s and 10 m/s.

4. Conclusions

Lower velocities favor ductile fracture mechanisms with higher energy absorption, while higher velocities promote brittle or comminuted fractures with reduced ductility. These findings support the hypothesis that loading rate is a critical factor in bone failure mechanics. The results provide a biomechanical basis for understanding fracture patterns in high-energy trauma and may assist in refining computational bone models and improving the design of orthopedic fixation devices.

References

[1] Donnelly E. Methods for assessing bone quality: a review. Clin Orthop Relat Res. 2010;469(8):2128–38.

[2] Hernandez CJ, Keaveny TM. A biomechanical perspective on bone quality. Bone. 2006;39:1173–81.

[3] [43] Kulić M, Bagavac P, Bekić M, Krstulović-Opara L. Ex Vivo Biomechanical Bone Testing of Pig Femur as an Experimental Model. Bioengineering. 2024; 11(6):572. https://doi.org/10.3390/bioengineering11060572.

41st Danubia-Adria Symposium Advances in Experimental Mechanics
September 23-26, 2025, Kragujevac, Serbia

Original scientific paper DOI: 10.46793/41DAS2025.019K

EXPERIMENTAL ANALYSIS OF HIGH-SPEED GEARBOXES

Nenad KOLAREVIĆ[1], Milosav OGNJANOVIĆ[2], Miloš STANKOVIĆ[3], Aleksandar DIMIĆ[4], Nikola DAVIDOVIĆ[5], Marko MILOŠ[6]

[1] 0000-0003-2836-7405, Faculty of Mechanical Engineering, Kraljice Marije 16, Belgrade, Serbia, E-mail: nkolarevic@mas.bg.ac.rs;

[2] 0000-0002-1118-0102, Faculty of Mechanical Engineering, Kraljice Marije 16, Belgrade, Serbia, E-mail: mognjanovic@mas.bg.ac.rs

[3] 0000-0002-4310-2184, Faculty of Mechanical Engineering, Kraljice Marije 16, Belgrade, Serbia, E-mail: mstankovic@mas.bg.ac.rs;

[4] 0000-0001-5495-0763, Faculty of Mechanical Engineering, Kraljice Marije 16, Belgrade, Serbia, E-mail: adimic@mas.bg.ac.rs;

[5] 0000-0002-0500-3388, Faculty of Mechanical Engineering, Kraljice Marije 16, Belgrade, Serbia, E-mail: ndavidovic@mas.bg.ac.rs;

[6] 0000-0002-1931-1170, Faculty of Mechanical Engineering, Kraljice Marije 16, Belgrade, Serbia, E-mail: mmilos@mas.bg.ac.rs;

1. Introduction

With the rise of rotation speed of the gears in the gearboxes several phenomena that can significantly affect the gearbox energy efficiency and reliability occur. A lot of experimental data is available in literature for peripheral speeds below 40-60 m/s. But above this value some load parameters are changing their trends so this value can be classified as a limit between low and high speed application. The main causes of power loss in gearboxes are tooth mesh losses, bearing losses, churning, windage, oil pocketing and gear drag [1]. Some literature shows that windage losses [2] which occur due to sliding friction of the high-speed gears in the oil-mist environment in the gearbox housing can be up to 30% or even more of the entire gear drive meshing losses. The phenomena of squeezing out the oil from the gear meshing area can also add more power losses in the system [3]. In the worst case when the backlash is very small, these phenomena can even create oil blockage. Some problems with hydrodynamic losses due oil retaining in some housing pockets can also lead to lower energy efficiency, Fig.1. All of the mentioned hydrodynamic losses are negligible in the low speed gearboxes, but in high speed gearboxes they can exceed basic gear teeth meshing losses and even become larger.

In the case of high speed gears, hydrodynamic losses represent a large portion of total power losses [4]. They can be approximately measured during gearbox operation at the maximum speed with no load. This means that these gearboxes have very low energy efficiency at the low load regimes because of high hydrodynamic losses. With power rise, the basic gear teeth meshing loss increases, while the increase in hydrodynamic losses is much less or negligible. The effect of this can be presented as an increase in energy efficiency of the high speed gearbox with the increase in load transmitted. Beside mentioned, some load parameters as dynamic factor lower their value, so power efficiency of high speed gearbox could reach even 0.99 value [5].

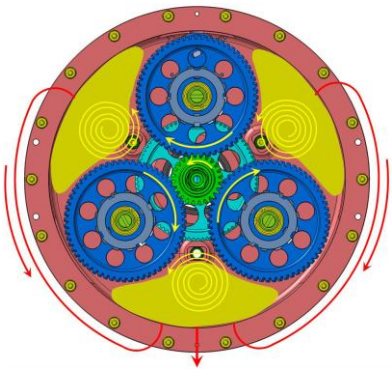

Fig. 1. Oil retaining pocket in gearbox housing [6]

For investigating the dependency of energy efficiency of the high speed gearbox with transmitted power increase, a special mechanical power circulation test rig [7] was developed at the EDePro company for testing its high speed gearboxes for aircraft application, i.e. for turbo shaft engines application. High speed gears can be found mostly in the aerospace industry. Every loss in power means lower thrust available for the aircraft. On the other hand, as all power losses are converted

to heat, more mass, through the larger heat exchanger, is added to the aircraft, which is also highly undesirable. So the increase in energy efficiency of such gearboxes is of great importance for future exploitation and performances of aircraft.

In this paper, an experimental investigation of hydrodynamic losses and basic gear meshing losses are presented for two types of high speed gearboxes. Also, the objective of this paper is to present and compare two types of test rigs for experimental measuring of gearboxes parameters.

2. Case study

The case study are two gearboxes one for helicopter application and other one for aircraft application. The concept used is split path gearbox, with power dividing intro 3 branches, Fig.2. The peripheral speeds of gears are in the area of high speed application. The power is brought with input gear 1 (green) which is engaged with three gears 2 (blue). In this way power is divided into 3 branches. Gears 2 are directly connected to smaller gears 3 (red arrows) on each of the three branches of the gearbox. Then those gears 3 are geared with output gear 4 which transmits all power further to the coupling through the splined shaft. Both gearboxes are designed for the same gas generator with power of 200 kW which is also developed at the EDePro company from Belgrade.

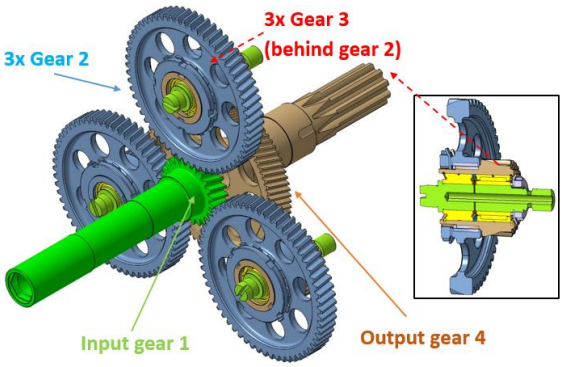

Fig. 2. Concept of the gearbox with power dividing into three branches [6]

The first gearbox, intended for helicopter application has a gear ratio of 6.67, see Fig.3. It reduces 40 000 rpm from the input shaft to 6 000 rpm of the output shaft. The peripheral speed of the first gear pair is around 100 m/s so it matches to high speed usage.

The second gearbox, intended for aircraft propeller drive has a ratio of 16, Fig.4. It reduces 40 000 rpm of input shaft rotation speed to 2 500 rpm of output shaft rotation speed. The peripheral speed of the first gear pair in this gearbox is around 76 m/s, which also matches to high speed usage.

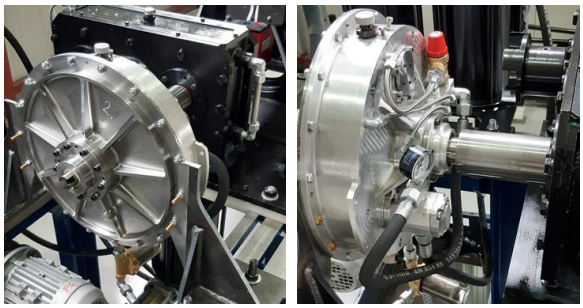

Fig. 3. High speed gearbox for helicopter application

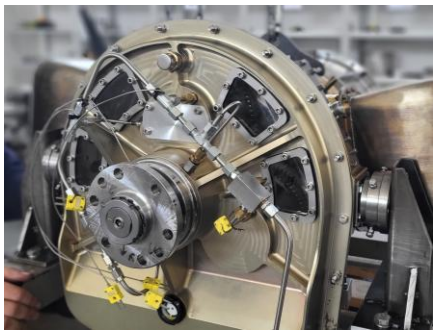

Fig. 4. High speed gearbox for propeller application

3. Test stand

The first one, helicopter gearbox, was experimentally tested on a test bench developed specially for the purpose of gears and gearboxes testing, Fig.5. A closed loop power circulation test rig, is developed as altered conventional one used only for gear experimental testing in order to accept two gearboxes facing each other. As it can be seen from Fig.5 in one branch of the device two high speed gearboxes (marked with numbers 6&7) are installed. They are placed in opposite position in order to connect the high speed shafts of each one together.

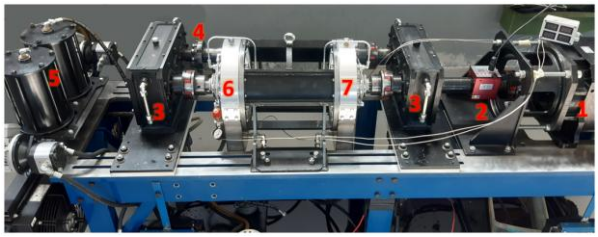

Fig. 5. Test stand with 2 gearboxes for helicopter application positioned opposite each other: (1) drive electromotor, (2) torque meter, (3) auxiliary gearboxes, (4) loading coupling, (5) oil supply system with pumps, (6&7) test articles – high speed gearboxes

From the right side in Fig.5, a drive electromotor (1) of 55 kW continual power is installed. This electromotor is used only to compensate for the

power losses in the system which are assumed not to be larger than 5% per gearbox, auxiliary and test. The entire system is driven by the electromotor at 6 000 rpm, except for the part which connects the high speed input shafts of the gearboxes which runs at 40 000 rpm (between 6 and 7). In order to achieve high precision and to minimize the misalignment of these shafts, a black cylindrical part is installed, see Fig. 5. Two auxiliary gearboxes (3) from each side of the branches are installed in order to connect the two central branches-shafts by transmitting the power at a distance between their axes. One branch is used to install the test article – high speed gearboxes (6) and (7), while the other one (behind the one in Fig. 5.) is used to install the loading coupling (4). By this coupling, the torque is introduced in the system in a steady state, in order to simulate the power inside the system. The torque is applied by coupling specially designed so it can be connected in arbitrary position, twisted for the desired angular deformation by level system as in Fig.6. By running the system at some rotational velocity, the torque simulates full power, trapped in the system of 2 branches, 2 auxiliary gearboxes and 2 testing high speed gearboxes. Outside of them, for example on the branch where the torque meter is installed, there is no power generated due to level system. But there is a need to overcome the resistance to rotation in the system, power loss, due to friction in gearboxes and bearings which is converted to heat. So, there is a need for an external electromotor which has to compensate only for those power losses. Lubrication and heat exchanging subsystems are also required together with an acquisition system for monitoring the controlling parameters.

Fig. 6. Level system for applying the to flange of the specially designed coupling

The second gearbox is experimentally tested in an open loop power circulation system, where the electromotor is used to drive the system with all available power and an engine free turbine is used as a brake, Fig. 7. In order to create a load, an actual turbine is installed on the input shaft. So, the maximum available power is the power of the electromotor, i.e. 55kW, which is much lower than the maximum gearbox operating power of 200 kW, but it serves well enough for determining the hydrodynamic losses and losses at that power.

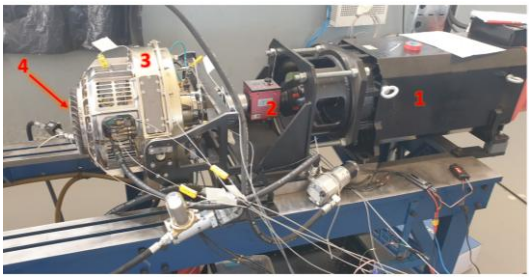

Fig. 7. Test stand with high speed gearbox for airplane application: (1) drive electromotor, (2) torque meter, (3) propeller gearbox, (4) free turbine

4. Experiments and results

The main advantage of the closed loop power circulating test rig is that it uses only the supply power equal to the power losses in the system. There is a need to differentiate between the power losses of the test rig, because it consists of two auxiliary gearboxes, and the power losses of the gearboxes which are tested. So, the first run is done on the required 6000 rpm with load and without the test articles – high speed gearboxes, in order to define the basic power losses of the test rig. The measured power losses of the empty system (without helicopter gearboxes) is 8.8 kW. This value represents the losses in the auxiliary gearboxes with the losses in the electromotor itself. Then during the test with the installed high speed gearboxes, as in Fig.5, the electromotor required the power of 23 kW in the first minute of operation. As time passes this power drops to 20.5 kW after a few minutes while it settled down on the value of 19 kW after more than 10 min. This is normal behavior due to phenomena of running in of the gears and bearings, oil temperature is raised to the balanced value of 70-80°C and with this the viscosity drops and consequent hydrodynamic losses and etc. Tests were done on 4 regimes, all at the same velocity of 6000 rpm. The first one is done without any load applied, the second one corresponds to 120 Nm (75kW), the third one is with 220 Nm (138kW) and the last one is with 320 Nm (200kW). Results for short tests of several minutes are shown in Table 1.

Table 1. Results of power measurement on torque meter

Case no.	T [Nm]	P [kW]	P_{tl} [kW]	P_{bl} [kW]	P_g [kW]	η [%]
1	0	0	17	5.2	5.90	-
2	120	75	19	6.6	6.20	0.92
3	220	138	21	7.7	6.65	0.95
4	320	200	23	8.8	7.10	0.97

In Table 1, T is the torque introduced to the system by coupling, P is the power simulated by the system, P_{tl} is the total power losses measured by the torque meter, P_{bl} is the basic power losses of the test

rig (without test articles), P_g is the calculated averaged power losses per high speed gearbox and η is the energy efficiency of high speed gearboxes.

For the short tests when there is a need to define the settling temperature of input cooled, output heated oil or bearing operating temperatures, natural frequencies, noise or energy efficiency, the open-loop power circuit test rig is the better solution to obtain these results. There is a need for only one gearbox, and all power which is required to pass through the test rig and the gearbox itself should be compensated by the electromotor. The second high speed gearbox for aircraft propeller application is tested in this way. Firstly, a test without any load at the designed 2500 rpm of output shaft speed was conducted and the power required was 3.4 kW. This are the basic power losses during the operation without load. The high speed bearing housing system actually used for free turbine application, input bearing system for gearbox, was tested separately and shows the value of 2.5 kW at 40 000 rpm. This fact indicates that the losses of gear meshing without load, all other gearbox bearings and lubricating losses are only 0.9 kW. After this one test, a turbine is installed on the input shaft in order to provide the load (due to air resistance of turbine rotation through the ambient air). As the electromotor is of not enough power this test was done on the maximal load that corresponds to 55 kW. The power loss on this test was estimated to a value of 3.9 kW which gives the energy efficiency of 0.93.

5. Conclusion

Based on the above, the power of 23 kW is continuously required to drive the system at 6 000 rpm with a closed loop circulation test rig, with torque of 320 Nm inputted on the special clutch on the auxiliary branch in order to simulate the behavior of gears exposed to 200 kW of power. In this way, the power spent over time is almost 10 times lower than in the case of an open-loop power circuit test rig. This is an economically prevailing advantage in case of long-term gearbox testing.

The first test shows that energy efficiency of the high speed gearbox increases as the applied load increases. The worst case is with very low load applied and running the gears without load is not recommended due to low dynamic behavior which is even reflected by the sound produced. There are several reasons why energy efficiency is increasing. In the first place is the fact that dynamic load factor lowers its value by increasing the unit load per tooth width for high speed gearboxes that operate on supercritical speeds. The other one is the fact that the basic load due to windage effect, bearing friction, churning, oil pocketing and etc. remains more or less independent at the same rotational velocity with the load applied. As power is increased, mostly gear teeth mesh losses are increasing by a small percent. So, results show the trend of efficiency increase with load as in reference [7].

The second test shows that the most basic power losses (without load) occur in the area (on the parts) which are exposed to the high speed. The bearing housing subassembly of input high speed shaft takes 2.5 of the total 3.4 kW (74%) which goes to gear meshing (including high speed pair) and all others bearings.

Acknowledgments

The presented paper is a result of the researches supported by MPNTR RP according to the contracts 451-03-137/2025-03/ 200105 and 451-03-136/2025-03/200213 since 4th February 2025. The authors wish to acknowledge and thank the company EDePro for support and for encouragement in the project realization.

References

[1] Anderson, N. E., Loewenthal, S. H. Effect of geometry and operating conditions on spur gear system power loss, *Third International Power Transmission and Gearing Conference*, California, 18-22 August, 1980.

[2] Eastwick, C. N., Johnson, G. Gear Windage: A Review, *Journal of Mechanical Design*, 2008, 130(3):034001-1.

[3] Delgado, I., Hurell, M. The Jetting Phenomena in Meshed Spur Gears, A*HS International 74th Annual Forum & Technology Display*, Arizona, 14-17 May, 2018.

[4] Mizutani, H., Isikawa, Y., Towsend, D. P. Effects of Lubrication on the Performance of High- Speed Spur Gears, *Fifth International Power Transmission and Gearing Conference*, Illinois, 24-27 April, 1989.

[5] Anderson, N.E., Loewenthal, S.H., Black, J.D. An Analytical Method To Predict Efficiency of Aircraft Gearboxes, *ASME. J. Mech., Trans., and Automation.* September 1986; 108(3), 424–432.

[6] Ognjanović, M., Kolarević, N., Stanković, M., *Reduktori turbovratilnih motora*, Akademska misao: EDePro – Engine Development and Production, 2024.

[7] Lee, G.-H., Park, Y.-J., Nam, J.-S., Oh, J.-Y., Kim, J.-G. Design of a Mechanical Power Circulation Test Rig for a Wind Turbine Gearbox. *Appl. Sci*. 2020, 10(9): 3240.

POSTER AND ORAL PRESENTATIONS

41st Danubia-Adria Symposium Advances in Experimental Mechanics
September 23-26, 2025, Kragujevac, Serbia

Extended abstract

DOI: 10.46793/41DAS2025.025U

EXPERIMENTAL STUDY OF HEAT EFFECT ON THE DEFORMATIONS OF AL/CU BIMETAL IN 3-POINT BENDING

Robert UŚCINOWICZ

0000-0003-4599-2632, Department of Mechanics and Applied Computer Science, Faculty of Mechanical Engineering, Bialystok University of Technology, 45C Wiejska, 15-351 Bialystok, Poland;
E-mail: r.uscinowicz@pb.edu.pl

1. Introduction

With the growing energy crisis and difficulties in obtaining new metals, layered composites are becoming more widely used, with aluminium-copper bimetal playing the dominant role. It is characterised by high electrical and thermal conductivity, high corrosion resistance, and relatively low density. The production costs of bimetal using rolling technology are low, and its use in a technical solution allows 30% to 50% savings compared to monolithic copper [1]. The composite is used in radiators, cables, cooling fins, heat exchangers, and other electronic and electrical components. However, the number of applications of Al/Cu bimetal is limited by the quite significant effect of heat on its elastic-plastic properties and structure. The purpose of the research conducted was to determine the effect of heat through growth and short-term withstanding of Al/Cu bimetal in the temperature range of up to 250 – 500 °C on its springback effect and the beginning of plasticity in its extreme layers under bending conditions.

2. Material and specimens

The experimental tests were carried out on aluminium-copper bimetallic samples in the shape of a cuboid strip with dimensions of 4 x 20 x 67 mm. They were cut from Al / Cu sheets produced by hot rolling by permanent deformational connection of sheets of electrolytic copper (CW004A) and pure aluminium (AW-1050A). The average percentage share of components in the Al/Cu bimetal is Cu - 51% and Al - 49%.

The samples were divided into two groups. Some samples were tested without thermal effects (T = 22 °C); the rest were annealed at temperatures of 250, 350, 450, 500 °C for 40 and 90 min.

The experimental studies included three-point bending tests of Al/Cu samples and microscopic analysis of the layer connection zone before and after plastic deformation of the samples.

3. Experimental setup

In the first stage of the investigation, three-point bending tests were performed. They were carried out on a hydraulic MTS Mini Bionix 858 machine, loading the samples perpendicularly to the lamination in a special device. Measurement of deformations and displacements (deflections) was performed using the Aramis 4M digital image correlation system from GOM. After mechanical tests, the bimetal structure was observed microscopically, which included a chemical analysis of the composition and measurement of the thickness of the diffusion layer formed on the Al/Cu interface because of thermal interactions. Observations were carried out on a Phenom XL electron microscope (SEM). The measurement of the thickness of the diffusion layer was performed by graphic analysis of SEM photographs, validating the results by linear analysis of the chemical composition.

4. Study of the springback of bimetal

As a result of heat exposure, irreversible changes occur in the mechanical properties of the Al/Cu bimetal. This is manifested by the effect of disturbed springback, i.e. loss of elastic properties after elastic-plastic deformation. This is treated as an operational defect, especially in the case of bending.

Springback in the tested Al/Cu bimetal was assessed and analysed by measuring the difference in angles $\Delta\phi$ during three-point bending in two states of sample deformation, i.e. before and immediately after unloading (Fig. 1).

It was found that with the increase in temperature in the range of 250 – 450°C, the values of angles $\Delta\phi$ increased significantly for the tested soaking times, and for the annealing time t = 40 min. the increase was linear. After soaking at 500°C, there was a slight decrease in the value of phi, which can be attributed to the developed brittle diffusion zone. The highest value of angle $\Delta\phi$ (springback)

obtained from the experiment for the Al/Cu bimetal was 3.2 deg.

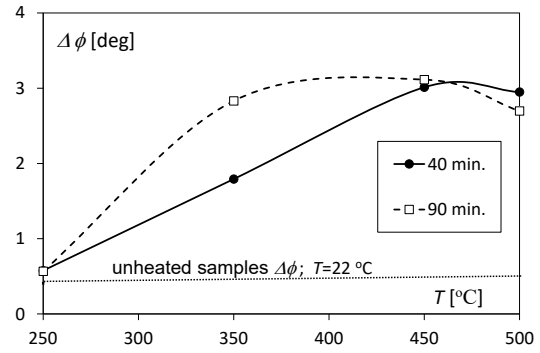

Fig. 1. Thermal effects of springback of bimetallic samples.

5. Identification of the composite plasticisation process

Experimentally, the bending curves did not reveal the beginning of plastic (physical) flow. To determine the actual values of the yield moments of the extreme bimetal layers, an analytical solution based on the experimental data was used. The changes in the yield moment M_p, depending on the temperature are shown in Fig. 2.

At 250 °C the M_p torque values for the annealing time of 40, 90 min were similar and amounted to approx. 12.8 Nm. They were slightly lower than the M_p value for the unannealed samples (13.6 Nm). In the temperature range of 350 – 500 °C the M_p values were similar (approx. 4 Nm), however, in relation to the temperature T = 250 °C a more than twofold decrease in the M_p value was observed.

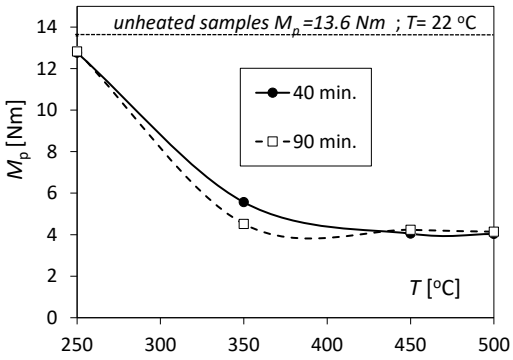

Fig.2. Changes in the bending moment M_p value under the influence of temperature.

6. Microscopic observations of the Al/Cu interface

SEM photographic observations allowed to measure of the diffusion zone thickness depending on the temperature for the tested annealing times (Fig. 3). It was found that in the case of unannealed samples (T = 22 °C) and annealed at 250°C for 40, 90 minutes, no copper diffusion into aluminium was observed. With increasing annealing temperature in the 350 – 500 °C range, the diffusion layer thickness increased exponential from 4.6 µm to 15.4 and 26.8 µm for times t = 40 and 90 min, respectively. Three intermetallic layers of different shades characterised by significant brittleness were distinguished at the interface.

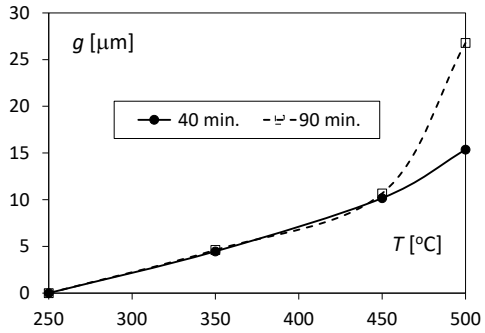

Fig. 3. Change in the diffusion's thickness zone under the influence of temperature.

7. Conclusions

- For samples heated at 450–500 °C, a six-fold increase in the springback angle was observed compared to the temperature of 250 °C.
- Heating at temperatures of 350–500 °C caused over two-fold decrease in the yield's value moment of the extreme layers of the Al/Cu bimetal compared to the lower temperatures tested.
- A strong exponential increase in the brittle's thickness diffusion zone was observed, causing a weakening of the Al/Cu joint.

Acknowledgements

The paper was prepared as part of the research project No. WZ/WM-IIM/4/2023 of Bialystok University of Technology, financed by the Polish Ministry of Science & Higher Education.

References

[1] Kim, I.-K.; Hong, S.I. Effect of Heat Treatment on the Bending Behavior of Tri-Layered Cu/Al/Cu Composite 522 Plates. Mater Des 2013, 47, 590–598.

41st Danubia-Adria Symposium Advances in Experimental Mechanics
September 23-26, 2025, Kragujevac, Serbia

Extended abstract

DOI: 10.46793/41DAS2025.027G

DYNAMIC CALIBRATION OF A MODEL OF A MIXED STRUCTURE BRIDGE DECK BASED ON DYNAMIC TESTS OF THE BRIDGE

Ghindea CRISTIAN LUCIAN[1], Cruciat RADU IULIU[2], Pricopie GHEORGHE ANDREI[3], Diaconu ADRIAN AURELIAN[4] , Racanel IONUT RADU[5]

[1] 0000-0001-9330-6145, Technical University of Civil Engineering Bucharest, Blvd. Lacul Tei 122-124, Sector 2, Bucharest, Romania, E-mail: cristian.ghindea@utcb.ro;

[2] 0009-0003-4940-3679, Technical University of Civil Engineering Bucharest, Blvd. Lacul Tei 122-124, Sector 2, Bucharest, Romania,, E-mail: radu.cruciat@utcb.ro;

[3] 0000-0001-6971-8983, Technical University of Civil Engineering Bucharest, Blvd. Lacul Tei 122-124, Sector 2, Bucharest, Romania, E-mail: andrei.pricopie@utcb.ro;

[4] 0009-0003-9782-2317, Technical University of Civil Engineering Bucharest, Blvd. Lacul Tei 122-124, Sector 2, Bucharest, Romania, E-mail: adrian-aurelian.diaconu@phd.utcb.ro;

[5] 0000-0003-3230-874X, Technical University of Civil Engineering Bucharest, Blvd. Lacul Tei 122-124, Sector 2, Bucharest, Romania, E-mail: ionut.racanel@utcb.ro;

1. Introduction

Considering the socio-economic importance of bridge structures, their acceptance testing is generally a mandatory requirement before the bridge is put into operation. The dynamic test is a component of the acceptance testing process used to verify the numerical model of the bridge structure from a dynamic perspective. This paper presents the procedure for conducting dynamic tests on a segment of a bridge with a mixed structure deck, under standard conditions using test loads.

The experimental findings served as the basis for structural verification of the bridge deck in terms of execution quality and for the numerical model calibration, for future references studies.

2. Experimental dynamic test of the bridge

The overpass located on the outskirts of Timisoara city, ensures the crossing of a single, non-electrified railway line by the Timisoara South Bypass.

The bridge has 8 spans, with a total length of approximately 331.62 meters, and it is composed of reinforced concrete beams at the end spans and a composite steel–concrete deck in the central zone, including the span that crosses the railway line.

In the steel–concrete composite section of the deck, the superstructure consists of continuous steel beams with three spans (40.30 + 55.30 + 40.30 m). In cross-section, the deck includes two continuous main steel girders and a central longitudinal beam, with the structure stiffened by steel crossbeams, bracings, and a reinforced concrete slab acting compositely.

The experimental testing procedure was made accordingly with the specific Romanian standard, STAS 12504-86 [1].

2.1 Experimental test assembly

The dynamic response of the bridge was evaluated using a test truck loaded with ballast, having a total mass of approximately 40 tons. Bridge accelerations were continuously recorded in real time during the entire crossing of the truck.

To generate a shock-type dynamic load, an artificial obstacle was placed on the roadway surface. To simulate various levels of dynamic excitation, the truck passed over it at different speeds.

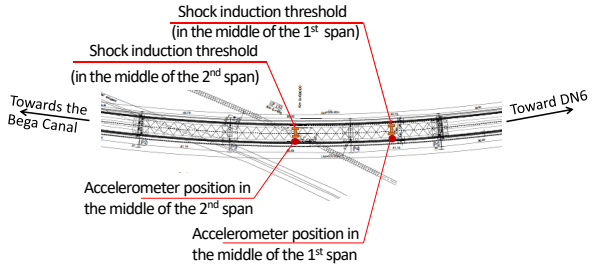

Fig. 1. The position of the accelerometers and the shock thresholds

For each obstacle, one can consider five incremental speed levels (10, 30, 50, 70 and 85 km/h, were used). For each passing of the test truck, accelerations were recorded along three orthogonal directions, at the positions indicated in Fig. 1.

3. Experimental results

Given that the excitation was predominantly vertical, the horizontal response of the deck was deemed not representative for the dynamic test.

		Vibration frecqency resulted from Modal FEM Analysis [Hz]		Distinct Vibration Frequency [Hz] / All tests				
Speed of the test truck [km/h]		Vertical Modal Participating Mass Ratios	Modal Frequency [Hz]	Speef of the test truck / 1st and 2nd position of the artificial obtacle				
				10	30	50	70	85
Vibraton frequencies bands [Hz]	0.1 ÷ 1 Hz	-	-	-	-	-	-	-
	1 ÷ 2 Hz	1.18%	1.42	1.44 1.48	**1.44***	1.48	1.44 1.48	**1.48***
	2÷ 3 Hz	0.61% **67.67%**	2.82 **2.95**	**2.12*** **2.28*** **2.88***	2.12 **2.40*** **2.68*** 2.88 2.92	**2.40*** **2.68*** **2.76*** **2.84*** 2.88	**2.80*** **2.84*** **2.88***	**2.40*** **2.84*** **2.88***
	3 ÷ 5Hz	-	-	3.68	-	-	-	-
	5÷ 10 Hz	-	-	-	-	8.64	-	-
	10 ÷ 12 Hz	18.14%	11.28	-	-	-	-	-
	12 ÷ 14 Hz	-	-	-	-	13.92	-	13.80
Average frequency [Hz]				2.55 Hz				
Median frequency [Hz]				**2.76 Hz**				
Note: * The frequencies with maximum amplitude in the Power Spectra of each recorded accelerogram								

Fig. 2. The results of the experimental testing of the bridge

The vertical acceleration records (accelerograms) capturing the bridge deck vibrations were subsequently analyzed to determine the frequency characteristics of the structural response [2]. For each recorded accelerogram, baseline correction and filtering procedures were applied, followed by the computation of power spectral densities, through which the dominant vibration frequencies were identified (see Fig. 2).

4. Modal FEM Analysis

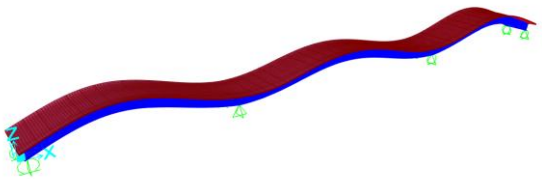

Fig. 3. Mode 4 with a frequency of 2.95 Hz, for a 67.57% modal participating mass ratio.

The modal shape of the predominant mode of the deck is presented in Fig. 3, in terms of modal participation mass ratios at vertical translation.

5. Dynamic calibration of the FEM model

As one can observe in Fig. 2, the frequency content of the bridge vibrations is very close to the predominant modal frequency of the FEM model. This experimental result assures that the real structure of the bridge deck has good behavior under loads, close enough to presumed behavior resulted from the FEM analysis. Although, one can observe that the stiffness of the FEM model is a little higher than the real structure. To perform subsequent analyses of the bridge's behavior under dynamic loads, the numerical model was calibrated based on the experimental findings.

Considering that the fundamental frequency depends on terms such structural mass (m) or structural stiffness (k), as results from Eq. 1, the numerical model calibration can be conducted in terms of mass or stiffness [3].

$$f_1 = 2\pi\sqrt{k/m} \tag{1}$$

Because the modal analysis is conducted mainly with respect to the dead weight of the structure, the only term which can be tweaked is structural stiffness. After some minor modification on the values of the Young Modulus of the structural materials and the stiffness of the connections between structural elements of the bridge deck, the model was calibrated in order that the fundamental vertical mode to be almost identical with the median value of the predominant frequencies of the recorded accelerograms. After the calibration, the resulting fundamental frequency is 2.76Hz, with a Modal Participation Mass Ratio of 68.27% (Fig. 4)

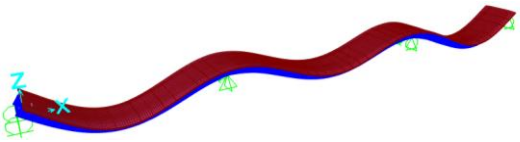

Fig. 3. The fundamental mode, after the calibration.

6. Conclusions

The experimental tests showed that the bridge has good behavior, but for future analysis the numerical model was calibrated to be tuned with the real structure in terms of fundamental frequency.

Acknowledgments

The results were obtained thanks to the project GnaC 2024-ARUST-UTCB-22.

References

[1] STAS 12504-86, "*Railway, Road and Footbridges. Load Testing of Superstructures*" Romanian Standards Association, 1986

[2] Ghindea, C. L., Racanel, I. R., Cruciat, R. I., Dynamic testing of a reinforced concrete road bridge. *Key Engineering Materials*, 2014, 601, 739–765.

[3] Chopra Anil K. *Dynamics of Structures, 3rd Edition*; Pearson Prentice Hall: Boca Raton, 2007.

Extended abstract DOI: 10.46793/41DAS2025.029K

CONSTITUTIVE MODELLING OF POLYMER FOAMS USING AN ASYMMETRIC POISSON'S RATIO

Márton KAMMERER[1], Attila KOSSA[2]

[1] Department of Applied Mechanics, Faculty of Mechanical Engineering, Budapest University of Technology and Economics, Műegyetem rkp. 3., Budapest, 1111, Hungary, E-mail: kammerer.marton@edu.bme.hu

[2] 0000-0003-3638-3237, Department of Applied Mechanics, Faculty of Mechanical Engineering, Budapest University of Technology and Economics, Műegyetem rkp. 3., Budapest, 1111, Hungary, E-mail: kossa@mm.bme.hu

1. Introduction

Open-cell polymeric foams exhibit a pronounced asymmetry when subjected to uniaxial tension and compression: the axial stress–strain curves and the accompanying lateral (transverse) strains differ drastically. This behavior can be traced back to the nonlinearity of the polymer matrix material coupled with the complex geometry of the cellular microstructure.

Hyperelastic constitutive models are the standard choice for modeling the elastic response of such materials. Yet a review of the literature reveals that even the most complex ones of the existing models [1] invariably fail to reproduce the dual character of tension-compression characteristics, particularly the lateral strains [2]. To overcome this limitation and capture the experimentally observed asymmetry we introduce a novel hyperelastic constitutive model asymmetric in Poisson's ratio.

2. Materials and methodology

The compressible Ogden–Hill hyperelastic constitutive model [1] is the prevailing model for describing polymeric foams, for which the strain energy density function is defined as:

$$W(\lambda_1,\lambda_2,\lambda_3) = \sum_{i=1}^{N} \frac{2\mu_i}{\alpha_i^2}\left(\lambda_1^{\alpha_i} + \lambda_2^{\alpha_i} + \lambda_3^{\alpha_i} - 3 + \frac{1}{\beta_i}\left(J^{-\alpha_i\beta_i} - 1\right)\right), \quad (1)$$

where λ_k $(k = 1,2,3)$ denote the principal stretches, J the volume ratio and N is the order of the material model. In ABAQUS, this model appears under the name Hyperfoam, and defines the β_i parameters as:

$$\beta_i = \frac{\nu_i}{1-2\nu_i}. \quad (2)$$

In some special cases, when $\nu_i = \nu$, this parameter can be associated with Poisson's ratio.

Building on this identity, we introduce an asymmetric variant where we use J to switch between "tension" $(J > 1)$ and "compression" $(J < 1)$ like cases and for these we use different Poisson's ratios:

$$W(\lambda_1,\lambda_2,\lambda_3) = \begin{cases} \sum_{i=1}^{N} \frac{2\mu_i}{\alpha_i^2}\left(\lambda_1^{\alpha_i} + \lambda_2^{\alpha_i} + \lambda_3^{\alpha_i} - 3 - \alpha_i \ln(J)\right), & J < 1, \\ \frac{2\mu}{\alpha^2}\left(\lambda_1^{\alpha} + \lambda_2^{\alpha} + \lambda_3^{\alpha} - 3 + \frac{1}{\beta}\left(J^{-\alpha\beta} - 1\right)\right), & J > 1, \\ \frac{1}{2}\left(W^{c}(\lambda_1,\lambda_2,\lambda_3) + W^{t}(\lambda_1,\lambda_2,\lambda_3)\right), & J = 1. \end{cases} \quad (3)$$

The "tension" part adopts a first-order Hyperfoam model, whereas the "compression" part is constrained to zero Poisson's ratio, a widely used approximation for open-cell polymeric foams [3].

Because uniaxial tension and compression tests provide the primary calibration data, it is convenient to write the corresponding 1st Piola–Kirchhoff stress in closed form, allowing direct parameter fitting against experimental curves.

$$P_1 = \frac{\partial W}{\partial \lambda_1} = \begin{cases} \sum_{i=1}^{N} \frac{2}{\lambda_1}\frac{\mu_i}{\alpha_i}\left(\lambda_1^{\alpha_i} - 1\right), & J < 1, \\ \frac{2}{\lambda_1}\frac{\mu}{\alpha}\left(\lambda_1^{\alpha} - \lambda_1^{-\alpha\nu}\right), & J > 1, \\ \frac{1}{2}\left(P_1^{c} + P_1^{t}\right), & J = 1. \end{cases} \quad (4)$$

The proposed model was calibrated and validated against uniaxial tension- and compression-test data obtained for an open-cell polymeric foam [4]. As illustrated in Fig. 1, the predicted stress–strain response reproduces the experimental curves with great accuracy.

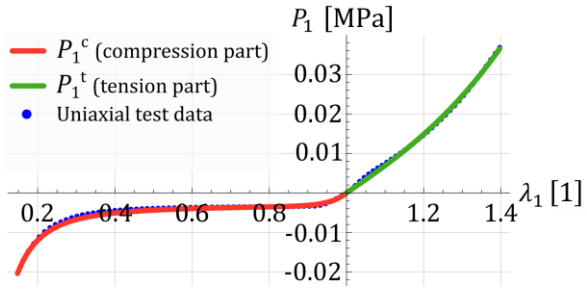

Fig. 1. Fitting on uniaxial test data.

Transverse strains were extracted from the uniaxial tests by post-processing recorded videos with a binarization technique. The measured trends confirm that Poisson's ratio of 0 is adequate in compression, while in tension incompressibility is the best approximation – an observation that was not anticipated. Consequently, the tensile branch of the Hyperfoam formulation collapses to the first-order, incompressible Ogden model.

For model validation we constructed a large-scale bending apparatus (Fig. 2), on which finite strain configurations can be achieved in discrete steps. The obtained reaction forces and geometrical datasets were later compared to FEM predictions.

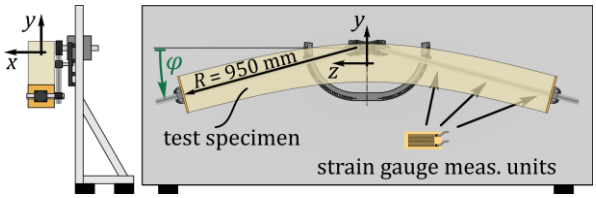

Fig. 2. Design of the large-scale bending apparatus.

All simulations were conducted in ABAQUS [5]. As a first approximation to emulate the proposed asymmetric constitutive law, the beam was partitioned into tensile- and compressive-dominant regions (Fig. 3), constructing the separated FEM model. Each region was assigned a Hyperfoam material definition with its own calibrated parameter set.

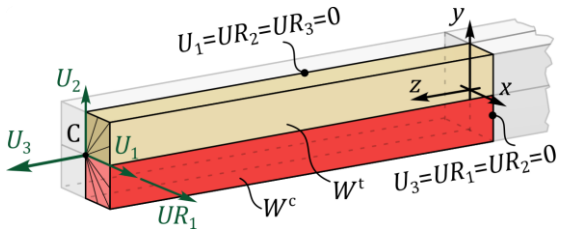

Fig. 3. The separated FEM model.

3. Conclusions

Simulation results indicate that in bending (where tension and compression arise simultaneously), the separated FEM model achieves reaction predictions on par with conventional Hyperfoam fits yet captures transverse strains with far greater accuracy (Fig. 4).

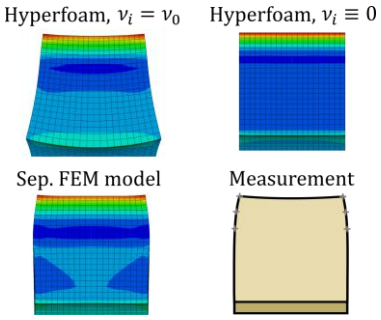

Fig. 4. Cross sectional view of the beam at $\varphi = 30°$ for multiple cases.

The collected evidence shows unambiguously that, in bending, the asymmetric hyperelastic formulation yields better results at transverse strains than its Hyperfoam counterpart. Motivated by this performance, we have coded dedicated UHYPER and UMAT subroutines for ABAQUS, providing a platform for complete studies and more complex loading scenarios. Future work will address numerical implementations of hyperelastic models that couple volumetric and isochoric behavior, including the present formulation.

4. Acknowledgements

This research was supported by the Hungarian National Research, Development and Innovation Office (FK 142457). This research was supported by the János Bolyai Research Scholarship of the Hungarian Academy of Sciences.

5. References

[1] R. W. Ogden, *Large deformation isotropic elasticity – on the correlation of theory and experiment for incompressible rubberlike solids*, 1972, Proc. R. Soc. Lond. 739-765.

[2] A. K. Landauer, X. Li, C. Franck, D. L. Henann, *Experimental characterization and hyperelastic constitutive modeling of open-cell elastomeric foams*, Journal of the Mechanics and Physics of Solids, 2019, 103701, Volume 133.

[3] G. Silber and C. Then. *Preventive Biomechanics: Optimizing Support Systems for the Human Body in the Lying and Sitting Position.* Springer Berlin Heidelberg, 2013.

[4] A. Kossa and Sz. Berezvai, *Novel strategy for the hyperelastic parameter fitting procedure of polymer foam materials*. Polymer Testing, Elsevier BV, 2016, 149–155.

[5] *ABAQUS Documentation,* Version 2022. Dassault Systèmes Simulia Corp, United States.

Extended abstract DOI: 10.46793/41DAS2025.031S

MECHANICAL RESPONSE OF PA6 UNDER ENVIRONMENTAL CONDITIONS: A DUAL APPROACH USING EXPERIMENTS AND NUMERICAL ANALYSES

Nicolae ȘTEFĂNOAEA[1], Olivia Laura PETRAȘCU[2], Adrian Marius PASCU[3]

1 0000-0003-1745-1978, „Lucian Blaga" University of Sibiu, Faculty of Engineering, Department of Industrial Machinery and Equipment, Emil Cioran, no. 4, Sibiu, Romania, E-mail: nicolae.stefanoaea@ulbsibiu.ro

2 0000-0002-6910-4727, „Lucian Blaga" University of Sibiu, Faculty of Engineering, Department of Industrial Machinery and Equipment, Emil Cioran, no. 4, Sibiu, Romania, E-mail: olivia.petrascu@ulbsibiu.ro

3 0000-0001-8720-138X, „Lucian Blaga" University of Sibiu, Faculty of Engineering, Department of Industrial Machinery and Equipment, Emil Cioran, no. 4, Sibiu, Romania, , E-mail: adrian.pascu@ulbsibiu.ro

1. Introduction

Polyamide 6 (PA6), also known as Nylon 6, is a thermoplastic material that belongs to the nylon polymer class. Its structure includes repeating amid groups (-CONH-) within the molecular chain. Due to its semicrystalline configuration, this polymer is characterized by outstanding mechanical properties, such as high tensile strength and a significant ability to resist impact [1], [2], [3].

This paper focuses on the impact of environmental factors on the mechanical and elastic characteristics of PA6, with the main objective of identifying how various external factors influence the mechanical and elastic characteristics of this material used in various industrial applications, all of which is intended to support future investigations on the behavior of these types of materials in different other working environments.

However, the interaction of these materials with various environmental factors leads to structural and functional changes that can compromise or, in some cases, improve their performance. Recent studies in the field of materials science and mechanical engineering are based on the impact of environmental factors such as temperature, humidity, ultraviolet radiation, and exposure to various chemicals on the mechanical and elastic properties of polymers.

2. Materials and method

This study aimed to determine the mechanical and elastic properties of the PA6 subjected to different exposure environments: ambient, distilled water, cooling oil, saline solution, and UV-C radiation by means of uniaxial tensile tests. The results obtained allow a comparative analysis of the influence of the working environment on the mechanical and elastic behavior of this type of polymeric material.

In addition to the experimental analysis, a numerical simulation of the mechanical behavior of the PA6 material was carried out using the Abaqus software to validate and correlate the results obtained in the physical tests. The shape and dimensions of the specimens used for the tensile tests are shown in Figure 1 and are realized in accordance with ISO 527-2:2012 [4], which covers uniaxial test methods for plastics.

Specimens for immersion in distilled water, cooling oil, or saline were first dried in an oven at 500°C for 24 hours in accordance with ISO 62:2008—Plastics: Determination of water absorption [5]. After exposure, the specimens were weighed again to assess the liquid uptake for distilled water, cooling oil, and saline solution, according to the procedure described in the standard. In the last step, after the drying process, the specimens were weighed once more to quantify the amount of liquid absorbed. Formula (1) was used to calculate the liquid uptake. The steps involved in preparing specimens for testing are shown in Figure 1.

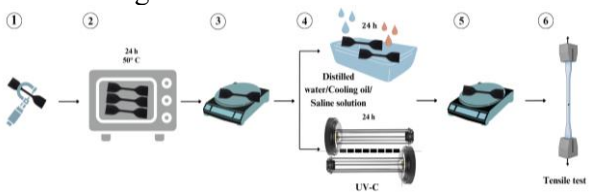

Fig. 1. Steps to perform the tensile test: 1-measure the specimens, 2 - oven drying, 3 - weighing after drying, 4 - immersion / exposure to the medium of interest, 5 - absorption weighing, 6 - uniaxial tensile test.

$$c = \frac{m_2 - m_1}{m_1} \times 100\% \quad (1)$$

3. RESULTS AND DISCUSSION

3.1 Experimental results

The results obtained from the uniaxial tensile tests performed out on specimens maintained in the five environments analyzed are presented in Figure 3. To ensure the accuracy and relevance of the data, ten specimens were used for each medium tested.

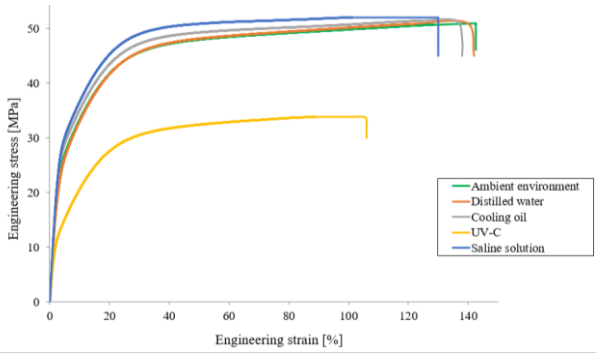

Fig. 3. Mean stress – strain curves for tensile testing of PA6 in five different environments.

3.2 Numerical results

To simulate the uniaxial tensile behavior of specimens made of PA6 material, a 3D model of the specimen was realized with the CATIA V5R20 software package. This model was imported into the ABAQUS software package, where it was discretized into C3D8R finite elements, and the material data, constraints, and loads related to each test performed experimentally were applied.

Thus, the specimen is fixed (recessed) at one end, and at the opposite end a displacement is applied in the direction of the longitudinal axis of the specimen, equal to the mean displacement recorded experimentally at the time of the occurrence of the breakage, as shown in Figure 4a. The 3D model of the tensile specimen discretized in C3D8R finite elements is presented in Figure 4b.

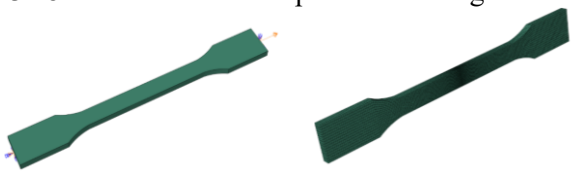

(a) with constraints and loads applied

(b) discretized in finite elements

Fig 4. The 3D model of the tensile specimen.

The plastic be behavior of the materials was defined using stress – strain curve obtained after the uniaxial tensile tests for all five studied cases. Figure 5 shows the comparative force-displacement curves (experimental vs. numerical/FEM) for specimens made of PA6 and tested at uniaxial tensile in the ambiental enviroment.

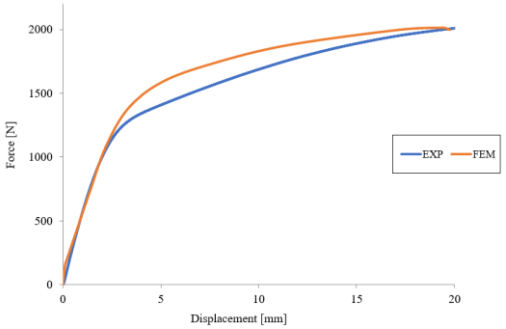

Fig 5. Results of numerical simulation using FEM.

4. CONCLUSIONS

Following the numerical simulations performed using the finite element method (FEM) for uniaxial tensile tests on specimens made of PA6 and comparing the obtained results with those determined from experimental tests, several conclusions can be drawn. Regarding the comparison between the force–displacement curves obtained experimentally and those generated through numerical simulation using FEM, it can be observed that there is a very good correlation between these curves (experimental vs. numerical) for all five studied environments (ambient conditions, distilled water, cooling oil, saline solution, and UV-C radiation exposure).

5. Bibliography

[1] R. Hsissou, R. Seghiri, Z. Benzekri, M. Hilali, M. Rafik, și A. Elharfi, „Polymer composite materials: A comprehensive review”, *Composite Structures*, vol. 262, p. 113640, apr. 2021, doi: 10.1016/j.compstruct.2021.113640.

[2] T. Liu, „A Bibliometric Analysis of the Performance of Advanced Materials Research from 2005 to 2012”, *AMR*, vol. 803, pp. 165–168, sep. 2013, doi: 10.4028/www.scientific.net/AMR.803.165.

[3] A. Molea, V. V. Merie, și R.-C. Suciu, Ed., *Materiale utilizate în construcția și întreținerea autovehiculelor*, Editura UTPRESS. Cluj_napoca, 2023.

[4] *ISO 527-2:2012 Plastics - Determination of tensile properties*.

[5] *ISO 62:2008 - Plastics - Determination of water absorption*, 2008.

41st Danubia-Adria Symposium Advances in Experimental Mechanics
September 23-26, 2025, Kragujevac, Serbia

Extended abstract

DOI: 10.46793/41DAS2025.033S

COMPARATIVE EVALUATION OF THE ELASTIC MODULUS IN CEMENT PASTES USING ULTRASONIC AND 3-MIN-CREEP TESTING

Sophie SCHMID[1], Olaf LAHAYNE[2], Bernhard PICHLER[3]

[1] 0000-0003-4781-3976, TU Wien, Karlsplatz 13, 1040 Wien, Austria, E-mail: sophie.schmid@tuwien.ac.at
[2] 0000-0002-5252-1356, TU Wien, Karlsplatz 13, 1040 Wien, Austria, E-mail: olaf.lahayne@tuwien.ac.at
[3] 0000-0002-6468-1840, TU Wien, Karlsplatz 13, 1040 Wien, Austria, E-mail: bernhard.pichler@tuwien.ac.at

1. Introduction

The elastic modulus E is a suitable material property for quantifying the influence of sample preparation, material age, and ambient conditions on the mechanical behavior of cement pastes, because E can be characterized efficiently using non-destructive methods. A comparison of results obtained from different independent test methods sheds light on the reliability and precision of the methods used, as well as on potentially necessary improvements and limitations in characterization. A comparative study is performed on cement pastes prepared from composite binders made of Portland cement, limestone, and calcined clay.

2. Materials and methods

Three cementitious binders: an ordinary Portland cement (OPC), a binary blend called limestone Portland cement (LPC) containing, by mass, 70% OPC and 30% limestone, as well as a limestone calcined clay cement (LC3) containing, by mass, 70% OPC, 15% limestone, and 15% calcined clay, are used to prepare cement pastes at an initial water-to-solid mass ratio of 0.45 [1]. Two independent test methods are used to determine the elastic modulus from 1 to 7 days after paste production, namely (a) ultrasonic testing and (b) hourly 3-min creep testing, see Fig. 1.

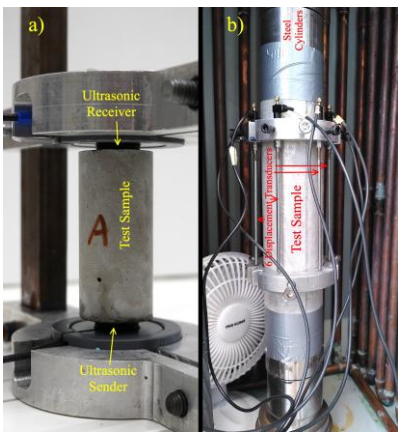

Fig. 1. Test setup for (a) ultrasonic and (b) creep testing.

Test repetitions are performed.

2.1 Ultrasonic tests

Non-destructive ultrasonic tests are conducted on cylindrical samples ($d = 3$ cm and $h = 6$ cm) once per day, from 1 to 7 days after paste production, approximately every 24 h. The test setup is shown in Fig. 1a). Longitudinal and transversal ultrasonic waves with a central frequency of 5 MHz are sent through the test setup. The times of flight of the ultrasound wave are measured. Preliminary tests showed that the results are independent of the frequency and the sample size.

2.2 Creep tests

Non-destructive 3-min creep tests [1,2] are conducted hourly on cylindrical samples ($d = 7$ cm and $h = 30$ cm), from 1 to 7 days after paste production. The test setup is shown in Fig. 1b). The cement paste samples are subjected to a compressive force corresponding to 15% of the material strength at the time of testing. The change of length of the sample is measured.

3. Data analysis

Ultrasonic tests are carried out four times for each sample and at each time instant of testing. The signal velocities v_L and v_T are computed by referring the measured times of flight of the ultrasonic pulses to the sample height. The theory of elastic wave propagation through isotropic media allows for calculating E based on the wave velocities and the mass density ρ [3]:

$$E = \rho \frac{v_T^2(3v_L^2 - 4v_T^2)}{v_L^2 - v_T^2}. \qquad (1)$$

Individual 3-min creep tests are evaluated based on the linear theory of viscoelasticity and Boltzmann's superposition principle, according to the evaluation strategy described in [1]. Values of the elastic modulus, the creep modulus, and the creep exponent are identified without making any constraining assumptions.

4. Results

The analysis of the results from ultrasonic testing allows for identifying two origins of fluctuations: variations between the samples and variations in the measurements of the times of flight, expressed in terms of wave velocities.

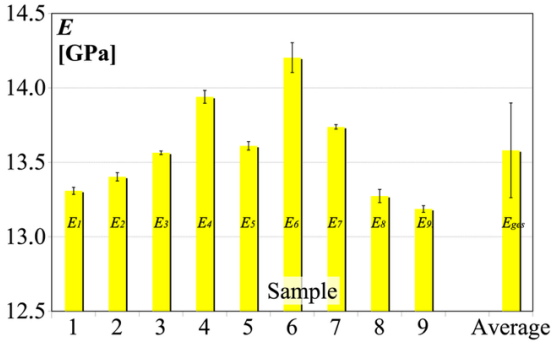

Fig. 2. Elastic modulus of OPC paste samples.

Up to nine cement paste samples are tested for each of the three materials. As for the OPC paste samples, the standard deviations ΔE_1 to ΔE_9 based on ρ and the four values of v_L and v_T are between 0.01 and 0.10 GPa corresponding to 0.09 and 0.70% of the mean values of E_i. For the mean value E_{ges} over all samples, the standard deviation ΔE_{ges} amounts to 0.32 GPa. This is equal to 2.3% of E_{ges}. For LPC and LC3 pastes, we get 2.4 and 2.7%. Therefore, variations between the samples are herein found to be the main source of deviations.

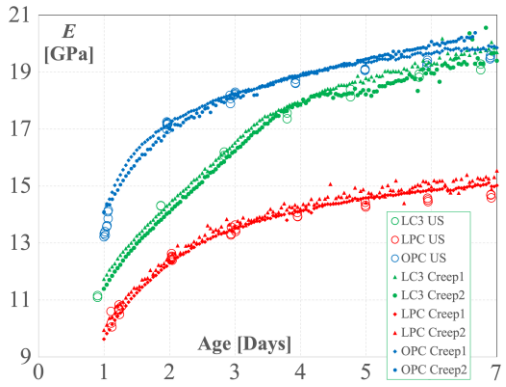

Fig. 3. Comparison of values of the elastic modulus, obtained from ultrasonic testing (large circles) and 3-min creep testing (small symbols).

Creep tests take much more time and effort than ultrasonic tests. Therefore, the number of investigated samples is smaller. Two creep test series are performed for each material, see Fig. 3. The mean difference between the two test-series of one material is about 1.9% for the LC3 paste, 1.6% for the LPC paste, and 1.4% for the OPC paste. These variations are slightly smaller than that of the ultrasonic tests.

The largest differences between ultrasonic test-related and creep test-related values of the elastic modulus amounts to 6%, see Fig. 3 for values of the elastic modulus obtained from ultrasound testing (large circles) and that obtained from 3-min creep testing (small symbols). The largest deviations are observed on the second day of the test series, when the microstructure of the cement paste is still undergoing significant changes due to cement hydration. From 2 days onward, the mean differences between the results of the two test methods are 1.6% for the LC3 and LPC pastes and 2.6% for the OPC paste.

5. Discussion and conclusion

The differences between the values of the elastic modulus from ultrasonic testing and 3-min creep testing are in the range of some 2%. This is the same order of magnitude as the variance between individual test samples. This variance is – to a certain extent – unavoidable. This indicates that a good test reproducibility is achieved for both test methods. The match between the two methods underlines the reproducibility of sample production, especially for the creep tests samples, which were prepared not concurrently, but with time lags of several weeks.

6. Outlook

The performance of ultrasonic tests on additional cement paste samples is recommended especially for future creep test series on cementitious materials, since it is little additional effort, but provides a reliable check of the results obtained in the analysis of the creep tests. The variance between individual samples can be minimized by using always the same sample preparation method. Test repetitions underscore the reliability of test results, because the variance between two samples will never be zero. The direct numerical comparison of ultrasonic and creep test results is recommended to be integrated into the test evaluation of ultrasonic and creep tests.

References

[1] Schmid, S. J., Zelaya-Lainez, L., Lahayne, O., Peyerl, M., & Pichler, B. (2025). Hourly three-minute creep testing of an LC3 paste at early ages: Advanced test evaluation and the effects of the pozzolanic reaction on shrinkage, elastic stiffness, and creep. *Cement and Concrete Research*, 187, 107705.

[2] Irfan-ul-Hassan, M., Pichler, B., Reihsner, R., & Hellmich, C. (2016). Elastic and creep properties of young cement paste, as determined from hourly repeated minute-long quasi-static tests. *Cement and Concrete Research*, *82*, 36-49.

[3] Kohlhauser, C. *Elasticity tensor determination by means of ultrasonic pulse transmission*, PhD thesis, TU Wien 2009.

41st Danubia-Adria Symposium Advances in Experimental Mechanics
September 23-26, 2025, Kragujevac, Serbia

Extended abstract DOI: 10.46793/41DAS2025.035M

EXPERIMENTAL ANALYSIS OF ELECTRIC SOOTER DYNAMICS

Zsombor MAGYARI[1], Roland Reginald ZANA[2], Dénes TAKÁCS[3]

[1] 0009-0008-6098-0086, Department of Applied Mechanics, Faculty of Mechanical Engineering, Budapest University of Technology and Economics, Budapest, Hungary, E-mail: magyari.zsombor.2003@gmail.com;

[2] 0000-0003-1081-2742, Department of Applied Mechanics, Faculty of Mechanical Engineering, Budapest University of Technology and Economics, Budapest, Hungary, E-mail: zana_r@mm.bme.hu;

[3] 0000-0003-1226-8613, Department of Applied Mechanics, Faculty of Mechanical Engineering, Budapest University of Technology and Economics, Budapest, Hungary, E-mail: takacs@mm.bme.hu;

1. Introduction

In recent years, electric micromobility vehicles (e.g., electric scooters, unicycles, skateboards, one-wheels, and segways) have gained significant popularity. From both traffic and environmental perspectives, micromobility vehicles have benefits, but controlling these vehicles poses a much more significant challenge for users. As a result, an increased number of road accidents involving personal injuries is realized world-wide. Therefore, exploring the dynamics of the vehicle-human system is essential for making micromobility vehicles safer. In our research, we aim to gather information about the motion of an electric scooter. Due to the small size of the vehicle, the rider's movement significantly influences the motion of the vehicle. Therefore, it is essential to acquire data on how the riders move on the vehicle. In this study, we also examine how accurately a neural network-based algorithm can determine the position of the rider's center of mass based on camera footage.

2. Mechanical modeling

The basic mechanical model of scooters, called the Whipple bicycle model [1,2], is shown in Fig. 1. It consists of four rigid bodies: the front and rear wheels, the handlebar-fork assembly, and the body. Considering all the geometric constraints among the bodies, the scooter has 9 degrees of freedom (DoF). Although the kinematic constraints and the assumption of a flat ground reduce further the DoF of the system, the rolling of the wheels on an ideally flat surface is not ensured in real environments. Hence, all the generalized coordinates

$$\mathbf{q}_\mathrm{m} = \left[X_\mathrm{R} \;\; Y_\mathrm{R} \;\; Z_\mathrm{R} \;\; \psi \;\; \varphi \;\; \vartheta \;\; \delta \;\; \phi_f \;\; \phi_r\right]$$

are needed in order to reconstruct the motion of the scooter from measurement data.

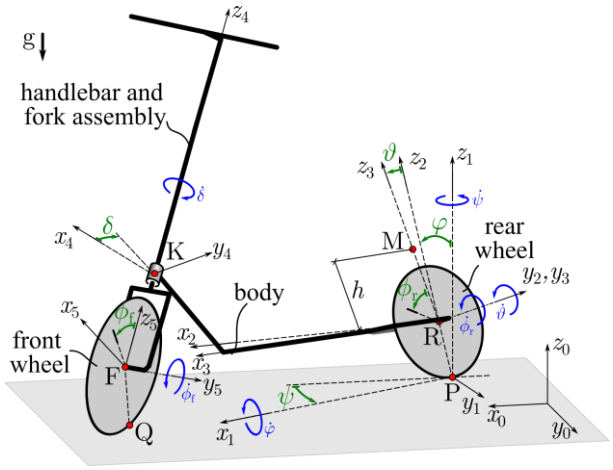

Fig. 1. Mechanical model of the electric scooter [2] with the generalized coordinates indicated.

3. Measuring the states of the scooter

3.1 Position measurement

To determine the global position of the scooter, we use an RTK GPS device, by which an accuracy of up to 5 cm can be achieved if continuous wireless data transmission is ensured for the device from the base station that helps the position correction.

3.2 Velocity measurement

The longitudinal velocity of the scooter is measured via the in-built Hall-effect sensor of the brushless electric motor that drives the Mi Electric Scooter 3. This sensor was used to obtain the rotational speed of the front wheel.

3.3 Steering angle measurement

The steering plays a fundamental role in controlling the scooter. On our experimental scooter, we do not measure the handlebar's angle directly. Instead, we use a timing belt and a pair of pulleys with a 1:1 transmission ratio, and transfer the angular motion to a parallel shaft, making only

minimal modifications to the original scooter design. A Novotechnik RFD-4021-736-223-411 sensor is installed on this parallel shaft, which measures with 0.352° resolution.

3.4 Angular position measurement

As shown in Fig. 1., the spatial orientation of the scooter is given by the sequence of rotations: yaw ψ, roll φ, and pitch ϑ. The sensor we used provides the orientation angles of the frame in accordance with this rotation order. The Bosch BNO085 inertial measurement unit (IMU) determines the yaw angle via a magnetometer related to the Earth's magnetic field. The roll and pitch angles are measured based on gyroscope with the accuracy of 0.01°.

4. Detection of the rider's motion state

To obtain the most detailed and accurate understanding of the rider's motion, we equipped the scooter with a camera. This allows us to record video footage in which the rider's movement can be observed. The USB camera records images at a 640×480 resolution with 30 fps. From the resulting video data, we aim to extract relevant information using a neural network-based image analysis. Namely, a skeleton model is fitted by the YOLOv8 algorithm [3], and the center of mass of the rider is estimated based on [4] and the detected positions of the joints. To evaluate the accuracy of this concept, the OptiTrack motion tracking system [5] was also used to determine the real joint positions. The predictions made by YOLOv8 were then compared to these measurements (see Fig. 2.)

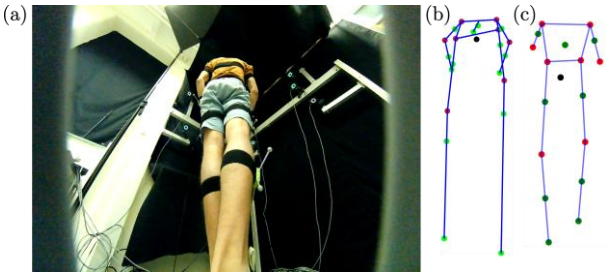

Fig. 2. (a) Snapshot taken with the camera mounted on the scooter, (b) Skeleton model generated via OptiTrack, (c) Skeleton model predicted by YOLOv8 model, along with the estimated center of mass.

Conclusion

The sensor-equipped scooter (see Fig. 3.) provides the opportunity to collect data on the movement of the human-scooter dynamic system and provides a unique opportunity to map human control, even in normal road traffic (see Fig. 4.).

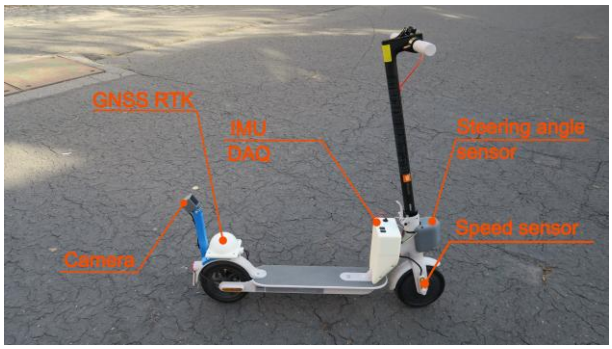

Fig. 3. The electric scooter equipped with a sensors and measurement data collection system

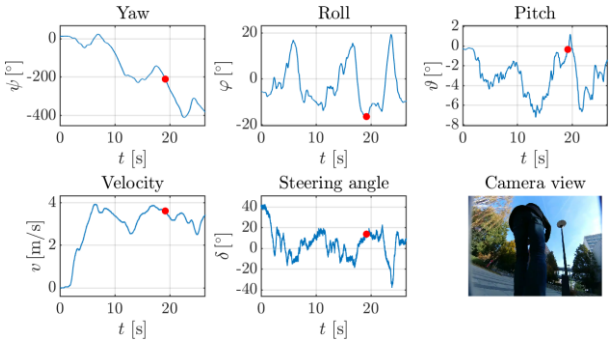

Fig. 4. Measured time signals, the red point indicates the time instant of the camera view.

Acknowledgments

The research was supported by the Bolyai János Research Scholarship of the Hungarian Academy of Sciences, the project NKFI-146201 awarded by the National Research, Development and Innovation Office, the University Research Scholarship Programme (EKÖP), the Ministry of Culture and Innovation, and the National Research, Development and Innovation Fund.

References

[1] Whipple, F.J.W. The stability of the motion of a bicycle, Quart. J. Pure Appl. Math. pp. 312–348, 1899.

[2] Horváth H. Zs., Takács D. Balancing riderless electric scooters at zero speed in the presence of a feedback delay. Multibody Syst Dyn (2024), https://doi.org/10.1007/s11044-024-10019-z

[3] Ultralytics. (2023). YOLOv8: Real-Time Object Detection and Segmentation.

[4] R. Hari Krishnan, V. Devanandh, Aditya Kiran Brahma, S. Pugaznenthi Estimation of mass moment of inertia of human body, when bending forward, for the design of a self-transfer robotic facility, Journal of Engineering Science and Technology Vol. 11, No. 2 (2016) 166 - 176

[5] Mihályi L., Ji Xunbi A., Orosz G., Dénes T. Data Collection for Learning the Dynamics and Control of an Electric Unicycle, The Evolving Scholar - BMD 2023, 5th Edition (2023) pp. 1-2.

41st Danubia-Adria Symposium Advances in Experimental Mechanics
September 23-26, 2025, Kragujevac, Serbia

Extended abstract DOI: 10.46793/41DAS2025.037M

EFFECTS OF STEERING ANGLE SATURATION ON STABILITY OF REVERSING TRAILERS

Levente MIHALYI[1], Denes TAKACS[1,2]

[1] 0009-0007-5901-0624, Department of Applied Mechanics, Faculty of Mechanical Engineering, Budapest University of Technology and Economics, Műegyetem rkp. 3., H–1111 Budapest, Hungary, E-mail: mihalyi@mm.bme.hu;

[2] 0000-0003-1226-8613, HUN-REN–BME Dynamics of Machines Research Group, Budapest, Hungary, E-mail: takacs@mm.bme.hu;

1. Introduction

Driver assistance systems are now a standard feature in modern passenger vehicles, primarily for improving safety and reducing fuel consumption. Extending these systems to freight transport is essential, particularly when addressing one of the most challenging maneuvers, the reversing. Reversing a long, articulated truck–semitrailer combination is inherently unstable, and requires active control to ensure safe maneuvering [1, 2].

The effect of steering angle saturation changes the dynamical properties of a truck–semitrailer combination. In this study, we examine the dynamics of a truck–semitrailer reversing maneuver and analyze how steering angle saturation affects the stability of the autonomous feature proposed for reversing a truck–semitrailer.

2. Mechanical model

To represent the dynamics of the articulated vehicle, a kinematic model with rigid wheels is adopted. The longitudinal speed V of the towing vehicle's rear axle is assumed to remain constant. This assumption is accepted in the literature, particularly for low-speed maneuvers. The configuration is depicted in Fig. 1. The truck and the trailer are represented as two rigid rods connecting the midpoint of the front F and rear axles R of the truck, and the hitch point K and axle T of the trailer, giving the so-called single-track model.

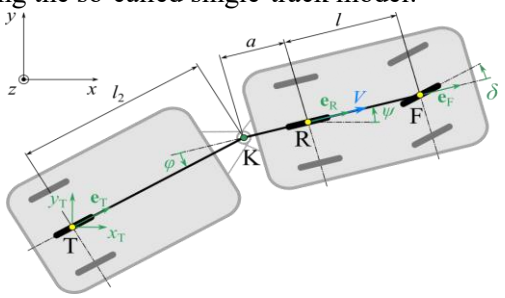

Fig. 1. Mechanical model of the truck–semitrailer

The vehicle combination is actuated exclusively through the steering angle δ of the truck's front axle. The motion is described by the vector of state variables: $\mathbf{x} = [x_R\ y_R\ \psi\ \varphi\ \delta\ \omega]^T$, where x_R and y_R denote the positions of the semitrailer's axle T in the global coordinate system, ψ is the yaw angle of the truck, and φ is the hitch angle of the trailer. Variables δ and ω are introduced in order to consider the dynamics of the steering mechanism as a PD-controlled one degree-of-freedom system: δ is the steering angle, ω is the steering rate. The governing equations are derived from the kinematic constraints:

$$\dot{x}_R = V\cos\psi, \quad \dot{y}_R = V\sin\psi, \quad \dot{\psi} = \frac{V}{l}\tan\delta, \quad (1)$$

$$\dot{\varphi} = -\frac{V}{ll_2}(l\ \sin\varphi + (l_2 + a\ \cos\varphi)\ \tan\delta), \quad (2)$$

and from the dynamics of the steering mechanism:

$$\dot{\delta} = \omega, \quad \dot{\omega} = -p(\delta - \delta_{\mathrm{des}}) - d\omega, \quad (3)$$

where p and d are the gains of the lower-level steering controller.

3. Steering angle saturation

The higher-level controller's duty is to stabilize the motion along the x-axis by means of the control law providing the desired steering angle

$$\delta_{\mathrm{des}}(t) = \mathrm{sat}(-P_y y_R(t-\tau) - P_\psi \psi(t-\tau) - P_\varphi \varphi(t-\tau)), \quad (4)$$

where P_y, P_ψ and P_φ are the control gains. The steering angle of the vehicle has a physical limitation. This phenomenon is considered in our model by the saturation function, which is smoothed near the limitation based on [3]. Saturating the steering angle changes the dynamics of the vehicle combination fundamentally by causing another source of nonlinearities in the system.

Time delay τ is also considered in the control loop, which has relevancy not only for human drivers (reactions time), but also for autonomous vehicles (e.g. image processing and computation time).

4. Results and validation

Bifurcation diagram representing the nonlinear effects of the steering angle saturation and considering the time delay in the control loop was conducted by numerical continuation using the Matlab package DDE-Biftool [4]. The results are validated on a small-scale test rig, shown in Fig. 2. The sensor setup provides high-precision position and angle data at 1 kHz sampling frequency.

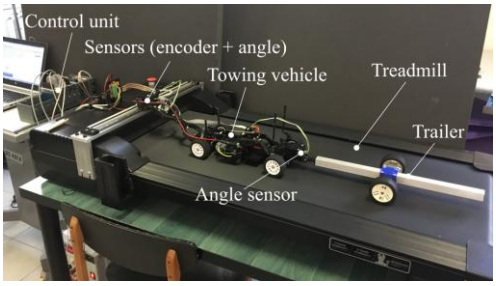

Fig. 2. Experimental setup

Both theoretical and experimental results are shown in Fig. 3 via a bifurcation diagram in the plane of the control gain P_ψ and the amplitude of the hitch angle φ. Gains related to linearly stable or unstable motion (i.e., zero amplitude) are denoted by green and red lines, respectively. The results of the theoretical calculations (solid lines) show an unstable limit cycle above the linearly stable region for the applied δ^{sat} saturation value at $P_\psi = 6$, meaning a subcritical Hopf-bifurcation. However, due to the steering angle saturation, the bifurcation branch folds back and turns into stable limit cycle. This phenomenon also infers the appearance of a bistable region, where the actually realized motion depends on the magnitude of the perturbation. In the high control gain region, a stable limit cycle is situated above the linearly unstable region. The experimental results (dashed lines) show good agreement with the theory. Amplitudes of the stable limit cycle match beyond expectations, and the fold point at the high gain region, when stable limit cycle turns into unstable, is also detected (amplitudes blow up). The phenomenon of hysteresis appears as relevant jumps in the amplitudes in the linearly stable cases (low gain region), however, small amplitudes (~3°) remain there due to noises and other inaccuracies in the experimental setup.

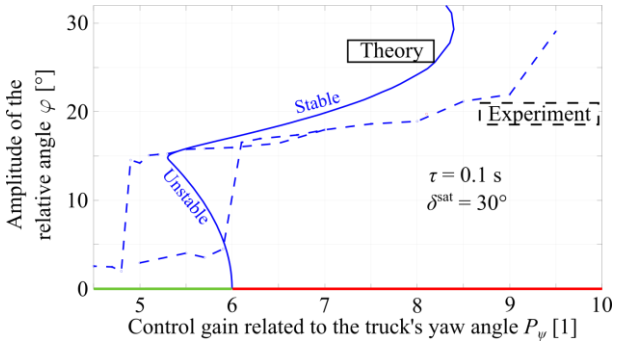

Fig. 3. Bifurcation diagram and its validation

5. Conclusions

In this paper, the rectilinear reversing of a truck–semitrailer was investigated using theoretical and experimental methods. A formerly designed controller, suitable for reversing the articulated vehicle was supplemented with saturation on the steering angle. The modified dynamics and the nonlinear behavior were revealed with bifurcation analysis and was verified with small-scale experimental results. This study has relevance in industry in assisting truck drivers while ensuring stability during maneuvering in reverse.

Acknowledgments

The project is supported by the Doctoral Excellence Fellowship Programme (DCEP) funded by the National Research Development and Innovation Fund of the Ministry of Culture and Innovation and the Budapest University of Technology and Economics; and by the project NKFI-146201 awarded by the National Research, Development and Innovation Office. D.T. is supported by the Bolyai János Research Scholarship of the Hungarian Academy of Sciences.

References

[1] Werling, M., Reinisch, P., Heidingsfeld, M., Gresser, K.: Reversing the General One-Trailer System: Asymptotic Curvature Stabilization and Path Tracking. *IEEE Transactions on Intelligent Transportation Systems* 2014, vol. 15, no. 2, pp. 627–636. 10.1109/TITS.2013.2285602

[2] Hafner, M., Pilutti, T.: Control for Automated Trailer Backup. 2017. 10.4271/2017-01-0040

[3] Vörös, I., Takács, D.: Lane-keeping control of automated vehicles with feedback delay: Nonlinear analysis and laboratory experiments, *European Journal of Mechanics - A/Solids*, 2022. https://doi.org/10.1016/j.euromechsol.2022.104509

[4] Engelborghs, K., Luzyanina, T., & Roose, D. (2002). Numerical bifurcation analysis of delay differential equations using DDE-BIFTOOL. *ACM Transactions on Mathematical Software*, 28(1), 1-21. https://doi.org/10.1016/S0377-0427(00)00472-6

41st Danubia-Adria Symposium Advances in Experimental Mechanics
September 23-26, 2025, Kragujevac, Serbia

Extended abstract DOI: 10.46793/41DAS2025.039S

MULTITECHNIQUE CHARACTERIZATION OF CEMENT PASTE WITH AND WITHOUT GRAPHENE OXIDE

Muhammad Shahid[1], Sophie Schmid[2], Olaf Lahayne[3], Agathe Robisson[4], Bernhard Pichler[5]

[1] 0009-0007-0180-0754, TU Wien, Institute of Mechanics of Materials and Structures, Karlsplatz 13/E202, Vienna, Austria, E-mail: muhammad.shahid@tuwien.ac.at

[2] 0000-0003-4781-3976, TU Wien, Institute of Mechanics of Materials and Structures, Karlsplatz 13/E202, Vienna, Austria, E-mail: sophie.schmid@tuwien.ac.at

[3] 0000-0002-5252-1356, TU Wien, Institute of Mechanics of Materials and Structures, Karlsplatz 13/E202, Vienna, Austria, E-mail: olaf.lahayne@tuwien.ac.at

[4] 0000-0002-2434-6175, TU Wien, Institute of Material Technology, Building Physics and Building Ecology, Karlsplatz 13/E207, Vienna, Austria, E-mail: agathe.robisson@tuwien.ac.at

[5] 0000-0002-6468-1840, TU Wien, Institute of Mechanics of Materials and Structures, Karlsplatz 13/E202, Vienna, Austria, E-mail: bernhard.pichler@tuwien.ac.at

1. Introduction

Graphene oxide (GO) is a "two dimensional" material that contains functional groups such as hydroxyl, carboxyl, and epoxy [1]. The oxygen-containing functional groups facilitate dispersion of GO in aqueous solution. GO sheets have a large tensile strength and a large specific surface area [2]. This provides the motivation to explore the effects of graphene oxide GO mixed into cementitious composites, in particular because it has been reported that GO improves the microstructure and mechanical properties [3]. This is setting the scene for the present contribution. It is focused on quasi-isothermal calorimetry for characterization of the hydration kinetics, and on uniaxial compressive strength tests providing insight into the most important mechanical material property in cement and concrete research.

2. Materials and methods

Ordinary Portland cement, GO, and distilled water are used for paste production. Cement pastes with and without GO are produced with an initial water-to-cement mass ratio (w/c) of 0.42. The dosage of GO is 0.09% by mass of cement. The cement paste without GO is referred to as "OPC paste", and the one with GO as "OPC+GO paste".

The used GO comes in aqueous solution. Thus, part of the mixing water required to reach the target w/c value comes from the GO solution. The amount of additionally added distilled water is defined accordingly.

2.1 Quasi-isothermal calorimetry

Quasi-isothermal calorimetry is carried out at 20 °C using TAM Air isothermal calorimeter. The specimens are mixed outside the calorimeter, in order to achieve the high mixing energy required to avoid agglomeration of any solid material constituents. Right after mixing, the fresh paste is inserted into the testing machine. According to the producer of the calorimeter, it takes 45 minutes until the stable quasi-isothermal conditions are reached, which are required for reliable measurements. Thus, the heat-release rate resulting from the hydration reaction can only be captured from 45 minutes onwards. The tests are continued until 24 hours after paste production.

2.2 Uniaxial compressive strength tests

Strength tests are performed on cylindrical specimens. Their diameter and height are equal to 30 mm and 60 mm, respectively. The destructive tests are conducted 1, 2, and 3 days after material production. For each cylinder, the uniaxial compressive strength is calculated as the maximum force sustained by the specimen divided by the cross-sectional area.

3. Results

3.1 Hydration kinetics

Heat evolution curves follow the typical cement hydration profile. They comprise an induction period, an acceleration period, and a deceleration period.

GO alters the cement hydration profile compared to the OPC paste. It increases the heat release rate during both the induction period and the acceleration period. In addition, the main hydration peak is reached earlier and it is higher in the presence of GO compared to the OPC paste, see Fig. 1. Thus, GO accelerates the hydration kinetics. This is in agreement with the pertinent literature [2].

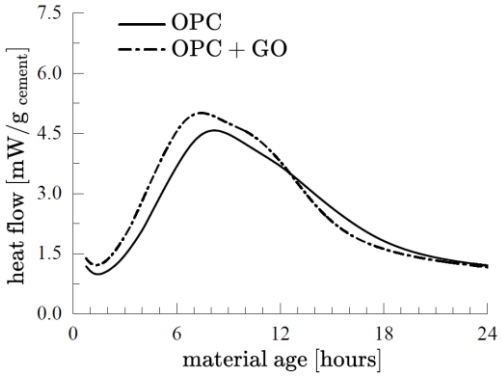

Fig. 1. Specific heat release rate as a function of material age

3.2 Uniaxial compressive strength evolution

The uniaxial compressive strength of the OPC paste and the OPC+GO paste, respectively, increases progressively with increasing material age. GO accelerates the early-age strength development, see Fig. 2. This is in agreement with the pertinent literature [2].

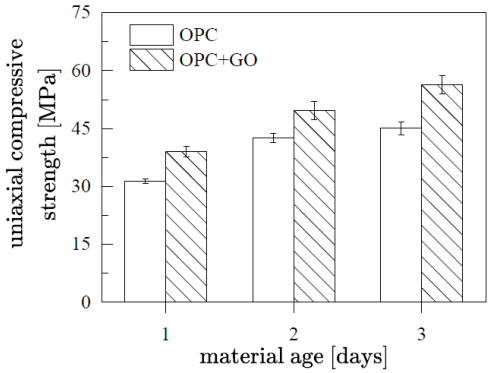

Fig. 1. Uniaxial compressive strength evolution as a function of material age.

4. Conclusion

From calorimetry and strength testing, the following conclusions are drawn:

1) The maximum heat flow of OPC with graphene oxide GO is increased by 10 % compared to OPC. Thus, GO exhibits the so-called “filler-effect” known from very finely ground limestone and/or silica powders.
2) The addition of graphene oxide GO with 0.09% mass of cement increases the early-age strength evolution of the OPC paste.

In the future, the presented experimental campaign will be enriched by adding two advanced characterization methods: (i) small angle oscillatory shear (SAOS) rheometry, in order to study the influence of GO on early-age structurization of cement paste in its gel-like state, and (ii) hourly three-minute creep testing, in order to study the influence of GO on the early-age evolution of the elastic modulus, the creep modulus, and the creep exponent of solid-state cement pastes [4].

Acknowledgments

Support of the technical teams at the Institute of Mechanics of Materials and Structures and the Institute of Materials Technology, Building Physics, and Building Ecology, of the Faculty for Civil and Environmental Engineering of TU Wien (= Vienna University of Technology) is gratefully acknowledged.

References

[1] D. R. Dreyer, S. Park, C. W. Bielawski, and R. S. Ruoff, ‘The chemistry of graphene oxide’, Dec. 14, 2010. doi: 10.1039/b917103g.

[2] H. Yang, H. Cui, W. Tang, Z. Li, N. Han, and F. Xing, ‘A critical review on research progress of graphene/cement based composites’, *Compos Part A Appl Sci Manuf*, vol. 102, pp. 273–296, Nov. 2017, doi: 10.1016/J.COMPOSITESA.2017.07.019.

[3] S. Lv, Y. Ma, C. Qiu, T. Sun, J. Liu, and Q. Zhou, ‘Effect of graphene oxide nanosheets of microstructure and mechanical properties of cement composites’, *Constr Build Mater*, vol. 49, pp. 121–127, 2013, doi: 10.1016/j.conbuildmat.2013.08.022.

[4] S. J. Schmid, L. Zelaya-Lainez, O. Lahayne, M. Peyerl, and B. Pichler, ‘Hourly three-minute creep testing of an LC3 paste at early ages: Advanced test evaluation and the effects of the pozzolanic reaction on shrinkage, elastic stiffness, and creep’, *Cem Concr Res*, vol. 187, Jan. 2025, doi: 10.1016/j.cemconres.2024.107705.

41st Danubia-Adria Symposium Advances in Experimental Mechanics
September 23-26, 2025, Kragujevac, Serbia

Extended abstract DOI: 10.46793/41DAS2025.041L

ANALYSIS OF TEST STRAIN IN A FOUR-POINT BENDING CALIBRATION SETUP FOR STRAIN GAGES

Thomas Lehmann[1], Tobias Jähnichen[2], Jörn Ihlemann[3]

[1] 0000-0001-7887-6772, Chemnitz University of Technology, Chair of Solid Mechanics, Reichenhainer Str. 70, 09126 Chemnitz, Germany, E-mail: thomas.lehmann@mb.tu-chemnitz.de;

[2] Chemnitz University of Technology, Chair of Solid Mechanics, Reichenhainer Str. 70, 09126 Chemnitz, Germany;

[3] 0000-0002-3831-0712, Chemnitz University of Technology, Chair of Solid Mechanics, Reichenhainer Str. 70, 09126 Chemnitz, Germany, E-mail: joern.ihlemann@mb.tu-chemnitz.de

1. Introduction

Strain analysis is of particular importance in experimental mechanics. For the measurement of very small strains, strain gages are often used due to their outstanding precision and accuracy. Thus, the calibration of strain gages (gage factor determination) is to be done considering high requirements [1]. Therefore, a four-point bending setup is suitable due to the clear defined strain distribution in the analyzing section, where the strain gages are applied [2]. The determination of the test strain is of particular importance here. In this contribution, two different measurement methods – using displacement transducers and 3D digital image correlation (DIC) – are applied for the determination of the test strain and compared. The DIC strain evaluation used here deviates from the method based on spline approximation of the displacements or coordinates, given, e. g., in [3].

2. Experimental setup and procedure

The test setup includes a four-point bending loading device, following [1], cf. Fig. 1. The force F is applied by a load application traverse and rollers to the specimen, which is designed as a narrow bending beam, made of aluminum (EN AW-6082, 20×20×320, w×h×l in mm). Furthermore, the specimen is supported by rollers, which are connected to a supporting structure. The four-point bending device is implemented in a 100 kN ZwickRoell testing machine. Four strain gages (two at the top, two at the bottom) of the type HBM/HBK 1-LY43-6/350 are applied in the analyzing section between the load application. Incremental displacement transducers (Heidenhain MT2571, contact measuring system) and a 3D DIC system (GOM Aramis 4M, adequate speckle pattern and measuring volume required) are used for the determination of the test strain ε_t in x-direction. Loading is carried out with a traverse speed of 1 mm/min and a maximum force $F_{\max} \approx 3$ kN.

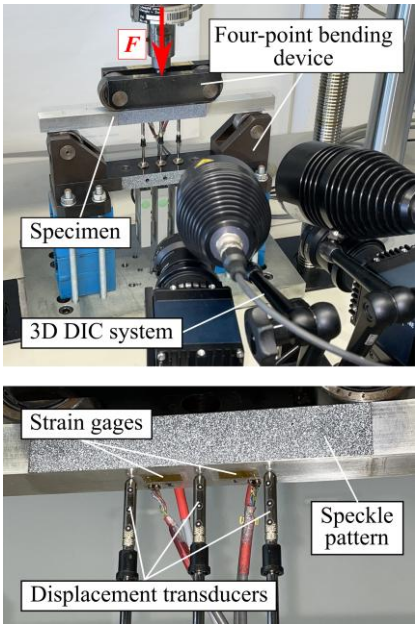

Fig. 1. Four-point bending test setup.

3. Strain and gage factor determination

Based on the constant curvature (circle arc) in pure bending, the test strain ε_t at the bottom side of the specimen is determined taking into account the height h, the distance between the displacement transducer tips a and the averaged deflection (displacement) differences p, cf. Fig. 2:

$$\varepsilon_{x\,t} = \varepsilon_t = \frac{h}{\frac{a^2}{p}+p-h} \tag{1}$$

Furthermore, using DIC, the test strain is calculated by approximating the DIC displacement data u_y with a circular arc fit. Using the resulting curvature radius ρ, the strain ε_x on the front and the test strain ε_t at the bottom side are defined by:

$$\varepsilon_x(y) = -\frac{y}{\rho(y)+y} \rightarrow \varepsilon_{x\,t} = \varepsilon_t = \frac{h}{2[\rho(y)+y]}. \quad (2)$$

Additionally, on the basis of ε_t and the bridge output $V_{\text{out}}/V_{\text{in}}$ (quarter bridge), the gage factor k is determined, cf. Eq. (3). The relative gage factor deviation $\Delta k/k_0$ (relative deviation of the determined gage factor from the value of the data sheet $k_0 = 2.11$) is then calculated by:

$$\frac{\Delta k}{k_0} = \frac{k-k_0}{k_0}, \text{ with } k = 4\frac{V_{\text{out}}/V_{\text{in}}}{\varepsilon_t}. \quad (3)$$

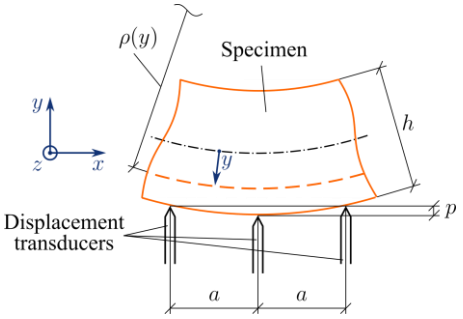

Fig. 2. Bending deformation, test strain determination.

4. Results

In the strain vs. force diagram for a representative test example shown in Fig. 3, good agreement of the strain results at the bottom of the specimen using the different methods is demonstrated (ε_t by displacement transducers, DIC; ε_{SG} by strain gages using k_0 – averaged for the two strain gages at the bottom).

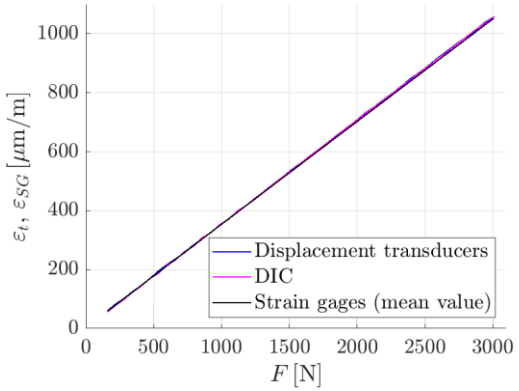

Fig. 3. Strains vs. force F using different methods for strain determination.

This is also directly reflected in the gage factor results. In Fig. 4, the relative gage factor deviation vs. the force is shown for the test example using the methods presented. Good agreement between the test strain determination methods with maximum deviations of $|\Delta k/k_0| \approx 1\,\%$ is observed at the higher loads (> 800 N). Furthermore, very good matching of both strain gage signals is demonstrated. Test series have shown, that good displacement transducer results are only achieved, as long as the surface quality of the contact area is high (disadvantage of the contact to the specimen).

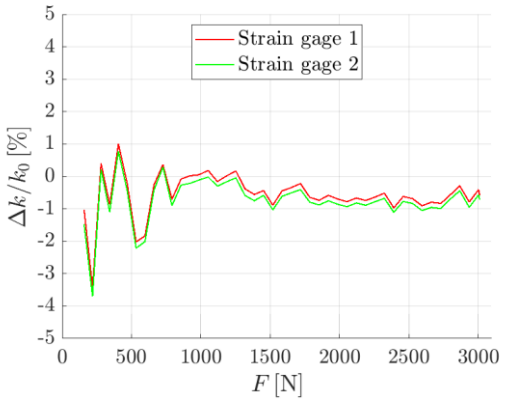

a)

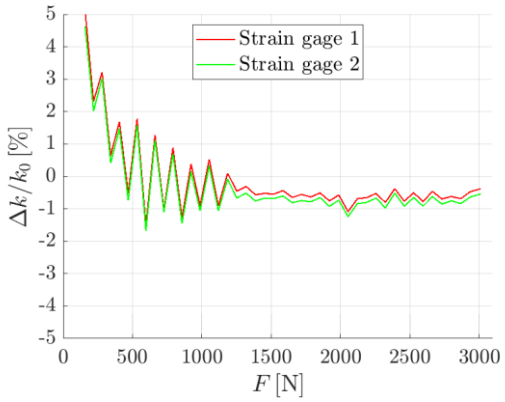

b)

Fig. 4. Relative gage factor deviation $\Delta k/k_0$ vs. force F, a) based on displacement transducers, b) based on DIC.

5. Conclusions

Precise strain analyses were carried out in a four-point bending calibration test setup for strain gages. The determined test strains using displacement transducers and 3D DIC show good agreement between the two methods and with the strain gage values (using k_0). Thus, good results are obtained for the gage factor (with limitations using displacement transducers) demonstrated by small relative deviations from the data sheet value, which are within the tolerance range of the strain gages.

References

[1] VDI/VDE standard 2635-1. *Experimental structure analysis - Metallic bonded resistance strain gauges - Characteristics and testing conditions*, 2024.

[2] Bergqvist, B. Equipment for highly accurate and repeatable strain gauge factor determination. *Strain*, 1972, 8(4), 170–176.

[3] Lehmann, T., Ihlemann, J. DIC deformation analysis using B-spline smoothing with consideration of characteristic noise properties. *Mater Today-Proc*, 2022, 62(5), 2549–2553.

41st Danubia-Adria Symposium Advances in Experimental Mechanics
September 23-26, 2025, Kragujevac, Serbia

Extended abstract DOI: 10.46793/41DAS2025.043M

STABILITY LOSS OF TAPE-SPRINGS UNDER COMPRESSIVE LOADS: A FINITE ELEMENT ANALYSIS

Péter MÁTÉ[1], András SZEKRÉNYES[2]

[1] 0000-0001-9432-8936, Budapest University of Technology and Economics, Faculty of Mechanical Engineering, Department of Applied Mechanics, Műegyetem rkp. 3., Budapest, Hungary, E-mail: peter.mate@mm.bme.hu;

[2] 0000-0002-2018-4471, Budapest University of Technology and Economics, Faculty of Mechanical Engineering, Department of Applied Mechanics, Műegyetem rkp. 3., Budapest, Hungary, E-mail: szeki@mm.bme.hu

1. Introduction

Tape springs are thin, cylindrical shells that have versatile usage, ranging from simple measuring tapes, through clockwork springs, up to space antennas, hinges and self-deploying structures. They provide easy and compact storage, yet they can be extended to be used as beam-like load bearing elements. Under opposite-sense bending load they can easily lose their stability in a snap-through phenomenon. Although the same-sense bending theoretically also results in a snap-through, experience shows that this cannot be realized as a torsional buckling mode emerges earlier. The usual applications make use either of their storability [1,2], the snap-through phenomenon [3], or the propagating moment, as it provides a practically constant [4], curvature-independent bending characteristic. Although they can be used as load bearing construction elements, their stability under compressive loads (their buckling behavior) was not analyzed. To plan measurements later, it was necessary to perform preliminary investigations to examine the expected behavior of these shell types.

2. Modeling methods

As a first step of the research, an extensive finite element analysis was performed on an arbitrary geometry to investigate the possible modes of stability loss. The finite element model is shown in Fig. 1. In its essence it corresponds to the basic Eulerian pinned-pinned boundary conditions, without restricting the torsion of the shell. The end cross-sections of the beam are not allowed to deform; their degrees of freedom are kinematically coupled to the reference nodes. As in a real scenario it is hard to accurately center the load to the cross-section centroid, the effect of the load position was also investigated. The reference nodes were simultaneously moved around in the $x - y$ plane on a grid shown in Fig. 2, and the buckling analysis was performed with a z directional, 1N compressive load. The first 10 eigenvalues were extracted in the 0-300 range.

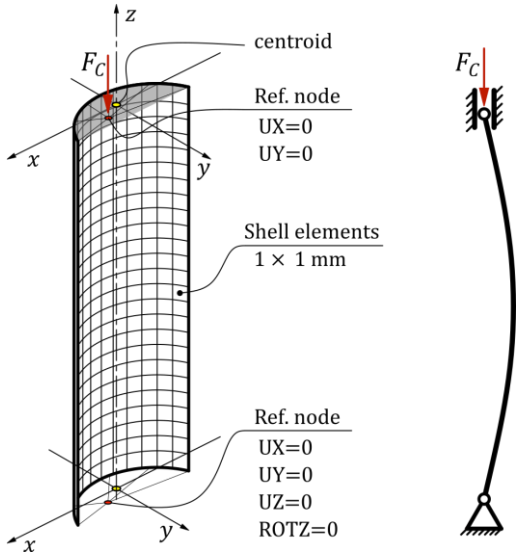

Fig. 1. The FE model and the load case

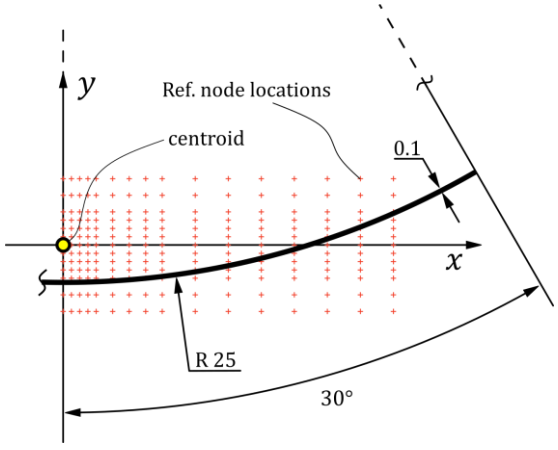

Fig. 2. The reference node locations and shell cross-section geometry

As the beam is prone to the local buckling of the cross-section, a nonlinear analysis was also performed on the shell with the same boundary conditions. For a stable simulation, the loading force was removed and replaced with a compressive displacement load.

3. Results

The results of the linear buckling analysis for the case when the reference nodes coincide with the cross-section centroid of the beam are shown in Fig. 3. Unexpectedly, the first three modes of stability loss include torsion, and only the fourth is the thoroughly investigated bending mode.

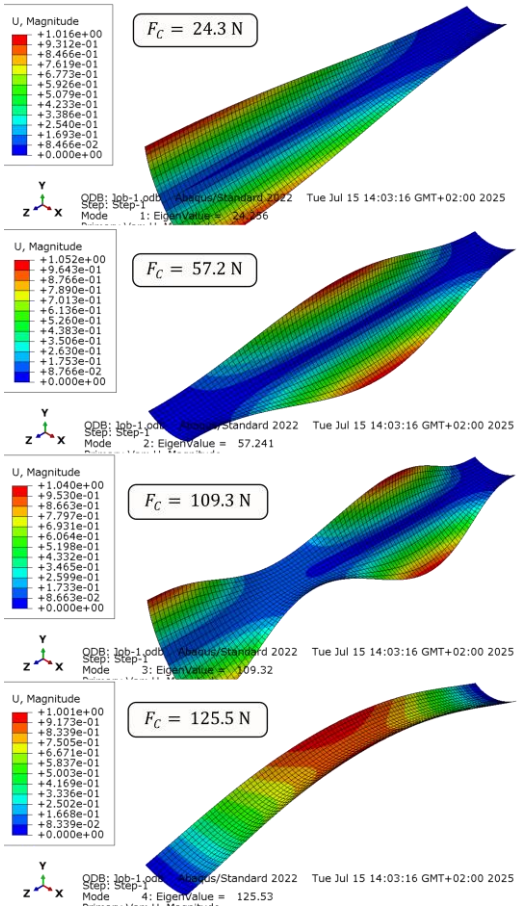

Fig. 3. The first four linear buckling modes when the shell is loaded through the centroid

The nonlinear solution led to a local buckling of the cross-section for every loading point, except for the centroid. The extracted critical force value was identified as the peak compressive load that the shell can withstand. To find the lowest critical force for each location, the first eigenvalue was plotted together with the results of the nonlinear simulations in Fig. 4.

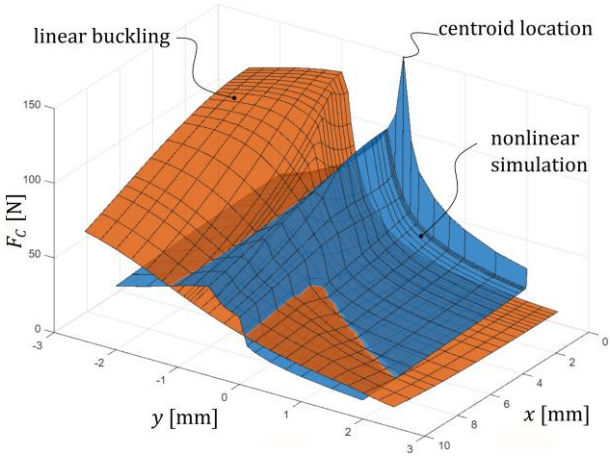

Fig. 4. Critical force values across the cross-section plane for both calculation methods

4. Conclusions

It was found that the critical force and the buckling mode may significantly be affected by the location of load. It was shown that both linear buckling and nonlinear simulations must be performed to find the expected critical force map if it cannot be guaranteed that the loading force is located at the cross-section centroid.

Acknowledgments

This work has been supported by the National Research, Development and Innovation Office (NRDI) under grant no. 145988.

References

[1] S. Seriani and P. Gallina. A Storable Tubular Extendible Member (STEM) parallel robot: Modelization and evaluation. In: *Mechanism and Machine Theory* 90 (Aug. 2015), pp. 95–107. issn: 0094-114X. DOI: 10.1016/j.mechmachtheory.2015.03.010

[2] S. Oberst, S. Tuttle, D. Griffin, A. Lambert, and R. Boyce. Experimental validation of tape springs to be used as thin-walled space structures. In: *Journal of Sound and Vibration* 419 (Apr. 2018), pp. 558–570. DOI: 10.1016/j.jsv.2018.01.014

[3] Ömer Soykasap. Analysis of tape spring hinges. In: *International Journal of Mechanical Sciences* 49.7 (Sept. 2007), pp. 853–860. DOI: 10.1016/j.ijmecsci.2006.11.013

[4] M. Martin, S. Bourgeois, B. Cochelin, and F. Guinot. Planar folding of shallow tape springs: The rod model with flexible cross-section revisited as a regularized Ericksen bar model. In: *International Journal of Solids and Structures* 188-189 (Apr. 2020), pp. 189–209. DOI: 10.1016/j.ijsolstr.2019.10.009

41st Danubia-Adria Symposium Advances in Experimental Mechanics
September 23-26, 2025, Kragujevac, Serbia

Extended abstract DOI: 10.46793/41DAS2025.045R

EXPERIMENTAL AND NUMERICAL ANALYSIS OF LASER-CUT PNEUMATIC SOFT ROBOT STRUCTURES

Kata RUZSA[1], Szabolcs BEREZVAI[2]

[1] Budapest University of Technology and Economics, Faculty of Mechanical Engineering, Department of Applied Mechanics, Műegyetem rkp. 3., Budapest, 1111, Hungary, E-mail: ruzsakata00@edu.bme.hu

[2] 0000-0002-6399-583X, Budapest University of Technology and Economics, Faculty of Mechanical Engineering, Department of Applied Mechanics, Műegyetem rkp. 3., Budapest, 1111, Hungary, E-mail: berezvai@mm.bme.hu

1. Introduction

Soft robotics has emerged as one of the most promising and rapidly evolving fields within robotics research. Unlike traditional rigid systems, soft robots are composed of highly compliant materials such as elastomers, allowing them to interact with their surroundings in more adaptable, safer, and biologically inspired ways [1]. Soft robotics also presents an opportunity to rethink actuation and control. Instead of relying on rigid mechanical linkages and electric motors, many soft robots utilize pneumatic actuators that mimic biological muscle behavior [2,3]. Combined with cost-effective fabrication techniques, like molding, 3D-printing, and laser cutting, these technologies make soft robotic systems increasingly accessible.

However, the highly nonlinear mechanical behavior of soft (rubberlike) materials coupled with complex fluid-structure interactions during pneumatic actuation presents significant challenges in design optimization. To address these, the optimal robot structure can be achieved through iterative finite element (FE) simulations.

This contribution presents the analysis of the mechanical behavior of laser-cut, pneumatically actuated soft robotic structures through experimental characterization and finite element simulations. By examining the mechanical response of different structural geometries and material compositions, the study contributes to a broader understanding of how soft robots can be used more effectively and widely in the future.

2. Robot layout, fabrication

For the analysis a PneuNet Bending Actuator was adopted based on the design description of the SoftRobotics Toolkit design library [3,4]. The soft robot structure (see Fig. 1.) consists of a series of channels and chambers inside an elastomer, which are inflated during pressurization and thus, creating the actuation. In this study, three base shapes (rectangle, triangle, ellipse) were manufactured, with two different line densities (high and low) for each shape.

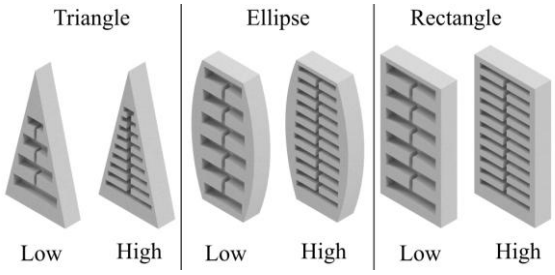

Fig. 1. Robot shapes with various line densities

The actuators were fabricated using laser-cut acrylic molds, for which an automated SVG shape generation tool was developed in Python to create the different actuator geometries with adjustable parameters. The bottom part of the actuator was cast from Elastosil M4601 material, while for the top (inflatable) part Ecoflex 00-30 and 00-50 two-component silicones were applied, thus altogether 12 robot variations were fabricated. After molding and degassing in a vacuum chamber, the specimens were cured in a drying oven. After that, the top and bottom parts of the soft robot structures were glued together using silicone adhesive.

3. Experimental investigation

The actuation of the soft robots was performed an Arduino-based pneumatic control board with pressure levels of $p = 35$ kPa and $p = 50$ kPa adjusted for Ecoflex 00-30 and 00-50, respectively. The deformation of the soft robots was analyzed with image processing methods using Motion Tracker Beta [5] software. As a result of the deformation analysis, the relation of the total bending angle $\theta(p)$, and the bending trajectory of the end point $\boldsymbol{\gamma}(p) = [x(p) \quad y(p)]^T$ was determined.

4. Material characterization

The material behavior of the Ecoflex and Elastosil materials can be described using Ogden's incompressible hyperelastic model, where the corresponding strain energy function is expressed using the Abaqus [6,7] formulation, as

$$U^{\text{Ogden}} = \sum_{i=1}^{N} \frac{2\mu_i}{\alpha_i^2}\left(\lambda_1^{\alpha_i} + \lambda_2^{\alpha_i} + \lambda_3^{\alpha_i} - 3\right) \quad (1)$$

where the corresponding material parameters μ_i and α_i were determined using experimental data, which were acquired from uniaxial tensile and compression using an Instron 3345 Single Column Testing System equipped with a 5kN load cell.

5. Finite element simulations

For the numerical simulation of the actuation process a full 3D FE model is built in Abaqus (version 2022) [7] using C3D8RH elements with hybrid formulation. The simulation was conducted in an automatic Python environment enabling the evaluation of various model parameters. The fluid-structure interaction of the chamber inflation was modelled using the Fluid Cavity Interaction approach with an incompressible gas model. During the inflation, the hyperelastic instability led to numerical convergence problems (i.e. the balloon-inflation problem [6]). To resolve this problem, the FE-simulations were performed using the arc-length method (RIKS analysis).

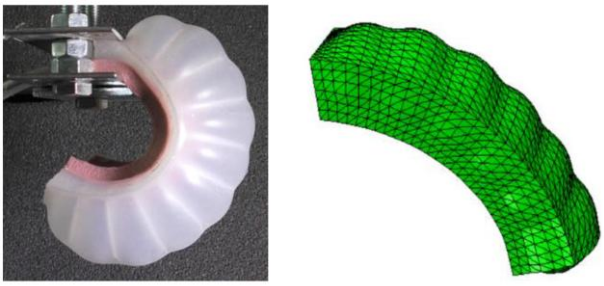

Fig. 2. Actuation (inflation) measurement and the finite element simulation of the soft robot actuation

6. Results

The comparison of the FE-simulation and the measurement results showed good agreement (see e.g. Fig. 3), indicating that the proposed material model and FE simulation approach are adequate for the analysis of such soft robot structures. Moreover, the results also revealed that both the robot shape and the line density significantly affect the maximal bending angle, and the end-point trajectory during actuation.

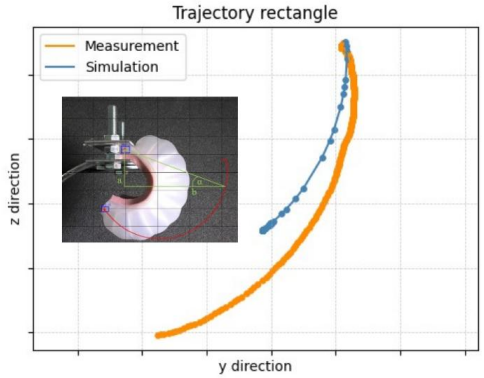

Fig. 3. The comparison of the image processing and simulation results of the end-point trajectory for a rectangular specimen with high line density made from Ecoflex 00-50 material

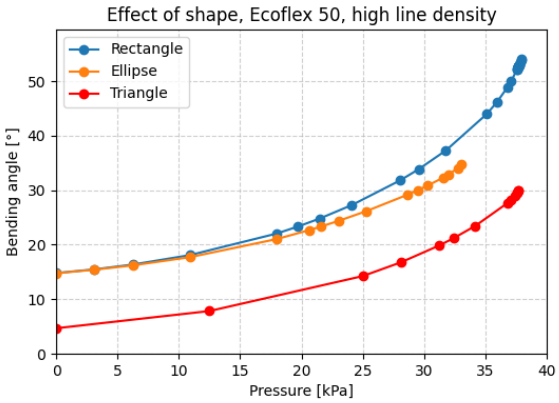

Fig. 4. The comparison of bending angles of the different robot shapes with high line density made from Ecoflex 00-50 material

Acknowledgments

The research was supported by the Hungarian National Research, Development and Innovation Office (NKFIH-NKKP-STARTING-149473), Szabolcs Berezvai was supported by the Janos Bolyai Research Scholarship of the Hungarian Academy of Sciences.

References

[1] Suzumori, K., Fukuda, K., Niiyama, R., Nakajima, K. *The Science of Soft Robots*, Springer Nature, Singapore, 2023.
[2] Mosadegh, B. et al. *Pneumatic Networks for Soft Robotics that Actuate Rapidly*. Adv. Funct. Mater., 2014, 24: 2163-2170.
[3] Shepherd, RF. et al. Multigait soft robot, *Proc. Natl. Acad. Sci. USA*, 2011, 108, 20400–20403.
[4] Soft Robotics Toolkit. www.softroboticstoolkit.com downloaded: 2025/07/30.
[5] Floch, K., Kossa, A. Motion Tracker Beta: A GUI based open-source motion tracking application, *SoftwareX*, 2023, 23, 101424.
[6] Holzapfel, G.A. *Nonlinear Solid Mechanics: A Continuum Approach for Engineering*; Wiley, 2000.
[7] ABAQUS 2022, Dassault Systèmes, Simulia Corporation, Providence, Rhode Island, USA

41st Danubia-Adria Symposium Advances in Experimental Mechanics
September 23-26, 2025, Kragujevac, Serbia

Extended abstract

DOI: 10.46793/41DAS2025.047B

OPTIMISING GAIT STABILITY ANALYSIS IN PATIENTS WITH MUSCULOSKELETAL DISORDERS

Kristóf BÁNYI[1], Zsófia PÁLYA[2], Mária TAKÁCS[3], Rita M. KISS[4]

[1] 0009-0009-3730-4773, Budapest University of Technology and Economics, Műegyetem rkp. 3, Budapest, Hungary, E-mail: kristof.banyi@gmail.com;

[2] 0000-0002-6295-3160, Budapest University of Technology and Economics, Műegyetem rkp. 3, Budapest, Hungary, E-mail: palya.zsofia@mogi.bme.hu;

[3] MÁV Hospital Szolnok, Verseghy út 6–8, Szolnok, Hungary, E-mail: drtakacsmaria@gmail.com;

[4] 0000-0003-3607-8435, Budapest University of Technology and Economics, Műegyetem rkp. 3, Budapest, Hungary, E-mail: rita.kiss@mogi.bme.hu;

1. Introduction

Gait stability is vital in musculoskeletal health, directly influencing quality of life. Nonlinear metrics such as entropy and fractal dimension enhance understanding of gait stability beyond traditional measures, thus improving diagnostic and physical therapy assessments. Entropy metrics measure the regularity of time-series data as a number between 0 and 2, with lower values signifying a more regular series. Fractal dimension quantifies the complexity and self-similarity of time-series data.

This study aimed to determine which input variable values influence approximate entropy (*ApEn*), sample entropy (*SampEn*), and Higuchi's fractal dimension (*HFD*) parameters' effectiveness for evaluating the stability of various individuals.

2. Materials and methodology

Eighty-one participants (ages 14–84, weights 43–124 kg, heights 149–189 cm) performed self-paced walking trials on an instrumented treadmill; ten were healthy and 71 had spinal or lower limb orthopaedic issues. Self-paced treadmill walking was recorded on an instrumented Zebris FDM-THM treadmill (Zebris Medical GmbH) for 2 minutes after a 5-minute accommodation to establish a stable gait. The trials were recorded with a sampling frequency of 100 Hz.

The recorder ground reaction force data enabled calculation of centre of pressure (CoP) coordinates during the recorded time interval in both the antero-posterior (AP) and mediolateral (ML) directions. The coordinates were filtered with a zero-phase 6th-order Butterworth filter with a cut-off frequency of 20 Hz. Since the trials were self-paced, participants walked at different speeds, leading to variations in the number of gait cycles. To eliminate the impact of varying gait cycle count on the analysed nonlinear metrics, each measurement was standardised by trimming and resampling to 45 gait cycles, equivalent to 4500 data points.

ApEn values were calculated using the corresponding function from the MATLAB Predictive Maintenance Toolbox. The calculation required defining an embedding dimension (m), a time delay (τ), and a similarity criterion radius (r), expressed as a percentage of the time series' standard deviation (STD) [1]. τ values were estimated using Average Mutual Information (AMI), selecting the first local minimum of AMI as the lag. m was then estimated using the False Nearest Neighbour (FNN) algorithm.

After estimating and selecting the collective embedding dimension and time delay values, the effect of r was examined through iteration. In each direction, for every participant, the *ApEn* values were calculated for every 2% of the STD at a 2–100% interval for the similarity radius.

SampEn, a data-length-independent modification of ApEn, required the same m values but no τ [2]. With the m values already selected, r was determined using the same iterative method. The final variable values can be found in Table 1.

Table 1. Determined input variables for the calculation of *ApEn* and *SampEn*.

Parameter	**m** [-]	**τ** [-]	**r** [% of STD]
AP *ApEn*	4	19	20
ML *ApEn*	4	26	15
AP *SampEn*	4	-	20
ML *SampEn*	4	-	10

HFD values range from 1 to 2, where 1 corresponds to a straight line and 2 to a line that is so complex that it fills the area of a two-dimensional plane [3]. Calculation requires defining the maxi-

mum number of sub-series composed of the original time series, herein referred to as k_{max} [4]. *HFD* values were calculated for all participants on an interval of 4–200, in increments of four. *HFD* values reached their plateau around a k_{max} of 60 in the AP and a k_{max} of 120 in the ML directions. All computational procedures, including parameter tuning were executed using MATLAB (The MathWorks Inc., Version R2023a).

3. Results

The purpose of the study was to investigate how the choice of input variables influences nonlinear metrics and their applicability to assessing gait stability. After providing a coherent method for calculating these metrics, it was important to evaluate how parameter tuning impacts the obtained results.

To analyse these effects, another intentionally off-tuned dataset was created with respect to the input parameters. Since most parameter values level out beyond certain input thresholds, further increases would result in minimal variation. Therefore, for calculating the off-tuned data set, much smaller input values were used than those originally determined. For the entropy-based metrics (*ApEn* and *SampEn*) the r was set to 5% of the STD (both Ap and ML). In the case of the *HFD*, a k_{max} value of 20 was used.

Comparisons between well- and poorly tuned datasets were conducted visually and statistically. For the visual method, we examined CoP trajectories of participants with the lowest and highest parameter values under each tuning condition. The statistical approach compared distribution shapes and outlier counts across calculation methods to determine tuning effects.

Visual inspection of CoP trajectories at entropy extremes showed that tuned AP *ApEn* clearly differentiated between participants: low values linked to short, irregular steps; high values to long, regular cycles. Similarly, higher ML *ApEn* values were usually paired with trajectories that had maintained a constant width. Poor tuning blurred these distinctions, producing heterogeneous trajectories and undermining interpretability. *SampEn* proved largely insensitive to tuning: extreme-value trajectories retained their shapes but overlapped across methods. *HFD*'s fractal dimensions also distinguished gait types regardless of k_{max}, although overlaps persisted. Only with tuned inputs in the ML *HFD* did the end-value trajectories diverge more clearly, with high values corresponding to more consistent step widths.

Statistical comparison of tuned versus off-tuned datasets showed that AP and ML *ApEn* distributions moved closer to normal when tuned, and AP *ApEn*'s outliers disappeared, improving data processability. *SampEn* showed mixed effects: tuned AP *SampEn* lost outliers but became less normal, while ML *SampEn* gained fewer outliers and retained near-normality. Tuning did not improve AP *HFD*'s distribution, but ML *HFD* became slightly more normal and cut outliers from three to two, hinting at a modest benefit.

4. Conclusions

The present study aimed to find suitable calculation methods for *ApEn*, *SampEn,* and *HFD* as these nonlinear metrics lack standardized reference values for gait stability evaluation. The various input variables of these metrics were tuned specifically on data gathered from gait, and the effects of the tuning were determined via comparison with a purposefully badly tuned dataset. The comparisons showed the large effect that input variable choice has on the final values and that the tuning had successfully resulted in values suitable for evaluating gait stability. The dataset incorporated a heterogeneous population, including both healthy participants and those with various musculoskeletal disorders, covering a broad range of age groups, weights, and heights.

Acknowledgments

This research was supported by the Hungarian Scientific Research Fund of the National Research, Development, and Innovation Office (Grant No K146308). PZ is supported by the EKÖP-24-4-I-BME-252 Hungarian Excellence Scholarship Program of the Ministry for Innovation and Technology.

References

[1] The MathWorks, Inc., Predictive Maintenance Toolbox documentation. https://www.mathworks.com/help/predmaint/index.html.

[2] Martínez-Cagigal, V. Sample entropy. https://www.mathworks.com/matlabcentral/fileexchange/69381-sample-entropy. Accessed October 17, 2023.

[3] Higuchi, T. Approach to an irregular time series on the basis of the fractal theory. *Phys D: Nonlinear Phenom*, 1988, 31(4), 277–283.

[4] Monge-Álvarez, J. Higuchi and Katz fractal dimension measures. https://www.mathworks.com/matlabcentral/fileexchange/50290-higuchi-and-katz-fractal-dimension-measures. Accessed October 2, 2024.

41st Danubia-Adria Symposium Advances in Experimental Mechanics
September 23-26, 2025, Kragujevac, Serbia

Extended abstract DOI: 10.46793/41DAS2025.049K

ALTERNATIVE METHOD OF STRESS PARAMETERS DETERMINATION DURING TENSILE TESTS USING METRIC ENTROPY AND DIC

Zbigniew L. KOWALEWSKI[1], Mateusz KOPEC[2], Grzegorz GARBACZ[3], Adam BRODECKI[4]

[1] 0000-0002-8128-0846, IPPT PAN, Pawińskiego 5B, 02-106 Warsaw, Poland, E-mail: zkowalew@ippt.pan.pl
[2] 0000-0001-9565-3407, IPPT PAN, Pawińskiego 5B, 02-106 Warsaw, Poland, E-mail: mkopec@ippt.pan.pl
[3] 0000-0001-9889-6439, Opole University of Technology, Opole, Poland, E-mail: g.garbacz@po.edu.pl
[4] 0000-0001-8303-1715, IPPT PAN, Pawińskiego 5B, 02-106 Warsaw, Poland, E-mail: abrodec@ippt.pan.pl

1. Introduction

The paper proposes a combined method for the mechanical properties assessment of composite materials based on the analysis of the internal dynamics of raw data from uniaxial tensile tests. Determination of the Kolmogorov-Sinai (K-S) metric entropy from the recorded data enables to find the tensile strength of materials. A correctness of the methodology proposed was verified by the full-filed DIC measurements. The main aim of this research is to present the combination of two different research methods: classical, analytical determination of K-S entropy on the basis of measurement data captured from uniaxial tensile tests and optical full-field displacement measurements collected by means of digital image correlation technique.

2. Materials and Methods

The material tested was a glass fibres based thermoplastic Elium acrylic. Elium 150, acrylic resin was developed and provided by the chemical group ARKEMA. The glass transition temperature of Elium 150 is around 105°C (T_g = 105°C). The resin contains an acceleration agent (acrylic monomer) for activating the catalyst that causes a reaction of polymerization at ambient temperature. A bidirectional glass fibres fabric provided by Chomarat Textiles Industries were used as the reinforcement. The material consisted fibres intersecting themselves in the warp and weft directions. The fabric has the same properties along both these directions. The repetition period of the fabric pattern is T = 7.8 mm and its fabric mass area (surface density) is close to ds = 600 g/m^2. More details of this material can be found in [1]. Since the composite containing of plain weave woven had the identical mechanical properties in the warp [0°] and weft [90°] directions, only two orientations, representing two different cases were selected in this study. The first group of rectangular-shaped specimens of 200 × 50 × 2.5 mm (Fig. 1) was cut out along the fibres direction, while the second one along direction inclined by an angle of 45° with regard to that of the fibres one.

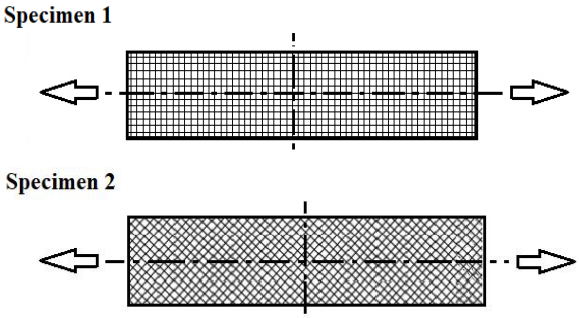

Fig. 1. Reinforcing fibres configurations in specimens tested.

A degree of physical and chemical processes' irreversibility is always expressed as a positive numerical value with the increase of entropy. According to Boltzmann, the entropy of the macroscopic state S is proportional to the thermodynamic probability. The relationship between statistical mechanics and chaos theory is reflected in the concept of the Kolmogorov-Sinai metric entropy [2, 3]. At the same time, Kolmogorov relied on the concept of statistical information proposed by Shannon [4], who describes the transmission of telecommunications signals. In this paper, the Kolmogorov-Sinai metric entropy for a discrete probability distribution is expressed by the formula:

$$S = -\sum_{i=1}^{N} p_i \, lnp_i \qquad (1)$$

where: N - the number of sub-intervals into which the data set of measurement results was divided; p_i

- the probability of the results in i interval, (whereby by definition $p \ln p \equiv 0$, if $p = 0$).

If the sub-intervals are equal ($p_i = 1/N$ for every i), then the entropy is expressed by the formula $S = \ln N$ taking the maximum value, which represents a specific number. On the other hand, if it is known that the results fall within one particular range, then the metric entropy will take the minimum value of $S = 0$, because $p_i = 1$.

3. Results and Discussion

Figure 2 presents the uniaxial tensile curves for both specimen types, in conjunction with selected images obtained from the DIC optical method.

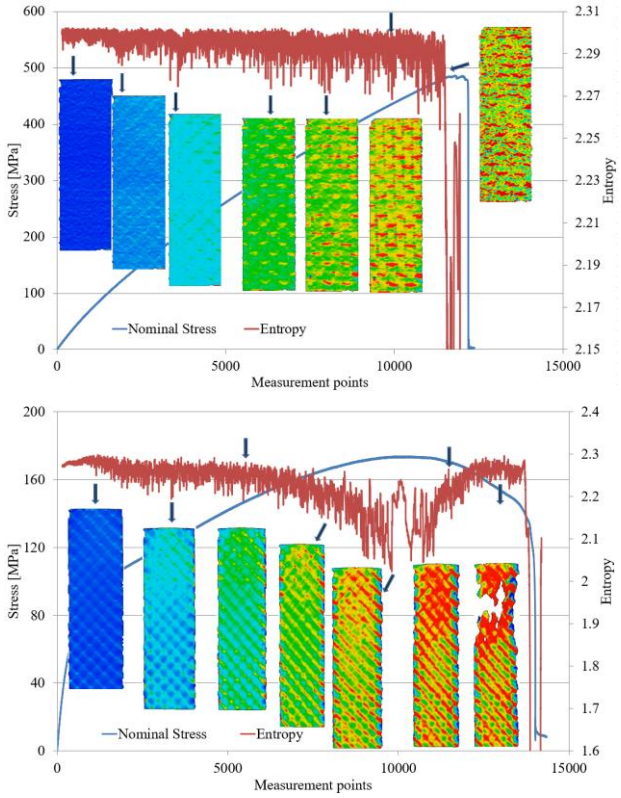

Fig. 2. Tensile curve in combination with K-S entropy diagram and DIC images as a function of measuring points for specimens 1 (top chart) and 2 (bottom chart).

The selection was made from approximately 1,000 images recorded for each specimen during the test. Stress, strain and DIC images were assigned to the successive measurement points. It was observed, that the specimen 1 is able to transfer stress more than twice as high as the specimen 2. Such behaviour of the material was related to the different location of the reinforcing phase fibres in relation to the direction of the tensile force. Deformation of the specimen 2 composite structure occurred at a much earlier deformation stage than in specimen 1. Also, the K-S entropy fluctuations of the nominal stress measurement data are more intense for this specimen. Moreover, the local minimum entropy correlates with the results elaborated on the basis of DIC images. A comparison of the ultimate tensile strength (UTS) values obtained by using different techniques was presented in Table 1.

Table 1. Comparison on ultimate tensile strength values obtained by using different techniques

	Ultimate tensile strength [MPa]	
	Specimen 1	Specimen 2
DIC	476	173
Extensometer	479	173
Entropy	476	173

The excellent agreement of these values indicates a great suitability and high accuracy of K-S entropy approach in determination of UTS. More details of this research can be find in [5].

4. Conclusions

Combination of the calculated K-S entropy and DIC measurements makes it possible to reflect basic phases of the tensile curve and objectively evaluate the selected mechanical properties of the composite material tested.

With regard to the composite in question, the proposed research methodology enabled determination of the correlation between the location of the reinforcing phase architecture in the matrix in relation to the load direction and deformation.

References

[1] Libura T., Boumbimba R.M., Rusinek A., Kowalewski Z.L., Szymczak T., Gerard P., Effect of uniaxial fatigue aging and fabric orientation on low impact velocity response of glass fibers/elium acrylic composite laminates. *Materials*, 2021, 14(15), 4089-1-23.

[2] Kolmogorov A.N., Entropy per unit Time as a Metric Invariant of Automorphism. *Doklady of Russian Academy of Sciences*, 1959, 124, 754-755.

[3] Sinai Y.G., On the Notion of Entropy of a Dynamical System. *Doklady of Russian Academy of Sciences*, 1959, 124, 768-771.

[4] Shannon C.E., A Mathematical Theory of Communication. *The Bell System Technical Journal*, 1948, 27, 379–423, 623–656.

[5] Kopeć M., Garbacz G., Brodecki A., Kowalewski Z.L., Metric entropy and digital image correlation in deformation dynamics analysis of fibre glass reinforced composite under uniaxial tension. *Measurement*, 2022, 205(112196), 1-6, 2022.

41st Danubia-Adria Symposium Advances in Experimental Mechanics
September 23-26, 2025, Kragujevac, Serbia

Extended abstract DOI: 10.46793/41DAS2025.051H

INFLUENCE OF TEMPERATURE ON MODE I FRACTURE TOUGHNESS OF A DUCTILE ADHESIVE.

Lukáš HORÁK[1], Jan KRYSTEK[2]

[1] 0009-0003-8975-2865, Faculty of Applied Sciences – University of West Bohemia, Technická 8, Pilsen, Czech Republic, E-mail: horakl@kme.zcu.cz;

[2] 0000-0002-2805-1542, Faculty of Applied Sciences – University of West Bohemia, Technická 8, Pilsen, Czech Republic, E-mail: krystek@kme.zcu.cz ;

1. Introduction

The main goal of this study is to quantify the effect of temperature on Mode I fracture toughness for a ductile adhesive. Later, this set of material parameters was used to simulate a Double Cantilever Beam (DCB) sample with various shapes of Traction-separation models to better capture the gradual failure of the adhesive under different thermal operating conditions.

2. Experiments

To describe the adhesive in its simplest form, we need a set of material parameters which are summarized in Table 1; the methodology for obtaining all of the specified parameters was in detail described in [1]. These are applicable primarily for brittle adhesive.

Table 1. Parameters for complex numerical simulation of brittle adhesive

Zone name	Parameter	Symbol	Unit
Elastic	Young's modulus	E	[Pa]
	Poisson's ratio	υ	[-]
	Shear modulus	G	[Pa]
Initiation of Fracture	Tensile failure strength	σ_f^T	[Pa]
	Shear failure strength	τ_f	[Pa]
	Tensile failure strain	ε_f^T	[-]
Crack Propagation	Strain energy release rate for mod I	G_I	[Jm^{-2}]
	Strain energy release rate for mod II	G_{II}	[Jm^{-2}]

To simplify the process in modelling same material parameters were used for modelling ductile adhesive with expansion to different traction-separation shapes. Araldite 2015 A+B was chosen as a representative of a ductile adhesive.

Mode I fracture toughness was evaluated by performing a DCB test which was chosen as a most suitable method [2]. Experiments were performed on a universal testing machine with a thermal chamber.

Temperature dependence of adhesive was evaluated in a range of negative and positive values of Celsius, with the highest one exceeding the glass transition temperature value. Before the experiment itself the samples were tempered to the desired temperature.

2.1 DCB Sample

During the loading of the DCB specimen with a constant crosshead rate, the crack growth has to be stable and no excessive bending with large plastic defamation should occur in adherends. For this purpose, numerical simulation of DCB samples were first analyzed to better choose the adherends material and thickness based on the approximation of material parameters in literature [3]. Based on that and by experimental verification samples were fabricated from two prismatic aluminums (EN AW-2024 T3) strips with thickness of 1.6 mm.

The constant thickness and alignment of the whole sample were ensured by use of several molds designed for this purpose. Geometry and dimensions of the sample are apparent from Fig. 1 where all of the values presented are in mm.

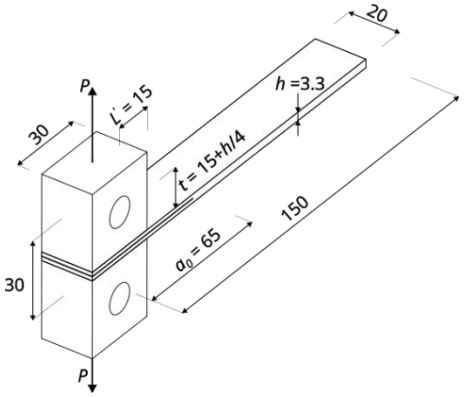

Fig. 1. Geometry of DCB sample [1].

2.2 Evaluation

For the evaluation of the strain energy release rate for mod I, the Modified Beam Theory reduction method was used as

$$G_I = \frac{3P\delta}{2B(a+|\Delta|)}. \quad (1)$$

Correction factor N was used on the compliance C and on the strain energy release rate G_I to capture the stiffening of the adherends due to use of block for load distribution. The crack length a was visually observed and measured from synchronized photographs taken during measurement. Force P was measured with a load cell and load point displacement δ with extensometer.

3. Simulations

All of the mechanical data of the adhesive was used for numerical simulations of DCB samples. These were performed with a study of traction-separation shapes. Some basic shapes were tested, as seen in Fig. 2, including bilinear, trilinear, parabolic, and exponential shapes as suggested in [4].

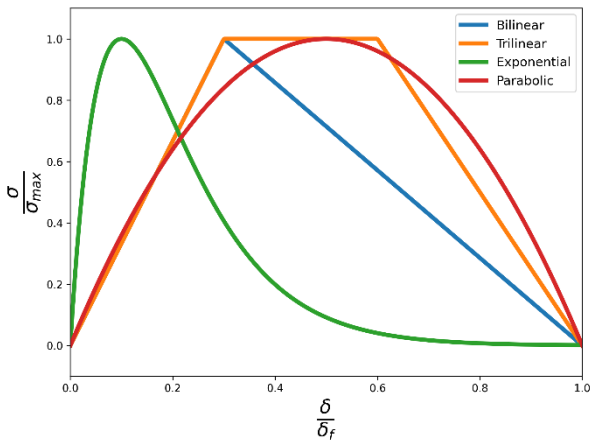

Fig. 2. Different forms of the traction-separation law.

For the purpose of easily defining the Traction-separation shape and future extension of the model the user material definition VUMAT was defined in finite element analysis software Abaqus.

4. Conclusions

In this work, the influence of temperature on Mode I fracture toughness of a ductile adhesive was studied, with a study of different traction-separation shapes to better capture adhesive degradation.

Acknowledgments

Work was supported by the project SGS-2025-015 of the University of West Bohemia.

References

[1] Horák, L., Krystek, J. Methodology and Determination of Parameters for Modeling Brittle Adhesive. In *Proceedings of the EAN 2024 - 62nd International Conference on Experimental Stress Analysis*, Božĺ Dar, 4-6 June, 2024;

[2] Banea, M.D., da Silva, L.F.M. Adhesively bonded joints in composite materials: An overview. In *Proceedings of the Institution of Mechanical Engineers, Part L: Journal of Materials: Design and Applications*, 2016, 223(1), pp. 1–18;

[3] Campilho, R.D.S.G., Pinto, A.M.G., Banea, M.D., Silva, R.F., da Silva, L.F.M. Strength Improvement of Adhesively-Bonded Joints Using a Reverse-Bent Geometry. Journal of Adhesion Science and Technology, 2011, 25(18), pp. 2351–2368;

[4] Dogan, F., Hadavinia, H., Donchev, T., Bhonge, P., Delamination of impacted composite structures by cohesive zone interface elements and tiebreak contact. Central European Journal of Engineering, 2012, 2(4), pp. 612–626;

Extended abstract DOI: 10.46793/41DAS2025.053H

INVESTIGATION OF RESIDUAL STRESS EVOLUTION DUE TO CYCLIC LOADING BY YIELD SURFACE TRACKING

Radim HALAMA[1], Michal KOŘÍNEK[2], Jiří ČAPEK[3], Karel TROJAN[4], Radim PETKOV[5], Adam GLADIŠ[6], Jiří HAJNYŠ[7], Nikolaj GANEV[8]

[1] 0000-0002-3546-4660, VŠB-Technical University of Ostrava, 17. listopadu 2172/15, Ostrava-Poruba, Czech Republic, E-mail: radim.halama@vsb.cz
[2] 0000-0001-5108-7909, VŠB-Technical University of Ostrava, 17. listopadu 2172/15, Ostrava-Poruba, Czech Republic, E-mail: michal.korinek@vsb.cz
[3] 0000-0002-0695-0619, Czech Technical University in Prague; Trojanova 13, 120 00 Prague, Czech Republic, E-mail: jiri.capek@fjfi.cvut.cz
[4] 0000-0001-9530-2586 Czech Technical University in Prague; Trojanova 13, 120 00 Prague, Czech Republic, E-mail: karel.trojan@fjfi.cvut.cz
[5] VŠB-Technical University of Ostrava, 17. listopadu 2172/15, Ostrava-Poruba, Czech Republic, E-mail: radim.petkov.st@vsb.cz
[6] VŠB-Technical University of Ostrava, 17. listopadu 2172/15, Ostrava-Poruba, Czech Republic, E-mail: adam.gladis.st@vsb.cz
[7] 0000-0002-9228-2521, VŠB-Technical University of Ostrava, 17. listopadu 2172/15, Ostrava-Poruba, Czech Republic, E-mail: jiri.hajnys.st@vsb.cz
[8] 0000-0002-3275-0207, Czech Technical University in Prague; Trojanova 13, 120 00 Prague, Czech Republic, E-mail: nikolaj.ganev@fjfi.cvut.cz

1. Introduction

Additive manufacturing (AM) technologies, particularly Selective Laser Melting (SLM), enable the production of complex metallic parts directly from powder. SLM, a powder bed fusion process, builds components layer-by-layer using a focused laser source. However, the inherent thermal complexity of the process, characterized by rapid heating and cooling cycles, leads to the formation of significant residual stresses (RS). The magnitude and distribution of these stresses are highly sensitive to process parameters such as laser power, scanning speed, and scanning strategy [1]. Within the context of AM, the most critical of these are macroscopic residual stresses, which can severely impact the structural integrity and fatigue life of as-built components.

This work investigates the reduction of these stresses by applying the yield surface tracking technique, an approach traditionally used for studying plastic anisotropy, implemented on an axial-torsional testing machine [2].

2. Material and methodology

The investigated material is Inconel 718, a precipitation-strengthened nickel-based superalloy containing elements such as Nb, Ti, and Al. When produced by SLM, its as-built microstructure is typically heterogeneous, characterized by columnar grains, fine dendritic structures, and the presence of interdendritic Laves phases [3]. This complex microstructure is a primary contributor to the high residual stresses observed in as-built components.

For this study, tubular thin-walled specimens were produced by the SLM process. The specimens were built in a vertical orientation using virgin powder and were tested in their as-built condition, without any post-process heat treatment.

The specimen geometry is based on the standard for low-cycle fatigue testing. Due to the nature of the AM process, the final dimensions deviated slightly from the nominal design. The actual measured dimensions of the gauge section were an inner diameter of 11.3 mm, an outer diameter of 13.9 mm, and a length of 28 mm.

2.1 Yield surface tracking

The evolution of residual stresses was investigated using a yield surface tracking method with a defined center point. The tubular geometry of the specimens allowed for the precise application and control of combined axial-torsional stress states, which is a prerequisite for this technique.

All experiments were conducted under stress control. The combined axial-torsional stress paths were defined by a specific angle, ψ_i, which governs the ratio of the stress rates. The sequence of the 16 applied loading paths is shown in Fig. 1.

The component stress rates, axial ($\dot{\sigma}$) and torsional ($\dot{\tau}$), were defined as:

$$\dot{\sigma} = \dot{\sigma}_{eqv} \cdot cos\psi_i \, , \dot{\tau} = \dot{\sigma}_{eqv} \frac{sin\psi_i}{\sqrt{3}}, \qquad (1)$$

where the equivalent stress rate ($\dot{\sigma}_{eqv}$) was set to a constant 1 MPa/s for each probing path. The unloading phases were performed at a faster rate of 10 MPa/s to reduce the total experiment time.

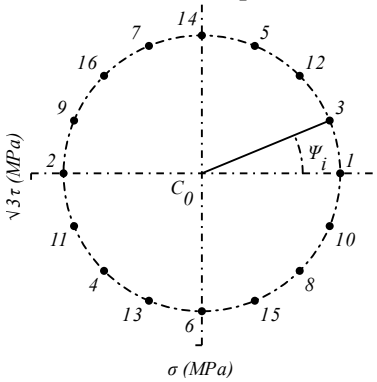

Fig. 1. Scheme of the loading paths applied during one yield surface tracking stage.

2.2 X-ray Diffraction Analysis

The evolution of the stress state was monitored using X-ray diffraction. Macroscopic residual stresses in both the axial and tangential (hoop) directions were determined using the conventional $sin^2\psi$ method. The measurements were performed at discrete points around the specimen's circumference at 30° intervals. To ensure a direct comparison, the irradiated spots were kept identical for all measurement steps: in the initial as-built state and after each of the three subsequent yield surface tracking stages. The size of the primary X-ray beam was defined by 4×0.5 mm² crossed slits.

In addition to the macroscopic stresses, the collected diffraction patterns were analyzed to extract key microstructural information. The stresses correspond to the γ-phase, which is the dominant component of the alloy. This included phase analysis to quantify the weight fraction of the constituent crystallographic phases. For the primary γ-phase, the analysis showed the evolution of crystallite size (D), microstrain (e), and the corresponding dislocation density (ρ). These parameters provide insight into the microstructural changes accompanying the mechanical relaxation of the residual stresses.

3. Results

The experimental results, graphically summarized in Fig. 2, confirm the effectiveness of the yield surface tracking method for residual stress reduction. The as-built specimen initially contained a high tensile stress state, with axial (σ_A) and tangential (σ_T) components of 673 MPa and 210 MPa, respectively. This corresponds to a von Mises equivalent stress (σ_{eqv}) of approximately 600 MPa.

The most significant stress relaxation occurred during the first of the three tracking stages, which alone reduced the equivalent stress by 67%. The subsequent two stages provided further, more gradual reductions. After the completion of all three stages, the final equivalent residual stress was lowered to 141 MPa. This constitutes a total reduction of over 76% from the initial as-built state, with the final axial and tangential components reaching stable values of 158 MPa and 49 MPa.

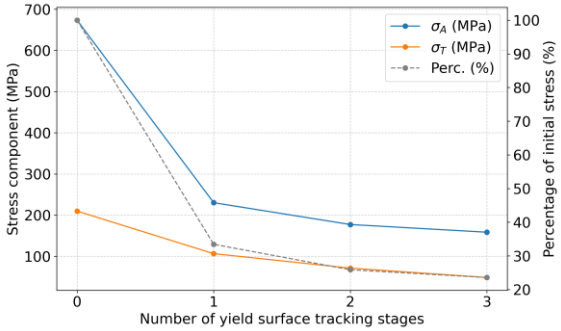

Fig. 2. Reduction of residual stress components as a function of the number of yield surface tracking stages. The secondary axis indicates the percentage of the initial equivalent stress.

4. Conclusions

The key contribution of this work is the novel application of the yield surface tracking technique, typically used for anisotropy studies, as an effective method for mechanical stress relaxation in as-built SLM Inconel 718. The method achieved a substantial reduction of more than 76% of the initial high residual stresses. The research also includes the development of a corresponding numerical simulation and the characterization of the material's cyclic response with a combined Chaboche-Voce model. This integrated experimental-numerical approach paves the way for a comprehensive simulation of the entire manufacturing and stress relaxation process.

Acknowledgments

The work on this paper was funded by the Czech Science Foundation grant 25-15579S.

References

[1] Bartlett, J. L., Li, X. An overview of residual stresses in metal powder bed fusion. *Addit Manuf*, 2019, 27, 131–149.

[2] Kořínek, M., Halama, R., Hajnyš, J., Střílka, D. Determination of the Initial Anisotropy of Inconel 718 manufactured by Additive Manufacturing. In *Proceedings of 61st International Conference on Experimental Stress Analysis*, Košice, 6-8 June, 2023; M. Hagara, M., Huňady, R., Eds.; TU Košice, Košice, 2024; pp. 102–106.

[3] Marchese, G., Atzeni, E., Salmi, A., Biamino, S. Microstructure and residual stress evolution of laser powder bed fused Inconel 718 under heat treatments. *J Mater Eng Perform*, 2021, 30, 565–574.

41st Danubia-Adria Symposium Advances in Experimental Mechanics
September 23-26, 2025, Kragujevac, Serbia

Extended abstract DOI: 10.46793/41DAS2025.055M

DEVELOPMENT OF CONSTRUCTION FOR THE TRANSFER OF HEAVY PRISMATIC PROFILES

Miroslav MILUTINOVIĆ[1], Aleksandar OKILJ[2], Sanjin TROHA[3]

[1] 0000-0002-1642-951X , University of East Sarajevo, Faculty of Mechanical Engineering, Vuka Karadzica 30, East Sarajevo, B&H Republic of Srpska, E-mail: miroslav.milutinovic@ues.rs.ba

[2] 0009-0009-9864-4413, University of East Sarajevo, Faculty of Mechanical Engineering, Vuka Karadzica 30, East Sarajevo, B&H Republic of Srpska, E-mail: aleksandarokilj1019@gmail.com

[3] 0000-0003-2086-372X, University of Rijeka, Faculty of Engineering, Vukovarska 58, Rijeka, Croatia, E-mail: sanjin.troha@riteh.uniri.hr

1. Introduction

Determining the load capacity of machine parts used in the transport of heavy profiles is a challenging, but also very responsible task for any engineer. This process requires a detailed analysis of loads, deformations and critical points where local damage or system failure can occur. In modern mechanical practice, the application of the finite element method (FEM) is becoming an indispensable tool due to its precision in predicting the behavior of materials, as well as the ability to quickly and efficiently vary geometry and boundary conditions [1,3]. FEM enables the simulation of real working conditions of the structure with minimal costs of experimental testing, which gives engineers wider possibilities in optimizing structural solutions. The load-bearing capacity of steel profiles is influenced by a number of parameters, among which the choice of material [4], the method of support and stiffening of elements, geometric shape, as well as the appearance of sources of stress concentration that can lead to the initiation of cracks and reduced reliability [5]. Each of these factors must be carefully considered in the design process to ensure the safety and longevity of the structure. Through this study, the process of variation of the geometry of the developed assembly for the transmission of massive profiles in the production hall is shown. The analysis was carried out taking into account key criteria such as the safety of the structure in operation and the overall reliability of the system. The results obtained indicate the importance of an integrated approach, where theoretical models and numerical simulations are combined with engineering experience in order to optimize the load-bearing capacity and long-term usability of the structure.

2. Description of the structure and selection of materials

One of the key steps in the development of a heavy-duty profile transmission assembly is the selection of the position and number of load-bearing elements. For the structure shown in Figure 1, four identical assemblies are used, which transmit a total load of a maximum of ≈1000 kg. The assembly is made of S235JR steel, while the supporting profiles are made as one-piece, i.e. they are cut from a 10mm thick board. The platform moves in two directions, that is, it lifts the load and transfers it to a certain position.

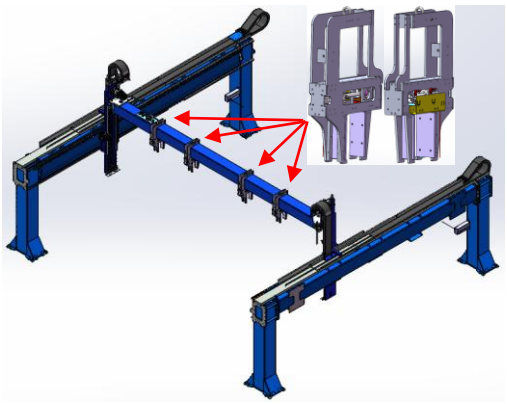

Fig. 1. Platform with 4 assemblies for receiving profiles

Table 1. Profile dimensions

Type	**Height** in mm	**Width** in mm
1	40	200
2	45	191
3	50	50
4	50	100
5	50	200
6	65	200
7	70	200
8	75	75
9	80	45

What is characteristic is that the cross-section of the profile that is transmitted varies (Table 1)

and that this system is used to capture and hold when changing the position of the profile. The opening and closing of the assembly is realized by a pneumatic cylinder.

3. Results

During testing, it was taken into account that the complete load is transferred over the upper arms, and that the support on the sides serves as a support so that the complete assembly does not slip off the platform. The analysis includes the variation of the curvature radius at critical points in order to select the optimal geometry with identical load capacity for a constant arm thickness. Figure 2 shows the distribution of Von Mises Stress when transmitting loads, and the diagram (Figure 3) shows the results obtained for the defined load for different radius values. The deformation values are below the permissible limits for all flute analyses. During the test, the maximum and evenly distributed load on all four assemblies during transport was taken because the load is always purchased from the same place and placed in a precisely defined position.

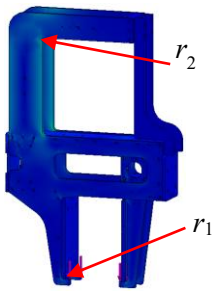

Fig. 2. Von Mises stress for load

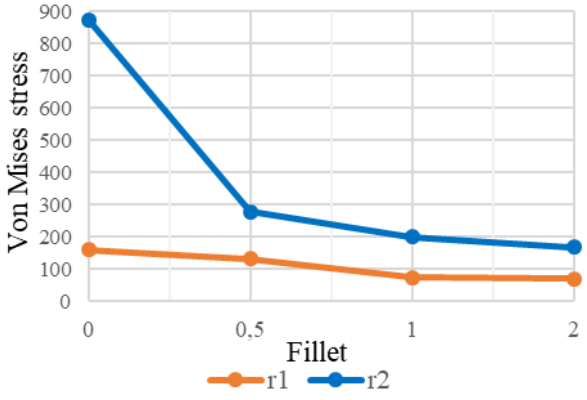

Fig. 3. Diagram of the change of Von Misses stress for different radius values.

4. Conclusions

Based on the results, it can be concluded that the radius of pain *r1* satisfies the defined loads, while the radius r_2 *less* than 1 mm does not meet the conditions and there would be a fracture on the arm. In order to meet the working conditions, and taking into account the loads and radii of the parts that are in contact with these parts, it was decided that the radius r_1 and r_2 should be made with the same values (Figure 4).

Fig. 4. Physical realization of assemblies in the production hall

The results in the exploitation process have shown that the assembly is very practical and satisfies the robustness and repeatability for different profile dimensions.

Acknowledgments

References

[1] Degtyarev, V., Chen, H., Moen, C., Peterman, K., Schafer, B., Torabian, S., Zhou, S. Finite element analysis of web crippling failure of cold-formed steel members: modeling recommendations based on a review of best practices. Annual Stability Conference, Structural Stability Research Council, 2023

[2] Farzanian, S., Louhghalam, A., Schafer, B.W., Tootkaboni, M. Geometric imperfections in CFS structural members: Part I: A review of the basics and some modeling strategies, Thin-Walled Structures, Volume 186, 2023, https://doi.org/10.1016/j.tws.2023.110619

[3] Khan, M.A.; Mustafa, R.F.; Siddiqi, Z.A.; Masood, R. Validation of AISI Design of Cold-Formed Steel Beams Using Non-Linear Finite Element Analysis. Appl. Sci. 2024, 14, 8492. https://doi.org/10.3390/app14188492

[4] Chandrasekhar, A., Sridhara, S., Suresh, K. Integrating Material Selection with Design Optimization via Neural Networks, https://doi.org/10.48550/arXiv.2112.12566

[5] Lee, Wei-chen., Zhang, Chen-hao. Computational consistency of the material models and boundary conditions for finite element analyses on cantilever beams, Advances in Mechanical Engineering, 2018, https://doi.org/10.1177/1687814018780029

41st Danubia-Adria Symposium Advances in Experimental Mechanics
September 23-26, 2025, Kragujevac, Serbia

Extended abstract

DOI: 10.46793/41DAS2025.057T

EXPERIMENTAL DETERMINATION OF THE EFFICIENCY OF A COMPOUND PLANETARY GEARBOX

Sanjin TROHA[1], Kristina MARKOVIĆ[2], Željko VRCAN[3], Filip ŠULJ[4], Miroslav MILUTINOVIĆ[5]

[1] 0000-0003-2086-372X, University of Rijeka, Faculty of Engineering, Vukovarska 58, Rijeka, Croatia, E-mail: sanjin.troha@riteh.uniri.hr

[2] 0000-0003-1569-7464, University of Rijeka, Faculty of Engineering, Vukovarska 58, Rijeka, Croatia, E-mail: kristina.markovic@riteh.uniri.hr

[3] 0000-0002-7005-4130, University of Rijeka, Faculty of Engineering, Vukovarska 58, Rijeka, Croatia, E-mail: zeljko.vrcan@riteh.uniri.hr

[4] 0009-0001-2077-0358, University of Rijeka, Faculty of Engineering, Vukovarska 58, Rijeka, Croatia, E-mail: filip.sulj18@gmail.com

[5] 0000-0002-1642-951X, University of East Sarajevo, Faculty of Mechanical Engineering, Vuka Karadzica 30, East Sarajevo, B&H Republic of Srpska, E-mail: miroslav.milutinovic@ues.rs.ba

1. Introduction

Planetary gear transmissions are essential components of industrial machinery due to their small size in relation to their rated power, high transmission ratios, and capability to transmit large torques within a compact design. They are widely applied in automotive, aerospace, and construction machinery industries owing to their reliable and efficient power transmission. The efficiency of planetary gearboxes directly influences energy consumption, operating costs, and environmental footprint. Power losses arise from gear and bearing friction as well as oil churning, and are determined by design parameters, manufacturing quality, lubrication properties, operating speed, and oil temperature. The accurate quantification of these losses is crucial for gearbox design, performance optimization, and durability, as well as for the development of energy-efficient control systems [1].

2. Design of the Experimental Gearbox

The experimental gearbox consists of two planetary stages connected in series (Fig. 1). The input shaft is the sun gear shaft of the first stage, while the output shaft is the planet carrier of the second stage. Both ring gears are stationary and fixed to the gearbox housing. The gears have a module of 1 mm in the first stage and 1.25 mm in the second stage, with an overall transmission ratio of approximately 19.6. The lubricating oil used is standard gear oil ER 90 BDS 14368-82.

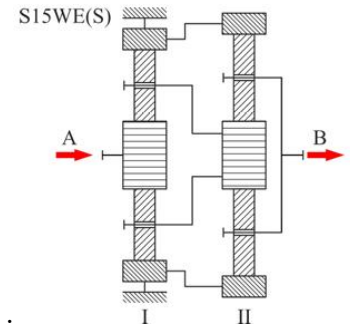

Fig. 1. Two-Carrier Gearbox

3. Test Rig and Measurement System

The test rig (Fig. 2) includes an asynchronous electric motor with VV/VF control for precise speed adjustment [2]. A torque meter positioned between the motor and the planetary gearbox measures the input torque, while a friction brake at the output simulates the load, with its torque precisely controlled by a screw mechanism and a digital force meter. Speed is monitored using a contactless

tachometer, and all data (torque, speed, forces) are collected in real time and processed by a computer for system performance and efficiency analysis. The measurements were conducted at multiple input torque levels (up to the nominal value of 5 Nm), at different rotational speeds (750 and 1500 min^{-1}), and at oil temperatures of 35 °C and 75 °C. Multiple measurements were performed for each parameter set, with system cooldown between measurements to ensure repeatability. Efficiency was evaluated as the output torque to input torque ratio, while considering the kinematic transmission ratio.

Fig. 2. Dynamic testing rig for planetary gear trains; 1 electric motor; 2 torsion meter; 3 planetary gear train; 4 gear coupling; 5 brake drum; 6 bearing; 7 friction brake; 8 lever; 9 force meter; 10 data acquisition system

4. Results and Analysis

The results have shown that efficiency increases with higher input torque due to the reduced relative share of friction and oil churning losses. Viscosity drops at elevated oil temperature (75 °C), improving efficiency, while increased speed (1500 min^{-1}) results in increased churning losses and reduced efficiency when compared to lower speed (750 min^{-1}) (Fig. 3). The largest deviations between experimental and theoretical values occur at lower torque loads, coming in good agreement with theoretical results as the load is increased towards the design load. The theoretical model is based on relative component efficiencies and empirical coefficients for additional losses. Observed deviations at lower loads arise from gearbox design details, highlighting the importance of tailored models for different gearbox types and sizes.

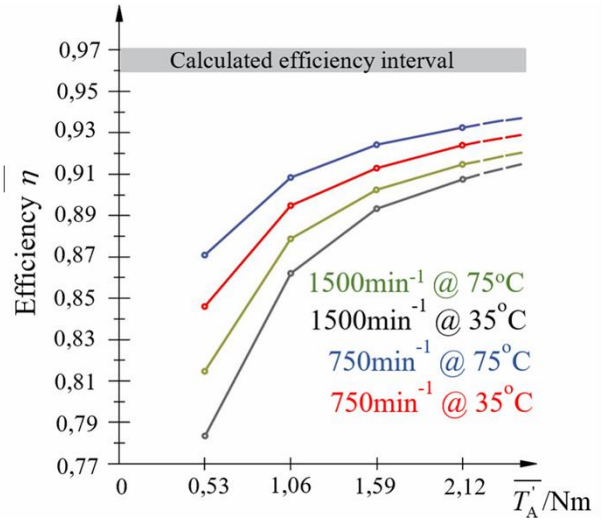

Fig. 3. The influence of input torque, oil temperature, and rotational speed on the mean efficiency of a planetary gearbox

5. Conclusions

The experimental investigation of the two-stage planetary gearbox demonstrated that increased load and oil temperature result in reduced losses, while higher speed increases churning losses. The calibrated theoretical model provides accurate efficiency estimation under nominal conditions, enabling the design of gearboxes optimized for operation with improved energy efficiency.

Acknowledgments

This work has been supported by the University of Rijeka under projects number uniri-iskusni-tehnic-23-298 and uniri-iskusni-tehnic-23-168.

References

[1] Troha, S; Milutinović, M; Vrcan, Characteristics and Capabilities of Two-Speed, Two-Carrier Planetary Gearboxes. Rijeka: University of Rijeka, Faculty of Engineering, 2024

[2] Šulj, F., Modelling of gearbox testing rig using the Autodesk Inventor software package (BSc thesis). Rijeka: University of Rijeka, Faculty of Engineering, 2024

41st Danubia-Adria Symposium Advances in Experimental Mechanics
September 23-26, 2025, Kragujevac, Serbia

Extended abstract DOI: 10.46793/41DAS2025.059R

EFFECT OF PRIOR CREEP ON TENSILE PROPERTIES OF AA2124/SiC COMPOSITES

Agnieszka RUTECKA[1], Zbigniew L. KOWALEWSKI [2]

[1] 0000-0002-0029-071X, Faculty of Civil Engineering, Warsaw University of Technology, Al. Armii Ludowej 16, 00-637 Warsaw, Poland, E-mail: agnieszka.rutecka@pw.edu.pl;

[2] 0000-0002-8128-0846, Institute of Fundamental Technological Research (IPPT PAN), Pawińskiego 5B, 02-106 Warsaw, Poland, E-mail: zkowalew@ippt.pan.pl;

1. Introduction

Tensile tests after prior creep were performed on materials like low-alloy C–Mn, 3Cr–Mo steels [1] and Inconel X-750 [2].

Metal matrix composites (MMCs) are known for their superior tensile strength and creep resistance compared to aluminum alloys, thanks to ceramic reinforcements.

The aim of this research, was to check how the tensile properties of the AA2124/SiC composites may change after prior creep.

2. Materials and methodology

Metal matrix composites (MMC) with AA2124 aluminum alloy as a matrix and SiC reinforcement of different grain size equal to 3μm and 0.6 μm and amount equal to 17 vol % and 25 vol % were investigated. A series of strain-controlled tensile tests were carried out at the strain rate equal to 0.0002 s^{-1} on the MTS 858 servo-hydraulic testing machine at ambient temperature [3]. Tensile tests were performed on both MMC types in the as-received state and the same materials subjected to prior creep. Creep tests were conducted at 300ºC and interrupted at a given value of strain, and subsequently, the specimens were subjected to the standard tensile examinations.

3. Results

As it was expected, the tensile curves for specimens after creep were characterized by a weaker stress response in comparison to those tested in the as-received state, Figs. 1-3. Moreover, the specimens after creep exhibited in most cases a higher strain at rapture in comparison to those tested in the as-received state. It has to be emphasized that the tensile curves for specimens made of the AA2124/SiC with the same content of SiC and the same particle size are similar to each other regardless of the creep stress applied previously to the specimens and value of strain at which the creep tests were interrupted. They differ in time to rapture, only.

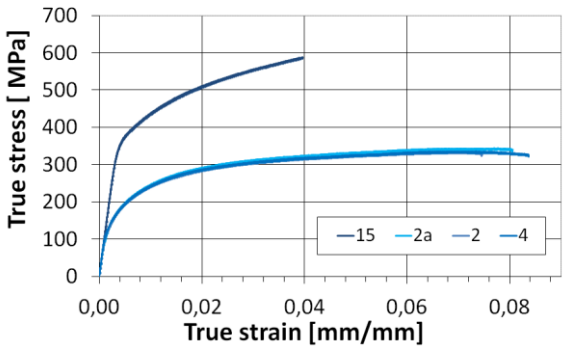

Fig. 1 Comparison of tensile curves for composite AA2124+17%SiC (3 μm) in the as-received state and after creep: specimen 15 represents material in the as-received state, specimens 2, 2a and 4 the same material after creep

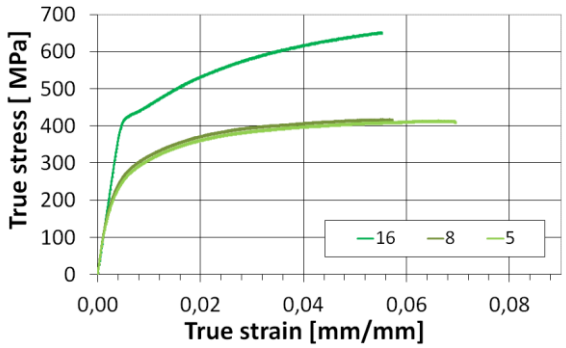

Fig. 2 Comparison of tensile curves for composite AA2124+17%SiC (0.6 μm) in the as-received state and after creep: specimen 16 represents material in the as-received state, specimens 5 and 8 the same material after creep

The lowest stress response was noticed for the AA2124+17%SiC (3 μm) with the lower SiC content and its coarser grain size, Fig. 1 and Fig. 4. The highest stress response was observed for the AA2124+25%SiC (0.6 μm) with the higher SiC content and its finer grain size, Fig. 3 and Fig. 4. On

the other hand, strain values at rupture were the largest for the AA2124+17%SiC (3 μm) and the smallest for the AA2124+25%SiC (0.6 μm).

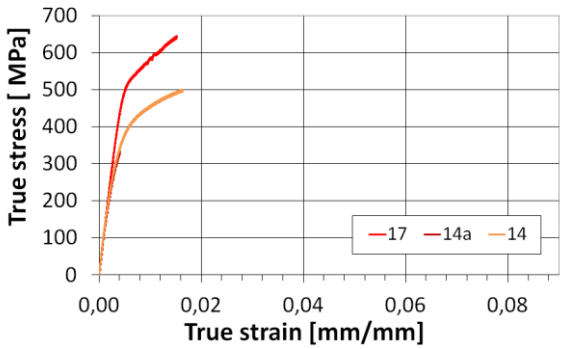

Fig. 3 Comparison of tensile curves for composites AA2124+25%SiC (0.6 μm) in the as-received state and after creep: specimen 17 represents material in the as-received state, specimens 14a and 14 the same material after creep

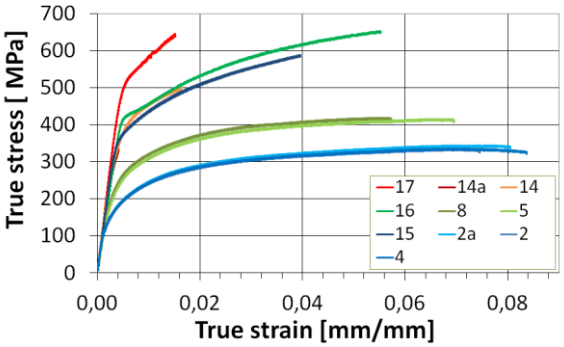

Fig. 4 Comparison of tensile curves for all composites tested in the as-received state and after creep

Based on the tensile characteristics for the materials in as-received state and after creep deformation, the elastic modulus and yield points were determined, Tables 1-2.

Table 1. Elastic modulus for the specimens in as-received state and after creep

Material	As-received [GPa]	After creep [GPa]
17% SiC, 3 μm	101	103
17% SiC, 0.6 μm	95	100
25% SiC, 0.6 μm	112	116

One can easily notice slight differences in values of the elastic modulus for the material in as-received state and after creep, Table 1. Slightly smaller values were obtained for specimens in the as-received state.

Table 2. Yield point at 0.2% offset strain for the specimens in as-received state and after creep

Material	As-received [MPa]	After creep [MPa]
17% SiC, 3 μm	383	174
17% SiC, 0.6 μm	436	247
25% SiC, 0.6 μm	528	382

Yield point values determined for the offset strain equal to 0.2% were 2.2, 1.8 and 1.4 times greater for the specimens in as-received state than those after creep for the AA2124+17%SiC (3 μm), AA2124+17%SiC (0.6 μm), AA2124+25%SiC (0.6 μm), respectively, Table 2.

4. Conclusions

The highest values of stress and the smallest strain at rapture were observed for the AA2124+25%SiC (0.6 μm). An opposite response was achieved for the AA2124+17%SiC (3 μm). Moreover, the tensile curves obtained for the specimens made of the same material, but with a different creep history, were similar to each other. Elastic modulus was slightly lower for the specimens tested in as-received state in comparison to those after creep. In the case of yield point values their variations were more significant depending on the material condition. Much greater values were obtained for the specimens in as-received state in comparison to those determined for the specimens subjected to prior creep.

Acknowledgements

The results presented in this paper have been obtained within the project “KosDeKom” (project no. 1576/B/T02/2011/40) with the National Science Center, Poland.

References

[1] Wang, H., Yang, S., Han, L., Yu, S., Ren, S., Zhang, G. Effect of prior oxidation and creep damages on subsequent tensile properties of low alloy steels. *Materials Research Express*, 2019, *6*(11), 116515.

[2] Arbel, A., Pande, C. S., The effect of prior monotonic creep on the resultant fracture toughness and tensile properties of Inconel X-750. *Journal of Materials Science*, 1988, *23*(9), 3375–3378.

[3] Rutecka, A., Kursa M., Pietrzak K., Kowalczyk-Gajewska K., Makowska K., Wyszkowski M., Damage evolution in AA2124/SiC metal matrix composites under tension with consecutive unloadings, *Arch. Civ. Mech. Eng.* 2020;20-4:1-18,135.

41st Danubia-Adria Symposium Advances in Experimental Mechanics
September 23-26, 2025, Kragujevac, Serbia

Extended abstract

DOI: 10.46793/41DAS2025.061T

DETERMINATION OF FOUR CHARACTERISTIC REGIONS IN THE STRESS–STRAIN RESPONSE OF APM FOAM UNDER COMPRESSION USING DVC

Zvonimir TOMIČEVIĆ[1], Borna BOŽOVIĆ[2], Daniel KYTÝŘ[3], Petr KOUDELKA[4]

[1] 0000-0001-9033-2639, University of Zagreb, Faculty of Mechanical Engineering and Naval Architecture, Ivana Lučića 5, 10000 Zagreb, Croatia, E-mail: zvonimir.tomicevic@fsb.unizg.hr

[2] University of Zagreb, Faculty of Mechanical Engineering and Naval Architecture, Ivana Lučića 5, 10000 Zagreb, Croatia, E-mail: borna.bozovic@fsb.unizg.hr;

[3] 0000-0001-7439-0580, Czech Academy of Sciences, Institute of Theoretical and Applied Mechanics, Prosecká 809/76 190 00 Praha 9, Prague, Czech Republic, E-mail: kytyr@itam.cas.cz;

[4] 0000-0003-1798-6120, Czech Academy of Sciences, Institute of Theoretical and Applied Mechanics, Prosecká 809/76 190 00 Praha 9, Prague, Czech Republic, E-mail: koudelkap@itam.cas.cz;

1. Introduction

The Advanced Pore Morphology (APM) foam element is a recently developed cellular material composed of spherical metallic elements with favourable mechanical properties. Owing to their ability to sustain large deformations under compression, APM foams are used as energy-absorbing structures, stiffening and damping elements, core layers, and fillers in composite materials. A major advantage lies in their straightforward application as fillers in hollow components, such as automotive parts, where they markedly enhance energy absorption with only a minimal weight penalty.

Although several studies have investigated APM foams [1, 2], their mechanical characterization remains limited. Hence, this investigation aims to determine the compressive behaviour of individual APM foam element under quasi-static loading through 3D strain measurement from an *in-situ* XCT compression test. Bulk kinematics were quantified using global Digital Volume Correlation (DVC) with finite element discretization [3], while global material behaviour was derived from mean nodal DVC strain levels obtained via the virtual gauge [4].

2. Experimental procedure

The investigated specimen was a spherical APM foam element with a diameter of 10 mm, characterized by an extremely high pore count of approximately 10^4 pores smaller than 0.1 mm. The pore radii span a wide range, from as small as 5 µm up to 2.1 mm. Although micropores dominate in number, the pore count decreases significantly with increasing pore size, reflecting the foaming process. The pores are not uniformly distributed, with a considerably greater number concentrated near the outer surface, while the highest average pore radius is shifted towards the periphery rather than the center. This distribution enables the formation of several large pores around the edges instead of a single central pore, a feature that may provide structural advantages and positively influence the mechanical performance of APM elements (Fig. 1).

An in-situ monotonic compression test was performed on a single APM foam element under displacement control at a prescribed stroke rate of 10 µm/s, with the loading sequence incorporating 20 programmed interruptions (see Fig. 2). After each interruption the maximum displacement was increased in increments of 250 µm, up to a total prescribed displacement of 5000 µm (Fig. 1). During each plateau the stroke was kept constant while the specimen was rotated through 360°, enabling volumetric imaging at defined load levels.

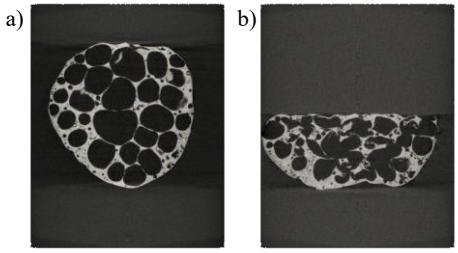

Fig. 1. Mid slices of the APM element in the a) reference configuration and at b) 50% deformation.

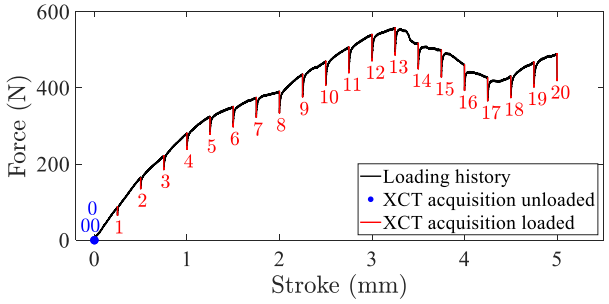

Fig. 2. Loading and acquisition history of the *in-situ* compression test.

CT scans were acquired using 1434 projections with an exposure time of 200 ms per projection. Data acquisition was performed with binning 2, a 2 mm aluminium filter, and a frame rate of 5 fps, resulting in a total duration of approximately 11 minutes per scan. The images were recorded at 8-bit gray-level depth. After cropping the extracted volumes of 665 × 751 × 601 voxels were defined with a spatial resolution of 17.92 µm/voxel. The maximum registered force during compression reached 560 N. The APM foam element exhibited a characteristic multi-stage compressive stress–strain response, and pronounced force relaxation was observed during the scanning process (Fig. 2).

3. Results and Conclusion

The DVC analysis was performed between the undeformed volume (scan 0) and 20 deformed volumes. From the measured displacement fields, principal strains were computed. The maximum principal strain field (ε_1), shown in Fig. 3, presents the strain distribution for the final scan. The resulting map reveals highly strained regions corresponding to macro cracks formed under compressive loading.

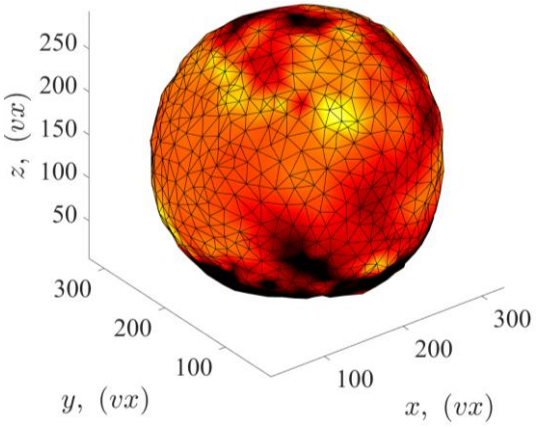

Fig. 3. An isometric view of the major eigen strain field calculated at the final loading step (*i.e.*, scan 20).

Using the virtual gauge, mean nodal strain levels were obtained (see Fig. 4). The results show that DVC-based measurements effectively capture the compressive response of APM foam (see Fig. 4) and clearly distinguish four characteristic regions of the stress–strain curve (i.e., elastic regime, pore collapse, localized deformation with shear band formation, and densification) which are less evident in the conventional stress–strain curve derived from machine loading data (Fig. 2). The formation of strained shear bands marks the onset of structural instability and progressive damage. Overall, the study highlights the advantages of volumetric 3D measurements for simultaneously characterizing global deformation behaviour and localized damage mechanisms in porous materials such as APM foam.

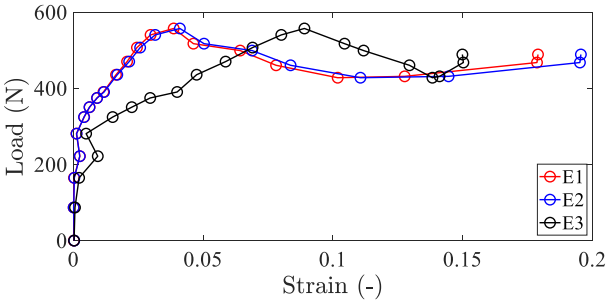

Fig. 4. Load-mean strain history over the *in-situ* compression test.

Acknowledgments

The present work was carried out as part of the GENKON project, funded by the European Union and the National Recovery and Resilience Plan (NPOO.C3.2.R3-I1.04.0121).

References

[1] Duarte, I., Vesenjak, M., Krstulović-Opara, L., Ren, Z. Compressive performance evaluation of APM (Advanced Pore Morphology) foam filled tubes. *Compos. Struct.* 2015, 134, 409–420.

[2] Vopalensky, M., Koudelka, P., Sleichrt, J., Kumpova, I., Borovinsek, M., Vesenjak, M., Kytyr, D. Fast 4D on-the-fly tomography for observation of Advanced Pore Morphology (APM) foam elements subjected to compressive loading. *Materials* 2021, 14(23), 7256.

[3] Mendoza, A., Neggers, J., Hild, F., Roux, S. Complete mechanical regularization applied to digital image and volume correlation. *Comput. Methods Appl. Mech. Eng.* 2019, 355, 27–43.

[4] Vrgoč, A., Tomičević, Z., Smaniotto, B., Hild, F. Characterization of glass fiber reinforced polymer via Digital Volume Correlation: Quantification of strain activity and damage growth. *Compos. Sci. Technol.* 2023, 234, 109932.

41st Danubia-Adria Symposium Advances in Experimental Mechanics
September 23-26, 2025, Kragujevac, Serbia

Extended abstract DOI: 10.46793/41DAS2025.063B

DEVELOPMENT OF A TEST DEVICE (FIXTURE) FOR DETERMINING THE PULL-OUT FORCE OF SWAGED BALL TERMINATIONS ON CONTROL CABLES

Milan BLAGOJEVIĆ[1], Živče ŠARKOČEVIĆ[2], Milan BOJOVIĆ[3], Ivica ČAMAGIĆ[4]

[1] 0000-0003-0710-5297, University of Pristina, Faculty of Technical Sciences, Knjaza Miloša 7, Kosovska Mitrovica, Serbia, E-mail: milan.blagojevic@pr.ac.rs

[2] 0000-0001-5110-6620, University of Pristina, Faculty of Technical Sciences, Knjaza Miloša 7, Kosovska Mitrovica, Serbia, E-mail: zivce.sarkocevic@pr.ac.rs

[3] 0000-0002-8655-1668, University of Kragujevac, Faculty of Engineering, Sestre Janjić 6, Kragujevac, Serbia, E-mail: milan.bojovic@uni.kg.ac.rs

[4] 0000-0003-4706-6333, University of Pristina, Faculty of Technical Sciences, Knjaza Miloša 7, Kosovska Mitrovica, Serbia, E-mail: ivica.camagic@pr.ac.rs

1. Introduction

The mechanical integrity of swaged ball terminations on control cables is a critical factor in the safety and reliability of aerospace, automotive, and industrial actuation systems [1,2]. While analytical models can estimate strength for idealized geometries, real terminations involve complex interactions between the ball, wire strands, and the mating seat defined by military and industry specifications [1,2]. The conditional-realistic ("pull-out") test reproduces the actual seating of the termination to directly measure maximum extraction force (F_{fail}) and to identify prevailing failure modes under service-representative constraints [3,4]. This approach captures combined effects of shear, localized indentation, and potential cable slippage, producing data suitable for design verification and quality assurance [3–5].

The present study outlines the experimental setup, testing procedure, and evaluation methodology for determining pull-out strength, aiming to establish reliable performance benchmarks for swaged ball cable terminations [4,5].

2. Materials and Methodology

The tensile testing is conducted using a Shimadzu AGS-X 10 kN universal electro-mechanical testing machine [6]. The test fixture is designed to be mounted on the testing frame using standard interface elements. The lower section of the fixture is configured avoid inducing stress concentrations and would provide a gradual load release. This prevents damage to the cable, in line with the requirement that the specimen remain serviceable after testing. The significant influence on reducing the tensile force at the end of the cable in a drum-based tensile testing setup of both the number of wraps and the friction coefficient [7]. It can be shown that the load decreases exponentially with increasing wrap count and friction, effectively distributing stress along the contact surface (Fig. 1). Testing equipment manufacturer offers a dedicated fixture for strand testing and one of its clamping halves was utilized for securing the cable during the tests (Fig. 2).

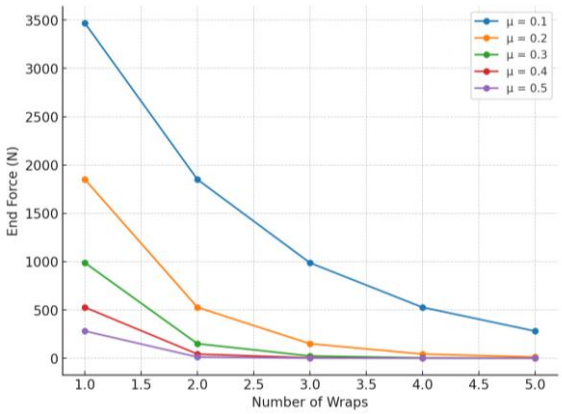

Fig. 1. Force in cable vs Number of wraps for different friction coefficients.

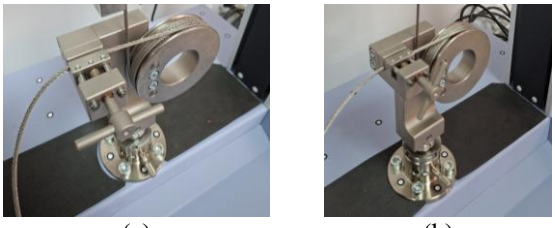

(a) (b)

Fig. 2. Cable placement in lower fixture: (a) 3 ¾ wraps, (b) 4 ¾ wraps.

The upper section of the fixture is designed to apply a concentrated load to the ball termination, enabling the shearing of the ball from the cable. The ball seat is manufactured to replicate service conditions as closely as possible, with a geometry that accurately reproduces the assembly into which the cable end is installed (Fig. 3).

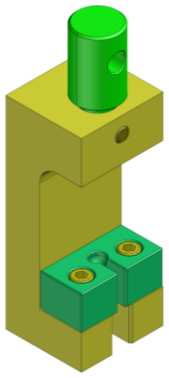

Fig. 3. Pull-out fixture (real-seat method).

3. Results

The testing is performed in two cases. First, for each production batch, the ultimate tensile load that the termination can sustain is determined under a crosshead displacement rate of 1 mm/min (Fig. 4). Subsequently, each cable is subjected to a proof load test at 2 kN, applied at a crosshead speed of 3 mm/min, held for 10 seconds, and then released (Fig. 5).

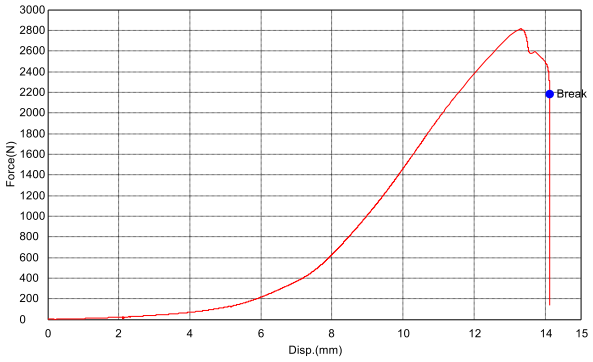

Fig. 4. Ultimate tensile load.

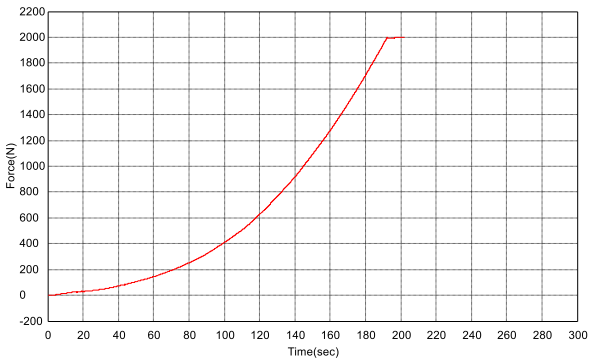

Fig. 5. Proof load test at 2 kN.

4. Conclusions

The developed pull-out test fixture, designed to replicate service conditions of swaged ball terminations on control cables, was experimentally validated through testing on over 100 cable specimens. The results confirmed the fixture's robustness, repeatability, and capability to accurately determine both ultimate tensile strength and proof load performance. This fixture is a significant and practical tool for quality control, certification testing, and research applications in aerospace, automotive, and industrial cable systems.

Acknowledgments

The part of this research is funded by Ministry of Science, Technological Development and Innovation of the Republic of Serbia, Contract no. 451-03-65/2024-03/200155.

References

[1] MIL-DTL-781. Terminal, wire rope swaging, general specification for. U.S. Department of Defense. (Active DoD specification covering swaged wire-rope terminals; testing and material requirements).

[2] MS20664. Single shank ball fittings. (Specification sheet; geometry and minimum strength requirements for ball-end fittings).

[3] Crosby Group. Wire rope end termination user's manual. (Application and installation procedures; guidance relevant to proof/load testing of swaged fittings).

[4] Zhang, C., Zhang, L., Luo, S., Zhao, Y., Zhang, J., & Xu, Y. Experimental study on the mechanical properties of the hot-cast anchors of Galfan-coated steel cables and locked-coil wire ropes at elevated temperatures. Constr Build Mater, 2023, 392, 131871. https://doi.org/10.1016/j.conbuildmat.2023.130917.

[5] Su, H., Ggg, G., Deng, L., Zhang, X., Li, J., Zhou, Q., Jia, C., Chen, X., Wang, P., & Li, D. Numerical and experimental research on the bearing characteristics and failure mechanism of zinc-cast socket termination for wire rope. Part 1: Methodology and theory. Eng Fail Anal, 2024, 167, 108957. https://doi.org/10.1016/j.engfailanal.2024.108957.

[6] Shimadzu AGS-X 10 kN https://www.ssi.shimadzu.com/products/materials-testing/uni-ttm/autograph-ags-x-series/index.html. Accessed August 5, 2025.

[7] ASTM A931-18. Standard test method for tension testing of wire ropes and strand. ASTM International, West Conshohocken, PA, 2018.

41st Danubia-Adria Symposium Advances in Experimental Mechanics
September 23-26, 2025, Kragujevac, Serbia

Extended abstract DOI: 10.46793/41DAS2025.065B

QUANTITATIVE DETERMINATION OF GLASS FIBER CONTENT IN FIBER-REINFORCED COMPOSITE MATERIALS

Milan BLAGOJEVIĆ[1], Živče ŠARKOČEVIĆ[2], Ivica ČAMAGIĆ[3]

[1] 0000-0003-0710-5297, University of Pristina, Faculty of Technical Sciences, Knjaza Miloša 7, Kosovska Mitrovica, Serbia, E-mail: milan.blagojevic@pr.ac.rs

[2] 0000-0001-5110-6620, University of Pristina, Faculty of Technical Sciences, Knjaza Miloša 7, Kosovska Mitrovica, Serbia, E-mail: zivce.sarkocevic@pr.ac.rs

[3] 0000-0003-4706-6333, University of Pristina, Faculty of Technical Sciences, Knjaza Miloša 7, Kosovska Mitrovica, Serbia, E-mail: ivica.camagic@pr.ac.rs

1. Introduction

During the operational use of fibre-reinforced composite components, structural defects such as cracks, delamination, or fibre breakage may develop due to mechanical overload, cyclic fatigue, environmental degradation, or manufacturing imperfections [1,2]. These defects can compromise the integrity of the load-bearing structure, resulting in a reduction of stiffness, strength, and overall performance. The propagation of such damage under service conditions not only shortens the component's lifespan but also increases the risk of sudden failure, which can have severe safety and economic consequences [1]. Understanding the underlying causes and mechanisms of crack formation is therefore essential for implementing effective preventive measures and improving the durability of composite structures [2].

"Burn-off" and resin removal techniques are widely applied in composite characterization to evaluate fibre–matrix ratios and detect potential structural inconsistencies [3-5]. The results provide insight into material uniformity and support the evaluation of possible links between fibre content and the occurrence of structural defects [4]. In this study, the mass fraction of glass fibres in a composite door panel was determined to assess whether material composition differences exist in defect-prone zones compared to unaffected areas.

2. Materials and methodology

The experimental procedure followed [3]. Mass measurements before and after combustion, as described in [3], enable precise quantification of the glass fibre content. Five specimens were prepared from the crack formation zone (Fig. 1), along with five control specimens intended to represent the characteristics of other areas of the panel (Fig. 2). The geometry of each specimen was precisely digitized using the ATOS optical measurement system [6] (Fig. 3a). This measurement and the resulting model enable accurate determination of the volume of each specimen.

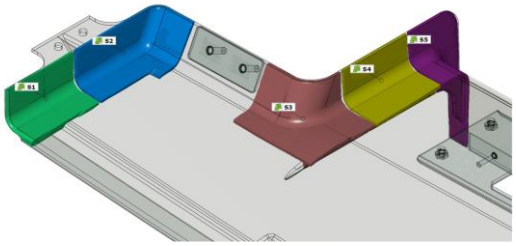

Fig. 1. Test pieces from the crack-affected zone.

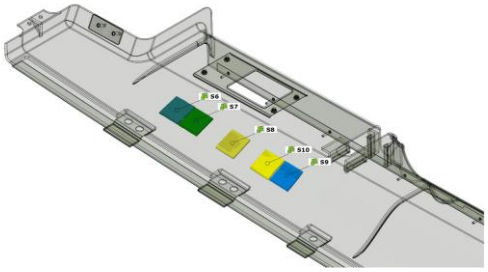

Fig. 2. Specimens made outside the crack formation zone – control specimens.

The mass of each sample before and after the test was precisely measured with an analytical balance (Figure 3b). The furnace with high-temperature combustion at 600 °C is used to remove the polymer matrix in the specimens (Fig. 3c). The specimens after burning contained a certain amount of powdered base material, so they were separated from the glass fibres (Figure 4).

3. Results

Figure 5 shows the density of the specimens, while Figure 6 shows the fiber glass content in the composite material.

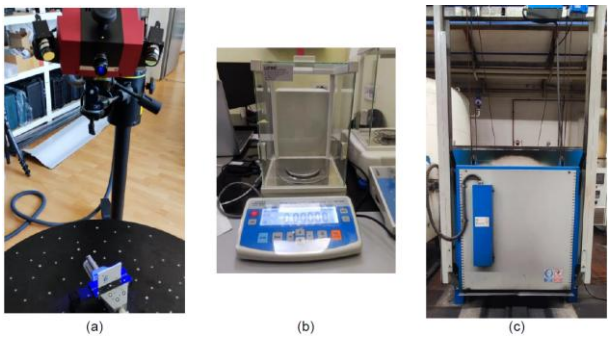

Fig. 3. Equipment used during testing:
(a) Optical measurement device ATOS,
(b) Analytical balance RADWAG,
(c) High temperature furnace Grejač Komerc.

Fig. 4. Specimens after exposing to high temperature, cleaned of base material and prepared for measurement.

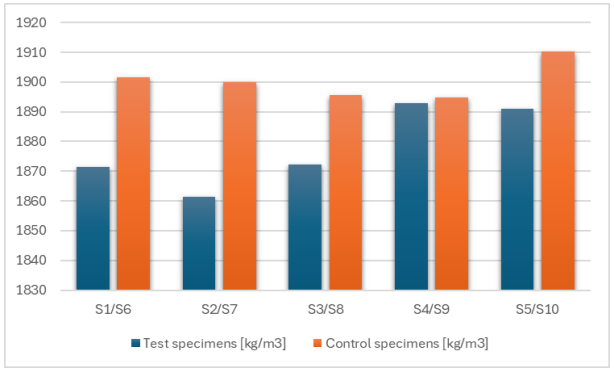

Fig. 5. Density of specimens

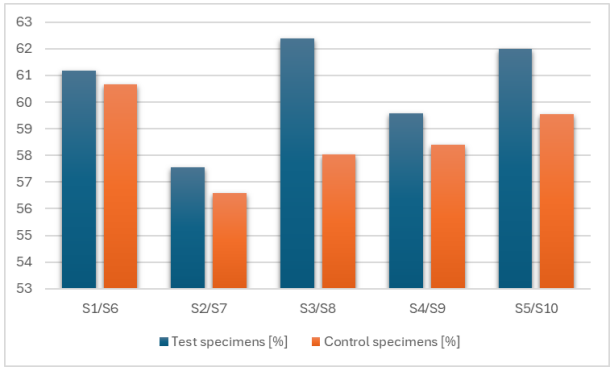

Fig. 6. Fiber Glass Content in the Composite Material

4. Conclusions

The results revealed a slightly higher average fibre mass fraction in the defect-prone zone compared to control areas, accompanied by a marginal decrease in density. This indicates potential microstructural irregularities such as voids, resin-rich areas, or incomplete fibre impregnation, which could influence local stiffness, stress distribution, and crack initiation mechanisms. These findings highlight the importance of combining compositional analysis with volumetric quality control to ensure consistent manufacturing quality and to improve the structural reliability of composite components in demanding operational environments.

The integration of [6] with high-precision optical 3D digitization and analytical mass measurement proved to be an effective approach for accurately determining the glass fibre content in fibre-reinforced composite panels.

Acknowledgments

The part of this research is funded by Ministry of Science, Technological Development and Innovation of the Republic of Serbia, Contract no. 451-03-65/2024-03/200155.

References

[1] Sharma, H., et al. Critical review on advancements on the fiber-reinforced composites. J. Mater. Res. Technol., 2023, 26, 10524–10541. https://doi.org/10.1016/j.jmrt.2023.07.179.
[2] Mohanraj, C., et al. Recent Progress in Fiber Reinforced Polymer Hybrid Composites. J. Compos. Mater., 2025, 59(2), 215–238. https://doi.org/10.1080/15440478.2025.2495911.
[3] DIN EN ISO 1172:1998. Textile-glass-reinforced plastics – Prepregs, moulding compounds and laminates – Determination of the textile-glass and mineral-filler content – Calcination methods; International Organization for Standardization: Geneva, Switzerland, 1998; Method B.
[4] Han, Z., et al. Comparative Study of Glass Fiber Content Measurement Methods. Appl. Sci., 2020, 10(15), 5130. https://doi.org/10.3390/app10155130.
[5] Fiber volume ratio. https://en.wikipedia.org/wiki/Fiber_volume_ratio. Accessed August 12, 2025.
[6] ATOS Optical 3D Scanning System. https://www.zeiss.com/metrology/en/systems/optical-3d/3d-scanning/atos.html. Accessed August 12, 2025.

41st Danubia-Adria Symposium Advances in Experimental Mechanics
September 23-26, 2025, Kragujevac, Serbia

Original scientific paper

DOI: 10.46793/41DAS2025.067T

NUMERICAL ANALYSIS OF BARREL LOADS IN THE DESIGN PHASE OF AN ARTILLERY SYSTEM

Bogdan TODOROVIĆ[1], Aleksandra OBRADOVIĆ[2], Nebojša HRISTOV[3], Damir JERKOVIĆ[4]

1. 0009-0008-4572-1318, Matikon GmbH & Co. KG, Milana Mijalkovića 21, Jagodina, Serbia, E-mail: bogdanto2000@gmail.com;

2. 0000-0001-7973-8590, Military Technical Institute, Ratka Resanovića 1, Belgrade, Serbia, E-mail: aleksandrazivkovicbm@gmail.com;

3. 0000-0002-8163-2223, University of Defence in Belgrade, Military Academy, Veljka Lukića Kurjaka 33, Belgrade, Serbia, E-mail: nebojsahristov@gmail.com;

4. 0000-0001-5182-7057, University of Defence in Belgrade, Military Academy, Veljka Lukića Kurjaka 33, Belgrade, Serbia, E-mail: damir.jerkovic@va.mod.gov.rs.

1. Introduction

The production and design of artillery weapons is a complex and expensive process. Usually, the design of such systems is based on the experience of previous models or their modifications. The tendency is to unify most of the basic elements, which are also used in other weapon systems. Tactical requirements generally define initial and boundary conditions during project setup. The basic element of every classic artillery system is the barrel, which is the most complex to design and produce.

The purpose of the paper is to present the process of barrel redesign, specifically changing a caliber of an existing barrel to a new caliber, taking into account various methods in order to determine the optimal design that would ensure the longest possible service life of the weapon system. In addition to the barrel design, an optimization of the propellant charge was carried out, i.e., variation of the gunpowder characteristics that directly affect the internal ballistic processes occurring in the barrel during firing.

The barrel was redesigned based on known data from an existing system and results obtained from the optimal configuration of gunpowder characteristics. The practical application of such a barrel is uncertain, which is why a numerical simulation of the loading conditions during firing was conducted. Numerical analysis was conducted by applying static stress in the region experiencing the maximum loads, along with variable loading conditions in the same area, to evaluate the structural durability of the designed barrel.

2. Conceptual design of the projectile and powder charge

In its original configuration, the M65 howitzer uses a two-part round. The propellant charge is caseless. Since the howitzer undergoes changing of caliber from the original caliber of 155 mm, by machining the barrel, the caliber is increased to 160 mm, resulting in a smoothbore barrel. A smoothbore barrel requires a different round design. The projectile already designed for this purpose and of this caliber is the Soviet mortar projectile for the M1943 mortar, shown in Fig. 1.

Fig. 1. Soviet mortar projectile 160 mm.

Its basic characteristics are presented in Table 1.

Table 1. Characteristics of the projectile's 160 mm

Characteristic	Value
Caliber	*160 mm*
Projectile length	*1350 mm*
Projectile weight	*42 kg*
Explosive charge weight	*30 kg*
Muzzle velocity	*343 m/s*
Range	*8200 m*

The smoothbore systems can also use projectiles with extendable stabilizers, as seen in

the 2A46 tank gun used on T-72, T-80, T-90, and M-84 tanks. This type of projectile design allows for achieving higher muzzle velocities and greater maximum ranges, but it also results in significantly increased barrel wall loading. For the purposes of this study, a projectile concept based on this design approach has been proposed.

A conceptual design is shown in Figure 2.

Fig. 2. Conceptual design of a 160 mm projectile.

The basic characteristics of the conceptual projectile design are shown in Table 2.

Table 2. Characteristics of the conceptual projectile's design

Characteristic	Value
Caliber	*160 mm*
Mass	*42,264 kg*
Center of mass, distance from nose	*0,409 m*
Center of pressure, distance from nose	*0,416 m*
Axial (Mass) moment of inertia	*0,138 kg m²*
Transverse moment of inertia	*1,78 kg m²*

Initially, the original propellant charge for the M65 model was used, and after optimizing the characteristics of the propellant, an internal ballistic calculation was performed. The optimization was realized by varying the values of the ballistic characteristics by ±2.5%, which is technologically justified and possible to implement. The calculation diagram is shown in Figure 3.

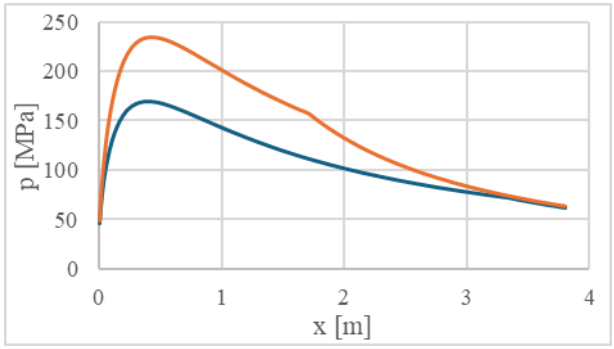

Fig. 3. Pressure changes as a function of projectile path (orange is optimal, blue is initial).

Based on the ballistic calculation using optimal parameters, the muzzle velocity of the projectile is 698.95 m/s, and with an elevation angle of 50°, the calculated range is approximately 11,5 km.

3. Barrel Dimensioning

The barrel was dimensioned according to the Huber-Mises-Hencky theory, i.e., the distortion energy criterion [3]. Based on Hooke's law, the specific strain energy can be represented as the sum of the specific volumetric deformation energy and the specific distortion energy [3].

$$(\sigma_t-\sigma_r)^2+(\sigma_r-\sigma_z)^2+(\sigma_z-\sigma_t)^2=2\sigma_e^{\,2} \tag{1}$$

After simplification, the following is obtained:

$$p_{1gr}^{\ IV}=\sigma_e\frac{a_{21}^{\ 2}-1}{\sqrt{3a_{21}^{\ 4}+1}}. \tag{2}$$

The ratio of the barrel's outer diameter to its inner diameter is given by:

$$a_{21}=\frac{r_2}{r_1}. \tag{3}$$

After inputting the data for the internal bore profile of the barrel, the external barrel profile is calculated using the equation derived from equations (2) and (3):

$$r_2=\frac{\sqrt{\sigma_e^{\,2}+\sqrt{4\sigma_e^{\,2}\cdot p^2-3p^4}}}{\sigma_e^{\,2}-3p^2}r_1. \tag{4}$$

The diagram of the elements of the longitudinal barrel cross-section, after calculation using equation (4), is shown in Figure 4.

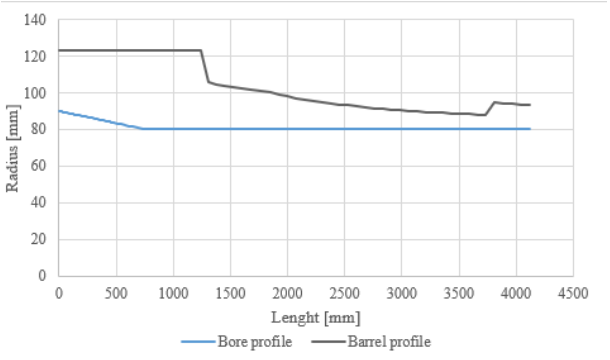

Fig. 4. Elements of the Longitudinal Barrel Cross-Section.

The CAD model of the barrel, with a total length of 3800 mm, dimensioned according to the aforementioned theory and using the properties of structural steel intended for barrel manufacturing, is shown in Figure 5.

Fig.5. CAD model of the barrel.

4. Numerical Stress Analysis of the Barrel During Firing

The numerical stress analysis of the barrel was performed using the FEMAP software package. The most heavily stressed part of the barrel, located in the projectile seating area, is at 439 mm from the start of the bore, as shown in Figure 6.

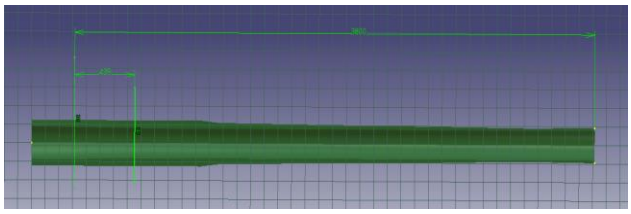

Fig. 6. Area of maximum stress in the barrel

During firing, the barrel walls are subjected to high stress levels, so the most critically loaded section was examined. The barrel was modeled as an axisymmetric 3D element, and only one quarter of the geometry was used for analysis, Figure 7. For discretization (meshing), a 3D tetrahedral finite element (four-node) with midside nodes was used. Boundary conditions were applied such that the front face is constrained from movement along the longitudinal z-axis. In the z-x plane, movement of all points along the y-axis is restricted, while in the z-y plane, movement of all points along the z-axis is constrained.

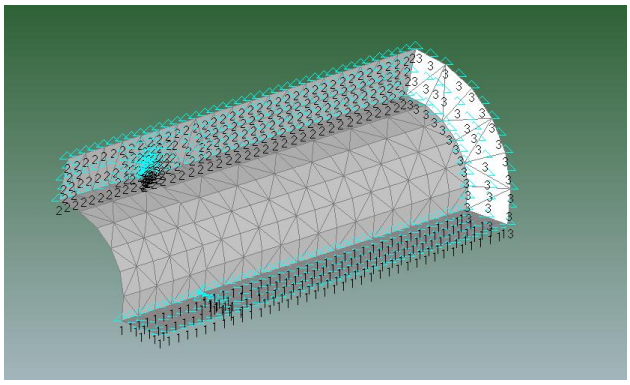

Fig. 7. Constraints on the Most Heavily Loaded Section of the Barrel.

The stress analysis was conducted under both static and dynamic loading conditions.

4.1 Static Stress Analysis

The load was applied normal to the inner surface, with maximum pressure intensity as shown in Figure 8.

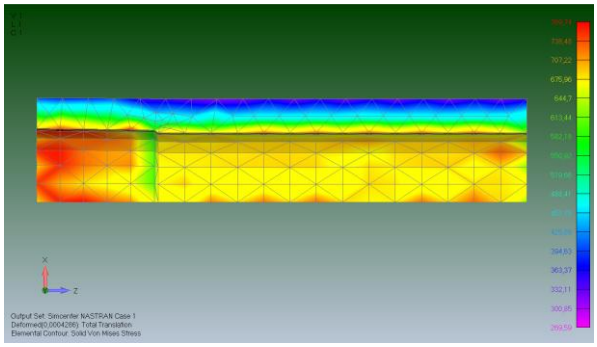

Fig. 8. Stress of the Critical Part of the Barrel in the Longitudinal Section.

The figure 9 shows the loading of the rear cross-section of the barrel, which corresponds to

the area of highest stress.

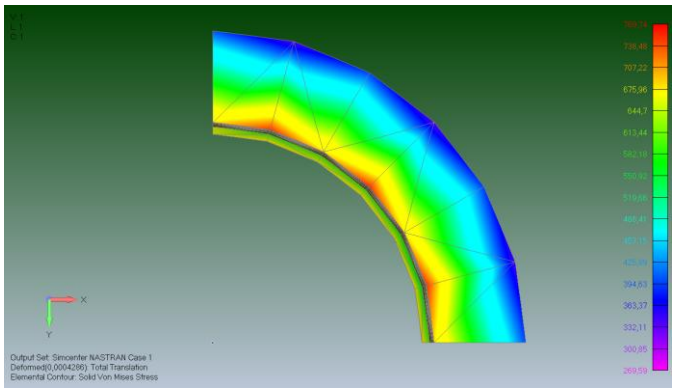

Fig. 9. Cross-section of the barrel at maximum stress

The scale indicates a maximum stress value of 769.74 MPa, which is below the yield strength of 800 MPa, meaning that the deformation occurs within the elastic range.

4.2 Dynamic Stress Analysis

For the calculation of the barrel's dynamic loading, a subroutine in the FEMAP software called NX Nastran with the Transient Dynamic / Time History function was used. During the numerical calculation of the dynamic pressure load, the boundary conditions were set the same as in the static loading case. The load was applied as pressure acting on the internal walls, similarly to the static test, but with a pressure variation law defined over time. In order for the software to compute the barrel loading over time intervals, it was necessary to specify the pressure values at moments defined by equal time steps Δt. The total time for the projectile to travel through the barrel is

0.01086 s, so the time step was set to Δt = 0.000128 s, and the calculation was performed in 81 steps.

The data on the pressure variation of the propellant gases inside the barrel at equal time intervals were generated for the numerical analysis according to the time-domain function, as shown in Figure 10.

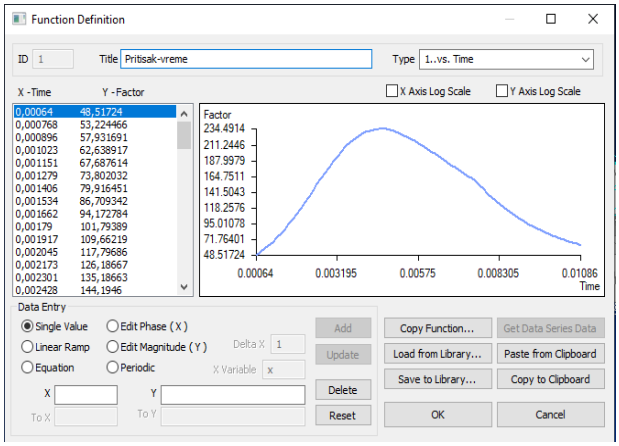

Fig. 10. Pressure variation function of propellant gases at the critical barrel cross-section.

Variation of maximum stress at the critical cross-section as a function of time is shown in Figure 11. The maximum stresses, as in the static analysis, occur on the inner part of the barrel, as shown in Figure 9. The stress value at any given time remains below 600 MPa, which is lower compared to the maximum values observed in the static stress analysis.

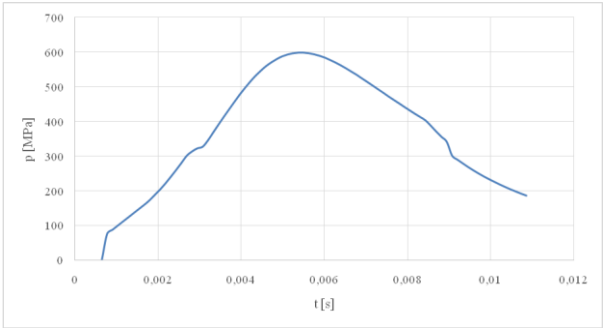

Fig. 11. Variation of maximum stress at the critical cross-section as a function of time.

5. Conclusions

The paper presents a methodology for the numerical calculation of barrel stress during firing in the design phase. The starting point is the improvement of the existing M65 howitzer system through recalibration to a smoothbore system of 160 mm caliber. Initial values for the projectile mass and propellant charge were taken from the mentioned system. An conceptual projectile design solution is provided, and an optimization of the propellant charge was performed. The results of the ballistic calculations demonstrate significant improvements compared to existing systems of the same caliber.

The crucial part of the work is the analysis of the barrel wall loading, aimed at assessing functionality and safe operation. The analysis was performed by numerical calculation of the part of the barrel subjected to the highest stresses, under both static and dynamic conditions. The stress value at any given moment remains below 800 MPa, which corresponds to the yield strength, so the entire deformation occurring during firing remains within the elastic domain. According to the obtained numerical results, it is evident that the barrel loading under dynamic conditions is of lower intensity, confirming that the design is well-conceived.

The next step in the design process is experimental validation. It is necessary to experimentally determine the characteristics of the weapon barrel material, measure the pressure intensity of the propellant gases, and determine the characteristics of the projectile contact surfaces. This approach would improve numerical analyses of fast processes for future research.

Acknowledgments

The paper is a part of the research done within the project of the University of Defence in Belgrade, No. VA-TT/1/24-26.

References

[1] Bogdanov J. *Osnovi konstrukcije ubojnih sredstava*; Medija centar „Odbrana“: Belgrade, 2020.
[2] Tančić LJ. *Klasična unutrašnja balistika*; VIZ (Vojnoizdavačni zavod): Belgrade, 2006.
[3] Ristić Z. *Mehanika artiljerijskih oruđa*; VIZ (Vojnoizdavački zavod): Belgrade, 2010.
[4] Tančić LJ. *Unutrašnjebalističko projektovanje*; Medija centar „Odbrana“: Belgrade, 2014.
[5] Kojić M. Slavković R, Živković M, Grujović N. *Metod konačnih elemenata I*; Mašinski fakultet u Kragujevcu: Kragujevac, 2010.
[6] Živković M.. *Nelinearna analiza konstrukcija*; Mašinski fakultet Univerzitet u Kragujevcu: Kragujevac, 2005.

41st Danubia-Adria Symposium Advances in Experimental Mechanics
September 23-26, 2025, Kragujevac, Serbia

Original scientific paper DOI: 10.46793/41DAS2025.071R

AUTOMATION OF CONSTITUTIVE MODEL PARAMETER IDENTIFICATION

Dragan RAKIĆ[1], Slobodan RADOVANOVIĆ[2], Miroslav ŽIVKOVIĆ[3]

[1] 0000-0001-5152-5788, Faculty of Engineering University of Kragujevac, Sestre Janjić 6, Kragujevac, Serbia, E-mail: drakic@kg.ac.rs;

[2] 0000-0002-8437-9016, Water Institute "Jaroslav Černi" Belgrade, Jaroslava Černog 80, Belgrade, Serbia, E-mail: slobodan.radovanovic@jcerni.rs;

[3] 0000-0002-0752-6289, Faculty of Engineering University of Kragujevac, Sestre Janjić 6, Kragujevac, Serbia, E-mail: zile@kg.ac.rs;

1. Introduction

For reliable stability analysis of geotechnical structures, accurate calibration of constitutive model parameters is essential. These parameters govern the simulated material response under load, and any uncertainty can lead to significant deviations in predicted behavior.

Conventional parameter determination relies on experimental testing of soil samples, whereby stress–strain measurements are used to infer individual model parameters according to their constitutive definitions. However, this manual fitting process is complex and time-consuming, particularly for soils, which exhibit highly nonlinear behavior.

To address these challenges, we propose an automated parameter identification procedure for constitutive models. The methodology is developed for the Modified Cam-Clay model (MCC), a widely adopted framework for simulating the mechanical response of soft clays and normally consolidated soils.

The first part of this paper presents the theoretical foundations and the implicit stress integration algorithm for the MCC model, implemented within the PAK [1] finite element software. For automated identification [2], the same integration scheme is translated into Python and applied at the level of single integration point. This point-wise approach is justified for homogeneous stress states, such as those encountered in standard laboratory tests (e.g., oedometer and triaxial tests).

In the second part of the paper, we describe the parameter identification program, which interfaces with the Python integration routine to perform optimization against experimental data. Finally, the developed identification algorithm is verified through a comparison of parameter estimates obtained from the PAK-based finite element implementation and those produced by the automated procedure.

2. Theoretical basis of the Modified Cam-Clay constitutive model

The yield surface of the MCC model [3] in space $q-\sigma_m$ is shown in Fig. 1.

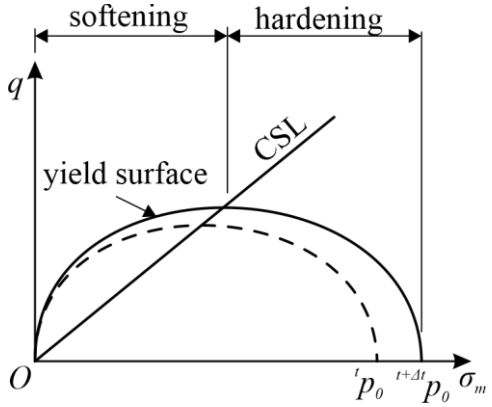

Fig. 1. Modified Cam-Clay model yield surface

The yield surface equation of MCC model is a function of stress states and has the form

$$f = q^2 - M^2\sigma_m\left(p_o - \sigma_m\right) \tag{1}$$

In equation (1), the quantity M represents the material parameter, while the quantities q and σ_m are the stress deviator

$$q = \sqrt{3J_{2D}} \tag{2}$$

and mean stress

$$\sigma_m = \sigma_x + \sigma_y + \sigma_z \tag{3}$$

The quantity p_0 defines the size of the yield surface according to the expression

$$ {}^{t+\Delta t}p_o = {}^{t}p_o \exp\left(\frac{-\Delta e_m^P}{{}^{t+\Delta t}b_V}\right) \tag{4} $$

where Δe_m^p is the increment of mean plastic strain, while

$$ {}^{t+\Delta t}b_V = \frac{k_s}{3\left(1+{}^{t+\Delta t}e\right)} \tag{5} $$

$$ k_s = \lambda - \kappa \tag{6} $$

The current porosity, in expression (5) is calculated according to

$$ {}^{t+\Delta t}e = \left(1+{}^{0}e\right)\mathrm{e}^{{}^{t+\Delta t}e_V} - 1 \tag{7} $$

where ${}^{0}e$ is the initial porosity of the material, while ${}^{t+\Delta t}e_V$ is the current volumetric strain.

The elasticity modulus of MCC constitutive model depends on the strain history and is defined according to

$$ {}^{t+\Delta t}E = 3\left(1-2\nu\right){}^{t+\Delta t}K \tag{8} $$

where is it

$$ {}^{t+\Delta t}K = \frac{1+{}^{t+\Delta t}e}{\kappa}\,{}^{t+\Delta t}\sigma_m \tag{9} $$

The algorithm for implicit stress integration [4] of the MCC model, using the previously shown theoretical foundations, implemented in the PAK program and in the Python code at the integration point level, is shown in Table 1.

Table 1. Stress integration algorithm for MCC model

Known at the beginning of time step: ${}^{t+\Delta t}\mathbf{e}$, ${}^{t}\mathbf{e}$, ${}^{t}\boldsymbol{\sigma}$, ${}^{t}\mathbf{e}^{p}$

A. Trial (elastic) solution:

$d\boldsymbol{\sigma} = \mathbf{C}^E d\mathbf{e}^E = \mathbf{C}^E\left({}^{t+\Delta t}\mathbf{e} - {}^{t}\mathbf{e}\right)$, ${}^{t+\Delta t}\boldsymbol{\sigma} = {}^{t}\boldsymbol{\sigma} + d\boldsymbol{\sigma}$

Calculation of stress invariants:

I_1, J_{2D}

$q = \sqrt{3J_{2D}}$,

Yield surface:

$k_s = \lambda - \kappa$, $e = \left(1+{}^{0}e\right)\exp\left(e_V\right) - 1$

$b_V = \frac{k_s}{3\left(1+e\right)}$, $p_o = {}^{t}p_o \exp\left(\frac{\Delta e_m^P}{b_V}\right)$

$f = g = q^2 - M^2\sigma_m\left(p_o - \sigma_m\right)$

B. Checking yield condition:

IF ($f < 0$) goto **E**

IF ($f \geq 0$) continue

Yield area check ${}^{t+\Delta t}\sigma_m^E \leftrightarrow \frac{1}{2}{}^{t}p_0$

$$ \frac{\partial f}{\partial \boldsymbol{\sigma}} = \frac{\partial f}{\partial q}\frac{\partial q}{\partial \boldsymbol{\sigma}} + \frac{\partial f}{\partial I_1}\frac{\partial I_1}{\partial \boldsymbol{\sigma}} + \frac{\partial f}{\partial {}^{t}p_0}\frac{\partial {}^{t}p_0}{\partial \boldsymbol{\sigma}} $$

$$ d\lambda = \frac{\frac{\partial f}{\partial \boldsymbol{\sigma}}^{\mathrm{T}}\mathbf{C}^E d\mathbf{e}}{\frac{\partial f}{\partial \boldsymbol{\sigma}}^{\mathrm{T}}\mathbf{C}^E\frac{\partial f}{\partial \boldsymbol{\sigma}} + {}^{t}p_0\frac{1+{}^{t+\Delta t}e}{k_s}\cdot\frac{\partial f}{\partial {}^{t}p_0}\mathbf{I}\frac{\partial g}{\partial \boldsymbol{\sigma}}} $$

C. Correction of dλ (local iterations):

$d\mathbf{e}^P = d\lambda\frac{\partial g}{\partial \boldsymbol{\sigma}}$, $d\mathbf{e}^E = d\mathbf{e} - d\mathbf{e}^P$

$d\boldsymbol{\sigma} = \mathbf{C}^E d\mathbf{e}^E$, ${}^{t+\Delta t}\boldsymbol{\sigma} = {}^{t}\boldsymbol{\sigma} + d\boldsymbol{\sigma}$

Calculation of new stress invariants:

I_1, J_{2D}

Yield condition:

${}^{t+\Delta t}e = \left(1+{}^{0}e\right)\exp\left({}^{t+\Delta t}e_V\right) - 1$,

${}^{t+\Delta t}b_V = \frac{k_s}{3\left(1+{}^{t+\Delta t}e\right)}$,

${}^{t+\Delta t}p_o = {}^{t}p_o \exp\left(\frac{\Delta e_m^P}{{}^{t+\Delta t}b_V}\right)$,

${}^{t+\Delta t}E = 3\left(1-2\nu\right){}^{t+\Delta t}K$

$f = q^2 - M^2\sigma_m\left(p_o - \sigma_m\right)$

D. IF ($ABS(f) \geq TOL$) goto **C** with new $d\lambda$:

${}^{t+\Delta t}\mathbf{e}^P = {}^{t}\mathbf{e}^P + d\mathbf{e}^P$

E. End: ${}^{t+\Delta t}\boldsymbol{\sigma}$, ${}^{t+\Delta t}\mathbf{e}^P$

3. Parameter Calibration of the Constitutive Model

The identification procedure is performed at the level of a single integration point, where homogeneous stress and strain states can be assumed. This localized approach isolates material behavior from boundary and geometric effects, making it directly comparable to standard laboratory tests.

As inputs, the algorithm accepts stress-strain histories obtained experimentally. Depending on the test setup, either the applied loading (stress-controlled) or the measured deformation (strain-controlled) path can be imposed. The numerical simulation replicates these paths exactly, ensuring that the same increments of loading or deformation are evaluated.

A scalar objective function quantifies the discrepancy between experimental and simulated responses. Commonly, this function is based on an error norm, such as the mean absolute or squared difference, possibly supplemented by weighting schemes that emphasize critical segments of the loading path (e.g., peak stress). Penalty terms enforce physical consistency by discouraging nonphysical behaviors, such as softening under

monotonic load or unbounded state variables. Simulations yielding unstable or divergent results incur large penalties.

Each model parameter is confined to a predefined interval reflecting prior geotechnical knowledge. These bounds prevent exploration of unrealistic regimes, enhance numerical stability, and accelerate convergence by reducing the viable search space.

A hybrid, two-stage optimization strategy ensures both global exploration and local precision:

- Global Search: An evolutionary algorithm (e.g., differential evolution) samples the parameter space broadly, locating low-error regions and mitigating entrapment in local minima.

- Local Refinement: A gradient-based or quasi-Newton method (e.g., L-BFGS-B) is initialized from the best global solution to achieve fine-scale convergence, leveraging derivative information for efficient adjustments.

This combined approach balances robustness and accuracy, yielding a parameter set that faithfully reproduces the experimental loading path.

4. Validation

Parameter identification was performed using oedometer test results, selected for their nearly homogeneous stress state within the specimen, which makes them particularly suitable for the proposed single-point calibration procedure. Initial lower and upper bounds for each constitutive parameter were set based on physical plausibility and geotechnical knowledge, ensuring that the optimization remained within realistic regimes.

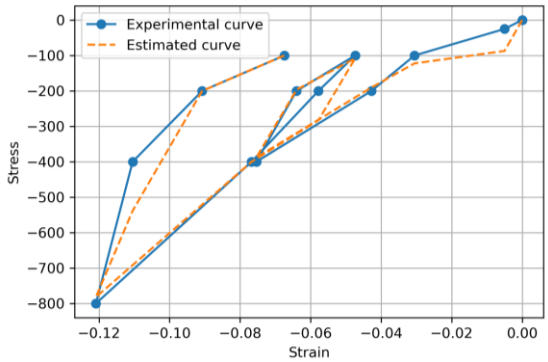

Fig. 2. Oedometer test 1: Experimental and estimated dependence

The resulting experimental stress-strain paths and the simulated model responses are overlaid in Fig. 2-Fig. 4, demonstrating close agreement across elastic, yield, and hardening phases. Quantitative assessment via maximum relative error and coefficient of determination (R^2) confirms that the calibrated model reproduces laboratory observations within acceptable tolerance, thereby validating the robustness and fidelity of the automated identification algorithm.

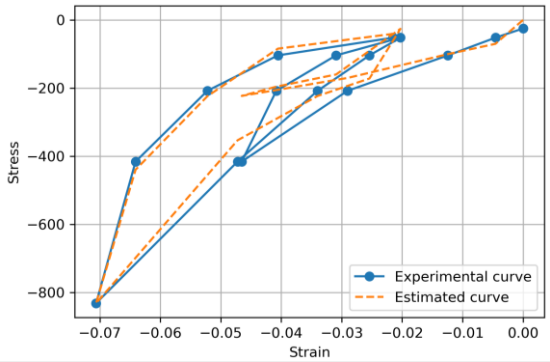

Fig. 3. Oedometer test 2: Experimental and estimated dependence

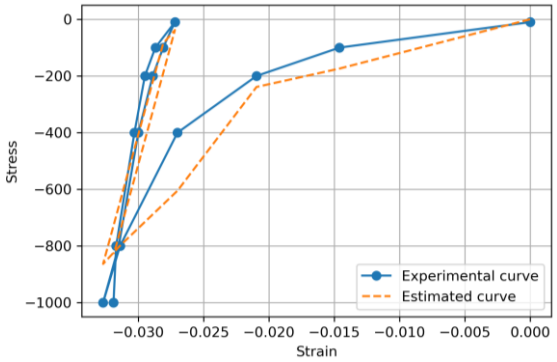

Fig. 4 Oedometer test 3: Experimental and estimated dependence

After completing parameter identification, a numerical simulation of the same oedometer test was executed in the PAK finite element program under identical boundary and loading conditions.

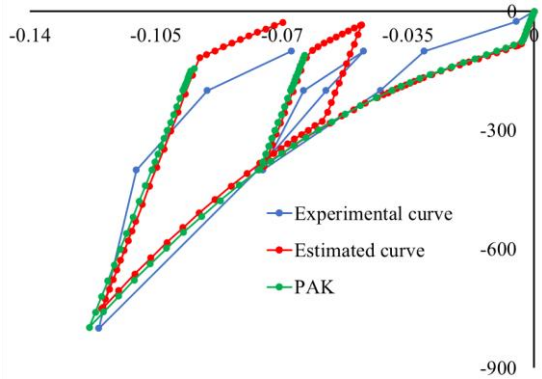

Fig. 5. Results of numerical simulation of oedometer test 1

The calibrated parameters were then applied in the Python-based integration routine over the same number of increments as in PAK. The results of

these simulations, alongside the experimental curves, are presented in Fig. 5-Fig. 7, further substantiating the equivalence of the standalone Python algorithm and the PAK implementation.

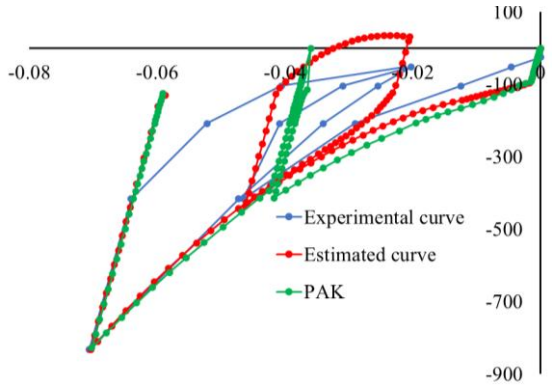

Fig. 6. Results of numerical simulation of oedometer test 2

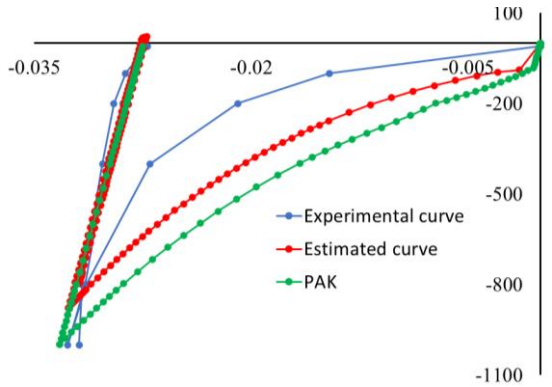

Fig. 7. Results of numerical simulation of oedometer test 3

The results indicate that the responses predicted by the automated identification closely match the experimental data, confirming the procedure's accuracy. Discrepancies between the Python-based and PAK simulations can be attributed to methodological differences: the Python routine performs point-wise stress integration without element mesh interactions, whereas the PAK implementation relies on full finite element discretization.

5. Conclusions

The conducted study demonstrates that the automated parameter identification procedure provides a reliable and efficient means of calibrating the constitutive model. By relying on oedometer test data, the method ensured stable convergence and consistent results within realistic geotechnical ranges.

The obtained simulations show that the approach is capable of capturing the full stress–strain behavior, including elasticity, yield and subsequent hardening. This consistency across both the standalone Python routine and the PAK program highlights the robustness and transferability of the calibration procedure.

While discrepancies between implementations were observed, these stem primarily from the inherent differences between point-wise stress integration and finite element discretization. Importantly, such deviations do not undermine the predictive capability of the method but instead underline the complementary strengths of simplified integration routines and full numerical simulations.

Overall, the proposed procedure offers a validated framework for parameter calibration that balances computational efficiency with accuracy. Its integration into broader numerical workflows can support more reliable geotechnical analyses and provide a solid foundation for future extensions to more complex soil constitutive models.

Acknowledgments

This research was supported by the Science Fund of the Republic of Serbia, #GRANT No 7475, Prediction of damage evolution in engineering structures - PROMINENT and by the Ministry of Science, Technological Development and Innovation, Republic of Serbia, Agreement No. 451-03-137/2025-03/200107.

References

[1] Živković, M., Kojić, M., Slavković, R., Grujović, N., Rakić, D., Dunić, V. PAK-S, Program for FE Structural Analysis of Solids and Structures, University of Kragujevac, Faculty of Engineering, Kragujevac, 2019.
[2] Furukawa, T., Sugata, T., Yoshimura, S., Hoffman, M. An automated system for simulation and parameter identification of inelastic constitutive models, Computer Methods in Applied Mechanics and Engineering, 2002, 191(21-22), 2235-2260.
[3] Borja, R. I., Lee, S. R, Cam-clay plasticity, part 1: implicit integration of elasto-plastic, Computer Methods in Applied Mechanics and Engineering, 1990, 78(1), 49-72.
[4] Bathe K.J, Finite element procedures, USA: Massachusetts Institute of Technology, 1996.

Original scientific paper DOI: 10.46793/41DAS2025.075A

FATIGUE PERFORMANCE COMPARISON OF STRENX 700 AND 55NiCrMoV7 STEELS

Dušan ARSIĆ[1*], Gordana Jovičić[2], Miroslav ŽIVKOVIĆ[3], Miloš PEŠIĆ[4], Marko TOPALOVIĆ[5], Djordje IVKOVIĆ[6], Marko DELIĆ[7]

[1] 0000-0003-0326-0898 , Faculty of Engineering University of Kragujevac, Sestre Janjić 6, Kragujevac, Serbia, E-mail: dusan.arsic@fink.rs

[2] 0000-0002-9799-5555 , Faculty of Engineering University of Kragujevac, Sestre Janjić 6, Kragujevac, Serbia, E-mail: gordana.jovicic@kg.ac.rs

[3] 0000-0002-0752-6289 , Faculty of Engineering University of Kragujevac, Sestre Janjić 6, Kragujevac, Serbia, E-mail: zile@kg.ac.rs

[4] 0000-0002-3405-5216 , Institute for Information Technologies, University of Kragujevac, Jovana Cvijića bb, Kragujevac, Serbia, E-mail: milospesic@uni.kg.ac.rs

[5] 0000-0001-6101-755X , Institute for Information Technologies, University of Kragujevac, Jovana Cvijića bb, Kragujevac, Serbia, E-mail: topalovic@kg.ac.rs

[6] 0000-0002-5747-7876 , Faculty of Engineering University of Kragujevac, Sestre Janjić 6, Kragujevac, Serbia, E-mail: djordje.ivkovic@fink.rs

[7] 0000-0001-5493-7569 , Faculty of Engineering University of Kragujevac, Sestre Janjić 6, Kragujevac, Serbia, E-mail: marko.delic@kg.ac.rs

Abstract

The increasing demand for lightweight and reliable structural components and tools in manufacturing engineering creates a need for accurate data regarding the fatigue performance of high-strength and tool steels. This paper presents an experimental and comparative investigation of the fatigue behavior of STRENX 700, a high-strength structural steel, and 55NiCrMoV7, a thermally stable hot-work tool steel. Fatigue tests were conducted using a stress-controlled, fully reversed tension-compression loading regime (R = –1) on smooth "dog-bone" specimens. The resulting S–N curves were used to evaluate fatigue strength and determine the material parameters using Basquin's relation. The results provide insight into the fatigue properties of these steels that have different industrial applications, but are tested under the same conditions. The fatigue performance, advantages, and trade-offs of each steel grade are discussed.

1. Introduction

Fatigue failure plays a crucial role in the durability of tools and components used in forging, turning (lathes), milling operations, and other related machining processes, where they are subjected to intense and repeated mechanical stresses. Tool steels like 55NiCrMoV7 [1] are often selected for these parts due to their toughness and thermal stability under elevated temperatures.

Steel 55NiCrMoV7 is most commonly used in forging dies and tooling under thermomechanical fatigue, because it has very good resistance to thermal shock and cracking, good mechanical properties at room and elevated temperatures, relatively high toughness at room and low temperatures, etc. Also, after heat treatment, this steel has good dimensional stability. It is intended for the manufacture of all types of forging dies and tools for hot work, molds for gravity casting of metals and plastics, tools for extrusion, etc. On the other hand, structural steels such as STRENX 700 [2] are known for their high yield strength and are optimized for lightweight structures, due to their high strength-to-weight ratios. In order to have an optimum machine design, considering the fact that 55NiCrMoV7 usually cost more, engineers need to choose the material of each part carefully, to use high-strength steel where possible, and to address thermomechanical fatigue where needed [3]. Engineers require comprehensive comparative fatigue data concerning these two types of steel in order to make the best decision, however, the current state of the art literature lacks direct comparison between them using the same testing equipment under the same conditions. This study aims to fill that gap.

2. Materials and Methodology

The STRENX 700 is a high-strength, low-alloy steel optimized for weldability and strength, with a nominal yield strength of around 767 MPa. 55NiCrMoV7 is a hot-work tool steel known for its excellent toughness, thermal shock resistance, and fatigue endurance after quenching and tempering [4].

Chemical compositions of steels STRENX 700 and 55NiCrMoV7 are given in Tables 1 and 2, respectively.

Table 1. STRENX 700 Chemical composition (wt. %):

C	Si	Mn	P	S	Al	Nb	V	Ti
0.11	0.093	0.64	0.009	0.017	0.017	0.088	0.19	0.14

Table 2. 55NiCrMoV7 Chemical composition (wt. %):

C	Si	Mn	P	S	Cr	Ni	Mo	V
0.55	0.3	0.7	0.035	0.035	1.1	1.7	0.5	0.12

55NiCrMoV7 was subjected to quenching and tempering to its optimal hardness range: 42–45 HRC.

To ensure uniformity and precision across all fatigue tests, cylindrical "dog-bone" specimens were meticulously machined from the STRENX 700 and 55NiCrMoV7 steel samples, adhering strictly to pre-defined internal standards that align with established guidelines [5]. The specimens were prepared to have a minimum diameter of 6.35 mm in the middle, where the failure occurs, and an external diameter of 12.7 mm for gripping by the machine. Dimensions of the specimens are shown in Fig. 1., while the actual untested specimen is shown in Fig. 2.

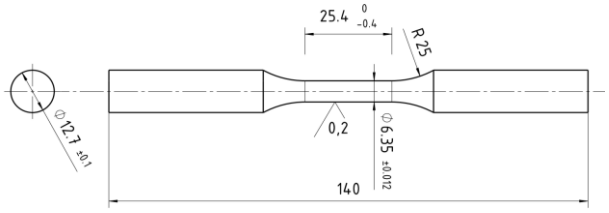

Fig. 1. Dimensions of the used dog-bone specimens

Fig. 2. Actual specimen before testing

2.1 *Static testing for mechanical characteristics assessment*

First, a Shimadzu Corporation servo-hydraulic testing machine (EHF EV101K3-070-0A) with a force of ±100 kN and ±100 mm stroke was used to perform uniaxial tensile tests on the specimens in order to ascertain their mechanical characteristics, i.e., static strength qualities [6]. Schematics of the testing equipment is shown in Fig. 3., while the actual testing machine and the used MFA25 extensometer [7] are shown in Fig. 4. and Fig. 5. respectively.

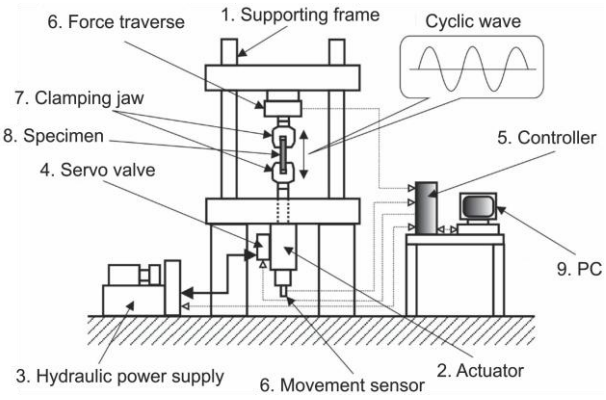

Fig. 3. Schematics of the testing equipment

Fig. 4. Shimadzu EHF EV101K3-070-0A

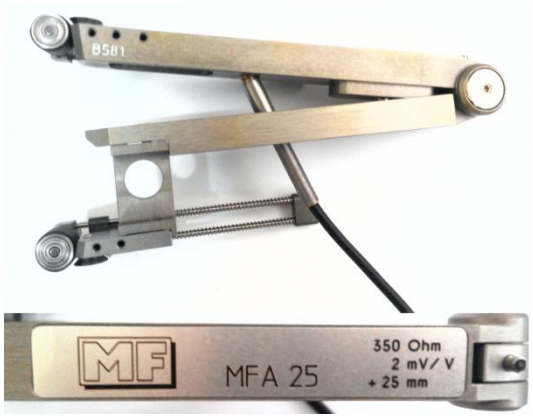

Fig. 5. MFA25 extensometer

Obtained mechanical characteristics of STRENX 700 and 55NiCrMoV7 grade steel are shown in Table 3.

Table 3. Mechanical characteristics of STRENX 700 and 55NiCrMoV7

Steel Grade	STRENX 700	55NiCrMoV7
Yield Strength $\sigma_{0,2}$ (MPa)	767.97	1450
Tensile Strength σ_M (MPa)	818.08	1600
Young's Modulus E (GPa)	228.89	212

2.2 Fatigue testing

Uniaxial fatigue testing was conducted at room temperature under a fully reversed stress ratio (R = –1) using smooth, cylindrical specimens. Stress-controlled loading was applied using a servo-hydraulic testing machine in accordance with ASTM E468 [8] and E739 [9] standards. For the STRENX 700 specimens [10], the fatigue testing was performed at load levels corresponding to ~70%, 65%, 60%, 45% and 40% of the material's yield strength (767.97 MPa), specifically 540 MPa, 500 MPa, 450 MPa, 350 MPa, and 300 MPa, respectively. Similarly, the 55NiCrMoV7 specimens were subjected to load levels that mirrored percentages of the STRENX 700's yield strength. Frequencies between 10–15 Hz were used depending on stress amplitude levels.

The fatigue life for each specimen was measured as the number of cycles to failure, defined by a complete fracture or separation of the specimen into two parts.

3. Results

The fatigue performance of STRENX 700 and 55NiCrMoV7 steels under cyclic loading is best visually presented using the S-N curves derived from the experimental data. These curves plot the applied stress level against the number of cycles to failure for each material, offering a clear comparison of their fatigue resistance.

Semi-log S-N curve for STRENX 700 obtained by interpolation and extrapolation of experimental results is shown in Fig. 6.

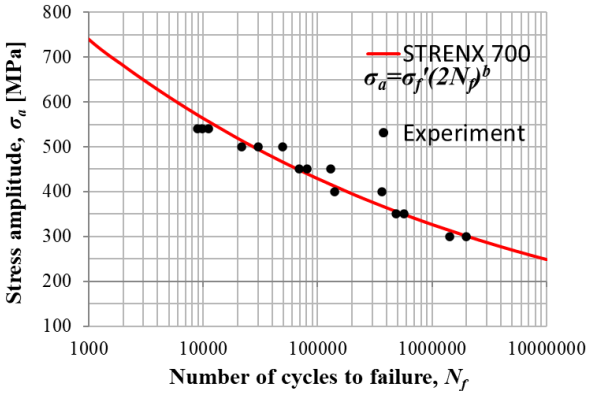

Fig. 6. S-N curve for STRENX 700

Likewise, the semi-log S-N curve for 55NiCrMoV7 steel obtained by interpolation and extrapolation of experimental results is shown in Fig. 7.

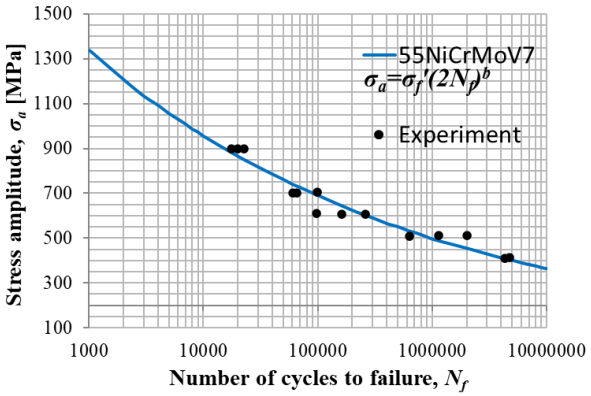

Fig. 7. S-N curve for 55NiCrMoV7

A diagram combining semi-log S-N curves for STRENX 700 and 55NiCrMoV7 is shown in Fig. 8.

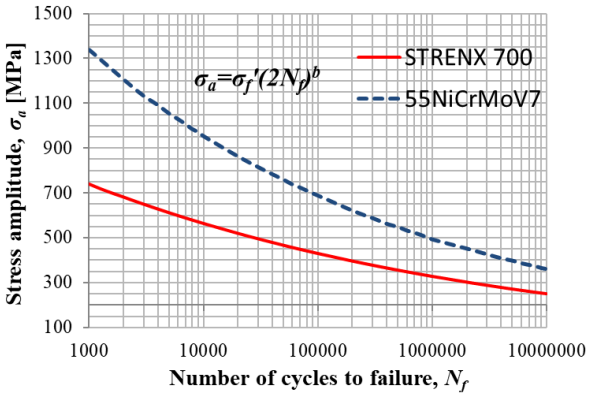

Fig. 8. S-N curves for STRENX 700 and 55NiCrMoV7

Steel 55NiCrMoV7 has a steeper S–N curve with better performance in the low-cycle fatigue regime but potentially reduced endurance in very high-cycle fatigue, compared to STRENX 700 which has a flatter S–N curve and whose fatigue performance does not decline as much when loaded with high-cycle fatigue.

55NiCrMoV7 shows superior performance at higher stress levels due to its toughness and tempered martensitic structure, making it suitable for heavy-duty and impact-loaded applications. This advantage diminishes as the number of cycles increases, as can be seen from Fig. 8.

The fatigue life results were processed to construct S–N curves and subsequently to determine parameters used in Basquin equation Eq. (1):

$$\frac{\Delta\sigma}{2}=\sigma_a=\sigma_f'\left(2N_f\right)^b, \quad (1)$$

where: σ_a is the true stress amplitude, and σ_f' is the fatigue strength coefficient. Furthermore, b is fatigue strength exponent, while $2N_f$ is the number of cycles to failure. For the analyzed steels, fatigue parameters are given in Table 4.

Table 4. Fatigue properties:

Steel Grade	Fatigue Strength Coefficient σ_f' [MPa]	Fatigue Strength Exponent b
STRENX 700	1814.61	-0.1181
55NiCrMoV7	3737.73	-0.1465

The Basquin parameters, calculated from the S-N curve data, are essential for quantitatively assessing the fatigue behavior of materials [5]. These parameters provide insights into the fatigue strength and fatigue life expectancy under varying stress conditions.

4. Conclusions

The findings of this study are consistent with previous research indicating that the fatigue life of materials is significantly influenced by their microstructure and mechanical properties [6].

This study demonstrated that while STRENX 700 offers comparable performance in high-cycle fatigue for structural applications, 55NiCrMoV7 holds advantages in low-cycle scenarios, as well as thermal resistance and cyclic toughness, particularly in high-load or thermally demanding environments. These findings may be used to guide material selection in designing metalworking machinery, as the price of 55NiCrMoV7 can be up to three times higher than that of STRENX 700, depending on grade/form and sourcing, although the difference is usually not that great.

Acknowledgments

This research was supported by the Ministry of Science, Technological Development and Innovation of the Republic of Serbia, contract No. 451-03-66/2024-03/200378, and by the Science Fund of the Republic of Serbia, #GRANT No. 7475, Prediction of damage evolution in engineering structures – PROMINENT.

References

[1] Zhang, Z., Delagnes, D., & Bernhart, G. Cyclic behaviour and plastic strain memory effect of 55NiCrMoV7 steel under low cycle fatigue. Rare Met, 2011, 30, 443–446.
[2] Ulewicz, R., Szataniak, P., Novy, F., Trsko, L., Bokuvka, O. Fatigue Characteristics of Structural Steels in the Gigacycle Region of Loading. Mater Today Proc, 2017, 4, 5979–5984.
[3] Moverare, J., Lancaster, R.J., Jones, J., Stekovic, S., & Whittaker, M. T. A review of recent advances in the understanding of thermomechanical fatigue durability and failure mechanisms in nickel-based superalloys. Metall. Mater. Trans. A, 2025, 56, 1115–1134.
[4] Arsić, D., Djordjević, M., Zivković, J., Lazić, V., Sedmak, A., Aleksandrović, S., Rakić, D., Experimental-numerical study of tensile strength of the high-strength steel S690QL at elevated temperatures, Strength Mater, 2016, 48(5), 687–695.
[5] ASTM International. ASTM E466-21: Standard Practice for Conducting Force Controlled Constant Amplitude Axial Fatigue Tests of Metallic Materials. West Conshohocken, PA, 2021.
[6] Milovanović, V., Arsić, D., Milutinović, M., Živković, M., Topalović, M. A comparison study of fatigue behavior of S355J2+N, S690QL and X37CrMoV5-1 steel. Metals, 2022, 12(7), 1199.
[7] Živković, J., Dunić, V., Milovanović, V., Pavlović, A., Živković, M. A modified phase-field damage model for metal plasticity at finite strains: Numerical development and experimental validation. Metals, 2021, 11(1), 47.
[8] ASTM International. ASTM E468-18: Standard Practice for Presentation of Constant Amplitude Fatigue Test Results for Metallic Materials. West Conshohocken, PA, 2018.
[9] ASTM International. ASTM E739-10(2015): Standard Practice for Statistical Analysis of Linear or Linearized Stress-Life (S-N) and Strain-Life (ε-N) Fatigue Data. West Conshohocken, PA, 2015.
[10] SSAB. Strenx® 700 Product Data Sheet. https://rockymountainsteel.com/wp-content/uploads/2023/04/Strenx-700.pdf Accessed July 29, 2025.

41st Danubia-Adria Symposium Advances in Experimental Mechanics
September 23-26, 2025, Kragujevac, Serbia

Original scientific paper DOI: 10.46793/41DAS2025.079P

EXPERIMENTAL DETERMINATION OF THE EFFECT OF AXIAL FORCE ON A HEADLESS SCREW CONNECTION

Anđela PEROVIĆ[1], Miloš MATEJIĆ[2], Vladimir MILOVANOVIĆ[3]

[1] 0009-0005-5637-9827, University of Kragujevac, Faculty of Engineering, Sestre Janjić 6, 34000 Kragujevac, Serbia, E-mail: andjela.perovic@kg.ac.rs;

[2] 0000-0003-0488-0992, University of Kragujevac, Faculty of Engineering, Sestre Janjić 6, 34000 Kragujevac, Serbia, E-mail: mmatejic@kg.ac.rs

[3] 0000-0003-3071-4728, University of Kragujevac, Faculty of Engineering, Sestre Janjić 6, 34000 Kragujevac, Serbia, E-mail: vladicka@kg.ac.rs

1. Introduction

Headless screws are commonly used fasteners in mechanical engineering, especially in applications where the screw must be flush with the surface it secures.

In real working conditions, this type of screw is often exposed to axial forces, which may result from tightening or from external loads. Therefore, it is important to understand how axial force affects a headless screw connection in order to ensure a reliable and strong joint. Monitoring the axial force, which may be either tensile or compressive, is a key factor in maintaining joint safety and preventing plastic deformation.

Recent studies have explored various non-destructive methods for determining axial force in screws. One such method is the ultrasonic technique based on the acoustoelastic effect, where the screw is divided into specific zones and the measurement error is typically below 10% [1]. By introducing corrections to the clamping length and using suitable sensors, this error can be reduced to below 3% [2]. In addition, advanced ultrasonic technologies allow for more accurate measurements by eliminating errors caused by poor sensor contact with the material [3]. On the other hand, experimental methods are used as a complement, as they are performed under actual load conditions and take into account factors such as friction and microslip [4,5].

The aim of this paper is to experimentally determine the axial force occurring in headless screws used to connect the outer and inner parts of a mechanical joint. The behavior of the screws under compressive load will be analyzed, and the results will contribute to a better understanding of the mechanical performance of headless screw connections.

Future research will focus on modifying screw parameters in order to examine whether the length and diameter of the screw affect its strength and behavior under load. In addition, the influence of repeated (cyclic) loading on headless screws will also be considered.

2. Connection achieved using headless screws

For the experimental investigation of axial force in the screws, it was necessary to create a prototype of the joint.

To connect the outer and inner parts of the joint, shown in Figure 1, headless screws were used. These screws conform to the DIN 913 standard, with a size of M5 and a length of 6 mm [6].

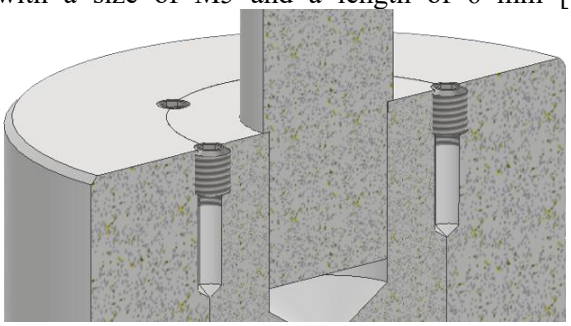

Fig. 1. Prototype of the joint connected with headless screws

Six holes for screws were made on each side of the joint to ensure repeatability of the experiment and to reduce possible random errors during testing or result analysis.

The tests were carried out on a SHIMADZU servohydraulic pulsator (testing machine) designed for precise testing of the mechanical properties of various materials.

This machine has the following specifications:

- Maximum force capacity: 100 kN,
- Operating frequency range: 0.01 Hz to 200 Hz,
- Force measurement accuracy: ±0.5% of full scale (FS),
- Stroke length: ±50 mm.

The test involved applying an axial compressive force with the pulsator on the inner part of the joint, which moves vertically downward, while the outer part of the joint was fixed. This setup generates axial force in the screws. Controlled axial loading was applied, and both the force and deformation of the screws were continuously measured.

To mount the prototype joint on the pulsator, it was necessary to design and manufacture additional auxiliary components: A plate fixed to the lower part of the pulsator, on which a hollow profile rests. The hollow profile is a separate component that rests partially on the plate and partially supports the outer part of the joint. The third and final component is a cylindrical part that fits into the upper jaw of the pulsator. During the experiment, this part applies pressure to the inner part of the joint. This is achieved by the gradual lowering of the upper part of the pulsator.

Figure 2 shows the main components of the joint and the auxiliary parts used for mounting the joint on the pulsator.

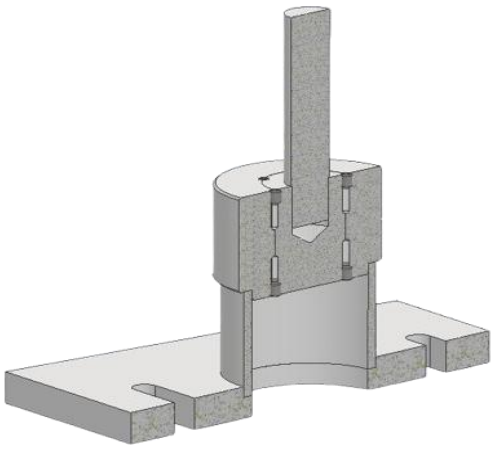

Fig. 2. Assembly of the joint and auxiliary components on the pulsator.

The plate is mounted on the lower part of the pulsator and is secured to it with two M15 screws to ensure a rigid connection between the joint structure and the pulsator.

This step is very important to prevent any movement of the joint during the experiment, as such movement would significantly affect the accuracy of the test results.

The joint is connected to the upper part of the pulsator through a component that fits into the jaw, where the jaw clamps firmly hold this part in place.

3. Axial force on a headless screw connection

In this study, the screws were tested under a static load of 60 kN.

Figure 3 shows the assembly of the joint prototype along with auxiliary components mounted on the pulsator before applying the axial compressive force.

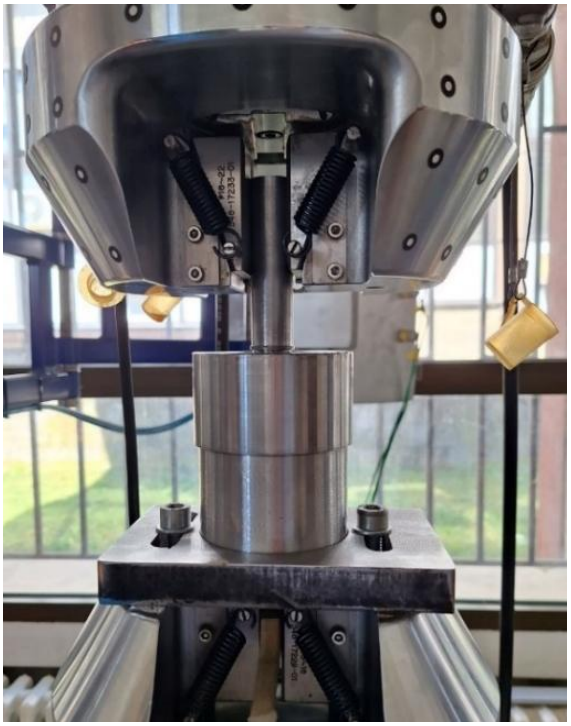

Fig. 3. Assembly of the joint and auxiliary components on the pulsator.

To obtain accurate results, the experiment was repeated multiple times. In total, six test series were performed.

The first three series involved testing two screws, size M5 and length 6 mm, positioned opposite each other. The distance between them was equal to the diameter defining the spacing of the screw holes, which in this case was 80 mm.

Gradual movement of the upper part of the pulsator applies force to the inner part of the joint via a component that fits into the jaw of the upper part of the pulsator.

The force increased steadily from 0 up to approximately 11 kN. The moment when the force

reached its maximum value was considered the point of failure.

From that point, the force dropped significantly, indicating the end of the test series. The results recorded by the pulsator's software were then saved in Microsoft Excel for further analysis.

In addition to force measurement, the software was set to continuously monitor the displacement of joint components during the application of force.

After the test, the joint was removed from the pulsator and prepared for the next series by installing new screws between the outer and inner parts of the joint. The entire assembly was then remounted on the machine. This procedure was repeated three times.

Figure 4 shows the joint assembly after the first test series. The inner part of the joint is visibly displaced from its initial position, and damage to the screws can be seen.

Fig. 4. Assembly of the joint and auxiliary components on the pulsator after the first test series.

The fourth, fifth, and sixth test series were performed by rotating the joint 180°.

This was made possible by the sufficient length of the hollow profile supporting the outer part of the joint. The purpose of rotating the joint was to ensure repeatability and achieve more accurate results.

During the testing, three different failure scenarios were observed, where either one or a combination of them could occur:

1. Damage to the thread on the inner side of the joint,
2. Damage to the thread on the outer side of the joint,
3. Damage to the thread on the contact surface between the joint parts, i.e., damage to the screw thread.

Figure 5 shows (a) the outer part of the joint and (b) the screws after the fourth test series. The images display the damage that occurred to the joint components during the experiment.

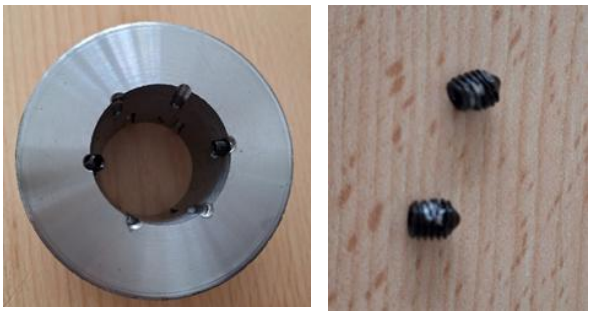

(a) **(b)**

Fig. 5. (a) Outer part of the joint and **(b)** screws after the fourth test series.

The last, sixth test series was performed with a single headless screw of the same dimensions as in the previous tests, instead of two screws.

4. Results

During the tests, the screws were subjected to a static compressive force that continuously increased from 0 kN up to the maximum force, which varied slightly between each test series.

The force values were measured continuously throughout the experiment. These values were recorded by the pulsator's software. At the end of each test series, the results were transferred to Microsoft Excel for further processing.

In addition to force, deformation values were also recorded. The deformation increased proportionally with the force until the maximum force was reached. From that point until the end of the series, the deformation began to decrease sharply.

Figure 7 shows a diagram of the results, illustrating the relationship between force and deformation for all six-test series.

The diagram displays the Z-axis representing the change in force, while the Y-axis represents the change in deformation dependent on the force.

Results from all series are combined into one diagram and are distinguished by different colors.

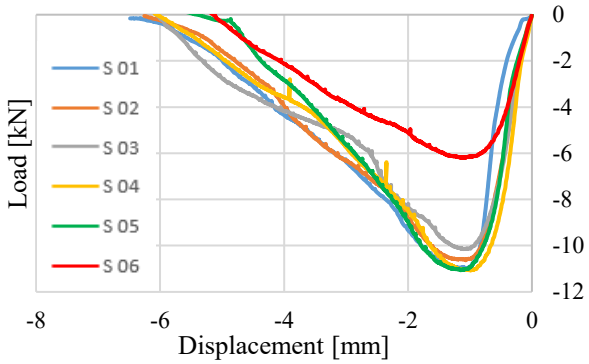

Fig. 7. Diagram of force versus deformation for six test series of headless screws.

As seen from the diagram, the compressive force sharply increases until it reaches the maximum value, which is similar for five repeated test series. This indicates that the experiment was performed correctly, with a low percentage of random errors. The cause of the small differences in values is difficult to determine. Random errors in the experiment may arise from instrumental variations, including temperature fluctuations, voltage variations, or mechanical vibrations.

The first five test series examined the effect of compressive force on two headless screws, size M5 and length 6 mm, with a maximum force of approximately 11 kN.

Further evidence of the experiment's validity and relevance of the results is shown by the sixth test series. This series tested the behavior of a single screw of the same dimensions under compressive load, where the maximum force was almost half compared to the tests with two screws. The maximum force value in this case was around 6 kN.

5. Conclusion

The experimental investigation of the effect of axial force on a headless screw connection, performed using a servohydraulic pulsator, enabled the analysis of the joint behavior under static compressive load. This study determined how headless screws behave under load and the maximum forces they can withstand. The results showed that two screws of size M5 and length 6 mm can withstand a force of approximately 11 kN, while a single screw of the same dimensions can withstand a force of about 6 kN.

Three types of possible damage were observed: on the internal threaded part of the joint, on the external part, and on the screw itself, indicating the complexity of the screw connection behavior under load.

The obtained results contribute to a better understanding of the mechanical behavior of such connections, provide a foundation for future research, and can serve as a basis for the design or optimization of connections using headless screws.

References

[1] Zhao, X.-X., Li, Y.-M., Liu, X.-G., Yao, K. Ultrasonic measurement on axial force of high-strength bolt in service. *Journal of Low Frequency Noise, Vibration and Active Control*, 2020, 39(3), 596–603. doi: 10.1177/1461348418815405.

[2] Liu, J., et al. Experimental and numerical studies of bolted joints subjected to axial excitation. *Wear*, 2016, 346–347, 66–77. doi: 10.1016/j.wear.2015.10.012.

[3] Pan, Q., Pan, R., Shao, C., Chang, M., Xu, X. Research Review of Principles and Methods for Ultrasonic Measurement of Axial Stress in Bolts. *Chinese Journal of Mechanical Engineering*, 2020, 33(1). doi: 10.1186/s10033-020-0431-x.

[4] Jing, X., Dai, H., Xu, W., Zhao, Y., Zhang, J., Yang, B. Axial Load Measurement of Bolts with Different Clamping Lengths Based on High-Frequency Ultrasonic ZnO Film Sensor. *Sensors*, 2023, 23(7), 3712. doi: 10.3390/s23073712.

[5] Hitachi Ltd, Kitazawa, S., Hitachi Ltd, Lee, Y., Patel, R. Noncontact measurement of bolt axial force during tightening processes using scattered laser ultrasonic waves. *ReJNDT*, 2023, 1(1). doi: 10.58286/28211.

[6] Deutsches Institut for Norming. DIN 913 - Hexagon Socket Set Screws with Plat Po. Deutsches Institut for Norming (DIN), 1980. https://www.aspenfasteners.com/content/pdf/Metric_DIN_913_spec.pdf. Accessed June 22, 2025.

Original scientific paper DOI: 10.46793/41DAS2025.083D

INITIAL EXPENDABLE TURBOJET PROTOTYPE TESTING EXPIRIENCES

Nikola DAVIDOVIĆ[1], Nenad Kolarević[2], Miloš Stanković[3], Marko Miloš[4]

[1] 0000-0002-0500-3388, Faculty of Mechanical Engineering, Kraljice Marije 16, Belgrade, Serbia, E-mail: ndavidovic@mas.bg.ac.rs

[2] 0000-0003-2836-7405, Faculty of Mechanical Engineering, Kraljice Marije 16, Belgrade, Serbia, E-mail: nkolarevic@mas.bg.ac.rs

[3] 0000-0002-4310-2184, Faculty of Mechanical Engineering, Kraljice Marije 16, Belgrade, Serbia, E-mail: mstankovic@mas.bg.ac.rs

[4] 0000-0002-1931-1170, Faculty of Mechanical Engineering, Kraljice Marije 16, Belgrade, Serbia, E-mail: mmilos@mas.bg.ac.rs

1. Introduction

Expendable turbojets, typically in thrust range from 40 to 400 daN, are used in target drones and missiles. Because of their usage they are designed to be simple and cheap rather to have some challenged performances according to [1],[2] and [3]. Also, because of their applications they are not requiring rigorous certifications as turbojets for man applications. Usually they are certificated together with the system in which they are installed. This paper is presenting experiences with initial prototype testing. At the moment when designed engine is produced and when some of component or subsystem testing are finished, we have to start with the very first tests. The point is that we will have to check performance of the engine which has to be running for the first time. If everything is fine during the first test and the results are very similar to expecting values it will be perfect. But usually in the engineering world it will not be the case. More than this we have to solve many small issues until we can run the prototype engine with confidence. On the other hand these days time for development is very limited, it is expected that such engine is ready for serial production in 12 to 18 months and consequently it is very important to accurately understand possible problems during initial testing. If we make wrong conclusions it will delay assigned development time and possibly come in position that development went to wrong direction. Technical papers usually describe achieved results but without complete picture of problem which they have to overcome in order to achieve development goals. With such motivation the material discussed at this paper describes what had to done to make prototype engine to run correctly and refers to the turbojet engine TJE-200 at the EDePro company.

2. Engine description

Turbojet engine TJE-200 consists of three stage axial compressor, through flow combustor with 12 centrifugal atomizers and single stage axial turbine, cross section of the engine is shown at Fig. 1. Maximum thrust is 185 daN and maximum rpm is 39450. The specific fuel consumption of the engine is 1.35 kg/danh. The maximum diameter of the engine is 270mm, while dry weight is 35kg. The starting system is air impingement at turbine, ignition is made by electric spark plug. Lubrication is based on spill out oil or kerosene system. The engine has directly coupled electric generator with maximum electric power of 1.5kW. The generator is directly coupled to engine shaft by means of innovative self-designed magnetic coupling which was the best solution in terms of vibrations comparing to commercial elastic coupling solutions. The compressor rotors were produced by CNC machining from steel 17-4 PH, while stators were produced from investment casted aluminum alloy. The combustor liner was produced from 310 stainless steel, while turbine rotor and stator were produced by investment casting of Inconel 713C according to [4]. The engine was balanced with maximum unbalance of 2gmm. The compressor, combustor and turbine were designed by EDePro company developed software based on previous empirical and experimental data.

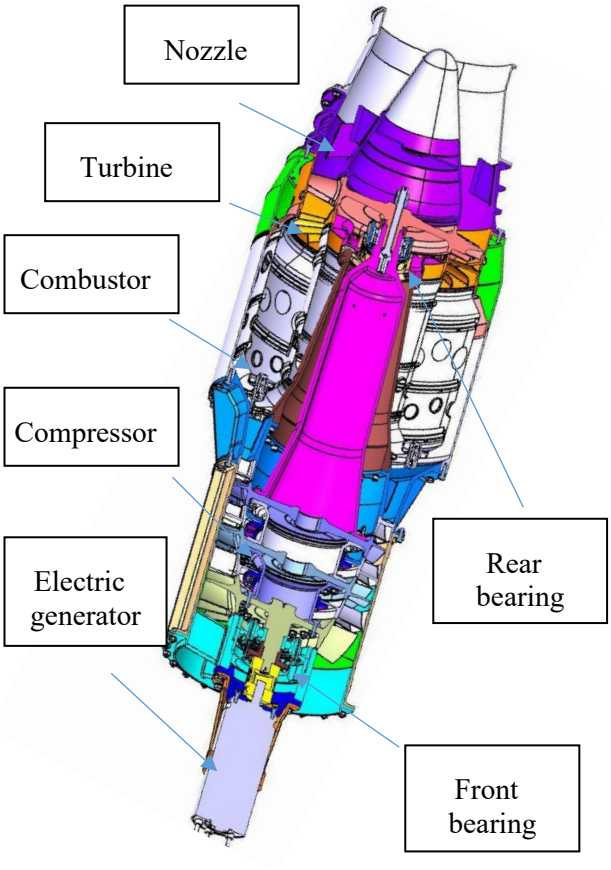

Fig. 1 Turbojet engine TJE-200 cut view

The engine rotor is supported at two elastic supports because the length of the shaft and rpm are not allowing rigid supports, according to [5] and [6]. Previous rotordynamic tests were performed to verify design and estimate the value of rotor displacement during operation. Photo from rotordynamic tests is shown at the Fig. 2.

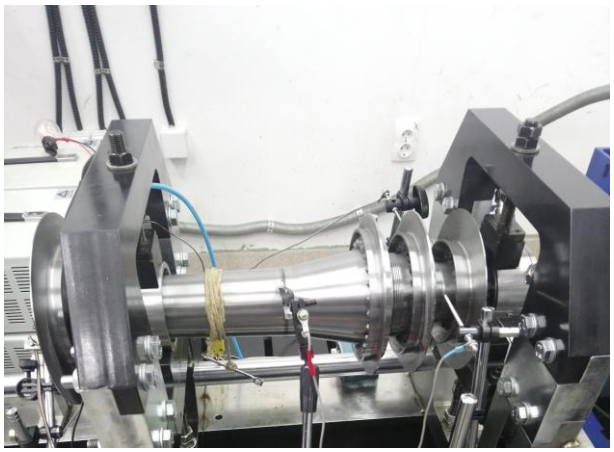

Fig. 2 Dummy rotor at rotordynamic test stand

3. Engine first tests

The first engine test shown the compressor surge issues during the starting approximately around 50% of the maximum rpm. In order to clarify the nature of the problem next test was done without nozzle. That test was successful with engine performances as expected. The position of the working line at the compressor map was in the expected range so the conclusion was that the problem was due to exhaust nozzle. Actually, the shape of the initial exhaust nozzle was dictated by some structural analysis results which shown that there are possible natural frequencies in the working range. After second analysis it was concluded that there is no force which could excite nozzle at desired frequency and that it will be almost impossible to satisfy required shape and pressure drop of the nozzle and to avoid such natural frequencies. The next tests were made without exhaust nozzle to verify mechanical behavior of the engine until the new designed nozzle was produced, as shown at the Fig. 3. The working lines without nozzle, with nozzle without central body and with final design nozzle are shown at the Fig. 4.

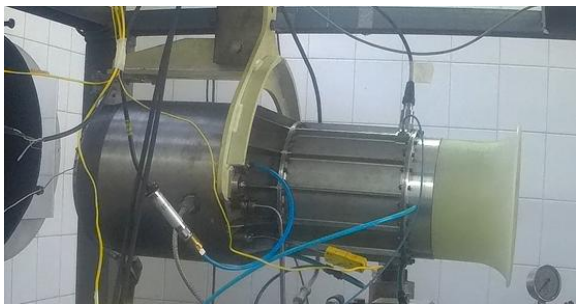

Fig. 3. TJE-200 at test without nozzle

The second issue during the first engine runs were increased level of vibrations during starts. Because the tests of rotordynamics which were done before engine tests it was obvious that increased vibrations are possibly due to some contacts between rotor and casing. After disassembling it was evident that there were contact between PTFE seals positions at compressor stators and compressor shaft. Because the compressor stators were assembled as two half's due to assembling it was very difficult to ensure the correct gap. As a solution, the radial gap was increased. No any contacts were detected in the following tests.

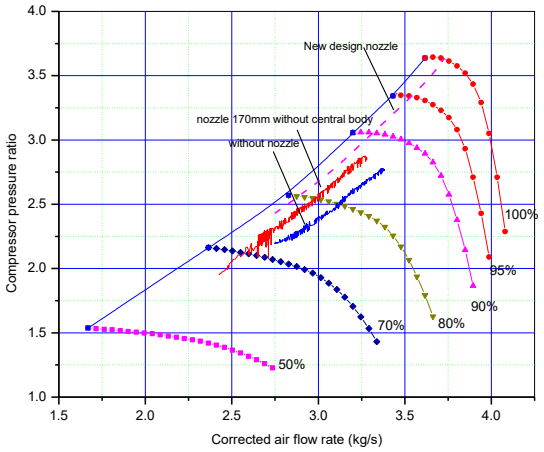

Fig. 4. Different working lines for different nozzles

The third problem during initial testing was related to electric generator caused vibrations. The first tests were carried out without electric generator which is directly coupled with engine shaft. Initial solution was to use the elastic commercial coupling. Although the coupling was factory balanced the increased vibrations were encountered. The reason was that the engine is supported at two elastic supports and when elastic coupling was connected to the shaft it was driven out of axis and it was producing undesirable unbalance. The problem was solved with innovative solution. Since that power and torque which have to be transferred by coupling are small (1.5kW and 0.35Nm) we introduced self-designed magnetic coupling. One part of the coupling is at the engine shaft and another at the generator shaft, with axial gap of around 1.5mm. The logic was simple, if the generator is not in direct contact with engine shaft it will not be able to produce vibrations. More than this, the engine can be balanced together with magnetic coupling.

The fourth major problem was related to the turbine stator vanes overheating. After most of the tests engine was disassembled in order to check component conditions. When the overheating problem was noticed at the turbine stator vane leading edge the small analysis was made. As the efficiency of the engine was ok it was concluded that overheating is consequence of non-uniform temperature field at the combustor exit. It was difficult to conclude at which regime it is dominant, starting or working. However, the actions were made to minimize that effect: the small pipes were introduced in each second dilution hole to enhance mixing (but with minimum effect on pressure drop) and the pressure swirl atomizers were replaced with smaller one in order to minimize droplet size especially during starting. After these changes no overheating issues were noticed.

The fifth problem which is worth to mention was rear bearing temperature. The lubrication system is of spill-out type. It means that the oil is injected in the bearing and then spilled out into the main flow. In order to minimize the flow rate of the oil and consequently losses of the oil the minimum portion of the oil is required. It is maintained with system of valves which are opened and closed with desired frequency. The so-called secondary air of the engine is used to transport that oil into the main flow and it is shown at the Fig. 5 and Ref. 1.

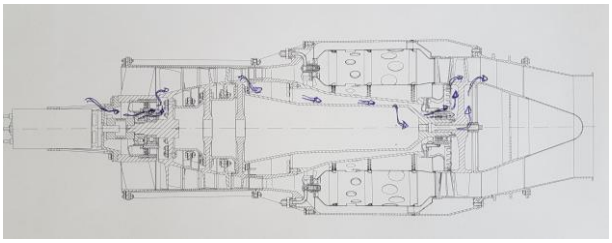

Fig. 5. Description of the secondary air flow

The point was that through rear bearing is passing the air taken from after the compressor which has temperature of around 180 ºC at the maximum rpm. Although bearing maximum temperature is declared as 250 ºC we wanted to keep that temperature below 150 ºC. Initially, very small amount of oil was injected (around 0.3g/s) and consequently the temperature of the bearing was always higher than temperature of incoming air. When the oil flow is increased to level of 1.5g/s the bearing temperature falls below air temperature. Again, since that oil is loosed it is more practical to use fuel for that purpose as in Ref. 2. The final solution is based on kerosene spill out system, small amount of fuel is injected into bearing area. Typically it increases specific fuel consumption for about 2-3% but avoiding any element in the lubrication system.

The summary of initial problems and corrections made are shown in the Table 1 and in the Fig. 6.

Table 1. Summary of the corrections

problem	***correction***
Compressor surge	Nozzle redesign
Increased vibration levels	Labyrinth seal gap correction
Electric generator increased vibration levels	Coupling redesign
Turbine stator vanes overheating	Corrected combustor dilution zone
Rear bearing temperature above desired limit	Corrected oil amount and lately switch to kerosene lubrication

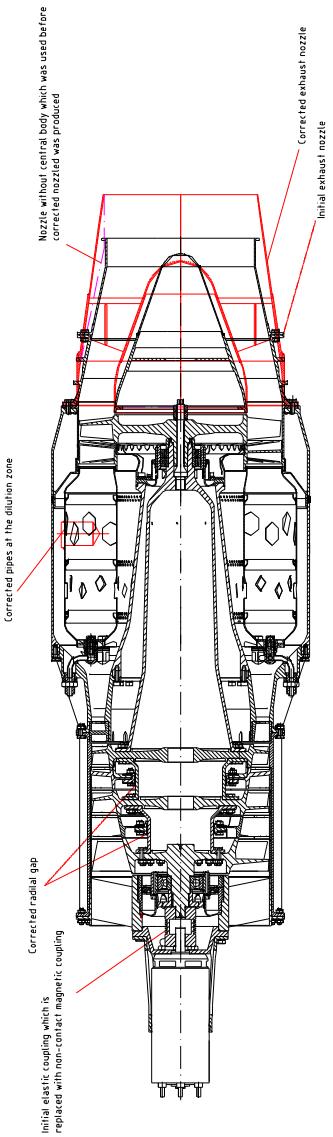

Fig. 6. *TJE-200 corrections during initial testing*

4. Conclusion

The initial engine testing is presented. The mentioned work was done from June to December 2018. i.e. in the period of six months. We have to underline that for one newly designed and produced engine engineers have to understand the behavior of the engine presented through measured data and through engine component conditions. It is very important to use knowledge, experience and logic to come to correct conclusion and perform appropriate action. Otherwise, wrong conclusions may drove to completely opposite side of solution causing loses of time allowed for certain project. The main contribution of these work is real now-how process in limited time line.

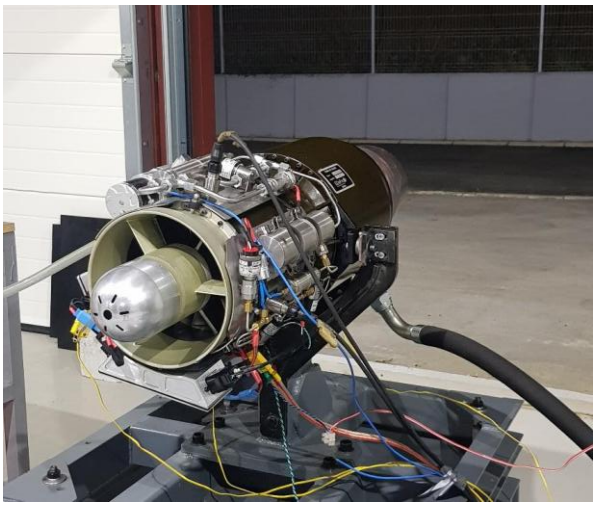

Fig. 7. Final version of the turbojet engine TJE-200 with subsystems at the test stand

Acknowledgments

The presented paper is a result of the researches supported by MPNTR RP according to the contracts 451-03-137/2025-03/ 200105 since 4th February 2025 and 451-03-66/2024-03/200213 since 5th February 2024. The authors wish to acknowledge and thank the company EDePro for the support.

References

[1] D.E.Barbeau (1981) *A Family of Small, Low Cost Turbojet Engines for Short Life Applications*, ASME 81-GT-205, 198

[2] J.F.Rideau, G.Guyader, A.Cloarec (2008) *Microturbo Families of Turbojet Engine for Missiles and Uav's From the TR60 to the New Bypass Turbojet Engine Generation*, In 44th AIAA/ASME/SAE/ASEE Joint Propulsion Conference and Exibit, Hartford, paper no: AIAA 2008-4590

[3] A.Bodemer, *Les Turbomachines Aeronautiques Mondiales*. Editions Lariviere, 1979.

[4] *Aerospace Structural Metals Handbook*, Air Force Material Laboratory, Air Force Systems Command, Wright-Patterson Air Force Base, Ohio, 1971.

[5] Г.С.Скубачевский, *Авиационные газотурбинные двигатели*, Машиностроение, Москва 1969.

[6] R.P.Dengler, L.E.Macioce, *Small, low-cost, expendable turbojet engine-I Design, fabrication and preliminary testing*. Report, NASA TM X-3392, 1976.

41st Danubia-Adria Symposium Advances in Experimental Mechanics
September 23-26, 2025, Kragujevac, Serbia

Original scientific paper DOI: 10.46793/41DAS2025.087A

HARDNESS MEASUREMENT OF ROLLING BEARING BALLS SUBJECTED TO MULTI-CYCLE CRYOGENIC TREATMENT

Jovana ANTIĆ[1], Žarko MIŠKOVIĆ[2], Danilo PEJČIĆ[3], Martin DIX[4], Alexander PIERER[5], Jürgen HEIDRICH[6], Matthias MILBRANDT[7]

[1] 0009-0002-6452-0294 Faculty of Mechanical Engineering, University of Belgrade, Kraljice Marije 16, Belgrade, Serbia, E-mail: jrantic@mas.bg.ac.rs;

[2] 0000-0002-8320-7191, Faculty of Mechanical Engineering, University of Belgrade, Kraljice Marije 16, Belgrade, Serbia, E-mail: zmiskovic@mas.bg.ac.rs;

[3] 0009-0007-1661-2924, Faculty of Mechanical Engineering, University of Belgrade, Kraljice Marije 16, Belgrade, Serbia, E-mail: dpejcic@mas.bg.ac.rs;

[4] 0000-0002-2344-1656, Institute for Machine Tools and Production Processes, Chemnitz University of Technology, Reichenhainer Str. 70, Chemnitz, Germany; Fraunhofer Institute for Machine Tools and Forming Technology IWU, Reichenhainer Straße 88, Chemnitz, Germany, E-mail: martin.dix@iwu.fraunhofer.de;

[5] 0000-0003-1881-8989 , Fraunhofer Institute for Machine Tools and Forming Technology IWU, Reichenhainer Straße 88, Chemnitz, Germany, E-mail: alexander.pierer@iwu.fraunhofer.de;

[6] Fraunhofer Institute for Machine Tools and Forming Technology IWU, Reichenhainer Straße 88, Chemnitz, Germany, E-mail: juergen.heidrich@iwu.fraunhofer.de;

[7] Fraunhofer Institute for Machine Tools and Forming Technology IWU, Reichenhainer Straße 88, Chemnitz, Germany, E-mail: matthias.milbrandt@iwu.fraunhofer.de;

1. Introduction

Rolling bearings are essential components in a wide range of mechanical systems, where they support loads and enable relative motion with minimal friction. Their operational reliability and service life strongly depend on the mechanical properties of the rolling elements.

Among various surface and heat treatment techniques, Deep Cryogenic Treatment (DCT) is a promising method for enhancing the performance of bearing steels. DCT is a process in which materials are cooled to cryogenic temperatures (typically below −150°C), maintained at that temperature for a defined period, and then gradually reheated under controlled conditions. This process leads to several beneficial microstructural changes, such as the transformation of retained austenite into martensite, precipitation of fine carbides, and redistribution of internal stresses. These effects can contribute to improved hardness, dimensional stability, and fatigue life.

For this research, bearing balls were selected because of their distinctive cooling patterns. Unlike bearing rings, which generally cool evenly, bearing balls experience notable temperature differences between their outer surface and inner core during cooling. These thermal gradients can influence residual stress distribution and microstructural evolution, making balls an excellent subject for studying the effects of DCT.

This study investigates the influence of multi-cycle Deep Cryogenic Treatment on the hardness of bearing balls made of 100Cr6 steel, intended for use in standard deep groove ball bearings (types 6306, 6308, and 6310). The test specimens were commercially available balls, previously subjected to conventional quenching (Q) and tempering (T). The aim is to determine whether DCT, when applied as an additional treatment after Q-T, leads to significant changes in hardness and whether the treated rolling elements maintain hardness values within the range required for reliable bearing operation.

2. Literature review

Numerous studies have demonstrated that the observed increase in hardness following DCT is largely attributed to the ultra-low temperatures used in the process. These conditions promote a more complete transformation of retained austenite into martensite—a significantly harder phase—than what is typically achieved through Conventional

Heat Treatment (CHT). Moreover, DCT can trigger the precipitation of fine secondary carbides and refine the microstructure, contributing to improved hardness through dispersion strengthening mechanisms.

To achieve a more comprehensive understanding of the effects of DCT on bearing steels, researchers have explored a wide range of treatment parameters, including soaking temperature and time, sample geometry, and thermal treatment sequences.

For example, a study [1] reported that cylindrical specimens of AISI 52100 steel (18 mm diameter, 10 mm height) showed a reduction in retained austenite from 14% to 3% after DCT at −180°C for 24 hours. This transformation corresponded with a 15% improvement in hardness. Similarly, another study [2] involving the same steel, 100Cr6, found that samples of 6 mm diameter and 6 mm height, treated at −185°C for 24 hours, exhibited an 18% increase in hardness. These enhancements were attributed not only to austenite-to-martensite transformation, but also to the precipitation of secondary carbides and grain refinement of martensite.

In [3], a different experimental setup employed a heat treatment sequence of quenching, tempering, DCT, and final tempering (Q–T–DCT–T) on 10 mm × 10 mm cylindrical samples made of AISI 52100 steel. The authors identified four main mechanisms responsible for property improvements: martensitic transformation of retained austenite, formation of eta-phase carbides, precipitation of ultrafine carbides, and enhanced microstructural uniformity. This sequence improved hardness by 10% compared to CHT.

Despite significant research efforts on standard test specimens (such as plates or cylinders), experimental data on the behavior of actual rolling elements remains scarce.

In the authors' previous study [4], bearing balls were subjected to a single-cycle DCT with a soaking temperature of −160°C for 24 hours, using cooling and heating rates of 1.5 K/min. For all bearing ball types, the change in hardness after DCT was less than 1%. The present investigation extends previous work by examining the effects of multi-cycle DCT on bearing balls.

Multi-cycle deep cryogenic treatment (DCT), involving repeated cooling and heating cycles, has been less frequently studied, especially in the context of bearing materials.

In [5], high-vanadium alloy steel was investigated under various DCT conditions, including two, four, and eight cycles with short soaking times, as well as single-cycle treatments with extended durations. The results indicated that both an increased number of cycles and prolonged cryogenic exposure led to a reduction in hardness, which was attributed to stress relaxation and changes in microstructural transformations.

This study focuses on exploring the effects of multi-cycle DCT on the hardness of commercially available 100Cr6 steel bearing balls, aiming to determine the treatment's potential as an additional step following quenching and tempering.

3. Experimental samples

The test specimens used in this study were rolling elements (balls) manufactured for use in 6306, 6308, and 6310 deep groove ball bearings, which are commonly used in conveyor idlers and other industrial applications.

The average diameters of the bearing balls were approximately 12.303 mm (6306), 15.081 mm (6308), and 19.052 mm (6310). All balls were made from 100Cr6 steel (SAE/AISI 52100), a high-carbon chromium alloy steel widely used for rolling bearing elements. This steel grade is classified as ball and roller bearing steel according to the SRPS EN ISO 683-17:2023 standard [6].

Table 1. Chemical Composition [%] of Bearing Steel 100Cr6

	C	Si	Mn	Cr	other
Chemical composition [%]:	1.00	0.25	0.35	1.50	-

All bearing balls were obtained in commercially available form, having already undergone conventional quenching and tempering. As a result, the DCT was applied after these standard heat treatments, rather than between quenching and tempering as is typically the case in some DCT protocols.

4. Process Parameters for Multi-Cycle Deep Cryogenic Treatment

The bearing balls were subjected to a multi-cycle DCT with the aim of investigating the effects of repeated thermal exposure on material properties. The full temperature–time profile is shown in Figure 1.

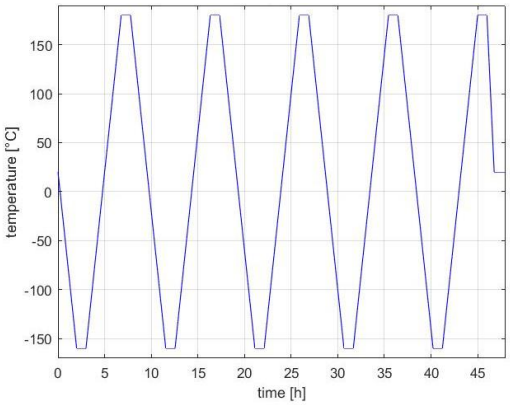

Fig. 1. Temperature Profile of Multi-Cycle Cryogenic Treatment

The process started at room temperature (~20°C) and involved a gradual cooling at a rate of 1.5 K/min down to a soaking temperature of −160°C, where the samples were held for 1 hour. After the cryogenic soak, the samples were heated to +180°C and again held for 1 hour. This cooling–heating cycle was repeated five times in total. After the final heating stage, the samples were cooled back to room temperature in a controlled manner, at a cooling rate of 1.5 K/min, to minimize thermal shock.

The treatment was performed in cryogenic chamber KK2000 using gaseous nitrogen as the cooling medium, under carefully controlled conditions to avoid thermal material shocking.

5. Hardness measurement

The hardness of the bearing balls was measured using the Zwick Roell ZHU 2.5 Universal Hardness Testing Machine, located in the accredited LIMES Laboratory (Laboratory for Testing of Machine Elements and Systems) at the Faculty of Mechanical Engineering, University of Belgrade.

Fig. 2. Zwick Roell ZHU 2.5 Universal Hardness Testing Machine (LIMES Laboratory, University of Belgrade)

The Rockwell hardness test was conducted in accordance with the latest standard SRPS EN ISO 6508-1:2024 [7], which replaced the previous SRPS EN ISO 6508-1:2017 version as of January 31, 2024. This national standard corresponds to the international EN ISO 6508-1:2023, titled *Metallic materials – Rockwell hardness test – Part 1: Test method*.

The Rockwell method determines hardness based on the depth of penetration (h) caused by a specific indenter under a controlled loading sequence, including a preload (minor) and total (major) force.

In this experiment, the HRC scale was used, employing a diamond cone (conical) indenter, which is standard for testing harder materials. The preload was 98.07 N, while the total force applied reached 1.471 kN. The HRC scale constants are N = 100 and S = 0.002 mm, leading to the following formula for calculating hardness:

$$HRC = 100 - \frac{h}{0.002}. \quad (1)$$

According to [8], the required hardness range for bearing balls is between 58 and 66 HRC, ensuring adequate performance and resistance to wear during operation.

6. Results

The measured hardness values of the bearing balls before and after the applied multi-cycle DCT are presented in Table 2. A slight decrease in hardness was observed across all three bearing types (6306, 6308, and 6310) following the treatment. The reduction ranged from 1.7 to 2.4 HRC, corresponding to a 2.59% to 3.72% decrease in hardness.

Despite the observed reduction, all hardness values after DCT remained within the recommended range of 58–66 HRC. It is important to note that a minor reduction in hardness does not necessarily imply a loss in overall material quality.

Table 2. Initial and Post-Treatment Hardness Values of Rolling Bearing Balls

	Hardness Before DCT [HRC]	**Hardness After DCT** [HRC]	**Change** [HRC]	**Percentage change** [%]
6306	64.5	62.8	-1.7	2.64
6308	64.6	62.2	-2.4	3.72
6310	65.6	63.9	-1.7	2.59

A similar trend was observed in [4], which applied a single-cycle DCT with a soaking temperature of −160°C for 24 hours and identical

cooling/heating rates of 1.5 K/min. Despite the extended soaking duration, the results also indicated a slight decrease in hardness after treatment, suggesting that DCT does not universally lead to increased hardness.

7. Conclusions

Rolling bearings are critical and widely used machine elements, making continuous improvement of their performance essential. One method employed to enhance the properties of metallic materials is DCT. Researchers have extensively investigated the effects of single-cycle DCT on bearing materials, whereas the influence of multi-cycle DCT remains relatively unexplored. Also, specimens were primarily cylindrical or disc-shaped, rather than actual rolling elements. In this study, commercially available rolling bearing balls were selected as specimens. Balls were chosen due to the significant thermal gradients between their surface and core, which are expected to make DCT effects on the material's microstructure more pronounced than in bearing rings.

This study examined the influence of multi-cycle DCT on the hardness of rolling bearing balls made of high-carbon chromium steel 100Cr6 (SAE/AISI 52100), which had previously undergone conventional quenching and tempering. The DCT process was precisely controlled, involving slow cooling and heating rates of 1.5 K/min, five repeated cryogenic cycles with a soaking temperature of −160°C held for 1 hour, followed by tempering at +180°C for 1 hour, and the use of liquid nitrogen as the cooling medium in a cryochamber.

The Rockwell hardness (HRC) measurements showed a slight decrease in hardness after DCT, ranging from 1.7 to 2.4 HRC, corresponding to a reduction of approximately 2.6–3.7%. However, all treated samples remained within the standard hardness range for bearing balls (58–66 HRC), indicating that the treatment did not compromise their applicability in rolling bearing systems.

Although a reduction in hardness was observed, this does not necessarily imply a decrease in overall performance. DCT is known to improve other material properties such as wear resistance, dimensional stability, reduction of residual stresses, and microstructural refinement. These benefits cannot be fully evaluated through hardness alone.

Future work will focus on additional characterization, including residual stress analysis, surface roughness, and dimensional stability, to gain a more comprehensive understanding of the impact of multi-cycle DCT on rolling bearing elements, as previously outlined in [9].

Acknowledgments

The results presented in this paper are the results of the cooperation between the Faculty of Mechanical Engineering at the University of Belgrade (Belgrade, Serbia) and the Fraunhofer Institute (Chemnitz, Germany) within a study supported by the Ministry of Science, Technological Development, and Innovation of the Republic of Serbia under Contract No. 451-03-137/2025-03/200105, dated February 4, 2025.

References

[1] Shunmuga Priyan, M., Siva, R.: Residual Stress and Wear Studies of Deep Cryogenically Treated SAE 52100 Bearing steel. *Journal of Mechanical Engineering*, 2019, 16(3), 91–104.

[2] Siva, R. S., Jaswin, M. A., & Lal, D. M.: Enhancing the Wear Resistance of 100Cr6 Bearing Steel Using Cryogenic Treatment. *Tribology Transactions,* 2012, 55 (3), 387-393.

[3] Kara, F., Cicek, A., Demir, H.: Effect of Deep Cryogenic Treatment on Microstructure, Mechanical Properties, and Residual Stress of AISI 52100 Bearing Steel. *Engineered Science*, 2023, 26.

[4] Antić, J., Mišković, Ž., Pejčić, D., Dix, M., Pierer, A., Heidrich, J., Demmler, M. The influence of cryogenic treatment on the hardness of rolling bearings' balls. In *11th International Scientific Conference IRMES 2025*, Vrnjačka Banja, Serbia, 19-21 June, 2025; pp. 1–4.

[5] Li, H., Tong, W., Cui, J., Zhang, H., Chen, L., Zuo, L. The influence of deep cryogenic treatment on the properties of high-vanadium alloy steel. *Materials Science and Engineering: A*, 2016, 662, 356-362.

[6] SRPS EN ISO 683-17:2023, Heat-treated steels, alloy steels and free-cutting steels - Part 17: Ball and roller bearing steels

[7] SRPS EN ISO 6508-1:2017, Metallic materials - Rockwell hardness test - Part 1: Test method

[8] Rulebook on Technical and Other Requirements for Roller Bearings, Official Gazette of the Republic of Serbia, No. 98/2016 and 66/2018

[9] Mišković, Ž., Antić, J., Pierer, A., Heidrich, J., Mitrović, R.: Deep cryogenic treatment of rolling bearings - initial experimental results, In *Proceedings of International Conference of Experimental and Numerical Investigations and New Technologies – CNN TECH 2024,* Zlatibor, Serbia, 5-8 July, 2024, , pp. 23.

Original scientific paper DOI: 10.46793/41DAS2025.091G

EXPERIMENTAL AND ANALYTICAL METHODS FOR DETERMINING INTERLAMINAR SHEAR STRENGTH OF COMPOSITES MADE BY FDM 3D PRINTING

Nenad GRUJOVIĆ[1*], Strahinja MILENKOVIĆ[2], Fatima ŽIVIĆ[3]

[1] 0000-0002-8765-2196, Faculty of Engineering, University of Kragujevac, Sestre Janjić 6, 34000 Kragujevac, Serbia, E-mail: gruja@kg.ac.rs;

[2] 0000-0002-5822-4846, Institute for Information Technologies, University of Kragujevac, Jovana Cvijića bb, 34000 Kragujevac, Serbia, E-mail: strahinja.milenkovic@kg.ac.rs;

[3] 0000-0003-2509-187X, Faculty of Engineering, University of Kragujevac, Sestre Janjić 6, 34000 Kragujevac, E-mail: zivic@kg.ac.rs;

1. Introduction

Fused Deposition Modeling (FDM) 3D printing of fiber-reinforced composites involves a complex interplay of materials, processing parameters, and environmental conditions that all influences resulting mechanical properties [1]. Different measurement methods are used to evaluate these effects on the final materials properties and performance. This paper presents experimental and analytical methods for determining interlaminar shear strength of PLA/PVDF composites made by FDM 3D printing.

2. Influential Factors in FDM 3D Printing of Composites

Fabrication of composites can be realised by FDM 3D printing which is a low-cost promising technology, but there are still significant challenges related to dimensional accuracy, repeatability and mechanical properties, due to a number of different influential factors governing the printing process, thus reflecting the final composite properties. In Main groups of influential factors and possible variables, for FDM 3D printing of fiber reinforced composites, are shown in Fig.1, including the variables representing the influence of the filament materials, processing parameters and external influences. For example, in the case of fiber reinforced composites, different methods are used for short, continuous or nano/micro reinforcing fibers [1–3]. Material-related factors essentially determine how the composite will be produced, including the subsequent measurement and characterization techniques to be used. Matrix material, fiber material and weight or volume fraction of reinforcements, together with fiber orientation (alignment during extrusion or intentionally designed in certain way) will further reflect on the interfacial bonding or adhesion between fiber and matrix.

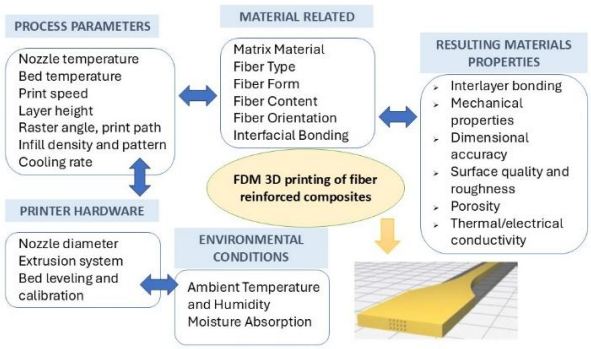

Fig. 1. Influential factors in FDM 3D printing of composites.

Process parameters have a major influence on the final composite properties [4]. Nozzle temperature affects matrix viscosity and fiber wetting and bed temperature influences adhesion and warping. Print speed impacts fiber alignment and extrusion consistency. Layer height affects interlayer bonding and surface finish, while raster angle and print path control internal structure and anisotropy, whereas infill density and selected pattern influences stiffness and strength. The cooling rate affects residual stresses and crystallinity.

Printer hardware like nozzle diameter limits fiber size and deposition rate and depending on the extrusion system (single or multiple nozzles) different phases within the composite can be simultaneously printed or not. Bed leveling and calibration affects dimensional accuracy. Ambient temperature and humidity affect material flow and bonding and moisture absorption is especially critical for hygroscopic materials.

3. Measurement and Characterization Methods

Different characterization methods are used for composites depending on the targeted material properties and specific applications. Mechanical properties can be determined by different methods, including tensile testing (ASTM D638 or ISO 527) to measure strength, modulus, elongation; flexural testing (ASTM D790) for bending behavior; impact testing (e.g. Charpy or ASTM D256) to assess toughness; interlaminar shear strength (ASTM D2344) for delamination resistance. Microstructural analysis is commonly done using scanning electron microscopy (SEM) to observe fiber-matrix interface, porosity and failure modes, while optical microscopy is used for layer morphology and fiber distribution analysis. The 3D internal structure, porosity and voids can be characterized through computed tomography (CT).

Thermal properties can be determined through differential scanning calorimetry (DSC) that can provide data on crystallinity, glass transition temperature (Tg) and melt temperature (Tm) and by using thermogravimetric analysis (TGA) for fiber content and thermal stability. Dynamic mechanical analysis (DMA) is advanced technology that can provide valuable data for dynamical mechanical behavior, including material viscoelastic behavior and damping.

Depending on the material type and final application, rheological behavior can be also demanded to determine flow behavior of composite melt or viscosity as a function of shear rate [5]. Dimensional and surface quality are very important and challenging with FDM printing since the printed parts commonly experience certain degree of warping in the case of poorly selected printing parameters, such as nozzle temperature not in accordance with Tg temperature of the printed materials. Post processing is usually applied to provide adequate surface roughness.

3.1 Interlaminar Shear Strength (ILSS)

Interlaminar Shear Strength (ILSS) is a critical mechanical property in laminated or layer-based structures, such as those produced by FDM printing, where layer bonding and interlayer adhesion is inherently weaker due to the layer-by-layer nature of the process. It reflects the material's ability to resist sliding between layers, which is often a failure mode in 3D printed composites and especially pronounced in the case of fiber reinforced composites. In laminated composites (like FDM-printed parts), interlaminar shear refers to in-plane shear between adjacent layers. These layers are typically bonded by weaker adhesive forces (e.g., diffusion bonding or partial melting in FDM). ILSS represents the maximum shear stress that a composite material can sustain between its layers before failure occurs. For FDM printing, it is necessary to ensure consistent fiber orientation, layer thickness, and infill pattern, whereas surface finish and voids can significantly affect results. The characterization of such samples needs to capture interlayer effects, by testing samples in different build directions (XY, XZ, YZ).

Shear stress in layered materials is calculated according to the equation (1):

$$\tau = \frac{F}{A} \tag{1}$$

where τ is shear stress, F, applied load parallel to the surface and A, area over which the load is applied. However, this basic formula assumes uniform shear over a flat interface, which is not the case in practice. Therefore, we use mechanical test methods that induce a dominant interlaminar shear stress state.

Standard methods to measure ILSS, commonly using universal testing machine, are short beam shear test (SBS) (ASTM D2344, ISO 14130), double notch shear test (ASTM D3846) and Iosipescu shear test (ASTM D5379). Additionally, digital image correlation (DIC) with high-resolution digital cameras is an optical method that tracks surface deformation to measure full-field strain distribution and is often used together with other standard tests for more insight into strain localization.

3.2 Short Beam Shear (SBS)

The SBS test is the most common method for measuring ILSS, relying on a three-point bending setup with a very short span-to-thickness ratio (~4:1). The test induces shear stress primarily in the mid-plane. In a beam under three-point bending, stress distribution includes bending stresses (normal stress) and shear stresses (transverse shear). A short span increases the shear component relative to bending, forcing failure in shear rather than in tension/compression. Therefore, the interlaminar shear stress is maximized at the mid-plane (neutral axis) of the beam, and can be calculated as approximate maximum shear stress (at neutral plane), according to the equation (2):

$$\tau = \frac{0.75\,F}{b \cdot d} \tag{2}$$

where F is maximum load before failure, b is sample width d, is sample thickness. This formula is derived from beam theory using first-order shear deformation theory (FSDT) and assumes: uniform shear stress distribution over the mid-plane; linear-elastic, isotropic behavior and negligible friction or support compliance.

Flexural Strength (σ_f) is also typically measured using a 3-point bending test (ASTM D790), according to the equation (3):

$$\sigma_f = \frac{3FL}{2bd^2} \quad (3)$$

where σ_f is Flexural strength (MPa), F is load at fracture, L is support span, b is sample width and d is sample thickness.

Materials characterization in scope of ILSS tests commonly include determination of failure modes and stress concentrations since ILSS tests often show delamination between layers, shear-induced cracking at the layer interface and fiber pull-out or matrix cracking. The point of the first significant load drop in the force-displacement curve typically indicates interlaminar shear failure. Microstructural properties such as layer adhesion (especially in FDM), voids/porosity, reinforcing fiber orientation and length and thermal residual stresses have significant effects on interlaminar shear strength. Standard SBS test for ILSS has certain limitations. The SBS test is not purely shear-dominant, and some bending stress exists. It is sensitive to sample geometry and surface quality. Stress redistribution or plasticity within composite phases can result in overestimate of ILSS. In FDM, results can vary significantly based on build direction and layer adhesion quality.

ILSS measurement can be complemented by considering advanced methods like finite element modeling (FEM) modelling that simulates 3D stress states and identifies true shear distributions, including possibility to account for nonlinear or viscoelastic material behavior. Furthermore, digital image correlation (DIC) can capture real-time strain fields, validating assumptions of uniform shear. Fractographic analysis is commonly used to analyze fracture surfaces and confirm interlaminar failure.

4. Case study

FDM 3D printed composite samples were made of polylactic acid (PLA) matrix, reinforced with α-phase polyvinylidenfluorid (PVDF) fibers [6]. We tested several build orientations, with pronounced differences between [0, 90] and [-45, +45] orientations (Fig 2a), regarding Interlaminar Shear Strength (ILSS). We performed uniaxial tensile test (Fig 2b) and three-point bending test (Fig. 2c). Samples with [-45, +45] orientation showed better tensile strength, since they could endure significantly higher strain in comparison to [0, 90] (almost two-fold increase). The point of the first significant load drop in the force-displacement curve that indicates interlaminar shear failure (Fig. 2c) was significantly higher in the case of samples with [-45, +45] orientation (approx. 10 mm displacement) compared to [0, 90] samples (approx. 6.9 mm displacement), thus indicating significantly better shear strength for [-45, +45] samples.

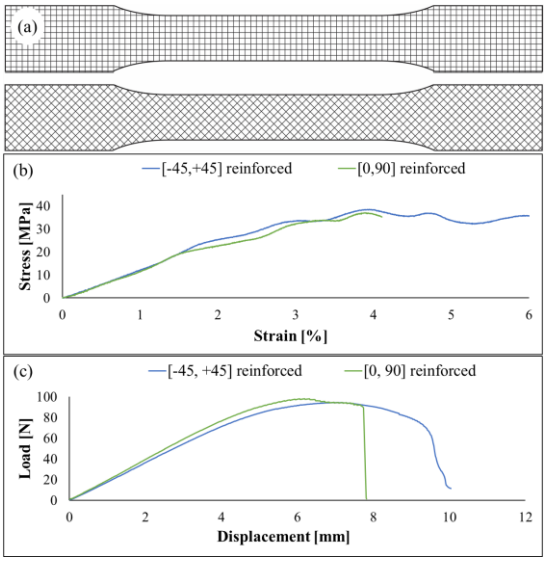

Fig. 2. a) Design of samples for 3D printing; b) Stress-strain curves for tensile tests; c) Load – displacement curves for three-point bending tests

Calculated values of interlaminar shear strength (ILSS) and flexural strength, according to the equations (2) and (3) and geometrical dimensions of the samples (width of 12.7 mm and thickness of 3.4 mm), are given in Table 1. These values are rough representations since they do not account for several other influential factors that need to be considered.

Table 1. Calculated approximate values of Interlaminar Shear Strength (ILSS) and Flexural strength

	Maximum load before failure [N]	Interlaminar Shear Strength (ILSS) [MPa]	Flexural strength [MPa]
[0, 90]	98	1.70	61.33
[-45, +45]	100	1.74	59.03

The numerical difference is small (0.04 MPa or about 2.35% difference) and may fall within the margin of experimental error or standard deviation of the testing method. Horizontally built [0, 90] samples may exhibit weaker interlayer bonding leading to lower ILLS. Inclined [-45, +45] samples

may allow better layer fusion, sometimes improving ILLS. Even a small improvement like 2.35% difference can suggest enhanced fusion or reduced voids in [-45, +45] orientation over [0, 90] orientation.

Material type in this test (PLA or PLA reinforced with PVDF can amplify or dampen orientation effects. Printing parameters (e.g., temperature, printing speed) can influence slightly better adhesion in one orientation, depending on the material type. The increase of 2.35% could be attributed to a more consistent deposition in [-45, +45] direction. Even the small difference of 2.35% may indicate more reliable interlayer performance, especially important for structurally critical parts. In the case of PLA/PVDF composite used here in the tests, fiber alignment due to orientation can slightly affect the shear strength. Also, as noted previously, stress redistribution or plasticity within composite phases can result in overestimate of ILSS.

Further study should be carried out, such as SEM microscopy to see if microstructural differences (e.g., voids, layer fusion) correlate with this small change. More samples across different orientations will be tested in the future for more accurate conclusions on the influences of build orientations on the total shear strength and ILLS. Therefore, further evaluation is needed, because calculated ILSS values indicate slight difference, while curves in Fig 2c clearly indicate significant differences between these two orientations.

It should be noted that composite preparation has a very important role for the final mechanical properties in the sense that it is necessary to provide consistent fiber orientation, layer thickness, and infill pattern what is rather challenging in 3D printing and especially in hand-layup of the reinforcing fibers. An inconsistent fabrication from these aspects can introduce unplanned anisotropy in the printed part and accordingly it is necessary to test samples in different build directions (XY, XZ, YZ) to capture interlayer effects. Also, surface finish and void content can significantly affect results, both governed by the complex interplay between different processing parameters. Additionally, environmental conditioning, such as influences originating from moisture or temperature pre-conditioning can greatly affect final properties of 3D printed parts.

5. Conclusions

Both experimental and analytical methods for determining interlaminar shear strength of PLA/PVDF composites made by FDM 3D printing showed that build orientation has significant influence on the resulting interlaminar shear strength. Simple analytical models can be used for rough estimations, but further analysis is needed to account for several influential factors such as geometrical dimensions, fiber and matrix properties and processing parameters of FDM printing, including viscoelastic behavior that cannot be captured by these simple models.

For high precision applications, even the small ILLS improvements can influence the design decisions. Specific orientations are selected for critical shear-loaded components. ILLS test method helps in optimizing part orientation to provide appropriate function and strength.

Acknowledgments

This paper is supported by the projects No. 451-03-137/2025-03/200107 and No. 451-03-136/2025-03/200378, Ministry of Science, Technological Development and Innovation, Republic of Serbia

References

[1] Li S, Cheng P, Ahzi S, Peng Y, Wang K, Chinesta F, et al. Advances in hybrid fibers reinforced polymer-based composites prepared by FDM: A review on mechanical properties and prospects. *Compos Commun* 2023, 40, 101592.

[2] Karimi A, Rahmatabadi D, Baghani M. Various FDM Mechanisms Used in the Fabrication of Continuous-Fiber Reinforced Composites: A Review. *Polymers* 2024, 16, 831.

[3] Ismail KI, Yap TC, Ahmed R. 3D-Printed Fiber-Reinforced Polymer Composites by Fused Deposition Modelling (FDM): Fiber Length and Fiber Implementation Techniques. *Polymers* 2022, 14, 4659.

[4] Khan S, Joshi K, Deshmukh S. A comprehensive review on effect of printing parameters on mechanical properties of FDM printed parts. *Mater Today Proc* 2022, 50, 2119–27.

[5] Njezic S, Zivic F, Savic S, Petrovic N, Pesic ZJ, Stefanovic A, et al. Analytical model of friction at low shear rates for soft materials in 3D printing. *Technol Health Care* 2024, 32, 3443–62.

[6] Milenkovic S, Slavkovic V, Fragassa C, Grujovic N, Palic N, Zivic F. Effect of the raster orientation on strength of the continuous fiber reinforced PVDF/PLA composites, fabricated by hand - layup and fused deposition modeling. *Compos Struct* 2021, 270, 114063.

Original scientific paper DOI: 10.46793/41DAS2025.095Z

MEASUREMENT OF PIEZOELECTRIC PROPERTIES OF HYDROGELS

Fatima ZIVIC[1*], Marija BRANKOVIC[2], Danilo PETROVIC[3], Petar TODOROVIC[4], Nenad GRUJOVIC[5]

[1] 0000-0003-2509-187X, Faculty of Engineering, University of Kragujevac, Sestre Janjic 6, Kragujevac, Serbia, E-mail: zivic@kg.ac.rs;

[2] 0009-0003-5228-4172, Institute for Information Technologies, University of Kragujevac, Jovana Cvijića bb, 34000 Kragujevac, Serbia, E-mail: marija.brankovic@uni.kg.ac.rs;

[3] 0009-0000-2292-8297, Faculty of Engineering, University of Kragujevac, Sestre Janjic 6, Kragujevac, Serbia, E-mail: petrovicdanilo1999@gmail.com;

[4] 0000-0003-3260-1655, Faculty of Engineering, University of Kragujevac, Sestre Janjic 6, Kragujevac, Serbia, E-mail: petar@kg.ac.rs;

[5] 0000-0002-8765-2196, Faculty of Engineering, University of Kragujevac, Sestre Janjic 6, Kragujevac, Serbia, E-mail: gruja@kg.ac.rs;

1. Introduction

Soft piezoelectric materials, such as hydrogels, have gained importance for diverse biomedical applications due to the possibility to mimic biological tissues, including cell signaling [1]. It is complex to accurately characterize their piezoelectric activity due to spatial inhomogeneity of the material, low electric outputs, instability of the signal, viscoelastic damping and high impedance. Also, determination of piezoelectric coefficients, important for analytical and numerical modelling is still challenging.

Measuring the low voltage output from piezoelectric hydrogels, which are soft and often deformable, requires highly sensitive instruments and careful noise mitigation. Common tools include high-impedance voltmeters, lock-in amplifiers, picoammeters, and low-noise or charge amplifiers to capture and condition weak signals. Techniques like Kelvin (four-terminal) sensing help reduce errors from contact resistance, especially in high-impedance materials. Advanced systems, such as portable devices with electrochemical impedance spectroscopy (EIS), enable precise low-current measurements. For evaluating piezoelectric coefficients, methods like laser Doppler vibrometry (LDV) and piezoresponse force microscopy (PFM) are used, often supported by numerical analysis for complex soft materials.

This paper presents measurement methods for piezoelectric hydrogels, with case study of custom measurement setup for low output voltage from actuated piezoelectric hydrogels and key aspects of good system design.

2. Piezoelectric hydrogels

Piezoelectric gels, or PiezoGels, are unique gels with crystalline structures exhibiting a polar arrangement [2]. PiezoGels are a type of piezoelectric material that generates electricity under mechanical stress. They consist of a 3D network of hydrophilic polymers with a unique crystalline, asymmetric structure, enabling efficient energy generation for sensors and biomedical uses. They also offer high sensitivity, chirality, strong electroactivity, stable polarization, and excellent extracellular matrix mimicry [2]. It is transparent, easily adaptable, and shape-changing; soft, flexible, stretchable, and biocompatible [2]. Piezoelectric hydrogels can be made from organic, inorganic, or hybrid materials. Traditional devices use piezoelectric polymers and ceramic oxides like perovskites. In polymeric hydrogels, interconnected polymer chains form a network that retains water. Natural polymers used include silk, collagen, starch, gelatin, chitosan, agarose, fibrin, dextran, alginate, heparin, and hyaluronic acid. Synthetic polymers used in the fabrication of hydrogels include polyvinyl alcohol (PVA), polyglycerol, sodium polyacrylate, polyacrylic acid, polyethylene oxide (PEO), polyacrylonitrile (PAN), and polyacrylamide (PAM), along with other synthetic polymers and copolymers. There is limited mention of hydrogels based on ceramic oxides in the literature. Among perovskite ceramic oxides, the most common in piezoelectric hydrogels are barium titanate (BaTiO3), lead titanate (PbTiO3), potassium niobate (KNbO3), and lead zirconate titanate ([Pb(Zr, Ti)O3]). Hydrogels based on supramolecular piezoelectric materials are organic and hybrid materials characterized by simple

synthesis, mechanical flexibility, multifunctionality, and adaptability.

Piezoelectric hydrogels are used in biomedicine to detect signals, promote healing, and boost tissue activity. In wearables, they monitor biological signals and support energy harvesting They also play a significant role in robotic systems [3]. As sensors, they detect fluid flow, vibrations, and flow direction. Integrated with ultrasonic transducers, they also aid diagnostics and internal condition monitoring [3].

3. Measuring low piezoelectric outputs

Measuring low voltage outputs from piezoelectric hydrogels (typically in the millivolt to a few volts range) requires sensitive techniques tailored to their soft, hydrated, and often deformable nature [2], [3]. Measurement methods for low voltage output from piezoelectric hydrogels commonly involve instruments with high sensitivity and take care to mitigate different influences that can interfere and affect output signals [4]. Stability of piezoelectric output signals, presence of noise and high impedance are recognised challenges, and it is still subject of research.

Common approaches include using a high-impedance voltmeter to preserve the hydrogel's low voltage output, a lock-in amplifier to detect low-level AC signals in noisy environments, and a picoammeter for current measurement. Various amplifiers are used, such as low-noise amplifiers to boost small signals for DAQ systems, and charge amplifiers that convert piezoelectric charge to voltage, ideal for dynamic signals due to their ability to handle the capacitive nature of piezo materials. Analogue signal conditioning is used for filtering and amplification before digitization. High sensitivity oscilloscope is used to view time-domain signals, especially for dynamic loading and is commonly paired with pre-amplifier and differential probes for noise immunity. Four-terminal (Kelvin) sensing uses combination of electrodes for current injection and voltage sensing, thereby eliminating the effects of contact and lead resistances [4]. This configuration is good for soft materials with a high impedance, as voltage loss across contacts can cause significant inaccuracy.

Advanced instruments have emerged focusing on measuring low electricity (~100 pA), such as small mobile devices combining potentiostat, galvanostat and frequency response analyser (FRA) for electrochemical impedance spectroscopy (EIS) that can be used as the highly sensitive background system for multichannel measurements, including supporting piezoelectric measurements [5].

Experimentally measuring piezoelectric coefficients is crucial for designing new composites, but direct methods are mostly limited to piezoresponse force microscopy (PFM), where AFM tip applies voltage to material surface and record resulting piezo response Most approaches instead calculate effective values, often using numerical methods for complex analysis. Laser doppler vibrometry (LDV) detects surface vibration velocities using laser interferometry. By applying electric field and measuring displacement, the effective piezoelectric coefficient can be calculated with high precision, even in soft or liquid-supported films. Certain interferometers can be adapted to track displacements from piezoelectric actuation, suitable for sub-nanometer displacement measurements.

4. Case study of custom measurement setup

Components of the measurement setup for low output voltage from actuated piezoelectric hydrogels are shown in Fig.1.

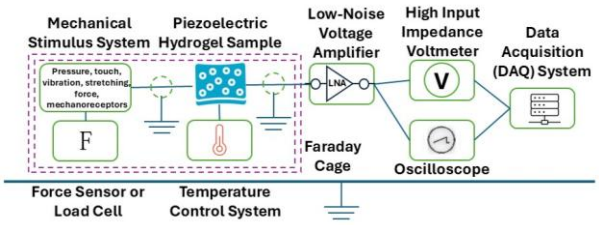

Fig. 1. Schematics of the measurement setup for low output voltage from actuated piezoelectric hydrogels.

Piezoelectric hydrogel sample generates voltage under mechanical stress produced by the mechanical stimulus system that can be provided by exerting pressure, touch, vibration, stretching, force or mechanoreceptors. The measurement setup for the low output voltage of a piezoelectric hydrogel needs to be highly sensitive and designed to minimize noise and impedance mismatches. The components typically used in such a setup are shown in Fig. 1, with piezoelectric hydrogel sample under mechanical stress generating the voltage. Mechanical stimulus system is used to apply a controlled force or strain to the hydrogel [6]. It can be provided by using various systems, such as linear actuator, vibration shaker, manual press with known force, or universal mechanical devices. Electrodes are usually made of gold, silver, carbon, or conductive inks and attached to both ends of the hydrogel or embedded in it [4]. Coaxial or triaxial

shielded cables are used to minimize electromagnetic noise.

Considering low level signals and potential noise disturbance, signal conditioning and measurement instruments are needed also, such as low-noise voltage amplifier or pre-amplifier, and high input impedance voltmeter or electrometer [7]. Low-noise voltage amplifier or pre-amplifier is required because piezoelectric signals are usually in the microvolt (μV) or millivolt (mV) range. High input impedance voltmeter or electrometer will prevent loading effects that could distort the measurements. Furthermore, oscilloscope can be used to observe transient signals in real time [8]. Data acquisition (DAQ) system is needed for digitizing and logging the signal, preferably with high resolution (≥16-bit ADC) and high impedance input.

Noise reduction and environmental controls are necessary to provide additional stability, such as Faraday cage and vibration isolation table. Faraday cage represents enclosure to shield the experiment from ambient electrical noise. Vibration isolation table minimizes mechanical noise from the environment. Proper grounding of all components is needed to reduce ground loops and interference.

Additional components are usually also present, such as force sensor or load cell to measure the applied force and correlate with voltage output. Temperature control system can be also provided to control the temperature since hydrogel properties can be temperature sensitive [9].

Mitigating noise and impedance mismatch in the measurement of low-voltage outputs from actuated piezoelectric hydrogels is crucial for obtaining accurate and reliable data [10]. These materials often generate very small electrical signals, and any distortion or loss can significantly affect signal interpretation. The critical elements that need to be addressed are:

- Impedance matching
- Minimizing noise
- Signal conditioning
- Connection quality and lead design
- Adequate grounding and isolation
- Environmental control
- Calibration and validation

Impedance matching is very important [10], [11] since piezoelectric hydrogels typically have high output impedance. If the input impedance of the measurement device is too low, signal attenuation and energy loss will occur. Possible solution is to utilize high input impedance buffer using a voltage follower circuit based on an operational amplifiers (op-amp) or instrumentation amplifier (in-amp) with input impedance $>10^9$ Ω. For piezoelectric outputs, a charge amplifier is very beneficial since it converts the high-impedance charge signal to a voltage, preserving the signal integrity. Low-noise preamplifier or low-noise, high-input-impedance amplifier close to the hydrogel can efficiently minimize signal loss over leads.

Minimizing noise is extremely important since the piezo signals are highly sensitive to it. The noise sources can originate from 1) electromagnetic interference (EMI) and RF noise, 2) thermal and Johnson noise or 3) mechanical noise. Preventing EMI and RF noise is typically done by using shielded cables, Faraday cage and proper grounding, as previously mentioned. Thermal and Johnson noise is present in all resistors and conductive materials and represents the random electrical noise generated by the thermal agitation of electrons in a conductor, even when no external voltage is applied. Thermal noise is caused by the thermal motion of charge carriers in any resistive material, and it is unavoidable and inherent to all electronic systems. To mitigate this effect, low-noise op-amps are suitable with minimal input bias current and voltage noise density. Also, if possible, cool environment with reduced temperature to lower thermal noise is beneficial, though that depends on the experimental setup feasibility. Mechanical noise can be mitigated by using vibration damping table to reduce unwanted or unintended activation of the piezoelectric effect in a hydrogel. Electrical wires can also affect piezoelectric signals [12], and strain decoupling can prevent it like using flexible leads or strain reliefs for cables to prevent mechanical disturbance from wires affecting the hydrogel. It will prevent additional complex loading through enabling separation or isolation of specific strain components (like axial, shear, or bending strains) in a hydrogel, especially important when multiple types of strain are present simultaneously.

Signal conditioning is done through filtering to remove unwanted noise and interference from the signal, by using a bandpass filter matching the expected frequency range of the piezoelectric signal to suppress low-frequency drift and high-frequency noise. Averaging is also used through software-based ensemble averaging (averaging multiple repetitions of a signal) across multiple actuation cycles to improve signal-to-noise ratio (SNR).

Connection quality and design of leads are crucial for ensuring signal integrity having

significant effects on signal quality. As short leads as possible are more beneficial for piezoelectric signals in this case, since long leads act as antennas and introduce noise [12]. Coaxial cables showed the best performance, but simple twisted-pair wires will also reduce EMI and improve signal quality. Low-leakage connectors will prevent current loss due to surface leakage, especially in humid or aqueous environments.

Adequate grounding and isolation is necessary and can be done in different ways, like differential measurements that can help in rejecting common-mode noise. For example, twisted pair wiring helps minimize the impact of electromagnetic interference by pairing signal lines and reducing the loop area for induced voltages. Isolated power supplies or battery-powered amplifiers are better since they eliminate power-line noise.

Environmental control through ensuring stability of humidity and temperature of the measuring setup is very important for piezoelectric hydrogels since they are sensitive to humidity and temperature, which can alter their electrical response.

Frequent calibration and validation of the measuring system is necessary by using known reference signals or standard piezoelectric materials since piezoelectric signals from hydrogels are very sensitive to different influences. It is beneficial to validate the linearity and frequency response of the entire signal chain before measuring actual samples.

5. Conclusions

Piezoelectric hydrogels are promising materials for tissue engineering, flexible wearables and sensing. However, accurate measuring of the output piezoelectric signals is complex and requires highly sensitive measurement setups. The critical elements that need to be addressed are impedance matching, minimizing noise, adequate signal conditioning, connection quality and lead design, adequate grounding and isolation, environmental control and regular calibration and validation.

Acknowledgments

This paper is supported by the project No. 451-03-137/2025-03/200107 and No. 451-03-136/2025-03/200378, Ministry of Science, Technological Development and Innovation, Republic of Serbia.

References

[1] Shi G, Su T, Li J, Wang A, Gao G, Tao B, et al. Biomimetic piezoelectric hydrogel system for energy metabolism reprogramming in spinal cord injury repair. *Theranostics* 2025;15:4955–69.

[2] Vijayakanth T, Shankar S, Finkelstein-Zuta G, Rencus-Lazar S, Gilead S, Gazit E. Perspectives on recent advancements in energy harvesting, sensing and bio-medical applications of piezoelectric gels. *Chem Soc Rev* 2023;52:6191–220.

[3] Du Y, Du W, Lin D, Ai M, Li S, Zhang L. Recent Progress on Hydrogel-Based Piezoelectric Devices for Biomedical Applications. *Micromachines* 2023;14:167.

[4] Sekitani T, Yokota T, Kuribara K, Kaltenbrunner M, Fukushima T, Inoue Y, et al. Ultraflexible organic amplifier with biocompatible gel electrodes. *Nat Commun* 2016;7:11425.

[5] Simić M. Portable Device for In-Situ Cyclic Voltammetry Measurements. 2024 47th *Int. Spring Semin. Electron. Technol. ISSE*, Prague, Czech Republic: IEEE; 2024, p. 1–5.

[6] Carravero Costa L, Pochard I, Buron CC, Jurin FE. Elaboration of Conductive Hydrogels by 3D Printer for the Development of Strain Sensors. *Gels* 2025;11:474.

[7] Mojena-Medina D, Martínez-Hernández M, De La Fuente M, García-Isla G, Posada J, Jorcano JL, et al. Design, Implementation, and Validation of a Piezoelectric Device to Study the Effects of Dynamic Mechanical Stimulation on Cell Proliferation, Migration and Morphology. *Sensors* 2020;20:2155.

[8] Azhari F, Tom C, Benassini J, Loh KJ, Bombardelli FA. *Design and characterization of a piezoelectric sensor for monitoring scour hole evolution*. In: Lynch JP, Wang K-W, Sohn H, editors., San Diego, California, USA: 2014, p. 906118.

[9] Guo X, Wang L, Jin Z, Lee C. A Multifunctional Hydrogel with Multimodal Self-Powered Sensing Capability and Stable Direct Current Output for Outdoor Plant Monitoring Systems. *Nano-Micro Lett* 2025;17:76.

[10] Koszewnik A, Grześ P, Walendziuk W. Mechanical and electrical impedance matching in a piezoelectric beam for Energy Harvesting. *Eur Phys J Spec Top* 2015;224:2719–31.

[11] Rathod VT. A Review of Electric Impedance Matching Techniques for Piezoelectric Sensors, Actuators and Transducers. *Electronics* 2019;8:169.

[12] Insabella RM, González MG, Acosta EO, Santiago GD. Dielectric antenna effects in integrating line piezoelectric sensors for optoacoustic imaging. *Meas Sci Technol* 2020;31:125103.

41st Danubia-Adria Symposium Advances in Experimental Mechanics
September 23-26, 2025, Kragujevac, Serbia

Original scientific paper DOI: 10.46793/41DAS2025.099P

INFLUENCE OF PALLET PLACEMENT METHOD ON BEAM BEHAVIOR IN RACK STRUCTURE

Mirjana PISKULIC[1], Rodoljub VUJANAC[2], Nenad MILORADOVIC[3], Mirko BLAGOJEVIC[4]

[1] 0009-0005-7199-1280, Faculty of Engineering University of Kragujevac, Sestre Janjic 6, Kragujevac, Serbia, E-mail: mirjana.piskulic@kg.ac.rs

[2] 0000-0002-8215-5668, Faculty of Engineering University of Kragujevac, Sestre Janjic 6, Kragujevac, Serbia, E-mail: vujanac@kg.ac.rs

[3] 0000-0001-6846-6091, Faculty of Engineering University of Kragujevac, Sestre Janjic 6, Kragujevac, Serbia, E-mail: mnenad@kg.ac.rs

[4] 0000-0002-0209-5010, Faculty of Engineering University of Kragujevac, Sestre Janjic 6, Kragujevac, Serbia, E-mail: mirkob@kg.ac.rs

1. Introduction

Selective pallet racks represent a key factor of modern warehouses. The geometry of the structure and the way of load distribution significantly influence the system's mechanical stability. Choosing the right racking structure and its mode of utilization is one of the first things to do in order to properly design the warehouse, making it functional and well organized. Storage systems are a major capital investment whose value depends on the design and how they fit into warehouses and processes, which can also affect the business.

Given the characteristics of pallet racks, typically built from cold-formed thin-walled steel sections, traditional welded or bolted joints are frequently replaced with semi-rigid, boltless connections that enhance assembly efficiency and save costs while keeping structural performance. Accordingly, adjustable storage systems are defined by European standards, such as Eurocode 3 [1]. As the moment-rotation characteristic is essential in describing connection behavior, research on beam-to-column connections has expanded significantly over recent decades, especially in the area of pallet racks [2]. To better understand the strength and behavior under variable loading, various studies, such as [3], have conducted experimental testing of boltless beam-to-column connections to better understand the limit states. In racking structures, placement of unit loads, whether it's transversal or longitudinal against racks, could have a direct influence on structural performance. This paper aims to analyze the effect of beam behavior for various placement methods, relying on the finite element method.

Numerical analysis of beam-to-column connections is used as a reliable tool and as an alternative to experiments in the design of rack structures. In [4] a detailed finite element model was developed for beam-to-column connection, validated through experiment, which simulates moment-rotation behavior without the need for expensive experiments. The stability of semi-rigid connections in racking systems was analyzed in [5], to demonstrate advantages of direct analysis method compared to traditional calculation methods.

Building upon prior research and integrating techno-economic analysis, this paper investigates how the placement method affects beam behavior in pallet rack structures through Finite Element Method (FEM) analysis in Autodesk Inventor software [6]. Future research should extend contact modeling and boundary conditions to enable a more robust validation and strengthen the reliability of the proposed design recommendations.

2. Techno-economic evaluation

One of the initial steps in designing a warehouse to be functional and well organized is to select the appropriate elements of the racking structure and ensure its optimal utilization. A comparative analysis will be performed depending on the method of unit load placement. Therefore, the design of warehouse with transverse and longitudinal placement will be considered. The design parameters include a storage space with dimensions: length 34500 mm x width 28500 mm x height 7500 mm, entry-exit zones oriented at the same level and on opposite sides, intended for storing unit loads in the form of loaded standard EURO pallets with dimensions: length 1200 mm x

width 800 mm x height 1200 mm and a weight of 1000 daN. An electric forklift with a side lift is used as a mean of transport and handling equipment, which determines the loading mode and access configuration for unit loads in each compartment.

According to [7], the techno-economic analysis was conducted based on available input data including space limitations, type of unit load and handling procedure. Analysis considered two different ways of placement with the same beam length: transversal and longitudinal.

With transversal placement, shown in Fig. 1 a), the weaker profile labeled as S80M was selected for the column and the profile labeled as R120L for the beam from [7], with two unit loads placed within a single compartment. The achieved total number of pallet units (capacity) is 1750, with the total mass of the rack structure approximately 37000 kg.

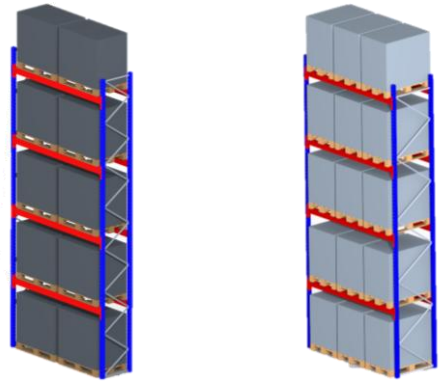

a) b)

Fig. 1. Placement method: a) transversal, b) longitudinal [6]

Conversely, with longitudinal placement shown in Figure 1 b), the stronger profile labeled as S80MH was chosen for the column and the profile labeled as R140L for the beam, with three unit loads per compartment. The achieved capacity is 2100 unit loads, with an overall structure mass of app. 28500 kg. Evaluated factors for further analysis are:

- number of unit loads per compartment,
- loads distribution along the beams,
- mass of the rack structure and
- cost of the structure obtained by its mass.

It was determined that longitudinal placement results in better capacity, lower overall structure mass, more rational material consumption and lower costs in the same available space, by the same transport equipment and equal beam span. Having identified longitudinal placement as the techno-economically optimal solution, the numerical analysis explores whether this choice also yields structural advantages by examining beam deformation and field of stress under varying placement methods. This closes the loop between practical application and structural behavior, ensuring comprehensive validation of the design decision.

3. Methodology of numerical analysis

To complement the techno-economic evaluation, the structural efficiency of selective pallet racks was assessed by beam deformation and stress analysis under different unit load placements through FEM analysis. Table 1 summarizes the key parameters for this analysis.

Table 1. Key parameters for placement methods

Type	Placement method	
	Transversal	**Longitudinal**
Column profile	S80M	S80MH
Beam profile	R120L	R140L
Material	S350GD UNI EN 10346	
Unit loads per compartment	2	3
Load per unit [daN]	1000	
Beam span [mm]	2700	

FEM enables parametric variation of design configurations to assess structural behavior under varying conditions and proper early-stage design development. The finite element mesh generation for both placement methods show a similar number of nodes and elements. That indicates similar discretization needs depending on the direction of load distribution and the shape of contact zones. These set the basis for understanding the results of stress and strain analysis.

Based on data obtained through techno-economic analysis, a solution with longitudinal placement was chosen as the optimal one, with higher capacity and lower overall mass and therefore, lower cost. A comparative study of this data with results obtained through FEM analysis will be performed to verify the solution in terms of carrying capacity.

3.1 Results obtained through FEM analysis

Analysis of beam deformation and stress was realized for a single compartment, i.e., two columns connected by a beam at a defined distance. Due to the limitations in finite element mesh generation caused by the complex geometry of their elements, the analysis was performed as a simplified in-plane frame model to ensure simulation reliability and efficient data processing. Boundaries were defined as fixed for the column bases and frictionless for the internal sides connecting the beam with the column

via the beam end connector. The frictionless option is applied to prevent movement in the plane normal to the face where the contact is made.

The entire surface contact between the bottom deck of the EURO pallet and the upper surface of the beam, caused by the transverse placement method, results in a load that is approximated as a uniform pressure of 0,0741 MPa. The deformed model for this method, obtained through FEM analysis, is shown in Figures 2 and 3, respectively.

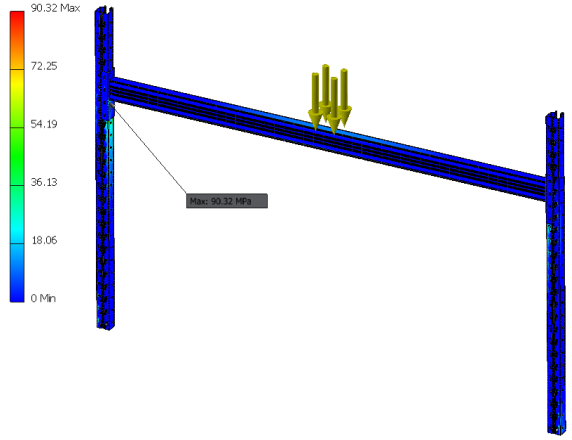

Fig. 2. Von Mises stress for transversal placement

Based on these results, it can be concluded that for transversal placement, as in Fig. 2 and Table 2, the maximum value of the von Mises stress is 90,32 MPa, which is below the maximum yield strength of 350 MPa, indicating that the value is within the elastic limits.

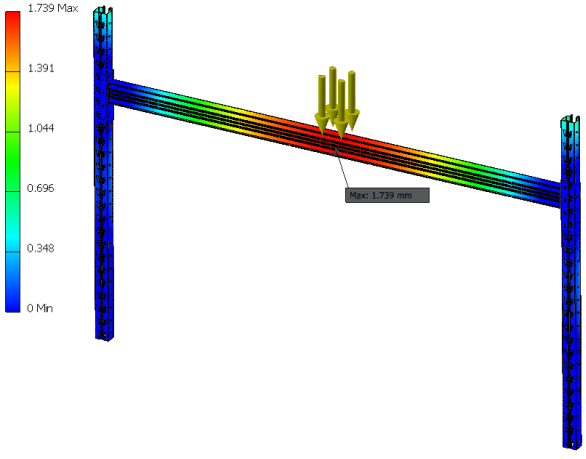

Fig. 3. Beam displacement for transversal placement

A displacement of 1,739 mm, as in Fig. 3, is a beam deformation that does not compromise functionality and is lower than the limit value of 6 mm for the beam profile R120L [7].

The smaller contact between the bottom deck of the EURO pallet and the upper surface of the beam in the longitudinal placement method results in a contact point at the appropriate distance. The beam load is considered as a force of 166,67 daN at each contact point where the bottom deck contacts the beam.

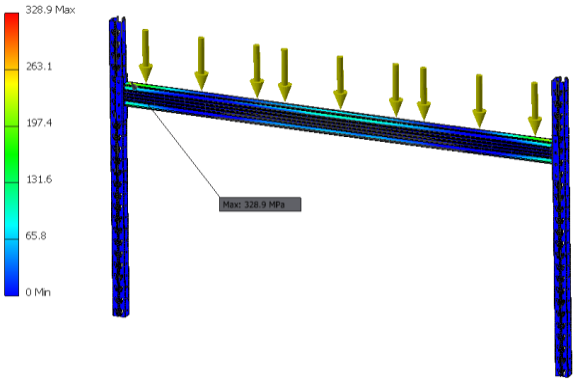

Fig. 4. Von Mises stress for longitudinal placement

The point contact on the beam results in higher stress values, as shown in Fig. 4. The von Mises stress reaches a maximum value of 328,9 MPa but remains below the maximum yield strength of 350 MPa. This indicates the value is still within safe limits, even though the applied load is the maximum load defined for this type of beam.

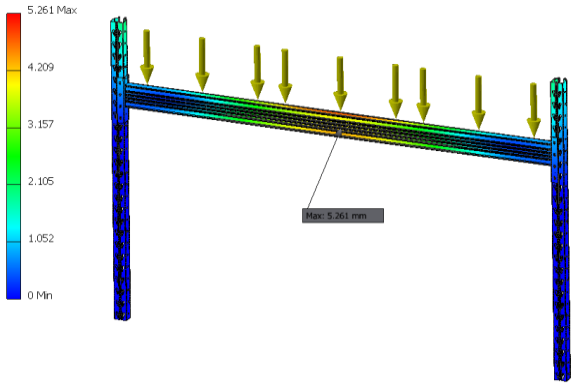

Fig. 5. Displacement for longitudinal placement

Although significantly larger than the transversal placement method, the displacement of 5,261 mm, shown in Fig. 5, does not affect the performance of the structure and it is lower than the limit value of 11 mm for the beam profile R140L [7]. Table 2 summarizes the results obtained through this comparative analysis.

Table 2. Key results obtained in the analysis

Type	Type of placement	
	transversal	**longitudinal**
Storage capacity [unit load]	1750	2100
Overall mass [kg]	~37000	~28500
Von Mises stress [MPa]	90,32	328,9
Displacement [mm]	1,739	5,261

3.2 Discussion of numerical approach

Since the bracing system in the cross-aisle direction, the opposite side of rack, as well as cross supports for transversal placement, were not taken into account due to the complexity of mesh generation, it is assumed that values would be lower than those obtained if other influential parameters were considered. That affects the maximum value of von Mises stress. Although the results remain within the yield strength, they confirm structural strength under the applied load for transversal placement. For the longitudinal one, significantly high stress values are affected as a result of the idealized contact model, which does not enable such a realistic load distribution. It results in higher deformation, which may be due to local geometric requirements along the support direction, as well as specific load distributions. These differences have a direct impact on the numerical results.

The absence of aforementioned imperfections makes current results slightly conservative, though still within acceptable limits. Despite the valuable insights provided by FEM and techno-economic analysis, it is important to acknowledge that current numerical models involve several simplifications:

- cross support beams are not included, although they are basic elements of transversal placement;
- some contacts are defined as bonded;
- as the static analysis was considered, the absence of other loads and conditions limits the accuracy of the obtained results.

To refine predictive modeling and the practical applicability of the obtained results, the following directions are proposed:

- integration of additional elements to better reflect load distribution and stiffness in racks;
- inclusion of other contact definitions, as sliding or friction, especially in the connection zones;
- expansion of load cases, to cover those not included, which would allow for a more robust validation of the preferred design solution.

4. Conclusions

The integration of techno-economic and numerical analysis confirmed that the placement method is represented as a key parameter in planning the utilization of available space, as well as carrying capacity. The longitudinal placement method represents the optimal solution built on advantages based on storage capacity and reduced mass, thereby enhancing economic and spatial utilization of available space. Additionally, this variant generates higher von Mises stress values and vertical deformations.

Although the transversal placement method exhibits slightly greater mechanical stability under the applied load, its capacity and overall mass do not reach the performance of longitudinal placement. On the contrary, results with significantly lower stress and displacement require heavier construction and its mass, which has a negative influence on the economic efficiency of the system.

Results indicate the need for careful balance between economic requirements and structural reliability. Depending on the project priority, whether it is the maximum capacity, lower mass or reduced deformation and stress, placement method must be strategically aligned with safety and long-term requirements. Although simplified models do not include all structural components, for both configurations beam deformation and Von Mises stress are within the permitted limits. Future research should focus on refining joint behavior, expanding connection modeling and incorporating other loads, to bring the model further to operating conditions and strengthen numerical validation.

References

1. Eurocode 3: EN 1993-1-1: 2005 Design of Steel Structures, Part 1-1: General Rules and Rules for Buildings, Part 1-3: General Rules—Supplementary Rules for Cold Formed Thin Gauge Members and Sheeting, Part 1-8: Design of Joints; European Union: Brussels, Belgium, **2005**.
2. EN 15512 Steel Static Storage Systems-Adjustable Pallet Racking Systems-Principles for Structural Design; CEN European Committee for Standardization, Brussels, **2009**.
3. Król, P.A.; Papadopoulos-Woźniak, M.; Wójt, J. Experimental Investigation on Shear Strength of Hooking-Type Beam-to-Column Joints, Applied in One of High Storage Pallet Racking Systems. Procedia Engineering **2014**, 91, 232–237, doi:10.1016/j.proeng.2014.12.052.
4. Vujanac, R.; Vulovic, S.; Disic, A.; Miloradovic, N. Numerical Analysis of Beam-to-Column Connection of Pallet Racks. IOP Conf. Ser.: Mater. Sci. Eng. **2018**, 393, 012009, doi:10.1088/1757-899X/393/1/012009.
5. Branquinho, M.A. Stability Analysis of Unbraced Steel Storage Racks: Discussions an Alternatives.
6. Autodesk Inventor 2025.
7. Vujanac, R.; Miloradovic, N. Fundamentals of storage and transportation systems; 1st ed.; Faculty of Engineering University of Kragujevac, Serbia: Kragujevac, 2023; ISBN 978-86-6335-102-8.

41st Danubia-Adria Symposium Advances in Experimental Mechanics
September 23-26, 2025, Kragujevac, Serbia

Original scientific paper

DOI: 10.46793/41DAS2025.103J

ANALYTICAL AND FEM ASSESSMENT OF A DOUBLE-SIDED BUTT-WELDED S1000QL SPECIMEN FOR TENSILE TESTING PREPARATION

Snežana JOKSIĆ[1], Jovana ŽIVIĆ[2], Marija MATEJIĆ[3], Miloš MATEJIĆ[4], Živče ŠARKOĆEVIĆ[5], Ivica ČAMAGIĆ[6]

[1] 0009-0002-1909-2462, University of Pristina, Faculty of Technical Sciences with temporary settlement in Kosovska Mitrovica, Knjaza Miloša 7, Kosovska Mitrovica, Republic of Serbia, E-mail: snezana.joksic@pr.ac.rs;

[2] 0000-0003-1936-7921, University of Pristina, Faculty of Technical Sciences with temporary settlement in Kosovska Mitrovica, Knjaza Miloša 7, Kosovska Mitrovica, Republic of Serbia, E-mail: jovana.d.zivic@pr.ac.rs;

[3] 0000-0002-0580-1718, University of Pristina, Faculty of Technical Sciences with temporary settlement in Kosovska Mitrovica, Knjaza Miloša 7, Kosovska Mitrovica, Republic of Serbia, E-mail: marija.matejic@pr.ac.rs;

[4] 0000-0003-0488-0992, University of Kragujevac, Faculty of Engineering, Sestre Janjić 6, Kragujevac, Republic of Serbia, E-mail: mmatejic@kg.ac.rs,

[5] 0000-0001-5110-6620, University of Pristina, Faculty of Technical Sciences with temporary settlement in Kosovska Mitrovica, Knjaza Miloša 7, Kosovska Mitrovica, Republic of Serbia, E-mail: zivce.sarkocevic@pr.ac.rs;

[6] 0000-0003-4706-6333, University of Pristina, Faculty of Technical Sciences with temporary settlement in Kosovska Mitrovica, Knjaza Miloša 7, Kosovska Mitrovica, Republic of Serbia, E-mail: ivica.camagic@pr.ac.rs

1. Introduction

High-strength quenched and tempered steels, such as S1000QL, are increasingly employed in applications where a high strength-to-weight ratio is essential, including heavy-duty structural components, transport equipment, and machinery subject to demanding service conditions. The combination of high tensile strength and relatively low weight offers significant design advantages. However, these benefits can only be fully realized if welded joints maintain comparable structural integrity and if testing protocols are robust enough to capture the actual mechanical performance. Achieving this requires a comprehensive approach that combines analytical calculations and numerical simulations, particularly finite element method (FEM) analyses, to predict and validate stress distributions, deformations, and potential failure mechanisms.

Numerous studies have addressed various aspects of thermal cycles, residual stresses, welding distortions, and fracture behavior in welded structures. While these works often focus on different materials, joint configurations, or manufacturing processes, their findings contribute valuable insights into the modeling and experimental validation of welded joints. Attarha and Sattari-Far [1] investigated the temperature distribution in thin welded plates using a combination of experimental measurements and finite element simulations. Their study demonstrated a high level of agreement between numerical predictions and measured data, establishing a reliable foundation for analyzing thermal behavior in welded structures. This approach is directly relevant to the present study, where thermal effects and resulting stresses in high-strength steels are of key interest. Derakhshan et al. [2] conducted numerical simulations and experimental validation to assess residual stresses and welding distortions in laser-based welding of thin structural steel plates in a butt joint configuration. Their results confirmed that the finite element model accurately predicted both residual stress distributions and distortion patterns. These findings emphasize the importance of coupling simulation with experimental verification, a principle also adopted in the current work. Syahroni and Purbawanto Hidayat [3] performed a three-dimensional finite element simulation of T-joint fillet welds to evaluate the influence of welding sequences on residual stresses and distortions. They concluded that the welding sequence plays a critical role in determining the magnitude and spatial distribution of residual stresses, as well as the final distortion of the joint. This insight highlights the

need for careful process planning in welding high-strength steels to minimize deformation and preserve dimensional accuracy. Dhage et al. [4] demonstrated that process parameters significantly influence final properties, a methodology applicable to welding, where such parameters determine joint integrity and service life. Kik and Górka [5] used simulations of laser and hybrid welding of S700MC steel T-joints to compare thermal cycles and stress distributions, offering insights useful for selecting optimal welding techniques for high-strength steels like S1000QL, where heat input control is critical for preserving microstructure. Stavropoulou et al. [6] carried out experimental and numerical studies on the mechanical cutting of Dionysos marble. Although the material and process differ significantly from steel welding, the study illustrates the broader applicability of combining experiments with numerical modeling to understand material removal and deformation mechanisms. Cui et al. [7] analyzed 2205 duplex stainless steel K-TIG welded joints using both simulations and experimental tests. Their results showed strong agreement between predicted and measured thermal and mechanical responses, reinforcing the necessity of cross-validation between numerical and experimental approaches—a methodology closely followed in the present work. Tanaka et al. [8] focused on crack propagation in welded joint structures, applying numerical simulation to study surface crack behavior. Their findings provided a deeper understanding of crack growth mechanisms, offering a foundation for improving the structural integrity and service life of welded components. This knowledge is particularly relevant for high-strength steels, where localized defects can rapidly compromise performance. Collectively, these studies demonstrate different numerical and experimental approaches available for analyzing welded joints.

In the present study, a double-sided butt-weld specimen representative of upcoming tensile tests was analyzed. The work began with an analytical weld calculation to estimate stress distributions and structural capacity. This was followed by a static finite element analysis to cross-validate stress and displacement predictions, thereby guiding specimen preparation and loading conditions. The combined analytical and numerical assessment aims to provide a reliable foundation for interpreting experimental test results, optimizing welding parameters, and ensuring that the mechanical performance of S1000QL welded joints meets the demands of high-strength structural applications.

2. Materials and Methods

2.1 Material

The base material considered in this study is 1000QL type high-strength steel. This high-strength steel is selected for applications requiring an exceptional strength-to-weight ratio combined with good toughness. For the purposes of the analytical weld calculation, a yield strength (R_{eH}) of 1050 MPa and an ultimate tensile strength (R_m) of 1100 MPa were adopted, values consistent with datasheet specifications for S1000QL.

2.2 Specimen Geometry

The tensile test specimen was designed with a rectangular cross-section measuring 15 × 20 mm. The joint configuration is a double-sided butt weld with a K-groove preparation, incorporating a 4 mm root gap between the flat surface on one side and the opposing K-prep tip on the other. The loaded length considered for the analytical calculation was 20 mm, corresponding to the net section under tensile loading. The model of the specimen is shown in Fig. 1.

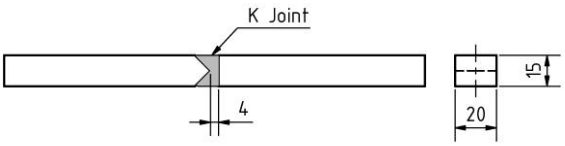

Fig. 1. Specimen dimensions

2.3 Analytical Weld Calculation

A comparative-stresses method was employed to assess the weld's capacity. The calculation assumed an axial force F_z = 128 kN. Under these loading conditions, the allowable stress was determined as σ_A = 505 MPa, the weld normal stress as σ = 426.667 MPa, and the reference stress as σ_S = 501.961 MPa. The verification check indicated that the weld design satisfies both static and fatigue loading criteria under the specified duty cycle (n_c = 2.622).

2.4 Finite Element Analysis (FEA)

A static finite element analysis was conducted using Autodesk Inventor Professional 2019 to evaluate the weld behavior. The weld interfaces were modeled with bonded contact conditions to ensure full load transfer across the joint. The mesh featured an average element size of 0.2 relative to the model dimensions, a minimum size of 0.3 of the average, and a grading factor of 2, without curved elements, providing an optimal balance between computational accuracy and efficiency. Boundary

conditions included a fixed constraint at one end of the specimen and an applied axial force of 128 kN at the opposite end.

3. Results

The results of the analytical calculation and the finite element analysis (FEA) are summarized in Table 1. The analytical method yielded a calculated weld normal stress of σ = 426.667 MPa, with a reference stress of σ_S = 501.961 MPa. The static FEA predicted a maximum von-Mises equivalent stress of 432.570 MPa in the weld region. The close agreement between the analytical and numerical values (difference < 1.5%) indicates that the simplified comparative-stresses approach provides a reliable estimation of the stress state under the given loading.

Table 1. Summary of analytical and numerical results

Name	Value	Unit
Stress (analytical σ)	426.667	MPa
Reference stress (σ_S)	501.961	MPa
Von Mises (FEA)	432.570	MPa
Max displacement (FEA)	0.434	mm

Fig. 2 presents a direct comparison between the analytical stress result and the FEA-derived von Mises stress, illustrating their close correlation.

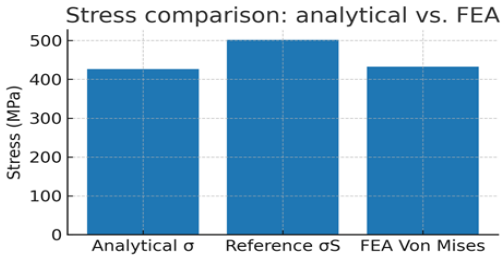

Fig. 2. Stress comparison between analytical results and FEA (von Mises)

The von Mises stress distribution obtained from the axial loading simulation is shown in Fig. 3.

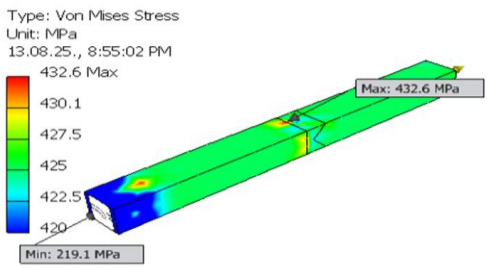

Fig. 3. Von Mises stress under axial loading

In addition to the stress distribution, the FEA predicted a maximum displacement of 0.434 mm at the free end of the specimen (Fig. 4). The corresponding minimum safety factor was also obtained from the simulation, indicating that the modeled weld joint remains within safe limits under the applied axial load of 128 kN.

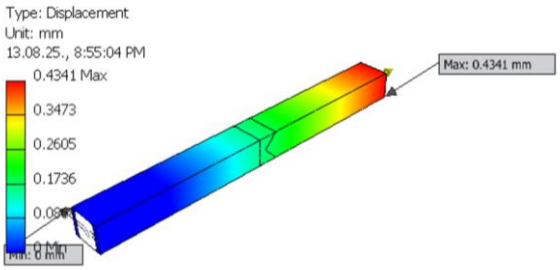

Fig. 4. Maximum displacement of 0.434 mm at the free end of the specimen

4. Results discussion

Analytical predictions and finite element (FEA) results demonstrate a high degree of agreement. The analytical weld normal stress (σ = 427 MPa) and reference stress (σ_S = 502 MPa) closely match the maximum von-Mises stress of 433 MPa obtained from the FEA simulation under an axial load of 128 kN. This close correlation confirms that the comparative-stresses method provides a reliable estimation of the stress distribution in the joint for the given geometry and loading conditions.

The FEA analysis predicts a maximum displacement of 0.434 mm, consistent with the expected stiffness of a double-sided butt weld specimen with a 15 × 20 mm cross-section. The safety factor distribution ranges from 0.64 to 1.26, with the default high-strength low-alloy (HSLA) steel material (R_{eH} = 276 MPa) applied in the simulation. Updating the FEA material parameters to reflect the actual yield strength of S1000QL (R_{eH} = 1050 MPa) is expected to proportionally increase the safety factor, maintaining values above unity throughout the joint under the applied static load.

Fatigue assessment further confirms the joint's adequacy, with a calculated cycle ratio of n_c = 2.622 for the specified pulsating load range (8–15 kN), which is significantly below the static test load. This indicates that the joint configuration satisfies the requirements for both static and cyclic loading within the designed operating range.

These results support proceeding with the planned tensile testing of straight specimens. The selected geometry and weld length are considered sufficient to represent the mechanical behavior,

while the close agreement between analytical and FEA results enhances confidence in the chosen loading protocol. Prior to experimental validation, it is recommended to:

- update FEA material properties to those of S1000QL,
- perform a mesh-sensitivity study at the weld toe and root to refine local stress predictions, and
- extend the FEA model to include elastoplastic material behavior for a more comprehensive structural assessment.

5. Conclusions

A combined analytical and finite element analysis (FEA) of a double-sided butt-welded S1000QL tensile specimen under a 128 kN axial load showed close agreement between analytical and numerical results, confirming the reliability of the simplified comparative-stresses method for preliminary strength evaluation in high-strength steels. The specimen geometry and weld configuration were found suitable for the planned tensile testing.

For improved simulation accuracy, it is recommended to update FEA material properties to S1000QL values, perform mesh-sensitivity studies at the weld toe and root, and incorporate elastoplastic material behavior. These refinements will enhance correlation between simulations and experimental results, enabling precise characterization of S1000QL welded joints and ensuring that the findings are applicable to real-world engineering applications.

Further research should focus on expanding the numerical model to include the effects of different welding technologies, variations in groove geometry, and actual heat input parameters. Special attention should be given to modeling the fatigue behavior of the joint under variable loading, as well as comparing the results with experimental data obtained from a larger number of specimens.

References

[1] Attarha, M.J.; Sattari-Far, I. Study on welding temperature distribution in thin welded plates through experimental measurements and finite element simulation. *J. Mater. Process. Technol*. 2011, 211(4), 688–694. doi:10.1016/j.jmatprotec.2010.12.003

[2] Derakhshan, E.D.; Yazdian, N.; Craft, B.; Smith, S.; Kovacevic, R. Numerical simulation and experimental validation of residual stress and welding distortion induced by laser-based welding processes of thin structural steel plates in butt joint configuration. *Opt. Laser Technol*. 2018, 104, 170–182. doi:10.1016/j.optlastec.2018.02.026

[3] Syahroni, N.; Purbawanto Hidayat, M.I. 3D Finite Element Simulation of T-Joint Fillet Weld: Effect of Various Welding Sequences on the Residual Stresses and Distortions. Numerical Simulation—*From Theory to Industry*, 2012. doi:10.5772/50015

[4] Dhage, G.S.; Pawar, R.; Patil, J. Experimental Studies On Surface Roughness of Spur Gear. REST *Journal of Emerging trends in Modelling and Manufacturing*. 2024, 10(4), 1–9. doi:10.46632/jemm/10/4/1

[5] Kik, T.; Górka, J. Numerical simulations of laser and hybrid S700MC T-joint welding. *Materials*. 2019, 12(3), 516. doi:10.3390/ma12030516

[6] Stavropoulou, M.; Giannakopoulos, K.; Exadaktylos, G. Experimental and numerical study of mechanical cutting of Dionysos marble. *7th National Congress on Mechanics,* 2004, 236–245.

[7] Cui, S.; Pang, S.; Pang, D.; Zhang, Q.; Zhang, Z. Numerical simulation and experimental investigation on 2205 duplex stainless steel K-TIG welded joint. *Metals*. 2021, 11(8), 1328. doi:10.3390/met11081323

[8] Tanaka, S.; Kawahara, T.; Okada, H. Study on crack propagation simulation of surface crack in welded joint structure. *Marine Structures.* 2014, 39, 315–334. doi:10.1016/j.marstruc.2014.08.001.

Original scientific paper DOI: 10.46793/41DAS2025.107P

QUASI-STATIC TENSILE TESTING OF HIGH-STRENGTH BALLISTIC STEEL USING DIGITAL IMAGE CORRELATION – PRELIMINARY STUDY

Miloš PEŠIĆ[1], Aleksandar BODIĆ[2], Marko TOPALOVIĆ[3], Snežana VULOVIĆ[4], Vladimir DUNIĆ[5], Vladimir MILOVANOVIĆ[6], Miroslav ŽIVKOVIĆ[7]

[1] 0000-0002-3405-5216, Institute for Information Technologies, Jovana Cvijića bb, Kragujevac, Serbia, E-mail: milospesic@uni.kg.ac.rs

[2] 0000-0002-1713-6540, Faculty of Engineering, Sestre Janjić 6, Kragujevac, Serbia, E-mail: abodic@uni.kg.ac.rs

[3] 0000-0001-6101-755X, Institute for Information Technologies, Jovana Cvijića bb, Kragujevac, Serbia, E-mail: topalovic@kg.ac.rs

[4] 0000-0001-5784-0906, Institute for Information Technologies, Jovana Cvijića bb, Kragujevac, Serbia, E-mail: vsneza@kg.ac.rs

[5] 0000-0003-1648-1745, Faculty of Engineering, Sestre Janjić 6, Kragujevac, Serbia, E-mail: dunic@kg.ac.rs

[6] 0000-0003-3071-4728, Faculty of Engineering, Sestre Janjić 6, Kragujevac, Serbia, E-mail: vladicka@kg.ac.rs

[7] 0000-0002-0752-6289, Faculty of Engineering, Sestre Janjić 6, Kragujevac, Serbia, E-mail: miroslav.zivkovic@kg.ac.rs

1. Introduction

High-strength ballistic steels are widely used in protective structures, military vehicles, and safety equipment due to their superior strength, hardness, and energy absorption capabilities, which are essential for resisting high-velocity impacts and ensuring structural integrity [1]. While their primary application is in high-strain-rate conditions, understanding their quasi-static behavior is equally important, as it provides baseline mechanical properties for material modeling and structural performance predictions.

The mechanical response of high-strength steels is strongly influenced by factors such as microstructure, chemical composition, and strain rate. Investigations of strain localization phenomena under varying loading conditions have shown that these materials can exhibit complex deformation patterns, particularly when subjected to dynamic or quasi-static tensile loads [2].

In recent years, full-field optical measurement techniques, particularly Digital Image Correlation (DIC), have gained prominence in the characterization of metallic materials. DIC enables non-contact, high-resolution mapping of strain fields over the specimen surface, allowing for a more detailed understanding of deformation mechanisms compared to traditional measurement methods. A comprehensive review of DIC applications in laboratory structural tests confirms its versatility in evaluating mechanical behavior and identifying strain localization zones [3].

This study presents quasi-static tensile testing of a high-strength ballistic steel specimen with full-field strain measurements obtained using a Digital Image Correlation (DIC) system. The objective is to determine the material's key mechanical properties, visualize strain distribution during deformation, and provide experimental data suitable for validation of future numerical simulations.

2. Materials and Methods

The material is S1100QL, a quenched and tempered high-strength steel commonly used in protective/ballistic applications. It has a low-carbon alloyed composition with Cr–Mo–Ni additions, exhibiting typical room-temperature properties of approximately 1.1 GPa yield strength and 1.25–1.55 GPa ultimate tensile strength.

Axisymmetric threaded tensile specimens were machined from plate stock. The gauge was lightly polished, then coated with a matte white base and a fine black speckle for DIC, as shown in Fig. 1.

Fig. 1. Threaded tensile specimen (S1100QL) with DIC speckle applied to the gauge.

Tensile tests were performed on a universal Instron machine in displacement control at 0.001 mm/min, under laboratory conditions. Force and crosshead displacement were acquired and synchronized with imaging. At least five repeats were conducted to check repeatability.

Full-field strain was measured with MatchID using a monochrome industrial camera and macro lens with symmetric continuous LED lighting. DIC settings (subset/step) were kept constant across all tests and chosen according to speckle size.

Axial engineering strain was obtained from a virtual extensometer along the gauge; engineering stress was computed from the measured force and initial area. Yield strength was determined by the 0.2% offset method; localization and necking were assessed from DIC major-strain maps.

3. Experimental setup

Universal testing machine. Quasi-static tensile tests were performed on a universal Instron frame in displacement control at a very low crosshead rate (0.001 mm/min). Axial force was measured by the machine load cell; crosshead motion was used only for control.

Specimen mounting. Axisymmetric threaded specimens were gripped coaxially. A small seating load was applied before recording to remove slack and ensure alignment. The gauge section was lightly polished and prepared for optical measurements.

Digital Image Correlation (DIC). Full-field strain was measured with a MatchID system using a monochrome industrial camera and a macro lens. Four continuous LED lights were arranged symmetrically around the gauge to provide uniform, shadow-free illumination and minimize glare, as shown in Fig.2. The gauge was coated with a matte white base and a fine black speckle. Calibration was performed before testing; correlation parameters were kept constant across repeats. Axial strain for the stress–strain curves was obtained from a virtual extensometer along the gauge.

Fig.2. DIC arrangement with four continuous LED lights providing symmetric illumination of the gauge region – left; magnified - right

Synchronization and reduction. Force and images were time-aligned through the acquisition software. Engineering stress was computed from the measured force and initial cross-sectional area; the 0.2% offset method was used for yield strength. Localization and necking were assessed from DIC major-strain maps.

4. Results and Discussion

4.1 Quasi-static stress–strain response

The S1100QL exhibits a steep elastic segment followed by a short uniform-plastic regime and a pronounced post-UTS softening due to necking (Fig. 3). Five repeats overlap closely in the elastic and early plastic range, indicating stable alignment and repeatable measurement. Scatter around the peak stress is modest, and all curves show a similar transition to localization with substantial post-necking ductility. The strength levels and overall curve shape are consistent with the expected behavior of quenched-and-tempered high-strength steels tested at very low rates.

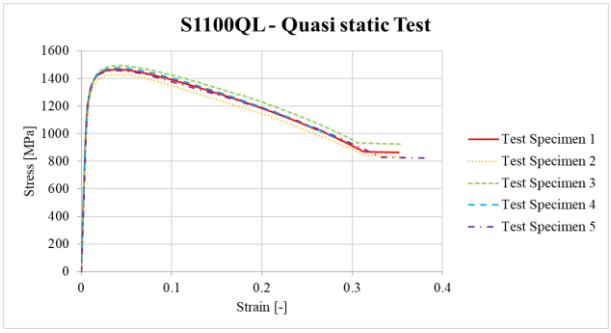

Fig. 3. Quasi-static engineering stress–strain curves for S1100QL

Fig. 3 shows the engineering stress–strain curves for S1100QL from five quasi-static tests. Strain was obtained with a DIC virtual extensometer in the

gauge, and the curves are marked at the 0.2% proof stress, the UTS, and the onset of localization.

4.2 Full-field strain evolution (DIC)

DIC maps confirm a clear progression from homogeneous straining to a sharply confined neck (Fig. 4). At the start of loading, the field is essentially uniform. With the onset of plasticity, a faint axial band forms at mid-gauge and steadily intensifies. As the curve approaches UTS, this band evolves into a dominant localization zone; strain gradients steepen while the surrounding field remains comparatively low. In the last frame before fracture, the major-strain peak is strongly concentrated within a narrow region, consistent with the observed post-UTS softening on the engineering curve and with pronounced lateral contraction.

Fig. 4 presents the evolution of the DIC major-strain field at four representative instants – start of test, early plasticity (band nucleation), localization growth, and the final pre-fracture frame – plotted with a common color scale and field of view.

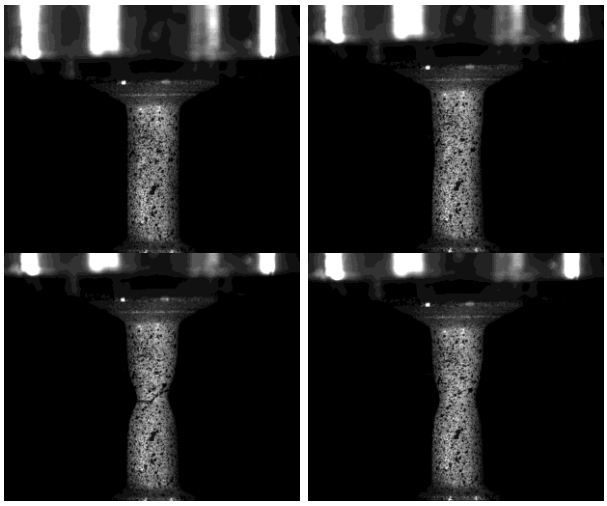

Fig. 4. DIC major-strain fields: baseline → band nucleation → localization growth → fracture (clockwise)

4.3 Necking and fracture appearance

Macroscopic inspection shows a single, centrally located neck with deformation confined to the gauge (Fig. 5). The overall appearance is consistent with ductile tensile failure controlled by localized necking typical of very high-strength Q&T steels.

Fig. 5 presents the fractured S1100QL specimen after a quasi-static test, indicating gauge-confined deformation and a single-neck failure mode.

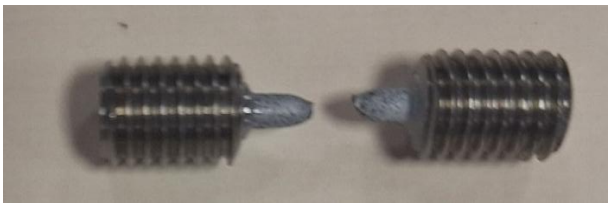

Fig. 5. Fractured S1100QL specimen; single neck centered in the gauge.

4.4 Implications for modeling

For parameter identification, the pre-necking segment of the true stress–strain curve (converted from engineering data using DIC-based strain) can be used, as it represents uniform deformation and yields robust rate-independent parameters. The onset of localization (from DIC) serves as a practical marker separating uniform from post-instability behavior. Because deformation becomes strongly confined after this point, model validation should prioritize field-level comparisons (major-strain maps and axial profiles) rather than relying on global elongation alone.

4.5 Measurement repeatability and uncertainty

Repeat tests show tight overlap in the elastic and early plastic range, and only modest scatter around the peak, indicating that the test alignment, gripping, and optical tracking were stable. Using identical DIC settings across repetitions minimized correlation-parameter bias, while four symmetric LED lights ensured uniform illumination and limited speckle glare. The remaining variability near UTS is consistent with specimen-to-specimen differences in the exact onset and sharpening of localization. Because global elongation can be biased by miniature threaded geometry, field-aware quantities (localization onset and local peak strain) together with classic strengths are emphasized.

4.6 Practical metrics for design and model calibration

For engineering use, three metrics are particularly informative and straightforward to extract from the present dataset:

- 0.2% proof stress – a conservative sizing parameter, directly read from the curves;
- UTS – an upper bound for load-carrying capacity before diffuse instability;
- Localization indicators from DIC – (i) global strain at localization onset, marking the transition from uniform to post-instability behavior, and (ii) the peak local major strain in the last frame, characterizing the severity of the neck.

In constitutive identification, the pre-necking true curve (converted using DIC-based axial strain) supports fitting rate-independent plasticity parameters (e.g., E, σ_y, and an isotropic hardening law K, n). The localization onset provides a practical delimiter for the fitting window, while the final DIC field offers a target for validating strain localization in finite-element simulations (e.g., comparison of major-strain maps and axial profiles rather than global elongation only).

5. Conclusions

Quasi-static tensile tests on S1100QL show a steep elastic response, a short uniform-plastic regime, and a rapid transition to localized necking. Full-field DIC confirmed the evolution from near-homogeneous straining to a single, centrally located neck with strongly confined major-strain just before fracture. Repeat curves overlapped closely, indicating stable alignment and measurement; the resulting strength levels and deformation pattern are consistent with the expected behavior of quenched-and-tempered high-strength steels at a very low rate. For engineering use and constitutive calibration, the pre-necking true stress–strain segment provides a reliable basis for rate-independent parameters, while DIC-based indicators – the global strain at localization onset and the peak local major strain – quantify the onset and severity of localization. These results establish a clean quasi-static baseline for S1100QL and a field-resolved reference for validating numerical simulations.

The present results are limited to very low loading rates and room temperature; as such, they establish a baseline for S1100QL under quasi-static conditions. Future work should pair these data with elevated strain-rate tests (e.g., tensile SHB) and temperature variations to cover the operating envelope used in protective applications. On the analysis side, reporting a work-to-fracture metric (area under the engineering curve up to the last frame) and a DIC-based neck width would add complementary measures of energy absorption and localization severity.

Acknowledgement

This research is partly supported by the Science Fund of the Republic of Serbia, #GRANT No 7475, Prediction of damage evolution in engineering structures – PROMINENT, and by the Ministry of Science, Technological Development and Innovation, Republic of Serbia, Agreement No. 451-03-136/2025-03/200378 and Agreement No. 451-03-137/2025-03/200107.

References

[1] V. Tarigopula, O. S. Hopperstad, M. Langseth, A. H. Clausen, F. Hild. A study of localisation in dual-phase high-strength steels under dynamic loading using digital image correlation and FE analysis. *arXiv preprint*, 2007, arXiv:0712.3921. DOI: 10.48550/arXiv.0712.3921.

[2] A. Weidner. Review on Strain Localization Phenomena Studied by Digital Image Correlation. *Advanced Engineering Materials*, 2021, 23(9), 2001409. DOI: 10.1002/adem.202001409.

[3] M. A. Mousa, M. M. Yussof, T. S. Hussein, L. N. Assi, S. Ghahari. A Digital Image Correlation Technique for Laboratory Structural Tests and Applications: A Systematic Literature Review. *Sensors*, 2023, 23(23), 9362. DOI: 10.3390/s23239362.

Original scientific paper DOI: 10.46793/41DAS2025.111P

QUASI-STATIC AND DYNAMIC BEHAVIOR OF VANADIUM-CARBIDE REINFORCED ALUMINUM ALLOY STUDIED VIA DIGITAL IMAGE CORRELATION – PRELIMINARY STUDY

Miloš PEŠIĆ[1], Aleksandar BODIĆ[2], Marko TOPALOVIĆ[3], Snežana VULOVIĆ[4], Vladimir DUNIĆ[5], Vladimir MILOVANOVIĆ[6], Miroslav ŽIVKOVIĆ[7]

[1] 0000-0002-3405-5216, Institute for Information Technologies, Jovana Cvijića bb, Kragujevac, Serbia, E-mail: milospesic@uni.kg.ac.rs

[2] 0000-0002-1713-6540, Faculty of Engineering, Sestre Janjić 6, Kragujevac, Serbia, E-mail: abodic@uni.kg.ac.rs

[3] 0000-0001-6101-755X, Institute for Information Technologies, Jovana Cvijića bb, Kragujevac, Serbia, E-mail: topalovic@kg.ac.rs

[4] 0000-0001-5784-0906, Institute for Information Technologies, Jovana Cvijića bb, Kragujevac, Serbia, E-mail: vsneza@kg.ac.rs

[5] 0000-0003-1648-1745, Faculty of Engineering, Sestre Janjić 6, Kragujevac, Serbia, E-mail: dunic@kg.ac.rs

[6] 0000-0003-3071-4728, Faculty of Engineering, Sestre Janjić 6, Kragujevac, Serbia, E-mail: vladicka@kg.ac.rs

[7] 0000-0002-0752-6289, Faculty of Engineering, Sestre Janjić 6, Kragujevac, Serbia, E-mail: miroslav.zivkovic@kg.ac.rs

1. Introduction

Vanadium-carbide reinforced aluminum alloys have attracted significant interest in recent years due to their enhanced strength-to-weight ratio, improved fatigue resistance, and refined microstructural stability, making them promising materials for lightweight protective structures and high-performance engineering applications [1, 2, 3]. The addition of vanadium carbide promotes grain refinement and precipitation strengthening, which can substantially improve mechanical performance under different loading regimes.

The mechanical response of aluminum alloys is strongly dependent on the strain rate, with dynamic loading often leading to increased flow stress and reduced ductility compared to quasi-static conditions [4]. Investigations of aluminum alloys such as 6005A-T6 and 5083 have shown that these materials exhibit notable strain rate sensitivity, which must be taken into account in structural design and numerical modeling.

Full-field optical measurement techniques, particularly Digital Image Correlation (DIC), have become indispensable in characterizing strain localization and deformation behavior in both quasi-static and high-strain-rate testing. Ultra-high-speed DIC has been successfully applied to capture deformation fields during impact events such as Taylor impact tests, providing detailed insight into localized plasticity and failure mechanisms [2, 3]. Moreover, DIC has been extensively used to assess the formability of aluminum alloys and to study crack initiation and propagation under various loading conditions, offering valuable data for fracture mechanics and forming limit analyses [5].

In this study, quasi-static and dynamic tensile testing of a vanadium-carbide reinforced aluminum alloy is presented, with full-field strain measurements obtained using Digital Image Correlation. The objective is to evaluate the influence of strain rate on mechanical behavior, visualize strain distribution during deformation, and provide experimental data for the future validation of computational models.

2. Materials and Methods

An Al–VC surface-reinforced layer was produced by laser surface alloying. Commercial VC powder was uniformly spread on an aluminum plate, and the surface was scanned in multiple laser passes, melting the Al surface and mixing VC into the melt pool. Alternating scan directions promoted homogenization; inert shielding and gentle post-cleaning removed loose residue.

Tensile flat dog-bone specimens were extracted so that the laser-alloyed zone spans the gauge. The same specimen design was used in both quasi-static and dynamic tests to enable direct rate comparisons. Surfaces in the gauge were lightly finished and coated with a matte white base plus a fine black speckle for DIC, as shown in Fig.1.

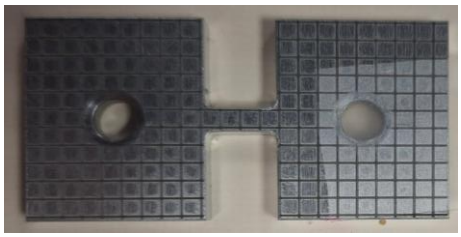

Fig. 1. Flat dog-bone tensile specimen with central neck prepared for testing; DIC grid applied over the gauge region

Quasi-static tensile tests were conducted on a universal Instron machine in displacement control at 0.001 mm/min under laboratory conditions. Force and crosshead displacement were recorded and time-aligned with imaging. Five tests were conducted to check repeatability.

Dynamic tensile tests were performed on a tensile SHB configuration targeting an average strain rate of ~ 1000 s^{-1}. Incident, reflected, and transmitted bar strains were measured with axial gauges and reduced using standard one-dimensional elastic-wave analysis. Stress equilibrium was verified by comparing $\sigma_{inc} + \sigma_{ref}$ with σ_{trans} over the analysis window.

Full-field strain was measured with MatchID software.

- QS: monochrome industrial camera with a macro lens and symmetric continuous LED lighting.
- SHB: high-speed camera with short exposure, hardware-synchronized to the SHB DAQ.

Calibration and correlation parameters (subset/step) were kept consistent within each regime and chosen based on speckle size. Axial strain was obtained from a virtual extensometer in the gauge.

For QS, engineering stress–strain curves were built from measured force and initial area with DIC-based axial strain; the yield strength was determined by the 0.2% offset method. For SHB, true stress–strain was derived from bar signals. Strain-rate sensitivity was quantified by comparing flow stress at matched plastic strain levels; DIC major-strain maps supported the discussion of localization and failure mode.

3. Experimental setup

Material fabrication. The Al–VC surface-reinforced layer was produced by laser surface alloying: VC powder was uniformly spread on an Al plate, then multiple laser passes melted the surface and mixed VC into the melt pool, forming a continuous composite layer upon solidification. Cross-sections were prepared separately to confirm layer continuity and thickness.

Specimens and fixtures (common to both regimes). Flat dog-bone specimens were extracted so that the laser-alloyed zone spans the gauge. Custom pin-loaded fixtures engaged the holes to avoid grip-induced damage and to ensure repeatable alignment. Gauge surfaces were finished and speckled for DIC.

Quasi-static tensile setup. Tests were run on a universal Instron frame in displacement control (0.001 mm/min) under laboratory conditions, as shown in Fig.2. Force and crosshead displacement were recorded and time-aligned with imaging; duplicate tests were performed to check consistency.

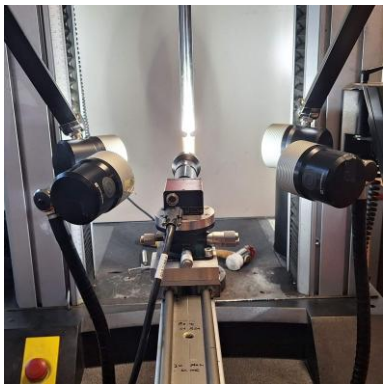

Fig. 2. DIC arrangement with four continuous LED lights providing symmetric illumination of the gauge region

Dynamic tensile (Split-Hopkinson Bar) setup. Dynamic tests used a tensile SHB configuration with adapters that pin-loaded the same flat specimen design, as shown in Fig.3. Axial strain gauges on the incident and transmitter bars recorded incident, reflected, and transmitted waves. Classical one-dimensional elastic-wave analysis was used to obtain specimen stress, strain, and strain-rate; stress equilibrium was checked by comparing $\sigma_{inc}+\sigma_{ref}$

with σ_{trans} over the analysis window. Tests targeted an average strain rate of ~1000 s^{-1}.

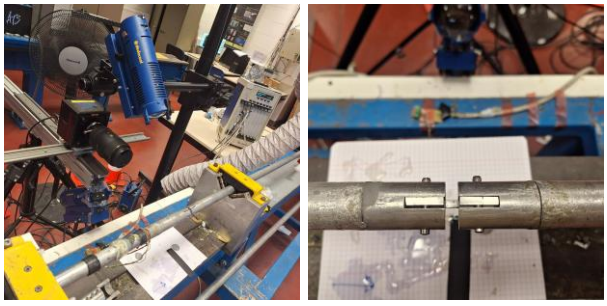

Fig.3. Tensile Split-Hopkinson Bar (SHB) setup: overall arrangement with high-speed camera and lighting - left; close-up of the flat dog-bone specimen mounted between the SHB tensile adapters - right

Digital Image Correlation and timing. DIC was performed in the MatchID software for both regimes. For QS, a monochrome industrial camera with a macro lens and continuous symmetric LED lighting was used. For SHB, a high-speed camera with short exposure was hardware-triggered from the SHB acquisition to ensure frame-accurate synchronization. Calibration and correlation parameters were kept consistent within each regime; axial strain was taken from a virtual extensometer along the gauge.

Data reduction and comparison metric. QS engineering curves were built from measured force and initial area with DIC-based axial strain. SHB analysis yielded true stress–strain. Strain-rate sensitivity was assessed by comparing flow stress at matched plastic strain levels; DIC maps were used to discuss strain localization and failure mode under the two loading rates.

4. Results and Discussion

4.1 Quasi-static stress–strain comparison (Al vs. Al–VC)

Fig. 4 compares the engineering stress–strain responses of the unreinforced aluminum (Al) and the laser-alloyed Al–VC test specimen tested under identical conditions. Both materials show a steep elastic segment with a similar initial slope, followed by measurable hardening and a smooth transition to localization. The Al–VC curve exhibits a higher proof/peak stress in the early plastic range, by roughly one order of 10% relative to Al, consistent with particle strengthening of the laser-alloyed layer.

Beyond approximately ε ~ 0.30 – 0.35, the curves converge and then cross: the unreinforced Al maintains slightly higher flow stress and continues to larger terminal strain, whereas Al–VC softens earlier and fractures at a somewhat lower global strain. This behavior indicates that while VC reinforcement raises initial strength, it also reduces the available work-hardening/ductility, leading to earlier localization – a trend corroborated by the DIC fields presented later.

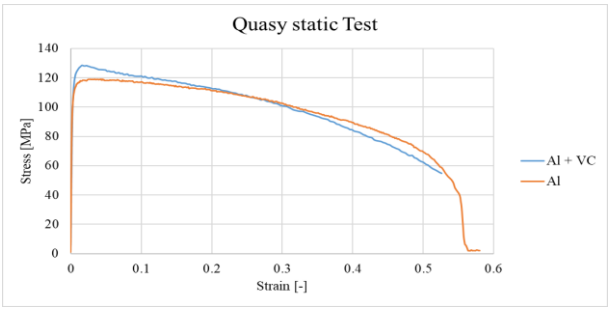

Fig. 4. Quasi-static engineering stress–strain curves of Al and Al–VC flat coupons – identical geometry and test conditions

Strain is obtained from a DIC virtual extensometer. Al–VC test specimen shows higher early strength (~8–10% above Al), whereas at larger strains the unreinforced Al carries slightly higher stress and reaches a larger terminal strain.

Fig.5 shows representative major-strain maps recorded by the camera for the Al-VC test specimen. The field is uniform at the start, a faint axial band appears with the onset of plasticity, and the band progressively intensifies and narrows near peak load, culminating in a sharply confined neck in the last frame. All frames are plotted with the same color scale and field of view to allow direct visual comparison.

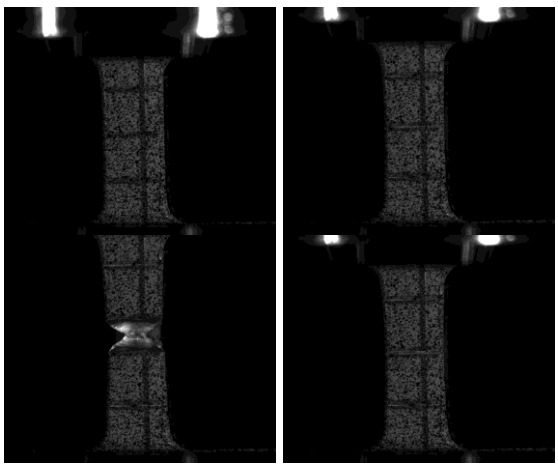

Fig.5. DIC major-strain fields (Al-VC test specimen): baseline → band nucleation → localization growth → fracture (clockwise)

4.2 *Dynamic vs. quasi-static tensile response (Al–VC)*

Fig. 6 compares quasi-static and dynamic responses of the Al–VC test specimens. After a brief transient, the dynamic curve stays approximately 20% higher in early plasticity and remains elevated while softening to a larger terminal strain – evidence of strain-rate strengthening with rate-dependent hardening tempered by progressive softening (e.g., adiabatic heating) as localization develops.

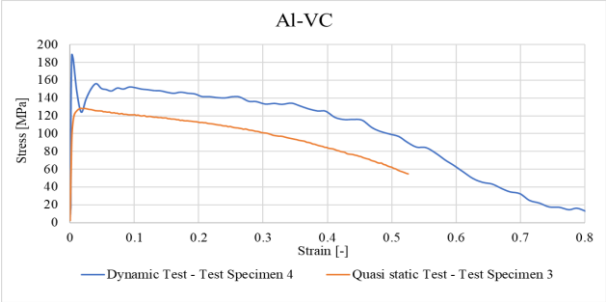

Fig. 6. Engineering stress–strain curves for the Al–VC flat test specimens under quasi-static and dynamic loading (identical geometry).

The dynamic curve shows an initial transient followed by a stable, higher flow level and a larger terminal strain than the quasi-static response.

Fig. 7 shows representative dynamic-test major-strain maps: an initially uniform field evolves into a central axial band that tightens into a narrow localization zone. In the last frame, the peak strain is strongly confined to the neck with steep lateral gradients, consistent with the gradual post-peak softening of the dynamic curve and the extended global strain to failure.

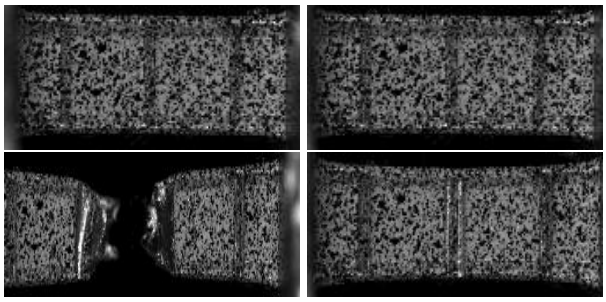

Fig. 7. Dynamic (SHB) DIC major-strain fields for Al–VC at four stages: baseline → band nucleation → localization growth → fracture (clockwise)

The curves and DIC fields show that Al–VC exhibits rate-dependent strengthening and sharper, more confined localization under dynamic loading compared with the quasi-static case. For concise quantification, the study reports classic strength values (0.2% proof, UTS) and two field-aware indicators: the global strain at localization onset and the peak local major strain before fracture, extracted consistently from the DIC analysis for each regime.

5. Conclusions

Quasi-static and dynamic tests on the laser alloyed Al–VC test specimens show a clean, repeatable tensile response: DIC captures the evolution from near-uniform straining to a single, gauge-centered neck, while dynamic loading sustains higher flow stress over a wide strain range and culminates in a sharper, more confined localization than the quasi-static case – establishing a concise, rate-dependent baseline and field-level validation targets for modeling.

For future work, complementary fractography and coupled thermo-mechanical simulations will be done to link microstructure to localization.

Acknowledgement

This research is partly supported by the Science Fund of the Republic of Serbia, #GRANT No 7475, Prediction of damage evolution in engineering structures – PROMINENT, and by the Ministry of Science, Technological Development and Innovation, Republic of Serbia, Agreement No. 451-03-136/2025-03/200378 and Agreement No. 451-03-137/2025-03/200107.

References

[1] D. Erdeniz, W. Nasim, J. Malik, *et al.* Effect of vanadium micro-alloying on the microstructural evolution and creep behavior of Al-Er-Sc-Zr-Si alloys. *Acta Materialia*, 2017, 124, 501–512. DOI: 10.1016/j.actamat.2016.11.033.

[2] X. Chen, J. Chen, W. Xi, *et al.* Effect of Vanadium Addition on Solidification Microstructure and Mechanical Properties of Al–4Ni Alloy. *Materials*, 2024, 17(2), 332. DOI: 10.3390/ma17020332.

[3] A. Kumar, C. Sasikumar. Effect of Vanadium addition to Al–Si alloy on its mechanical, tribological, and microstructure properties. *Materials Today: Proceedings*, 2017, 4, 10768–10772. DOI: 10.1016/j.matpr.2017.01.026.

[4] A. S. Khan, H. Liu. Variable strain rate sensitivity in an aluminum alloy: Response and constitutive modeling. *International Journal of Plasticity*, 2012, 36, 1–14. DOI: 10.1016/j.ijplas.2012.02.001.

[5] R. P. Bigger, A. Carpenter, N. Scott, *et al.* Dynamic Response of Aluminum 5083 During Taylor Impact Using Digital Image Correlation. *Experimental Mechanics*, 2018, 58(6), 913–923. DOI: 10.1007/s11340-018-0392-5.

Original scientific paper DOI: 10.46793/41DAS2025.115B

EXPERIMENTAL VALIDATION OF FRICTION STIR WELDING PARAMETERS FOR EN AW 6060 T6 ALUMINUM ALLOY

Aleksandar BODIĆ[1], Vladimir MILOVANOVIĆ[2], Miroslav ŽIVKOVIĆ[3], Miloš PEŠIĆ[4], Dušan Milojević[5], Marko TOPALOVIĆ[6]

[1] 0000-0002-1713-6540, Faculty of Engineering University of Kragujevac, Sestre Janjić 6, Kragujevac, Serbia, E-mail: abodic@uni.kg.ac.rs;

[2] 0000-0003-3071-4728, Faculty of Engineering University of Kragujevac, Sestre Janjić 6, Kragujevac, Serbia, E-mail: vladicka@kg.ac.rs;

[3] 0000-0002-0752-6289, Faculty of Engineering University of Kragujevac, Sestre Janjić 6, Kragujevac, Serbia, E-mail: zile@kg.ac.rs;

[4] 0000-0002-3405-5216, Institute for Information Technologies, University of Kragujevac, Jovana Cvijića bb, Kragujevac, Serbia, E-mail: milospesic@uni.kg.ac.rs;

[5] Wacker Neuson Kragujevac DOO Kragujevac, Braće Nikolića 20A, Kragujevac, Serbia, E-mail: dusanmilojevic.kg@gmail.com

[6] 0000-0001-6101-755X, Institute for Information Technologies, University of Kragujevac, Jovana Cvijića bb, Kragujevac, Serbia, E-mail: topalovic@kg.ac.rs

Abstract

This paper presents an experimental validation of chosen process parameters for friction stir welding (FSW). The study was conducted on specimens made of aluminum alloy EN AW 6060 T6. Emphasis was placed on evaluating the effects of tool rotation speed, welding speed, and vertical force on weld quality and mechanical performance. Welding was performed using a cylindrical FSW tool with specified welding parameters. The welded joints were subjected to tensile and bending tests according to international standards. The strength and ductility of specimens machined from welded joints were analyzed. For this study, a set of welding parameters is carefully chosen based on experience and standards. These parameters should produce joints with the best mechanical properties that are comparable to the base material. The results provide valuable experimental data that validate the chosen process parameters, and can facilitate practical application of FSW for EN AW 6060 T6 aluminum alloy. This paper contributes to improvement and process optimization in industrial settings.

1. Introduction

Friction Stir Welding (FSW) is an innovative solid-state joining technique used extensively for aluminum alloys, which enables welding without melting the material [1]. The process utilizes a specially designed cylindrical tool that generates frictional heat through rotation and pressure, resulting in localized plastic deformation and material mixing to form a high-quality weld [1]. FSW is particularly important for aluminum because it overcomes common fusion welding issues such as solidification cracking and porosity, resulting in joints with superior mechanical properties, close to the base metal itself [2]. This makes it highly suitable for industries like aerospace, automotive, and marine, where lightweight, strong, and defect-free aluminum joints are critical. EN AW 6060 T6 alloy presents several challenges to the FSW technique due to its high strain-hardened state and sensitivity to thermal input. Excessive heat can lead to softening and loss of mechanical properties in the heat-affected zone, while insufficient heat results in poor material flow and defects like tunnel voids. Additionally, the alloy's strong tendency to form surface oxide layers complicates tool-material interaction. The aluminum oxide (Al_2O_3) layer acts as a mechanical and chemical barrier between materials. Therefore, proper choice of tool design, rotation speed, vertical force, and traverse speed is required in order to achieve defect-free welds with consistent strength and integrity, enabling further industrial adoption.

This paper aims to experimentally test chosen FSW parameters, such as tool rotation speed and welding speed, for EN AW 6060 T6 aluminum alloy. It further seeks to validate weld quality through mechanical testing, ensuring that the joints

meet required strength and ductility standards for reliable industrial applications.

2. Materials and Methodology

2.1 Friction Stir Welding (FSW) technique

Friction stir welding (FSW) is a solid-state joining technique in which the base material does not melt [1]. Instead, heat generated by friction between the rotating tool and the workpieces softens the material, bringing it into a plasticized state. A specially designed cylindrical tool with a probe stirs and forges the materials together, resulting in joint formation. The process is highly nonlinear, involving large plastic deformations, elevated temperatures, and material flow in the weld zone. According to the international standard EN ISO 25239-1:2020 [2], FSW is divided into five stages. The first involves tool rotation and its downward movement toward the workpieces. The second, known as the plunging stage, includes penetration of the probe until the tool shoulder contacts the surface, generating increasing heat and accumulating displaced material. In the third stage, translational motion along the joint line begins, creating the weld. Here, the probe encounters less-heated material, which is softened by friction and transported to the rear of the tool, while new material is engaged at the front. The fourth stage marks the end of translational motion, and the fifth concludes with tool withdrawal from the solidified weld zone. A schematic of the FSW process is shown in Fig. 1.

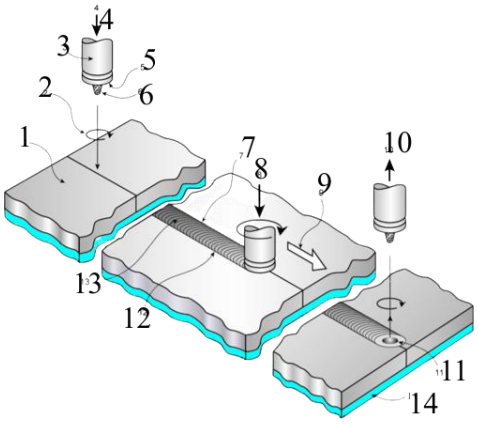

Fig. 1. Schematics of the FSW process

This figure first appeared in EN ISO 25239 standard [2], then Milčić et. al. [3] made it more accurate with the inclusion of the support plate, and we further enhanced this image from [3], which is available via CC BY 3.0 license, by adding a bigger font more suitable for double column paper. Schematic of the FSW process [2] shown in Fig. 1. depicts: 1) base material, 2) tool rotation direction, 3) welding tool, 4) downward tool movement, 5) tool shoulder, 6) tool probe, 7) advancing side of the weld, 8) axial (vertical) force, 9) welding direction, 10) upward tool movement, 11) exit hole, 12) retreating side of the weld, 13) weld face, and 14) support plate. The particular tool that was used for the welding of the studied plate is shown in Fig. 2.

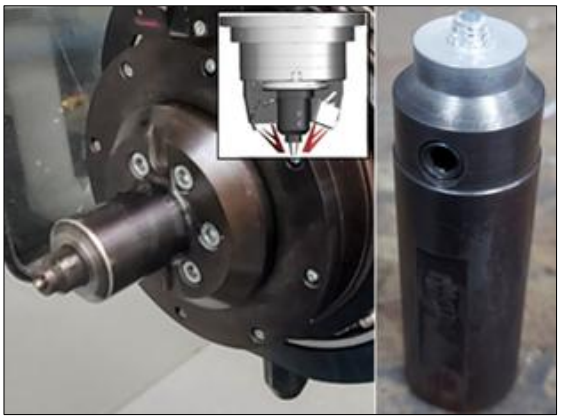

Fig. 2. FSW tool

The welding parameters are given in Table 1.

Table 1. FSW parameters

Probe length [mm]	**Welding speed** [mm/min]	**Axial force** [kN]	**Tool rotation speed** [rpm]	**Dwell time** [s]
3.7	1300	9	1650	0.2

The zoomed-in picture of the upper side of the weld is shown in Fig. 3.

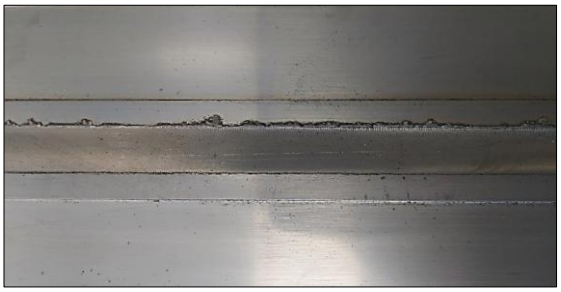

Fig. 3. The upper side of the weld

The zoomed-in picture of the exit hole is shown in Fig. 4.

Fig. 4. The FSW exit hole

The welded plates have reinforcement ribs on their back side, which can be seen in Fig. 5.

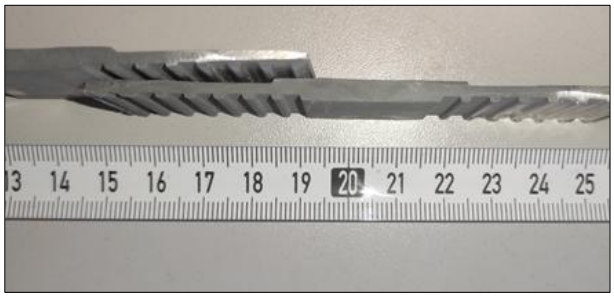

Fig. 5. The side view of EN AW 6060 T6 plates

A water jet machine is used to cut out specimens for bending and tension testing, as can be seen in Fig. 6. The figure also shows the welding direction.

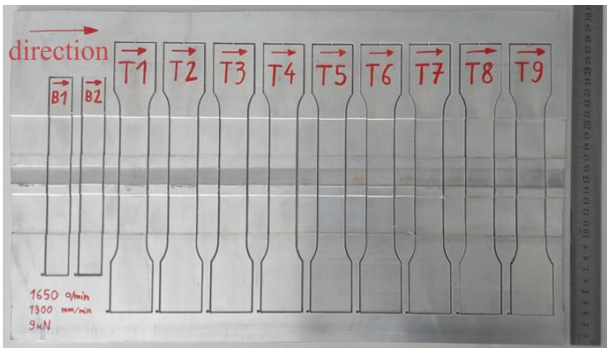

Fig. 6. Aluminum alloy welded plate with cut-out specimens

The specimens B1 and B2 are used for penetration and bending testing, which will not be discussed in this paper; instead, we will be focusing on the tension test performed using flat dog-bone specimens shown in Fig. 7.

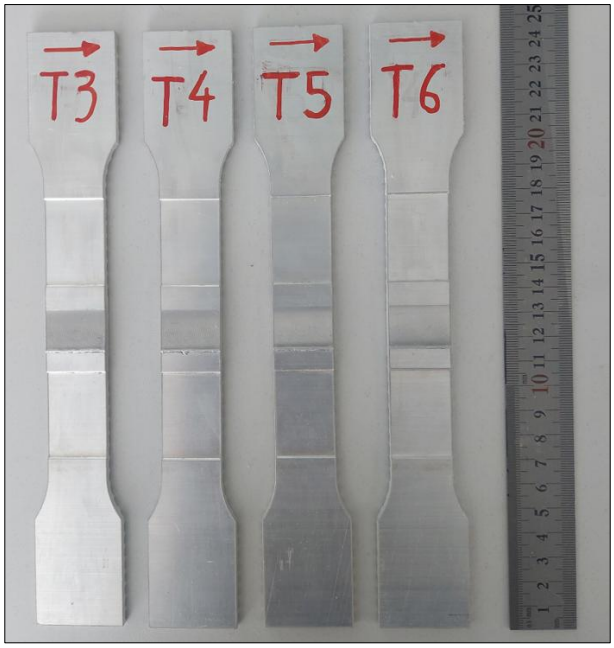

Fig. 7. Actual tension specimens before testing

2.2 Static tension testing for mechanical characteristics assessment

Uniaxial tensile tests were carried out on the specimens using a Shimadzu servo-hydraulic machine (EHF EV101K3-070-0A) with a capacity of ±100 kN and a stroke of ±100 mm. The purpose of the tests is to determine FSW weld mechanical properties, i.e., static strength parameters [4]. The testing machine is shown in Fig. 8.

Fig. 8. Shimadzu EHF EV101K3-070-0A

3. Results

The base material thickness in the weld region is 4 mm. Although tensile failure in welded joints typically initiates in the heat-affected zone [5], in this case, fracture is anticipated in the base material outside the weld due to profile geometry, where ribs reduce the cross-sectional thickness locally to 2 mm. Testing on specimens T3 and T4 confirmed this hypothesis, with the crack occurring precisely in the 2 mm-thick section between the ribs, as can be seen in Fig. 9.

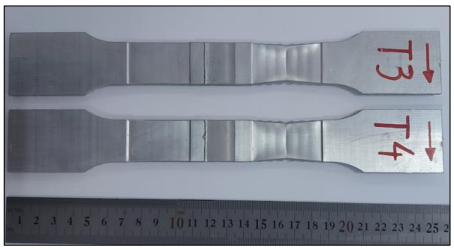

Fig. 9. T3 and T4 specimens after testing

According to EN 755-2 standard, the yield strength of EN AW 6060 T6 (Rp0.2) is 150 MPa, while the tensile strength (Rm) is 190 MPa. The EN ISO 25239 standard for friction stir welding requires that the welded joint achieve a minimum

tensile strength of 0.7 Rm, i.e., 133 MPa. In specimens T3 and T4, material failure was observed at loads of 225.83 MPa and 225.56 MPa, respectively, indicating that the welded joints met the quality requirements. Stress-strain curves for T3 and T4 specimens are shown in Fig. 10.

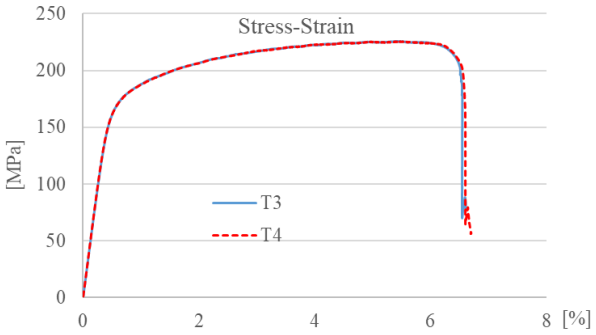

Fig. 10. Stress-Strain curves for T3 and T4

In order to remove the influence of ribs, they were removed by manual machining (fine grinding) of T5 and T6 specimens, reducing the thickness of the samples to 2 mm along their entire length. However, this led to the significant reduction of mechanical properties, with material failure occurring at 145.25 MPa and 114.85 MPa for T5 and T6 specimens, respectively. Stress-strain curves for T5 and T6 specimens are shown in Fig. 11.

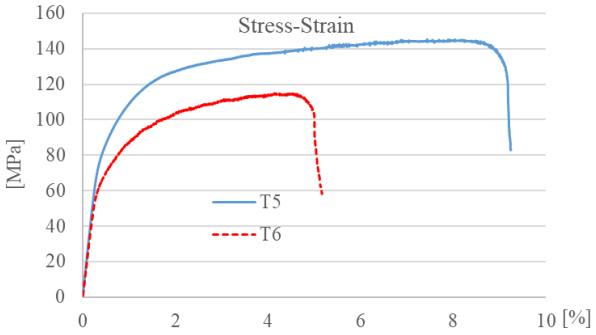

Fig. 11. Stress-Strain curves for T5 and T6

This significant reduction means the T6 specimen does not satisfy the safety criteria for a welded joint that prescribes a minimum tensile strength of 0.7 Rm, i.e., 133 MPa.

4. Conclusions

While the initial welded joints satisfied EN ISO 25239 requirements, manual machining that reduced the thickness to 2 mm caused a significant drop in tensile strength, so much so that specimen T6 failed to meet the minimum standard, highlighting the detrimental effect of post-weld modification.

Acknowledgments

This research was supported by the Ministry of Science, Technological Development and Innovation of the Republic of Serbia, contract No. 451-03-66/2024-03/200378, and by the Science Fund of the Republic of Serbia, #GRANT No. 7475, Prediction of damage evolution in engineering structures – PROMINENT.

References

[1] Thomas, W. M., Nicholas, E. D., Needham, J. C., Murch, M. G., Templesmith, P., Dawes, C. J. Friction stir welding. International Patent Application No. PCT/GB92/02203; U.S. Patent No. 5,460,317, 1991

[2] EN ISO 25239:2020, Friction stir welding — Aluminium (Parts 1-5). International Organization for Standardization: Geneva.

[3] Milčić, D., Laban, M., Arsić, D., Nikolić, R., Hadzima, B., Konjatić, P. Improvement of welded joint quality obtained by friction stir welding. IOP Conf. Ser.: *Mater. Sci. Eng*., 2018, 393, 012107.

[4] Dunić, V., Živković, J., Milovanović, V., Pavlović, A., Radovanović, A., Živković, M. Two-Intervals Hardening Function in a Phase-Field Damage Model for the Simulation of Aluminum Alloy Ductile Behavior. *Metals*, 2021, 11(11), 1685.

[5] Lee, S., Kim, B.C., Kwon, D. Fracture Toughness Analysis of Heat-Affected Zones in High-Strength Low-Alloy Steel Welds. *Metallurgical Transactions A*, 1993, 24A, 1133–1145.

Original scientific paper DOI: 10.46793/41DAS2025.119C

RESIDUAL STRESS-INDUCED DAMAGE IN BRAKE DRUMS

Dobrivoje ĆATIĆ[1], Vladimir ĆATIĆ[2],

[1] 0000-0003-3636-8301, Full Profesor, Faculty of engineering, University of Kragujevac, 34000 Kragujevac, 6 Sestre Janjić Street, Serbia, caticd@kg.ac.rs

[2] 0009-0006-9268-8317, Software engineer, HTEC Group, Bulevar Milutina Milankovica 7DJ, Belgrade 11070, Serbia, vladimir.catic@htecgroup.com

1. Introduction

The braking system represents one of the vital subsystems of the complex mechanical system of a motor vehicle. Together with the steering system and the tires, it plays a decisive role in the active safety of motor vehicles and road users [1]. Brakes, as the actuators of individual subsystems, have a particularly important role in considerations of the reliability of motor vehicle braking systems due to their operating conditions and their influence on vehicle safety [2]. In motor vehicles, two basic types are used: drum (radial) brakes and disc (axial) brakes. On the rear wheels of heavy vehicles, drum brakes are most commonly applied. Because of their good characteristics, these brakes are also applied on the front wheels of motor vehicles, especially on vehicles with larger mass. Since the rear-wheel brakes also serve as the actuators of the parking (auxiliary) brake, the importance of drum brakes for the reliable and safe operation of motor vehicle braking systems is evident.

Based on the failure modes, effects, and criticality analysis (FMECA) of drum brake components in motor vehicles, it has been determined that the brake linings and the brake drum exhibit the highest criticality [3]. Criticality represents a relative measure of the severity of failure mode consequences and the frequency of their occurrence.

The concept of residual stresses refers to internal stresses that exist in materials and structures independently of any external loads [4]. In metals, particularly in steels, residual stresses may arise due to [5]:

- non-uniform chemical composition,
- unequal plastic deformations during transformations at room or elevated temperatures,
- unequal plastic deformations caused by non-uniform heating or cooling in different zones of the cross-section,
- structural deformations associated with volume changes in the structure, for example during steel hardening processes,
- non-uniform plastic deformations in the cross-section of a machine element induced by service loading at room or elevated temperatures.

With regard to residual stresses in brake drums, it is important to note that brake drums are manufactured from a special type of cast iron, which is thermally conductive and wear-resistant.

2. Failure analysis of drum brakes

In drum brake systems for motor vehicles either complete or partial failures may occur [3]. Complete failures, which are rare, arise when the brake is unable to generate any braking torque. Partial failures, on the other hand, lead to a significant deterioration in the drum brake's operating characteristics, including braking torque, operating temperature, braking uniformity, and the intensity of noise generated during braking.

Failures that lead to a reduction in braking torque are commonly referred to as friction failures. These can be either permanent or transient. Permanent friction failures of a drum brake may result, among other causes, from damage to the drum and the brake shoe linings.

Overheating of drum brake components occurs when the heat generated by converting the vehicle's kinetic energy during motion exceeds the amount of thermal energy that brake components can dissipate to the surroundings. This situation arises during prolonged braking on downhill descents, frequent use of the brakes, or incomplete brake release when the brake is not actively engaged. Sustained high operating temperatures of drum brake parts can lead to thermal overloading and burning of the brake shoe lining material. In addition, overheating of drum brake components may cause: deformation of elements (drum ovality, shoe distortion), drum cracking, the occurrence of

blue spots and martensitic patches on the drum friction surface, brake lining damage, changes in material properties (e.g., loss of elasticity of return springs), accelerated aging of brake cylinder sealing elements, etc.

The most common types of damage to the brake drum of motor vehicle braking systems occurring during operation are [6]: cracked drum, cracks caused by overheating, contamination of the friction surface with grease, occurrence of martensitic spots, deep grooves on the sliding surface, blue discoloration of the sliding surface, polished surface, drum deformation, excessive wear, thinning of the drum, circumferential cracking of the drum's mounting ring and radial cracking of the mounting ring at the bolt holes. The subsequent sections present a detailed analysis of brake drum failures resulting from residual stresses induced by operational regimes and service conditions during use.

3. Thermal cracks

Heat-checking or thermal cracks appear as a series of narrow, short, and shallow cracks on the braking surface of the drum (Fig. 1) [6]. They occur under normal operating conditions due to alternating heating and cooling of the friction surface of the drum and are considered a typical characteristic of drum brakes. These cracks do not affect braking torque or other functional parameters. Because of their shallow depth, thermal cracks usually wear away during operation as the friction surface of the drum undergoes normal wear, but they reappear again as a result of the braking process. However, there is a possibility that over time heat-checking may develop into more serious cracks, which would require drum replacement. Therefore, during routine inspections of a vehicle's braking system, special attention should also be paid to the condition of thermal cracks on the drum.

Fig. 1. Heat-checking.

As shown in Fig. 1, thermal cracks appear on the friction surface of the drum that is closer to the mounting plate. On the opposite side, where the drum is cooled more evenly, such cracks are almost absent. All thermal cracks are oriented in the axial direction of the drum. This indicates that they occur as a result of tangential tensile stresses on the friction surface that arise during the cooling of the drum. How can the formation of thermal cracks be explained?

During braking, intensive local heating of the contact surfaces between the drum and the brake linings occurs. As the temperature rises, the diameter of the material layers near the friction surface of the drum increases. This expansion is constrained by the adjacent layers of material that are less heated. Consequently, the outer layers of the drum wall are subjected to tensile stresses, while the inner layers are subjected to compressive stresses. If the total stresses in the outer layers exceed the yield strength, plastic deformation and an increase in drum diameter will occur. When the friction surface cools, its diameter decreases. This contraction is resisted by the plastically deformed outer shell. As a final result of the non-uniform heating and cooling of the drum wall, compressive residual stresses are formed in the plastically deformed outer layers of the drum wall, while tensile tangential residual stresses occur in the interior. It can be assumed that the maximum values of tensile tangential stresses appear in the surface layers of the friction surface. Their intensity is evidently greater than the tensile strength of the drum material, which leads to crack formation.

4. Cracked drum

The most common cause of cracking in brake drums is residual thermal stress, which develops due to uneven heating and cooling during operation. In some cases, the intensity of residual stresses alone may be sufficient to initiate a crack. More frequently, residual stresses are superimposed with service stresses caused by external loads. If the total stress exceeds the tensile strength of the material, a crack will occur, its size being proportional to the stress intensity. Even small cracks in the drum wall can, over time and under dynamic loading, lead to complete drum failure. This raises the question of establishing a criterion for when the brake drum should be replaced, depending on the crack dimensions.

A cracked drum (Fig. 2.) [6] can be detected through visual inspection. The crack typically runs in the axial direction and extends through the entire

wall of the drum. It always appears perpendicular to the sliding direction of the brake shoe.

Fig. 2. Cracked drum.

The reduction of drum wall thickness, either due to wear or due to machining aimed at eliminating detected defects, additionally decreases the static strength of the drum and increases the likelihood of crack formation. In the drum section where a crack has developed, elastic deformations are more pronounced, which leads to an uneven pressure distribution along the arc length of the friction lining and to a significant reduction of the braking torque. As a consequence, brake vibrations become strongly pronounced. Depending on the cause of origin, cracks in the drum may occur during the entire service life of the component. A cracked drum must be replaced, which means that this type of failure leads to the complete failure of the brake drum.

5. Brake drum deformation

As with cracked drums, the most common cause of brake drum deformation is residual thermal stress resulting from uneven heating and cooling of the drum during operation. Residual stresses are superimposed with service stresses. If the total stress exceeds the yield strength of the drum material, permanent plastic deformations occur, leading to a loss of concentricity of the friction surface. The circular shape of the friction surface transforms into an oval.

It is important to note that possible causes of drum ovality may also include improper storage of the drum, incorrect tightening during installation, or dropping the drum onto a hard surface during routine vehicle maintenance. In all these cases, residual stresses arise due to uneven plastic deformations at room temperature. However, the decisive factor for further use of the drum is the magnitude of the resulting deformation.

Variation in drum diameter at different points along the braking surface, as well as uneven wear of the drum and brake linings, are indicators of an out-of-round drum. The magnitude of drum deformation is determined by measuring the drum diameter (Fig. 3) [6] at different points on the braking surface.

Fig. 3. Measurement of drum deformations.

On each brake drum, the manufacturer marks the values of the internal diameter of a new drum and the maximum permissible diameter, beyond which mandatory replacement is required. If the maximum measured diameter of the drum's friction surface is smaller than the maximum permissible diameter, the drum can be machined in order to restore concentricity. Otherwise, the drum must be replaced. This means that deformed drums belong to the group of conditionally repairable components.

6. Martensite spots

Martensite spots appear as extremely hard, slightly raised dark patches on the friction surface of the brake drum (Fig. 4) [6]. The presence of these dark spots indicates that the drum has been exposed to operating temperature regimes that caused structural changes in the drum material. During rapid cooling of a heated drum made of gray cast iron, the austenitic structure of the material, with a face-centered cubic lattice, transforms into a martensitic structure with a body-centered cubic lattice. The structural transformation of austenite into martensite results in a relative increase in the material volume, which leads to the formation of raised dark spots on the drum's friction surface.

Fig. 4. Martensite spots.

Due to structural changes in the material, compressive residual stresses occur in the martensitic zones, leading to an increase in material hardness. The color change of the drum material with a martensitic structure can be explained by the presence of graphite in the material structure. Namely, during rapid cooling of gray cast iron, carbon atoms do not have time to diffuse out of the austenite crystals, but remain in the material in the form of graphite needles or flakes.

In general, during the cooling process of steel or gray cast iron, structural stresses arise at the moment of transformation from austenite to martensite due to a significant increase in specific volume. Since martensitic transformation takes place at a temperature at which the material is no longer plastic, residual stresses form immediately. The surface layers of the material with a martensitic structure, due to the volume increase, tend to separate from the austenitic core. As a result, compressive stresses develop in the surface layer, while tensile stresses appear in the core (Fig. 5a) [5]. With further cooling of the material, martensitic transformation continues in the deeper layers. Consequently, the initial stress distribution changes so that the maximum compressive stress shifts from the surface toward the interior, as shown in Fig. 5b).

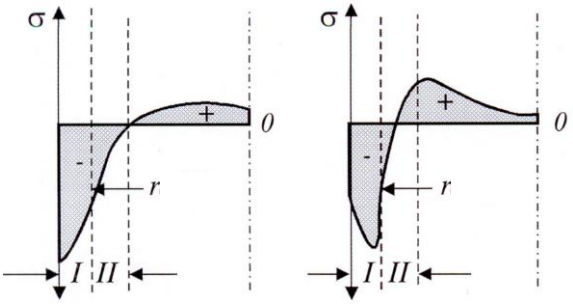

a) b)

Fig. 5. Schematic of structural stress formation in Cooling Zones I and II: a) onset of martensitic transformation, b) completion of transformation.

The presence of raised, hard, dark spots on the friction surface of the brake drum reduces the effective contact area between the drum and the brake linings. This in turn leads to a decrease in braking torque, severe local heating, uneven wear of the brake linings, brake pedal pulsation, and the occurrence of vibrations and excessive noise during braking. In addition to structural residual stresses, intense local heating and non-uniform cooling of the friction surface give rise to thermal residual stresses. The complex stress state resulting from the combined effect of residual and service stresses causes deformation of the brake drum and the initiation of fatigue cracks on the friction surface. Failure to detect martensitic spots in a timely manner and eliminate the cause of brake drum overheating inevitably leads to mandatory drum replacement.

7. Conclusions

Residual stresses have a significant influence on the service properties and operational life of machine elements. Therefore, it is important during the design phase of machine structures to devote appropriate attention to the causes and consequences of residual stresses.

Residual stresses formed during manufacturing or during service of the brake drum are superimposed with stresses caused by external loading. As a result, the stress state within the brake drum is highly complex and often leads to damage in the form of cracks and deformations, necessitating replacement.

Timely detection of such damage and the implementation of appropriate corrective measures can enhance the reliability and safety of the motor vehicle braking system. In addition, maintenance costs are significantly reduced.

Acknowledgments

This paper is the result of research conducted under the author's contract No. 451-03-137/2025-03/200107, dated February 4, 2025.

References

[1] Todorović, J. *Braking of motor vehicle*, (in Serbian), Institute for textbooks and teaching aids, Beograd, 1988.

[2] Day, A. *Braking of road vehicles*, Elsevier Inc, 2014.

[3] Ćatić, D., Glišović, J., Miković, J., Veličković, S. Analysis of failure causes and the criticality degree of elements of motor vehicle's drum brakes, *Tribology in Industry*, 2014, 36(3), 316-325.

[4] Edited by Schajer, S. G. *Practical residual stress mea-surement methods*, John Wiley & Sons Ltd, 2013.

[5] Josifović, D. *Testing of mechanical structures I*, (in Serbian), Faculty of mechanical engineering from Kragujevac, 2000.

[6] *Maintenance and installation manual*, https://www.accuridecorp.com/sites/default/files/resources/2021-6/WE3.000%20 Rev.% 202% 20Gunite%20Brake%20Drum%20Service%20Manual.pdf, Accessed on: 25. 04. 2025.

41st Danubia-Adria Symposium Advances in Experimental Mechanics
September 23-26, 2025, Kragujevac, Serbia

Original scientific paper DOI: 10.46793/41DAS2025.123M

INFLUENCE OF CRACKS ON THE STRUCTURAL STABILITY OF CYLINDRICAL STEEL EQUALIZATION TANKS

Vladimir MILOVANOVIĆ[1], Stefan DIKIĆ[2], Saša SPASENIĆ[3], Mileta RISTIVOJEVIĆ[4], Sreten SPASENIĆ[5], Aleksandar BODIĆ[6], Miloš PEŠIĆ[7]

[1] 0000-0003-3071-4728, Faculty of Engineering, University of Kragujevac, Sestre Janjić 6, Kragujevac, Serbia, E-mail: vladicka@kg.ac.rs

[2] 0000-0003-2700-0628, University of Belgrade Faculty of Technology and Metallurgy, Karnegijeva 4, Belgrade, Serbia, E- mail: sdikic@tmf.bg.ac.rs

[3] Kontrol Inspekt D.O.O., Mladena Mitića 12, Belgrade, Serbia, E-mail: spasenic_sale@yahoo.com

[4] 0009-0004-7775-2232, Kontrol Cert D.O.O., Obalskih Radnika 13, Belgrade, Serbia, E-mail: miletaristivojevic@gmail.com

[5] Kontrol Inspekt D.O.O., Mladena Mitića 12, Belgrade, Serbia, E-mail: kontrolinspekt@yahoo.com

[6] 0000-0002-1713-6540, Faculty of Engineering, University of Kragujevac, Sestre Janjić 6, Kragujevac, Serbia, E-mail: abodic@uni.kg.ac.rs

[7] 0000-0002-3405-5216, Faculty of Engineering, University of Kragujevac, Sestre Janjić 6, Kragujevac, Serbia, E-mail: milospesic@uni.kg.ac.rs

1. Introduction

Above-ground cylindrical steel tanks are indispensable assets in water and wastewater infrastructure. In equalization services, they buffer diurnal and industrial inflow variability, dampen “shock” pollutant loads, and stabilize downstream treatment functions, consistently shown to improve effluent quality and operational resilience [1].

Even when tanks are designed and operated within code provisions, long-term performance depends on how structural demand interacts with the service environment and maintenance practices. The technical literature documents characteristic failure modes – loss of containment by corrosion-induced wall thinning, local joint distress, and roof/shell instabilities – through forensic case studies that combine inspection, measurement, and finite-element analysis to reconstruct the damage sequence and define preventive measures [2].

Wastewater headspaces and wetted zones present particularly aggressive conditions for carbon and stainless steels due to variable pH, dissolved sulfides, chlorides, and microbiologically influenced corrosion. Recent reviews emphasize corrosion monitoring and mitigation as central to lifecycle reliability of storage and process tanks in treatment facilities [3].

Within this broader context, this study focuses on durability-oriented design, inspection, and risk-informed maintenance programs for tanks operating in wastewater service, drawing on established roles of equalization, observed failure mechanisms, and evidence from prior research and case histories.

2. Tank Description and Methods

2.1 Geometry, construction, and service

The investigated subject of this paper is an above-ground cylindrical steel equalization tank (nominal diameter 8.0 m, total height 17.6 m), assembled from bolted, factory-coated panels arranged in twelve courses (I–XII). Courses I–V use thin panels (t = 2.5 mm), course VI intermediate panels (t = 2.99 mm), and courses VII–XII thicker panels (t = 3.4 mm). The tank operates at atmospheric pressure in wastewater service with variable filling. Thin panels (2.5 – 2.99 mm) show low yield/UTS levels (~270–315 MPa), while the 3.4 mm panels exhibit significantly higher strength (ReH = 420 MPa, Rm = 571 MPa), consistent with micro alloyed composition.

2.2 Finite-element model of the tank

FE [4] model of the tank was created with course-wise thickness zoning (I–XII), simply supported at the base ring to prevent rigid-body motion, as shown in Fig. 1. The model is created

within Simcenter Femap [5] software using 2D plate finite elements and consists of 278204 elements and 278832 nodes. The average element size is approximately 40 mm.

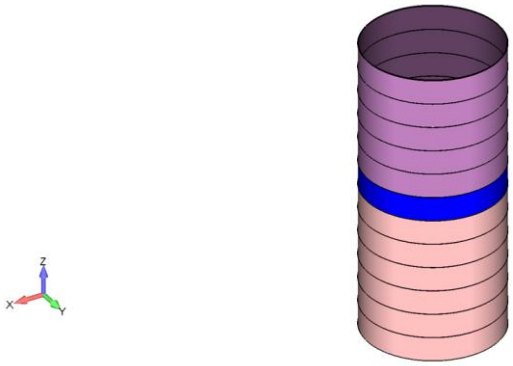

Fig.1 FE model with course-wise thickness zoning (I–XII)

2.3 Experimental monitoring and initial crack modeling

In service conditions, digital radiography was performed on representative wall samples, which revealed localized corrosion defects of varying extent. Pitting was observed both on exposed steel surfaces and beneath silicone-coated regions, including at the lap joints of bolted connections. Metallographic analysis (Fig. 2) of corroded samples confirmed the absence of an effective anticorrosive layer and showed progressive surface and subsurface degradation. In advanced cases, coalescence of pits led to detachment of larger fragments of metal, resulting in discontinuities resembling through-thickness cracks.

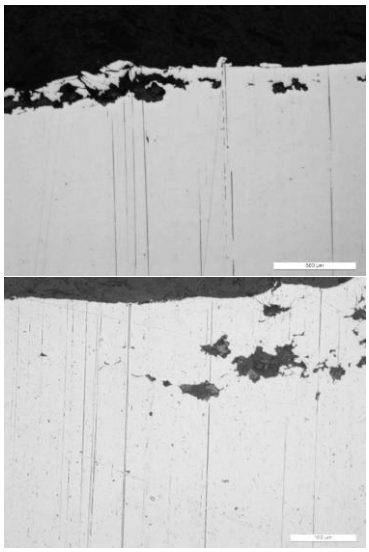

Fig. 2. Cross-sectional surface micrograph

Based on these inspection findings, a finite-element model of the tank was developed with an explicitly introduced initial crack in the ring 2 region (Fig. 3).

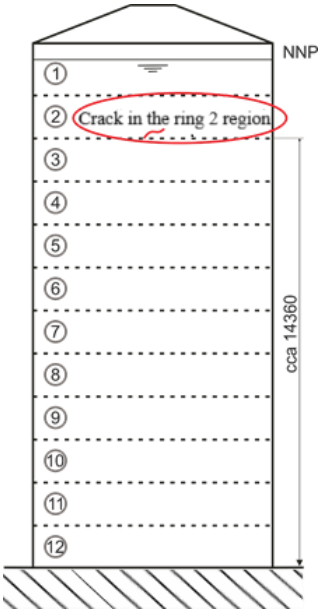

Fig. 3. Initial crack in the ring 2 region

2.4 Loading and boundary conditions

For design operating conditions, hydrostatic head of h = 17.0 m, liquid density ρ = 1000 kg/m³ (wastewater), and gravitational acceleration g = 9.81 m/s² are considered.

The hydrostatic pressure distribution for h=17 m and ρ=1000 kg/m³ is given in Fig. 4.

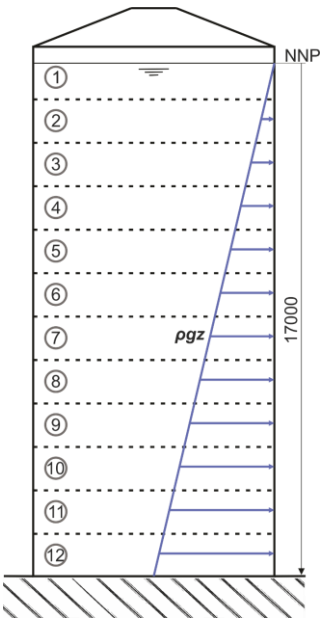

Fig. 4. Hydrostatic pressure diagram for h=17 m and ρ=1000 kg/m³

3. Results and Discussion

3.1 FEA results of tank without crack

The von Mises stress distribution on tank model without crack is shown in Fig. 5. Peak stress values occur in the lower courses, where hydrostatic pressure is greatest, with maximum equivalent stresses reaching approximately 200 MPa.

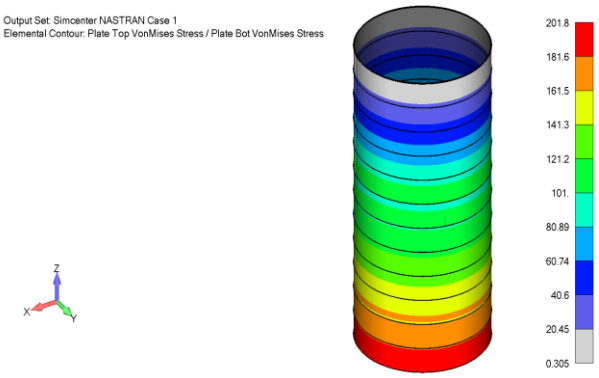

Fig. 5. Equivalent von Mises stress distribution in the intact tank model

3.2 Effect of the crack on stress distribution

When an initial crack was introduced in the ring 2 region, significant local stress amplification was observed. The von Mises stress field around the crack tip exhibits a highly localized concentration, with values exceeding 450 MPa (Fig. 6). This peak stress surpasses both the yield strength (R_{eH} = 270–315 MPa for thin panels) and the ultimate tensile strength of the 2.5 mm wall panels.

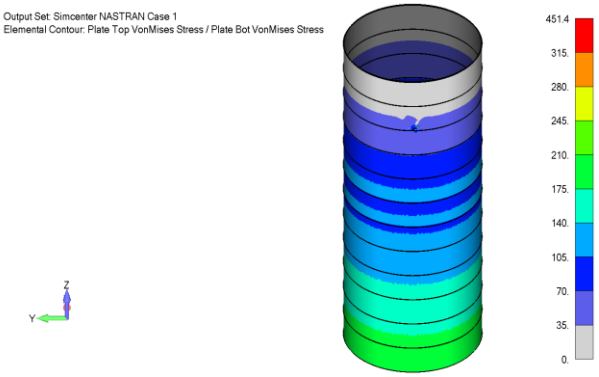

Fig. 6. Equivalent von Mises stress distribution in the tank model with modeled crack in the ring 2 region

Fig. 7 provides an enlarged view of the stress state in the region of ring 2, highlighting the localized stress concentration around the modeled crack. The contour plot clearly illustrates the redistribution of equivalent stresses in the vicinity of the defect, where sharp gradients develop as a result of crack–tip effects. The crack perturbs the otherwise smooth hoop stress distribution, introducing discontinuities across the ring joint.

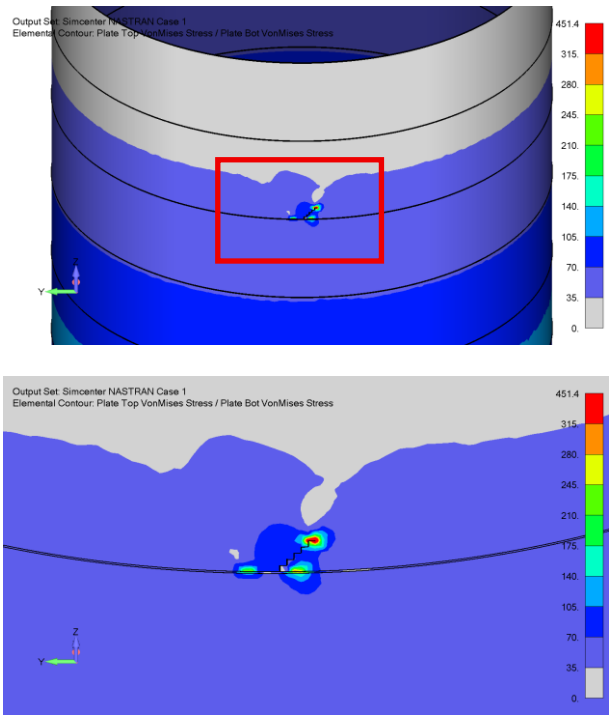

Fig. 7 Localized von Mises stress distribution around the modeled crack in ring 2

3.3 Comparative assessment

A direct comparison between the intact and cracked models highlights the pronounced influence of the defect. While the intact model remains in the elastic range with stresses below yield, the cracked configuration shows stress intensities well above the material capacity. These results suggest that even a relatively small initial crack at a ring joint can act as a critical trigger for structural instability, potentially leading to uncontrolled crack propagation and loss of containment.

The analysis emphasizes the importance of continuous inspection and early detection of cracks in bolted-panel tanks, as localized overstress conditions can develop rapidly under routine hydrostatic loading. Preventive maintenance and reinforcement of critical joints should therefore be prioritized in durability-oriented management of wastewater tanks.

4. Conclusions

This study presented a finite-element analysis of a cylindrical steel wastewater equalization tank, with particular emphasis on the effect of an initial crack at the ring 2 region. The intact model showed stress levels consistent with elastic shell theory,

with maximum equivalent stresses remaining below the yield limit and displacements within acceptable serviceability ranges.

By contrast, the cracked configuration revealed highly localized stress intensification around the crack tip, with equivalent von Mises stresses exceeding both the yield and ultimate tensile strength of the thin (2.5 mm) wall panels. These results demonstrate that even small cracks introduced at course joints can act as critical defects, triggering localized plastification and posing a significant risk of crack propagation under routine hydrostatic loading.

The comparative assessment highlights the vulnerability of bolted, thin-walled steel tanks in aggressive wastewater environments, where defects can drastically alter the structural response. The findings emphasize the need for durability-oriented design, regular inspection, and risk-informed maintenance strategies to ensure the long-term reliability of such assets.

While the present study demonstrated the critical influence of localized cracks on the structural response of cylindrical steel wastewater tanks, several aspects merit further investigation:

- Fracture mechanics assessment – A full fracture mechanics analysis, including stress intensity factor (SIF) evaluation and crack growth simulations, would provide quantitative insight into the propagation potential under cyclic filling and emptying conditions.
- Material degradation effects – Incorporating corrosion-induced wall thinning, pitting, and microbiologically influenced corrosion into the finite-element framework would yield more realistic predictions of long-term performance of such structures.
- Experimental validation – Laboratory testing on representative bolted panel joints with artificial cracks would strengthen the numerical findings and help calibrate constitutive models for thin-walled steels.
- Monitoring and inspection strategies – Future work should explore the integration of non-destructive evaluation (NDE) methods, acoustic emission monitoring, and digital twins for early detection and life-cycle management of cracks.
- Mitigation measures – Structural retrofits, such as local reinforcement of ring joints or use of composite overlays, should be investigated as practical interventions to reduce stress concentration and delay crack propagation.

Overall, advancing the modeling, monitoring, and preventive maintenance of thin-walled steel tanks is essential for ensuring structural integrity and operational resilience in wastewater service environments.

Aknowledgment.

This research is partly supported by the Science Fund of the Republic of Serbia, #GRANT No 7475, Prediction of damage evolution in engineering structures – PROMINENT, and by the Ministry of Science, Technological Development and Innovation, Republic of Serbia, Agreement No. 451-03-136/2025-03/200378 and Agreement No. 451-03-137/2025-03/200107 and Contract No. 451-03-136/2025-03/200135.

The authors wish to acknowledge and thank the company Kontrol Inspekt D.O.O. in Belgrade for support and for encouragement in the research realization.

References

[1] C.-T. Chang and B.-H. Li, “Optimal design of wastewater equalization systems in batch processes,” *Computers & Chemical Engineering*, vol. 30, pp. 797–806, 2006.

[2] F. Trebuňa, F. Šimčák, and J. Bocko, “Failure analysis of storage tank,” *Engineering Failure Analysis*, vol. 16, no. 1, pp. 26–38, 2009. doi:10.1016/j.engfailanal.2007.12.005.

[3] E. Khamis, T. E. Reyad, and D. E. Abd-El-Khalek, “*Corrosion assessment and mitigation in wastewater systems: a comprehensive review*,” *npj Materials Degradation*, vol. 9, Article 95, 2025.

[4] M. Kojić, R. Slavković, M. Živković and N. Grujović, „*Metod konačnih elemenata I*“, Mašinski Fakultet Univerziteta u Kragujevcu, Kragujevac, 1998.

[5] *FEMAP User Guide Version 11.2*, Siemens PLM Software Inc., 2015.

41st Danubia-Adria Symposium Advances in Experimental Mechanics
September 23-26, 2025, Kragujevac, Serbia

Original scientific paper DOI: 10.46793/41DAS2025.127N

STRUCTURAL ASSESSMENT AND REDISIGN OF THE WATER CHAMBER IN A DOMESTIC GASIFICATION BOILER

Filip Nastić[1], Mladen Josijević[2], Davor Končalović[3], Dušan Gordić[4], Vladimir Vukašinović[5]

[1] 0000-0002-2164-6658, Faculty of Engineering, Sestre Janjić 6, Kragujevac, Serbia, E-mail: filip.nastic@uni.kg.ac.rs;

[2] 0000-0001-9619-0897, Faculty of Engineering, Sestre Janjić 6, Kragujevac, Serbia, E-mail: mladen.josijevic@fink.com;

[3] 0000-0003-1207-2653, Faculty of Engineering, Sestre Janjić 6, Kragujevac, Serbia, E-mail: davor.koncalovic@kg.ac.rs;

[4] 0000-0002-1058-5810, Faculty of Engineering, Sestre Janjić 6, Kragujevac, Serbia, E-mail: gordic@kg.ac.rs;

[5] 0000-0001-6489-2632, Faculty of Engineering, Sestre Janjić 6, Kragujevac, Serbia, E-mail: vladimir.vukasinovic@kg.ac.rs;

1. Introduction

Residential heating boilers burn fuels to heat water, which flows through a network of pipes and radiators to warm the house [1]. One type of residential heating boiler characterized by its high efficiency is the gasification boiler. Gasification boilers operate with an efficiency of around 85% [2] compared to a classic wood boiler with an efficiency of around 63% [3]. The gasification boilers use a controlled amount of oxygen and precisely defined temperatures to transform the solid biomass into gas, which is later combusted to generate the needed heat [4]. The technology behind gasification boilers is called biomass gasification – a thermochemical conversion of organic feedstock under high-temperature conditions, through which biomass is converted to syngas. Syngas composition varies, but it is mainly composed of CO, H_2, N_2, CO_2, and some hydrocarbons (CH_4, C_2H_4, C_2H_6, etc.) [5].

A variety of papers have investigated gasification boilers and attempted to optimize their operation and design. The IEA Bioenergy annual report [6] analyzed the product spectrum (organics, char, gas, water) from fast pyrolysis of aspen poplar wood, depending on process temperature. It was shown that with an increase in temperature, the yield of gas also increases. Similar research was done by Raibhole and Sapali [7], namely, they investigated how the flow rate of oxygen influenced the syngas composition. They concluded that the optimal mass flow of oxygen is around 8 kilograms per hour, when the participation of H_2 in syngas is the highest. Karmarković et al. [8] investigated the combustion chamber of the gasification boiler to find its optimal design. Drosatos et al. [9] described the computational fluid dynamics simulation of syngas combustion and the heat transfer in a domestic wood gasification boiler to further optimize its operation. Hopan et al. [10] investigated emissions from 111 measurements on solid fuel household boilers, among which was a hefty number of gasification boilers. One of the conclusions was that emissions-wise, a significant improvement was observed when the gasification boiler was operated by a trained operator.

Overall, regardless of the type of boiler, the heated water is kept in the boiler water wall, hereinafter referred to as the “water chamber” (Fig. 1). To the authors’ knowledge, the pressure of 3 bars is considered as critical pressure of the water in the water chamber, which triggers the activation of the safety valve. This paper investigates how the critical pressure of the water of 3 bars will influence the water chamber with a wall thickness of 5 millimeters, and the possibility of mitigating the displacements without increasing the thickness of the wall.

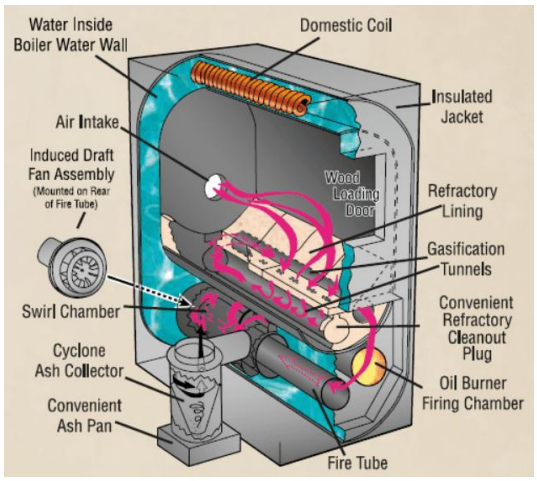

Fig. 1. Section view of a gasification boiler [11]

2. Materials and methods

The three-dimensional model of the water chamber (Fig. 2) and the static analysis were done in the "CATIA V5R21" software. There is a variety of studies that used CATIA for modeling and analysis. For example, Mohamad et al. [12] did a design and static structural analysis of a race car chassis using CATIA, Pinca-Bretotean and Chete [13] did a static analysis of a rolling chassis, Anggono and Riyadi did a finite element analysis of a truck frame [14], Hernandes et al. [15] examined the structural optimization using CATIA finite element analysis and optimization.

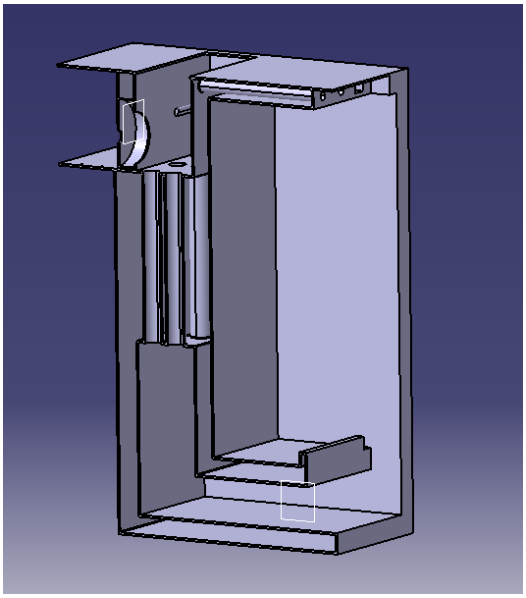

Fig. 2. Three-dimensional model of the water chamber

To give a better insight into the analyzed water chamber, the characteristics of the domestic gasification boiler are shown in Table 1.

Table 1. Characteristics of the analyzed domestic gasification boiler

Power	*20 kW*
Boiler dimensions	*H: 1412 mm, W: 984 mm, L: 841 mm*
Gasification chamber dimensions	*H: 600 mm, W: 500 mm, L: 500 mm*
Gasification chamber volume	*150 l*
Diameter of the flue pipe	*80 mm*
Water flow rate	*0.238 l/s*

The rendered model of the analyzed boiler is given in Fig. 3.

Fig. 3. Rendered model of the analyzed boiler

3. Results

The first iteration of the static analysis of the original water chamber under given pressure resulted in a transitional displacement magnitude of 10.28 millimeters (Fig. 4).

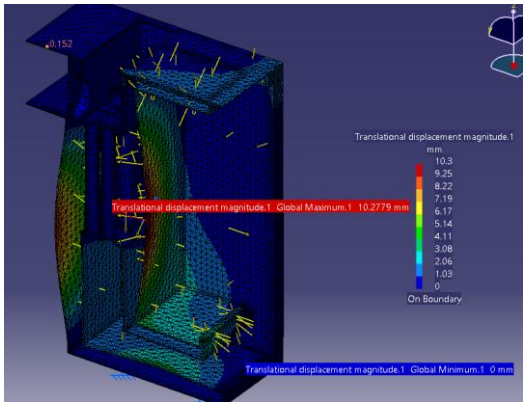

Fig. 4. Static analysis – first iteration

To mitigate these displacements, the chamber design was adapted by adding stiffening rods (Fig. 5). Subsequently, the second iteration of the static analysis revealed relocated, but decreased, displacements with a local maximum of 4.29 millimeters.

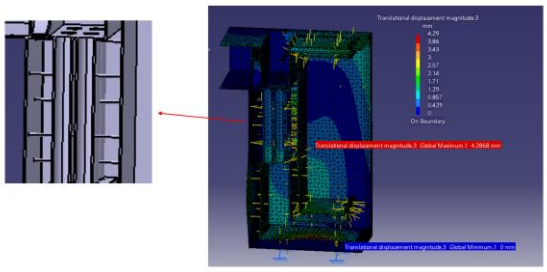

Fig. 5. Static analysis – second iteration

The stiffening rods were added in every following iteration at the place of maximal local displacements. Analogously, the third iteration (Fig. 6) resulted in local maximal displacement of 4.15 mm.

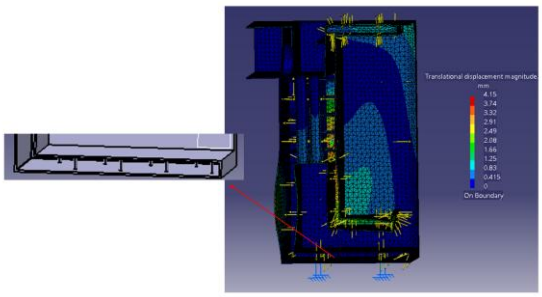

Fig. 6. Static analysis – third iteration

In the fourth iteration, the displacements were relocated with a maximal intensity of 4.29 millimeters (Fig. 7).

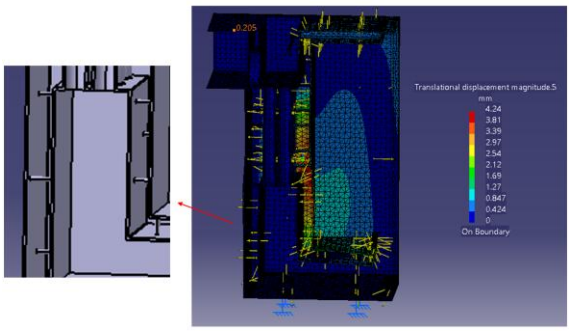

Fig. 7. Static analysis – fourth iteration

The same scenario happened two more times (Fig. 8 and Fig. 9) with transitional displacement magnitudes of 4.29 (fifth iteration) and 1.39 millimeters (sixth iteration).

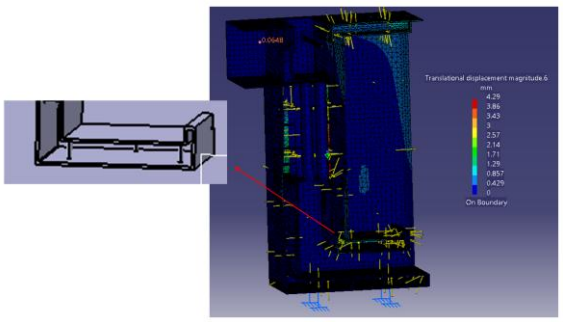

Fig. 8. Static analysis – fifth iteration

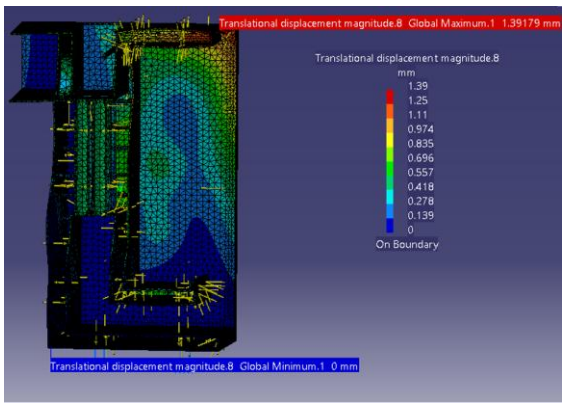

Fig. 9. Static analysis – sixth iteration

After six iterations of static analysis of the water chamber, the non-critical values of displacements were obtained (1.39 millimeters), consequently, defining the final design of the chamber (Fig. 10). Accordingly, it was proven that displacement mitigation of the water chamber is possible using only stiffening rods, i.e., without increasing the wall thickness.

Fig. 10. Final water chamber design

4. Conclusion

The object of the analysis was a water chamber of a domestic gasification boiler. The water chamber was tested at 3 bar water pressure. The first analysis resulted in critical displacements of around 10.3 millimeters, which led to the conclusion that the water chamber needs a redesign.

The redesign was done in six iterations. At every iteration, stiffening rods were added at the place of the highest displacements. The last iteration resulted in a non-critical displacement of 1.39 millimeters. The analysis as a whole showed that the mitigation of the displacements is possible without increasing the wall thickness, i.e., using only stiffening rods.

References

[1] acwholesalers. https://www.acwholesalers.com/Weil-McLain-381359305/p175679.html. Accessed August 27, 2025.

[2] Alternate Heating. Wood Gasification as Next-Generation Wood Burning Technology. https://alternateheatingsystems.com/resources/blog/wood-gasification-as-next-generation-wood-burning-technology/. Accessed August 28, 2025..

[3] Biomass Magazine. EPA Lists Efficiencies of Qualified Outdoor Boilers. https://biomassmagazine.com/articles/epa-lists-efficiencies-of-qualified-outdoor-boilers-10263. Accessed August 28, 2025.

[4] Green Power. What is a “real pyrolysis boiler”. https://greenpower.equipment/articles/what-is-a-real-pyrolysis-boiler/. Accessed August 28, 2025.

[5] Zhang, Y., Cui, Y., Chen, P., Liu, S., Zhou, N., Ding, K., et al. Gasification Technologies and Their Energy Potentials. *Sustainable Resource Recovery and Zero Waste Approaches,* 2019, 193–206. https://doi.org/10.1016/B978-0-444-64200-4.00014-1

[6] IEA Bioenergy Annual report 2006. https://www.ieabioenergy.com/wp-content/uploads/2013/10/IEA-Bioenergy-2006-Annual-Report.pdf. Accessed August 28, 2025.

[7] Raibhole, V.N. & Sapali, S.N. Simulation of biomass gasification with oxygen/air as gasifying agent by ASPEN plus. *Advanced Materials Research*, 2013, 622-623:633–8. https://doi.org/10.4028/WWW.SCIENTIFIC.NET/AMR.622-623.633.

[8] Karmarković, R., Novčić, Đ., Nikolić, M., Karamarković, M., Šimunović, D. Eksperimentalno ispitivanje gasifikacionog kotla: dizajn komore za sagorevanje. *Procesna Tehnika,* 2018, 30, 1, 20–26. https://doi.org/10.24094/PTC.018.30.1.20 .

[9] Drosatos, P., Nesiadis, A., Nikolopoulos, N., Margaritis, N., Grammelis, P., Kakaras, E. CFD Simulation of Domestic Gasification Boiler. *Journal of Energy Engineering* 2016, 143, 2. https://doi.org/10.1061/(ASCE)EY.1943-7897.0000406.

[10] Hopan, F., Chmelář, M., Kremer, J., Dej, M., Vojtíšek-Lom, M., Vicente, ED., et al. In-situ investigation of real-world emissions from 111 measurements on solid fuel household boilers. *Science of The Total Environment,* 2025, 981. https://doi.org/10.1016/J.SCITOTENV.2025.179564.

[11] Alternate Heating Systems. https://b2396119.smushcdn.com/2396119/wp-content/uploads/2019/10/small-WG-no-top-feed.png?lossy=2&strip=1&webp=1. Accessed August 28, 2025.

[12] Mohamad, M. L., Rahman, M. T. A., Khan, S. F., Basha, M. H., Adom, A. H., Hashim, M. S.M. Design and static structural analysis of a race car chassis for Formula Society of Automotive Engineers (FSAE) event. *Journal of Physics: Conference Series*, 2017. https://doi.org/10.1088/1742-6596/908/1/012042.

[13] Pinca-Bretotean, C. & Chețe, G. Static Analysis Of A Rolling Chassis Using Catia V5, *International Journal of Engineering*, 2012, ISSN 1584-2673.

[14] Anggono, A. D., Riyadi, T. W. B. Finite element analysis of truck frame by using CATIA V5. *AIP Conference Proceedings*, 2018, 1977. https://doi.org/10.1063/1.5042949.

[15] Hernandes, J. A., Ferreira, R. T. L., De Faria, A. R., Meleiro, R.M. An assessment of structural optimization using Catia V5. *SAE Technical Papers*, 2008. https://doi.org/10.4271/2008-36-0183.

Original scientific paper DOI: 10.46793/41DAS2025.131K

INFLUENCE OF FEED RATE ON SURFACE ROUGHNESS OF AL6088 ALLOY IN THE BALL BURNISHING PROCESS

Vladimir KOČOVIĆ[1], Dragan DŽUNIĆ[2], Sonja KOSTIĆ[3], Živana JOVANOVIĆ PEŠIĆ[4], Milan ĐORĐEVIĆ[5], Ljiljana BRZAKOVIĆ[6], Đorđe VUKELIĆ[7]

[1] 0000-0003-1231-0041, Faculty of Engineering, Sestre Janjić 6, Kragujevac, Serbia, E-mail: vladimir.kocovic@kg.ac.rs

[2] 0000-0002-1914-1298, Faculty of Engineering, Sestre Janjić 6, Kragujevac, Serbia, E-mail: dzuna@kg.ac.rs

[3] 0000-0002-6120-6139, Academy of Professional Studies Šumadija - Department in Kragujevac, Kosovska 8, Kragujevac, Serbia, E-mail: skostic@asss.edu.rs

[4] 0000-0002-1373-0040, Faculty of Engineering, Sestre Janjić 6, Kragujevac, Serbia, E-mail: zixi90@gmail.com

[5] 0000-0001-5941-3262, Academy of Professional Studies Šumadija - Department in Kragujevac, Kosovska 8, Kragujevac, Serbia, E-mail: mdjordjevic@asss.edu.rs

[6] 0000-0003-0583-0583, Academy of Professional Studies Šumadija - Department in Trstenik, Radoja Krstića 19, Trstenik, Serbia, E-mail: ljbrzakovic@asss.edu.rs

[7] 0000-0003-2420-6778, Faculty of Technical Sciences, Trg Dositeja Obradovića 6, Novi Sad, Serbia, E-mail: vukelic@uns.ac.rs

1. Introduction

Ball burnishing is a cold surface finishing process used to improve the roughness and other surface characteristics of aluminum alloys, resulting in enhanced wear, corrosion, and fatigue resistance. The process is based on the plastic deformation of surface irregularities using a hard, polished ball that is pressed against the workpiece under controlled forces.

The key ball burnishing parameters that significantly influence the final surface roughness of aluminum include the applied force, burnishing speed, number of passes, and lubrication conditions. Studies have shown that multiple passes increase surface smoothness; however, beyond a certain threshold, additional passes do not yield substantial improvements due to saturation of plastic deformation. Moreover, moderate force levels (50–300 N) combined with low burnishing speeds (~0.05 mm/rev) have demonstrated the best results in reducing the surface roughness parameter Ra.

Burnishing processes - including ball, roller, and diamond burnishing - are recognized as effective methods for enhancing the surface properties of aluminum alloys, particularly in terms of roughness reduction and hardness improvement.

Asadbeygi et al. experimentally investigated and optimized the influence of burnishing process parameters on aluminum alloy 2036, achieving a significant decrease in roughness and an increase in hardness [1]. Similarly, Cagan focused on the aluminum–lithium alloy Al8090, analyzing the effects of burnishing force, burnishing speed, and number of passes, comparing results under dry conditions and with minimum quantity lubrication (MQL), while also evaluating environmental aspects [2].

Ferencsik and Varga optimized diamond burnishing of EN AW-2011 alloy, providing detailed insights into the dependence of final roughness on selected process parameters [3]. Yuan et al. applied chaos theory to analyze the nonlinear characteristics of surface roughness in aluminum alloys, showing that burnishing parameters strongly influence surface micro-geometry [4].

Özkul [5] confirmed that ball burnishing substantially improves the surface quality of Al6013 alloy, whereas Dimitrov developed a digital model of the process - based on experiments with bronze and aluminum alloys - for parameter optimization using artificial intelligence [6]. Labuda et al. investigated burnishing of EN AW-6060 aluminum tubes, demonstrating improvements

in hardness, roughness parameters, and the material ratio of welded joints [7].

A comparative study by Harish Shivalingappa [8] examined the differences between ball and roller burnishing for Al2024 alloy, while Swirad reported a reduction in surface topography amplitude of up to 94%, providing a detailed analysis of changes in areal textures [9]. Amdouni et al, using response surface methodology, modeled and optimized ball burnishing of aluminum alloy 2017A-T451, identifying optimal parameters for reducing roughness and increasing microhardness [10].

Overall, the reviewed literature confirms that optimizing burnishing process parameters - including force, speed, number of passes, and lubrication conditions - can lead to substantial improvements in the surface integrity of aluminum alloys. These findings provide a solid foundation for further research aimed at tailoring the process to specific technical requirements and sustainable manufacturing practices.

The authors in this paper [11, 12, 13, 14, 15] address the burnishing process and the influence of its parameters on the surface finish quality of various materials, including wood, aluminum alloys, and steel alloys.

In this study, experimental investigations were carried out on Al6088 alloy using a specially designed ball burnishing tool on a universal lathe. The aim was to analyze the influence of feed rate on surface roughness parameters (Ra and Rz) and to evaluate surface characteristics through Abbott–Firestone (bearing area) curves.

2. Experimental Procedure

The experimental investigations were carried out on a universal lathe Pus-1500. The work material was Al6088 aluminum alloy with a diameter of 80 mm, selected to minimize elastic deformation under the penetration force of the ball. The workpiece was clamped in a three-jaw chuck and additionally supported by a tailstock center, which further reduced elastic deformation.

Preliminary machining was performed in the longitudinal direction using a cemented carbide tool with positive cutting geometry. The cutting parameters were a spindle speed of 500 rpm and a feed of 0.2 mm/rev. After preparation, surface plastic deformation was carried out with a specially designed tool for the ball burnishing process. Burnishing was performed using a steel ball of 10 mm diameter at a penetration depth of 0.05 mm.

The aim of the experiments was to investigate the influence of feed rate on the surface quality achieved by ball burnishing. The workpiece length was divided into five cylindrical sections, each 15 mm long. The first section (labeled 0) served as the reference surface and was not subjected to burnishing. Its surface roughness was measured in five zones. The other four sections were burnished with feed rates of 0.05 mm/rev, 0.08 mm/rev, 0.1 mm/rev, and 0.28 mm/rev, respectively (Fig. 1). Roughness measurements were performed in the same way as for the reference section, in five radial zones, using an INSIZE ISR C-002 profilometer.

Fig. 1. Surface of Al6088 workpiece with cylindrical sections treated by ball burnishing under different feed rates

3. Results and Discussion

The results of surface roughness measurements obtained by ball burnishing at different feed rates are presented in Table 1. For each feed, measurements were performed at five circumferential positions (1, 3, 5, 7, and 9) to ensure repeatability. Presented values correspond to the average roughness parameters (Ra and Rz) with standard deviations.

Table 1. Average values of Ra and Rz with standard deviations for different feed rates

Feed rate (mm/rev)	Ra (μm) ± st.dev	Rz (μm) ± st.dev
0.05	1.40 ± 0.15	6.45 ± 0.30
0.08	1.48 ± 0.09	6.80 ± 0.28
0.10	1.62 ± 0.09	7.47 ± 0.71
0.28	1.71 ± 0.06	8.63 ± 1.17
Unburnished	1.77 ± 0.25	8.44 ± 1.19

Fig. 2 and 3 illustrate the relationship between feed rate and the roughness parameters Ra and Rz. A clear decreasing trend is observed as feed decreases. The lowest values are achieved at 0.05 mm/rev, where Ra and Rz are significantly reduced compared to the unburnished reference surface. This confirms that feed rate is the dominant factor in improving surface finish.

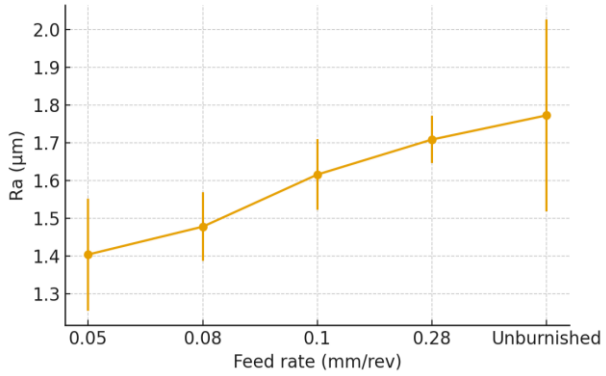

Fig 2. Average Ra values versus feed rate with standard deviation

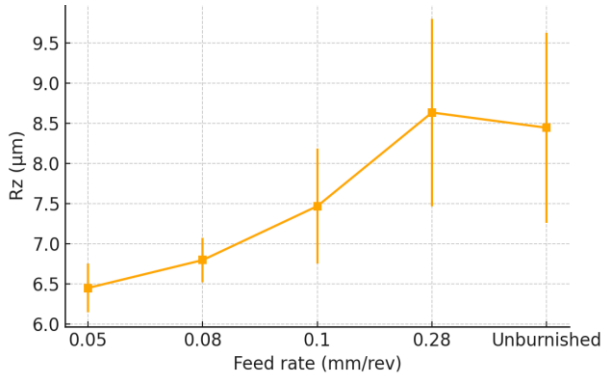

Fig. 3. Average Rz values versus feed rate with standard deviation

In addition to average roughness, Fig. 4 presents the material ratio curves (Abbott-Firestone curves) for all investigated feed rates. The unburnished surface exhibits the steepest slope and highest profile heights, indicating pronounced irregularities. Burnished surfaces, especially at 0.05 mm/rev, show smoother curves and lower Rmax values. This demonstrates an improved load-bearing capacity and higher wear resistance potential, which aligns with the expected benefits of ball burnishing.

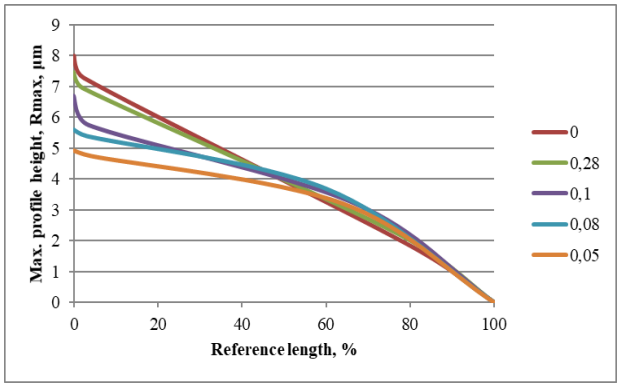

Fig. 4. Material ratio curves (Abbott-Firestone) for different feed rates

The experiments confirm that decreasing the feed rate in ball burnishing significantly improves surface integrity. At the optimal feed of 0.05 mm/rev, the surface roughness parameter Ra was reduced by ~21% compared to the unburnished condition, while Rz decreased by ~24%. Higher feed rates (0.28 mm/rev) provided only slight improvements over the reference surface.

These findings are consistent with the literature, where low feed rates are reported to yield the best surface quality [1, 10]. The improved Abbott-Firestone curves confirm the enhanced functional properties of burnished surfaces, such as increased load-bearing capacity and improved wear resistance [5, 9].

Overall, the obtained results demonstrate that feed rate plays a crucial role in ball burnishing. Lower values (0.05–0.08 mm/rev) should be applied when the goal is to achieve minimal roughness and optimal surface integrity of aluminum alloys

4. Conclusions

This study investigated the influence of feed rate on the surface quality of Al6088 alloy subjected to ball burnishing. Based on the experimental results, the following conclusions can be drawn:

- ✓ Ball burnishing significantly improves surface roughness parameters compared to the unburnished condition.
- ✓ The feed rate was confirmed as the dominant process parameter affecting surface finish.
- ✓ The lowest values of Ra (1.40 µm) and Rz (6.45 µm) were obtained at the feed of 0.05 mm/rev, representing reductions of approximately 21% and 24% compared to the unburnished surface.
- ✓ The Abbott-Firestone (bearing area) curves showed that surfaces treated with lower feed rates have improved load-bearing capacity and reduced profile heights, which enhances their functional performance.
- ✓ The repeatability of measurements at multiple circumferential positions confirmed the reliability of the results.

Overall, the findings indicate that lower feed rates (0.05–0.08 mm/rev) should be applied to achieve optimal surface integrity of aluminum alloys processed by ball burnishing. These results are consistent with previous research and provide a solid basis for further optimization of burnishing parameters in sustainable manufacturing practices.

Acknowledgement

This paper is the result of research conducted under the author's contract No. 451-03-137/2025-03/200107, dated February 4, 2025, and partly supported by the Ministry of Science, Technological Development and Innovation, Republic of Serbia.

References

[1] Asadbeygi, A.; Rezaei, H.; Jalali Aghchai, A. Experimental investigation and optimization of the effect of burnishing process parameters on surface roughness and hardness of Al 2036. In Proceedings of the ASME 2023 International Mechanical Engineering Congress and Exposition, Volume 3: Advanced Manufacturing, New Orleans, Louisiana, USA, 29 Oct–2 Nov 2023; ASME: New York, NY, USA, V003T03A022. https://doi.org/10.1115/IMECE2023-111731

[2] Cagan, S.C. Surface quality and environmental impact analysis of ball burnishing on Al8090 aluminum–lithium alloy. Materials, 2025, 18, 1252. https://doi.org/10.3390/ma18061252

[3] Ferencsik, V.; Varga, G. The influence of diamond burnishing process parameters on surface roughness of low-alloyed aluminium workpieces. Machines, 2022, 10, 564. https://doi.org/10.3390/machines10070564

[4] Yuan, Z.; Zhou, Z.; Jiang, Z.; et al. Evaluation of surface roughness of aluminum alloy in burnishing process based on chaos theory. Chinese Journal of Mechanical Engineering, 2023, 36, 2. https://doi.org/10.1186/s10033-022-00828-8

[5] Özkul, İ. Ball burnishing process effects on surface roughness for Al 6013 alloy. Turkish Journal of Engineering, 2019, 3(1), 9–13. https://doi.org/10.31127/tuje.421135

[6] Dimitrov, D.M. Digital modeling and AI-driven optimization of ball burnishing process parameters. Materials Research Proceedings, 2024. https://doi.org/10.21741/9781644903377-46

[7] Labuda, W.; Wieczorska, A.; Charchalis, A. The influence of the burnishing process on the change in surface hardness, selected surface roughness parameters and the material ratio of the welded joint of aluminum tubes. Materials, 2024, 17, 43. https://doi.org/10.3390/ma17010043

[8] Harish; Shivalingappa, D. The influence of ball and roller burnishing process parameters on surface integrity of Al 2024 alloy. Materials Today: Proceedings, 2020. https://doi.org/10.1016/j.matpr.2020.02.614

[9] Swirad, S. Changes in areal surface textures due to ball burnishing. Materials, 2023, 16, 5904. https://doi.org/10.3390/ma16175904

[10] Amdouni, H.; Bouzaiene, H.; Montagne, A.; et al. Modeling and optimization of a ball-burnished aluminum alloy flat surface with a crossed strategy based on response surface methodology. International Journal of Advanced Manufacturing Technology, 2017, 88, 801–814. https://doi.org/10.1007/s00170-016-8817-8

[11] Tadic, B.; Todorovic, P.M.; Luzanin, O.; et al. Using specially designed high-stiffness burnishing tool to achieve high-quality surface finish. International Journal of Advanced Manufacturing Technology, 2013, 67, 601–611. https://doi.org/10.1007/s00170-012-4508-2

[12] Randjelovic, S.; Tadic, B.; Todorovic, P.M.; et al. Modelling of the ball burnishing process with a high-stiffness tool. International Journal of Advanced Manufacturing Technology, 2015, 81, 1509–1518. https://doi.org/10.1007/s00170-015-7319-4

[13] Babic, M.; Kocovic, V.; Vukelic, D.; Mihajlovic, G.; Eric, M.; Tadic, B. Investigation of ball burnishing processing on mechanical characteristics of wooden elements. Proceedings of the Institution of Mechanical Engineers, Part C: Journal of Mechanical Engineering Science, 2016, 231(1), 120–127. https://doi.org/10.1177/0954406216641711

[14] Tadic, B.; Randjelovic, S.; Todorovic, P.; Zivkovic, J.; Kocovic, V.; Budak, I.; Vukelic, D. Using a high-stiffness burnishing tool for increased dimensional and geometrical accuracies of openings. Precision Engineering, 2016, 43, 335–344. https://doi.org/10.1016/j.precisioneng.2015.08.014

[15] Kanovic, Z.; Vukelic, D.; Simunovic, K.; Prica, M.; Saric, T.; Tadic, B.; Simunovic, G. The modelling of surface roughness after the ball burnishing process with a high-stiffness tool by using regression analysis, artificial neural networks, and support vector regression. Metals, 2022, 12(2), 320. https://doi.org/10.3390/met12020320

41st Danubia-Adria Symposium Advances in Experimental Mechanics
September 23-26, 2025, Kragujevac, Serbia

Original scientific paper DOI: 10.46793/41DAS2025.135JP

EFFECT OF ELECTRON BEAM PROCESSING PARAMETERS ON THE SURFACE ROUGHNESS OF TITANIUM SAMPLES: PART II

Živana JOVANOVIĆ PEŠIĆ[1], Aleksandra VULOVIĆ[2], Strahinja MILENKOVIĆ[3], Đorđe ILIĆ[4], Dragan DŽUNIĆ[5],

[1] 0000-0002-1373-0040, Faculty of Engineering, Sestre Janjić 6, Kragujevac, Serbia, E-mail: zixi90@gmail.com

[2] 0000-0002-6726-3134, Faculty of Engineering, Sestre Janjić 6, Kragujevac, Serbia, E-mail: aleksandra.vulovic@kg.ac.rs

[3] 0000-0002-5822-4846, Institute for Information Technologies, Jovana Cvijića bb, Kragujevac, Serbia, E-mail: strahinja.milenkovic@fink.rs

[4] 0009-0007-3907-8023, Faculty of Engineering, Sestre Janjić 6, Kragujevac, Serbia, E-mail: djordje.ilic@kg.ac.rs

[5] 0000-0002-1914-1298, Faculty of Engineering, Sestre Janjić 6, Kragujevac, Serbia, E-mail: dzuna@kg.ac.rs

1. Introduction

Titanium and its alloys are widely recognized as preferred materials in biomedical engineering, especially for orthopedic implants such as artificial hip joints, owing to their outstanding biocompatibility, corrosion resistance, low density, and favorable mechanical characteristics [1, 2]. Among them, the Ti-6Al-4V alloy is particularly prominent for hip implant applications because of its superior strength-to-weight ratio, high resistance to corrosion in physiological environments, and strong capacity to facilitate osseointegration [3]. In addition, titanium possesses a comparatively low elastic modulus relative to other metallic biomaterials, which helps to mitigate stress shielding and ensures more effective load transfer to the surrounding bone [4].

Although titanium offers many beneficial properties, the clinical performance of titanium implants is strongly influenced by the material's surface characteristics. Parameters such as surface roughness, chemistry, and topography are widely recognized as key determinants of biological interactions at the bone–implant interface [5, 6]. Among these, surface roughness is particularly significant, as it regulates cellular responses, impacting adhesion, proliferation, differentiation, and ultimately the integration of bone tissue [7].

A substantial body of research indicates that moderately rough surfaces (with an average roughness, Ra, of 1–2 μm) support osteoblast differentiation and improve bone-to-implant contact when compared to both smoother and excessively rough surfaces [8]. In contrast, overly smooth surfaces may promote fibrous tissue encapsulation, whereas excessively rough ones can provoke inflammatory reactions and accelerated wear [9]. Additionally, surface roughness influences the mechanical interlocking between the implant and bone, a key factor for achieving primary stability and reducing micromotion during the initial healing phase [10]. Inadequate primary stability can delay or prevent osseointegration, ultimately jeopardizing the long-term success of the implant.

Recognizing these critical implications, considerable efforts have been devoted to the development of surface modification techniques to optimize implant surface properties. Conventional approaches, including grit blasting, acid etching, anodization, and plasma spraying, have been widely employed to enhance the surface characteristics of titanium [11, 12]. In recent years, electron beam processing has emerged as a promising technique, offering precise control over surface morphology, microstructure, and roughness, while minimizing the risk of chemical contamination [13].

A comprehensive understanding of the relationship between electron beam processing parameters—particularly the number of passes—and surface roughness is fundamental to the design of implants with superior biological performance. In this context, the present study provides a systematic evaluation of the effect of pass number on the surface roughness of titanium specimens processed under a fixed beam current of 1.0 mA, offering

critical insights into the refinement of surface modification strategies aimed at enhancing clinical outcomes in hip joint arthroplasty.

In summary, the experimental setup maintained a constant electron beam current of 1.0 mA while systematically varying the number of passes (2, 4, 8, and 16) to investigate its influence on the surface roughness of titanium samples.

2. Materials and Methods

Commercially available titanium alloy was selected for specimen preparation. Rectangular samples with dimensions of 70 mm × 20 mm × 5 mm were machined and subsequently subjected to mechanical grinding and polishing using P4000-grade silicon carbide abrasive paper to ensure a uniform initial surface finish [14]. Following polishing, all specimens underwent ultrasonic cleaning in ethanol and were dried with compressed air to eliminate residual surface contaminants.

Surface modification was conducted using a Probeam EBG 45-150 K14 electron beam welding system. Each specimen was subdivided into four treatment zones, each measuring 10 mm × 10 mm, and exposed to 2, 4, 8, or 16 electron beam passes, respectively (Fig. 1). The processing was performed at room temperature under high-vacuum conditions, with the beam current fixed at 1.0 mA and an acceleration voltage ranging from 60 to 150 kV. A raster-scanning approach was employed to ensure homogeneous surface modification across the designated treatment areas.

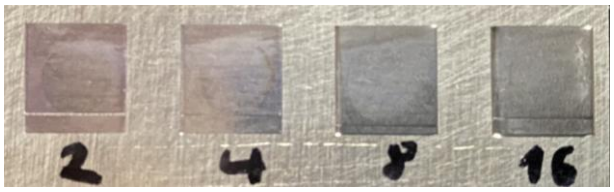

Fig. 1. Titanium specimens after electron beam processing

Surface roughness characterization was performed using an INSIZE ISR C-002 portable contact profilometer, equipped with a diamond-tipped stylus to trace the surface topography and detect vertical displacements for precise profiling. Measurements were conducted in accordance with ISO 4287 standards over a 4 mm evaluation length, with three independent measurements recorded for each treated zone to ensure representative data. The acquired roughness parameters served as the basis for a quantitative assessment of the influence of electron beam pass number on titanium surface properties.

3. Results and Discussion

Fig. 2 shows the surface roughness profile of the polished titanium specimen prior to electron beam processing, serving as a baseline for subsequent comparisons. The polished surface exhibits relatively low roughness, with average values of Ra ≈ 0.65 μm and Rz ≈ 4.43 μm, indicating a smooth and uniform finish suitable for surface modification studies.

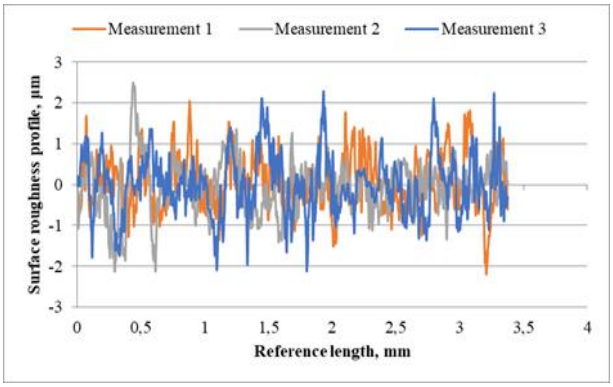

Fig. 2. Surface roughness profile of the polished titanium specimen prior to electron beam processing

Fig. 3–6 present the roughness profiles of samples subjected to 2, 4, 8, and 16 electron beam passes at a constant beam current of 1.0 mA.

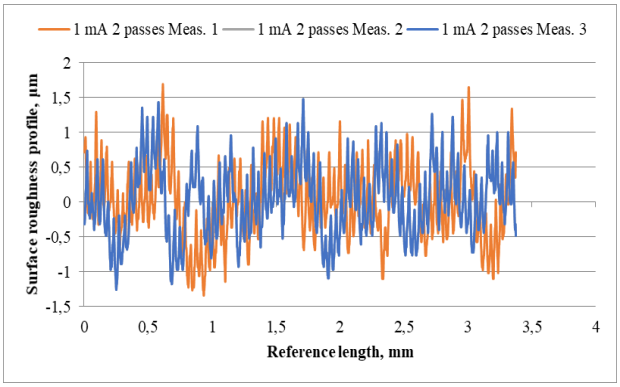

Fig. 3. Surface roughness profile of the titanium specimen after 2 electron beam passes at 1.0 mA

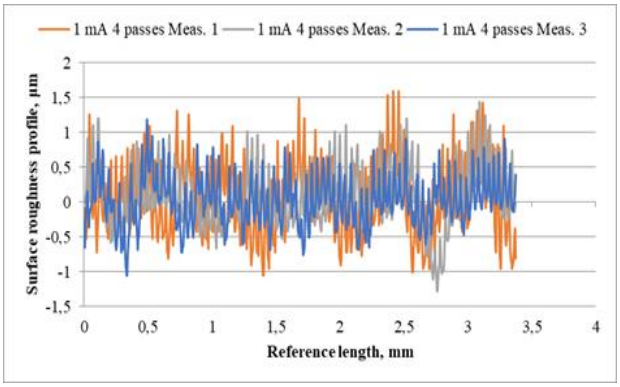

Fig. 4. Surface roughness profile of the titanium specimen after 4 electron beam passes at 1.0 mA

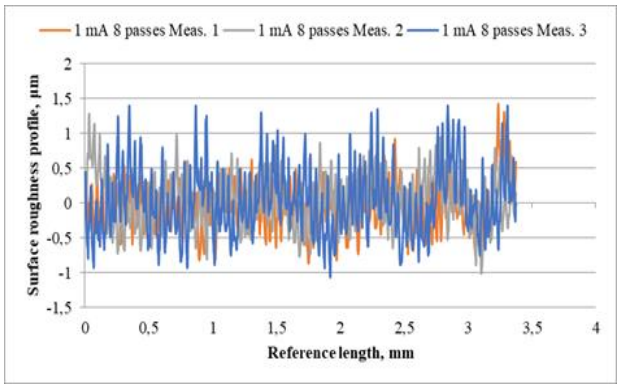

Fig. 5. Surface roughness profile of the titanium specimen after 8 electron beam passes at 1.0 mA

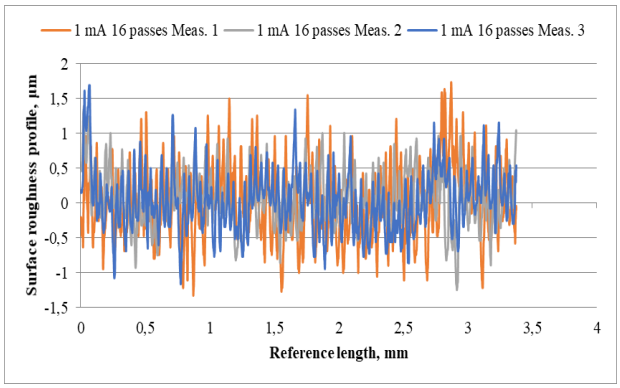

Fig. 6. Surface roughness profile of the titanium specimen after 16 electron beam passes at 1.0 mA

Quantitative analysis of the roughness parameters (Table 1) reveals a clear influence of pass number on surface topography. After two passes, both Ra and Rz decrease significantly (Ra ≈ 0.50 µm, Rz ≈ 2.83 µm), suggesting that localized melting and re-solidification during electron beam processing smoothen the initial asperities. Increasing the number of passes to four continues this trend (Ra ≈ 0.43 µm, Rz ≈ 2.54 µm), indicating progressive surface homogenization.

Table 1. Average surface roughness parameters (Ra and Rz) of titanium specimens subjected to electron beam processing with different numbers of passes at a constant beam current of 1.0 mA

Passes	Ra avg (µm)	Rz avg (µm)
0	0.655	4.429
2	0.498	2.832
4	0.431	2.535
8	0.373	2.351
16	0.432	2.848

The lowest roughness values are observed at eight passes (Ra ≈ 0.37 µm, Rz ≈ 2.35 µm), demonstrating that this processing condition achieves an optimal balance between energy input and surface reflow. However, with sixteen passes, a slight increase in both Ra and Rz is recorded (Ra ≈ 0.43 µm, Rz ≈ 2.85 µm), which may be attributed to cumulative thermal exposure, repeated remelting, and potential microstructural coarsening. This non-linear behavior highlights that increasing the number of passes beyond a certain threshold does not necessarily improve surface smoothness and may even reintroduce surface irregularities.

These findings align with literature reports indicating that surface modification via high-energy beams can initially level micro-asperities, but excessive energy input may lead to roughness recovery due to localized melting instabilities and solidification dynamics [13]. In comparison with conventional surface treatments such as grit blasting or acid etching, which can produce non-uniform surfaces and introduce chemical residues [11], electron beam processing provides precise control of surface morphology and reproducible roughness adjustment without contamination.

The measured Ra values remain below 1 µm across all samples, well within the range suitable for promoting osseointegration, as moderate roughness levels (Ra ≈ 1–2 µm) are often cited as optimal for bone–implant integration [8]. While the processed surfaces in this study are smoother than those typically achieved through mechanical or chemical texturing, the ability to finely tune surface roughness with electron beam passes demonstrates strong potential for optimizing implant surface properties.

4. Conclusions

This study systematically investigated the influence of electron beam processing parameters—specifically the number of passes—on the surface roughness of titanium specimens at a constant beam current of 1.0 mA. The findings demonstrate that the number of passes plays a critical role in controlling surface morphology, with a clear trend observed:

- ✓ Electron beam processing initially reduced both Ra and Rz values, with the lowest roughness achieved after eight passes (Ra ≈ 0.37 µm, Rz ≈ 2.35 µm).
- ✓ Increasing the number of passes beyond this point resulted in a slight roughness increase, likely due to cumulative thermal effects, repeated remelting, and microstructural coarsening.
- ✓ The process produced smooth, uniform surfaces without chemical contamination, demonstrating the high precision and controllability of electron beam surface modification.

These results indicate that electron beam processing offers a versatile and reproducible approach for tailoring implant surface characteristics, enabling fine adjustment of roughness to levels suitable for improved osseointegration and clinical performance. Future work will focus on correlating these topographical modifications with mechanical properties and biological responses to optimize surface treatments for orthopedic applications such as hip joint replacements.

Acknowledgement

The research presented in this paper was conducted within the project "Development and Optimization of Surface Topography for Improved Hip Implant Performance – DOST-HIP," supported by the Center for Scientific Research of the Serbian Academy of Sciences and Arts (SANU) and the University of Kragujevac.

References

[1] Long, M.; Rack, H.J. Titanium alloys in total joint replacement—a materials science perspective. Biomaterials, 1998, 19(18), 1621–1639. https://doi.org/10.1016/S0142-9612(97)00146-4

[2] Geetha, M.; Singh, A.K.; Asokamani, R.; Gogia, A.K. Ti based biomaterials, the ultimate choice for orthopaedic implants–A review. Progress in Materials Science, 2009, 54(3), 397–425. https://doi.org/10.1016/j.pmatsci.2008.06.004

[3] Niinomi, M. Mechanical properties of biomedical titanium alloys. Materials Science and Engineering: A, 1998, 243(1–2), 231–236. https://doi.org/10.1016/S0921-5093(97)00806-X

[4] Navarro, M.; et al. Biomaterials in orthopaedics. Journal of the Royal Society Interface, 2008, 5(27), 1137–1158. https://doi.org/10.1098/rsif.2008.0151

[5] Brunette, D.M. The effects of implant surface topography on the behavior of cells. The International Journal of Oral & Maxillofacial Implants, 1988, 3(4), 231–246.

[6] Tengvall, P.; Lundström, I. Physico-chemical considerations of titanium as a biomaterial. Clinical Materials, 1992, 9(2), 115–134. https://doi.org/10.1016/0267-6605(92)90056-Y

[7] Sharan, J.; Lale, S.; Koul, V.; Mishra, M.; Kharbanda, O. An overview of surface modifications of titanium and its alloys for biomedical applications. Trends in Biomaterials and Artificial Organs, 2015, 29, 176–187.

[8] Albrektsson, T.; Johansson, C. Osteoinduction, osteoconduction and osseointegration. European Spine Journal, 2001, 10(2), S96–S101. https://doi.org/10.1007/s005860100282

[9] Kienle, J.M.; Diefenbeck, L.; Schmidmaier, M. Biomaterials for bone implant coatings. Advanced Drug Delivery Reviews, 2015, 94, 280–295. https://doi.org/10.1016/j.addr.2015.04.013

[10] Szczęsny, G.; Kopec, M.; Politis, D.J.; Kowalewski, Z.L.; Łazarski, A.; Szolc, T. A review on biomaterials for orthopaedic surgery and traumatology: From past to present. Materials, 2022, 15(10), 3622. https://doi.org/10.3390/ma15103622

[11] Wennerberg, A.; Albrektsson, T. Effects of titanium surface topography on bone integration: A systematic review. Clinical Oral Implants Research, 2009, 20(s4), 172–184. https://doi.org/10.1111/j.1600-0501.2009.01775.x

[12] Variola, F.; Brunski, J.B.; Orsini, G.; Tambasco De Oliveira, P.; Wazen, R.; Nanci, A. Nanoscale surface modifications of medically relevant metals: State-of-the-art and perspectives. Nanoscale, 2011, 3(2), 335–353. https://doi.org/10.1039/C0NR00485E

[13] Bliznyuk, U.; Chernyaev, A.; Ipatova, V.; Nikitchenko, A.; Studenikin, F.; Zolotov, S. Electron beam processing of biological objects and materials. In Ion Beam Technology and Applications; Artun, O., Ed.; IntechOpen: London, UK, 2023. https://doi.org/10.5772/intechopen.112699

[14] Ramskogler, C.; Warchomicka, F.; Mostofi, S.; Weinberg, A.; Sommitsch, C. Innovative surface modification of Ti6Al4V alloy by electron beam technique for biomedical application. Materials Science and Engineering: C, 2017, 78, 105–113.

41st Danubia-Adria Symposium Advances in Experimental Mechanics
September 23-26, 2025, Kragujevac, Serbia

Original scientific paper

DOI: 10.46793/41DAS2025.139D

2D AXISYMMETRIC VS. 3D SOLID ELEMENT PHASE-FIELD DAMAGE MODELING

Vladimir DUNIĆ[1], Aleksandar BODIĆ[2], Miroslav Živković[3]

[1] 0000-0003-1648-1745, University of Kragujevac Faculty of Engineering, Sestre Janjić 6, Kragujevac, Serbia, E-mail: dunic@kg.ac.rs;

[2] 0000-0002-1713-6540, University of Kragujevac Faculty of Engineering, Sestre Janjić 6, Kragujevac, Serbia, E-mail: abodic@uni.kg.ac.rs;

[3] 0000-0002-0752-6289, University of Kragujevac Faculty of Engineering, Sestre Janjić 6, Kragujevac, Serbia, E-mail: miroslav.zivkovic@kg.ac.rs;

1. Introduction

Phase-field damage modeling (PFDM) is very popular among researchers and engineers, because it offers applications to various fields of interest. Investigating damage in structures and predicting its evolution, which can lead to material stiffness degradation and structural failure, is the most interesting aspect. Various research groups at the top world universities have implemented the latest findings into the commercial and research finite element method (FEM) codes, and the PFDM will probably be recognized technique for structural safety monitoring.

However, the practical application is in one of the top interests, but some disadvantages decrease the possibility of efficient and accurate FEM simulations. One of them is the need for a fine FE mesh in the zone where material damage is expected, which makes models with large numbers of degrees of freedom and huge computational time. In this scope, it is important to implement the PFDM for various types of finite elements such as 2D axisymmetric elements, which can decrease the size of the problem by modeling only a cross-section of the axisymmetric structure.

In this paper, we have implemented a previously developed PFDM theory into the 2D axisymmetric element and compared the simulation results to the 3D solid element for the well-known large strain circular bar example.

2. Phase-field damage model for 2D axisymmetric element

Recently developed, the critical-total strain based PFDM implementation, presented in [1], was introduced as a user-friendly approach which can be easily applied for simulation of damage evolution in ductile materials. The details are given in several papers published at conferences [2,3] and journals [1,4,5,6], but here, the main equation will be repeated. The internal potential energy consists of elastic, plastic and fracture parts as:

$$W_{int} = W_e + W_p + W_f. \tag{1}$$

The elastic strain energy is:

$$W_e = (1-d)^2 \frac{1}{2} \boldsymbol{\sigma}_0 : \boldsymbol{\varepsilon}_e, \tag{2}$$

where $\boldsymbol{\sigma}_0$ is the Cauchy stress tensor, $\boldsymbol{\varepsilon}_e$ is the elastic strain tensor, and d is damage variable. The plastic part of the internal strain energy is:

$$W_p = (1-d)^2 (\sigma_{yv} \bar{\varepsilon}_p + (\sigma_{y0,\infty} - \sigma_{yv}) \left(\bar{\varepsilon}_p + \frac{1}{n} e^{-n\bar{\varepsilon}_p} \right) + \frac{1}{2} H \bar{\varepsilon}_p^2), \tag{3}$$

where σ_{yv} is the yield stress, $\bar{\varepsilon}_p$ is the equivalent plastic strain, $\sigma_{y0,\infty}$ is the saturation hardening stress, n is the hardening exponent and H is the hardening modulus. The fracture strain energy density is:

$$W_f = G_v [d + \frac{l_c^2}{2} |\nabla d|^2], \tag{4}$$

where G_v is the specific fracture energy per unit volume and l_c is the characteristic length. By derivation of the equilibrium of external and internal potential energy, the final form of the equilibrium equation can be found as:

$$Div\boldsymbol{\sigma} + \boldsymbol{b} = 0. \tag{5}$$

The plasticity yielding condition law is:

$$\bar{\sigma}_{eq} - \sigma_{yv} - (\sigma_{y0,\infty} - \sigma_{yv})(1 - e^{-n\bar{\varepsilon}_p}) - H\bar{\varepsilon}_p = 0. \tag{6}$$

Finally, the phase-field damage evolution law can be derived as:

$$G_v [d - l_c^2 \nabla^2 d] + g'(d) \max (\psi_e + \psi_p - G_v/2) = 0, \tag{7}$$

where ψ_e and ψ_p are the effective elastic and plastic strain energy.

The critical fracture energy G_v can be calculated by finding the effective critical strain energy as $G_v/2$, what gives:

$$G_v = \frac{\sigma_{yv}^2}{E} + 2\sigma_{yv}\left(\varepsilon_{cr} - \frac{\sigma_{yv}}{E}\right) + 2\left(\sigma_{y0,\infty} - \sigma_{yv}\right)\left[\left(\varepsilon_{cr} - \frac{\sigma_{yv}}{E}\right) + \frac{1}{n}\left(e^{-n\varepsilon_{cr}} - e^{-n\frac{\sigma_{yv}}{E}}\right)\right] + H\left(\varepsilon_{cr}^2 - \frac{\sigma_{yv}^2}{E^2}\right). \quad (8)$$

where ε_{cr} is the critical total equivalent strain, and E is the elasticity modulus.

3. Finite element models and material parameters

The presented critical-total strain based PFDM is implemented into the software PAK-DAM v25 [7] for the 3D solid and 2D axisymmetric element. Both implementations can be tested for the well-known circular bar necking example [8]. For that purpose, a large strain von Mises plasticity constitutive model is used and logarithmic strain measure [9].

Dimensions of the half of the bar which is modeled by 2D axisymmetric and 3D solid elements are given as follows: bottom radius is 6.35mm, while the upper side is 1% larger – 6.4135mm, length is 26.67mm. The imperfection is prescribed to trigger the necking at the position where the radius is smaller. The 2D axisymmetric model has 96 elements with mid-side nodes which gives 345 nodes in total.

In Figure 1, the boundary and loading conditions for a 2D axisymmetric finite element model are given. A cross-section of the ¼ of the specimen is modeled, so the y-symmetry boundary conditions are prescribed at the bottom side, while the opposite side is loaded by prescribed displacements which are connected by equations in the y-direction to the node on the central axis. In Figure 2, the same data are given for the 3D solid finite element model. One quarter of the half of the bar is modeled while symmetry boundary conditions are prescribed at appropriate surfaces. On the bottom side, also, the y-symmetry boundary conditions are necessary as well as loading conditions defined by prescribed displacements. The 3D model has 648 finite elements with mid-side nodes, which gives in total of 3388 nodes. As it can be noticed, the 3D model is approximately 10 times larger, and refinement of the mesh for a more detailed simulation is practically impossible.

The simulation is performed by the Full Newton iterative method with line search. The solution is obtained in 40 steps with a displacement increment of 0.2 mm, up to the total displacement of 8 mm.

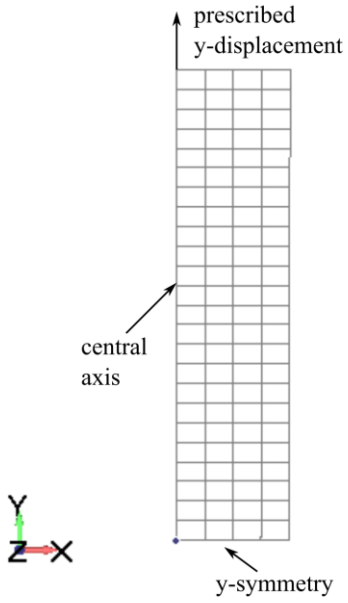

Fig. 1. 2D axisymmetric finite element model with boundary and loading conditions.

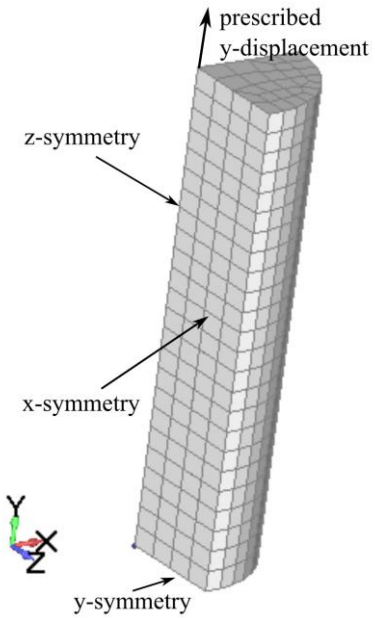

Fig. 2. 3D solid finite element model with boundary and loading conditions.

4. Simulation results

The simulation is performed to show the functionality of the critical-total strain based PFDM implementation into the both 2D axisymmetric and 3D solid finite elements in PAK-DAM v25 software [7].

Table 1. Material parameters

Parameter	Value	Parameter	Value
Young modulus	210.4 [GPa]	Exponential hardening	16.93 [-]
Poisson's ratio	0.3118 [-]	Linear hardening	0.12924 [-]
Yield stress	0.45 [GPa]	Critical eq. strain	1.2 [-]
Saturation stress	0.715 [GPa]	Characteristic length	0.5 [mm]

In Figure 3, the equivalent plastic strain field is given in 31. and 32. time step, as the critical strain is achieved at that moment.

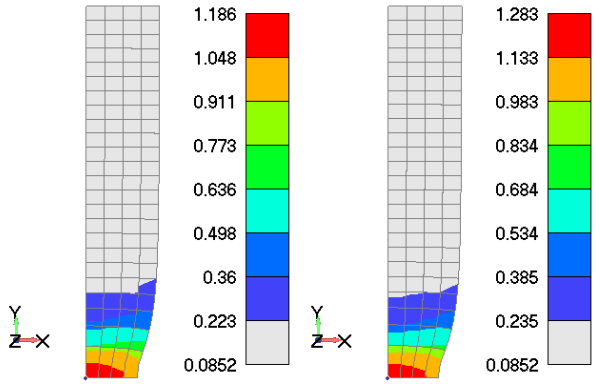

Fig. 3. Equivalent plastic strain field in 31 (left) and 32 (right) time steps for a 2D axisymmetric FE model.

In Figure 4, the damage field is given for the steps 32 and 33, as an important detail which verifies the control over the damage onset by critical equivalent strain.

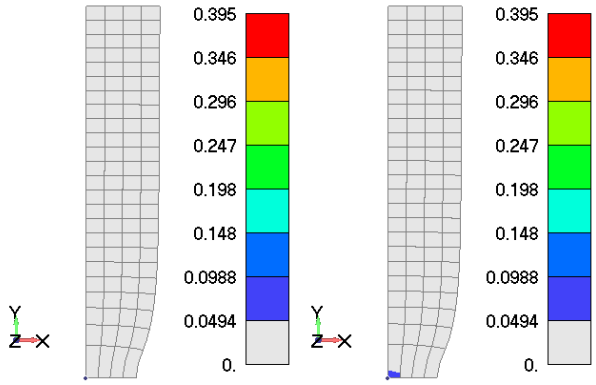

Fig. 4. Damage field in 32 (left) and 33 (right) time steps for a 2D axisymmetric FE model.

In Figure 5, the damage field is given for the last time step for both the 3D solid and 2D axisymmetric models to compare the obtained results.

In Figure 6, the equivalent plastic strain field is given for the last time step for both the 3D solid and 2D axisymmetric models to compare the obtained results.

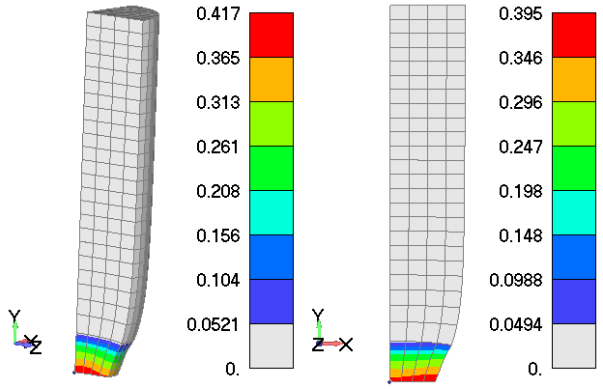

Fig. 5. Damage field in the last (40) time step for 3D solid (left) and 2D axisymmetric (right) FE model.

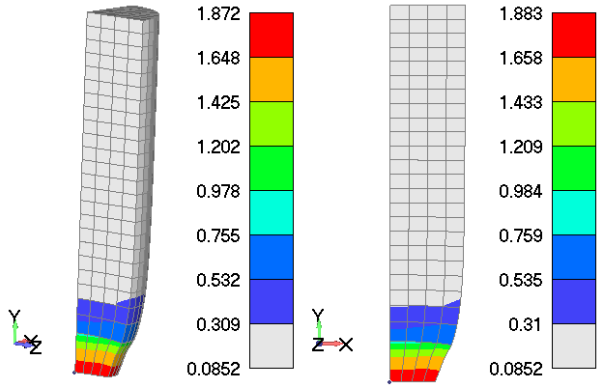

Fig. 6. Equivalent plastic strain field in the last (40) time step for 3D solid (left) and 2D axisymmetric (right) FE model.

In Figure 7, the damage field evolution at the end of the simulation is given for the last six time steps for the 2D axisymmetric model.

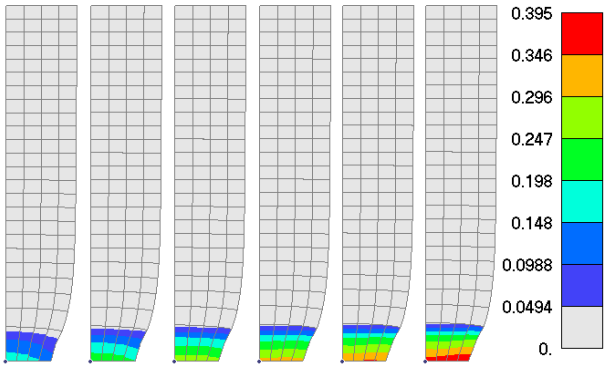

Fig. 7. Damage evolution in 2D axisymmetric FE model in the last six time steps (35-40 from left to right) of the simulation.

In Figure 8, the constraint force vs. displacement diagram at the upper side of the model is given for both the 3D solid and 2D axisymmetric models to compare the responses.

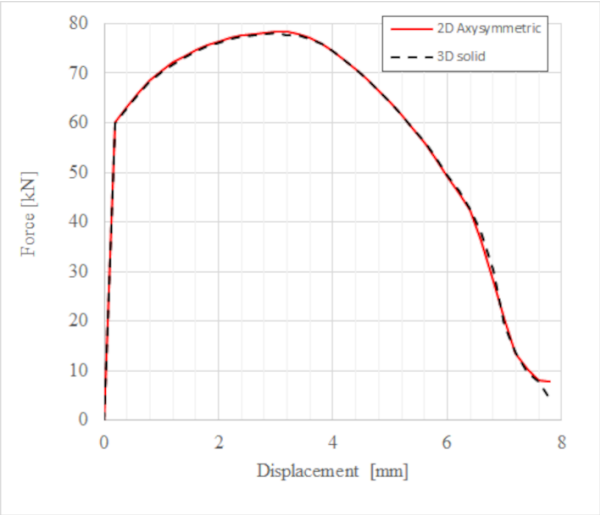

Fig. 8. Force-displacement response for 2D axisymmetric and 3D solid FE model

5. Discussion and conclusions

The simulation results presented in previous sections offer many points of interest for discussion. Firstly, the material parameters given in Table 1, define the stress-strain response of the material, but one important parameter for the PFDM simulation is the critical equivalent strain which is set to 1.2. As, the equivalent plastic strain defines the yield stress function in eq. (6), when the critical value is reached in time step 32 (Figure 3.), in the next time step 33, the damage occurs (Figure 4.). It is one time step later because the solution procedure is defined in a partitioned manner, so the damage field is late for one time step with respect to the displacement field. In Figure 5, it can be seen that the damage field achieves a similar level for both 2D axisymmetric and 3D solid FE models, but small difference (less than 5%) can be noticed. A similar situation is for the equivalent plastic strain field at the last time step, given in Figure 6, but the difference is less than 1%. Figure 7 shows the evolution of the damage field in the specimen across the cross-section in the necking zone. Although, relatively coarse mesh is used, the increase of damage zone can be observed. Finally, in Figure 8, the force-displacement response of the circular bar model is compared for the 3D solid and 2D axisymmetric FE models and the overlapping of the diagrams is obvious.

At the end, by analyzing the obtained results, it can be confirmed that both implementations of PFDM are functional and that the proposed method can be used for real structures. In this case, large strain nonlinear analysis with the Von Mises plasticity model and exponential hardening function is used, which is one of the most advanced simulations in the field. Of course, the advantage of a 2D axisymmetric finite element is obvious for the computational time necessary to solve the problem, but for detailed analysis, the 3D solid element can be used successfully.

Acknowledgments

This research is supported by the Science Fund of the Republic of Serbia, #GRANT No 7475, Prediction of damage evolution in engineering structures – PROMINENT and by the Ministry of Science, Technological Development and Innovation, Republic of Serbia, Agreement No. 451-03-137/2025-03/200107.

References

[1] Dunić, V., Gubeljak, N., Živković, M., Milovanović, V., Jagarinec, D., Djordjevic, N. Experimental Characterization and Phase-Field Damage Modeling of Ductile Fracture in AISI 316L, *Metals*, 2024, 14(7), 787.

[2] Dunić, V., Živković, M., Milovanović, V. Phase-field Fatigue modeling in ductile materials, *The 9th European Congress on Computational Methods in Applied Sciences and Engineering - ECCOMAS 2024*, Lisbon, Portugal, 3-7 June 2024. (e-source)

[3] Dunić, V., Živković, M.; Critical total-strain based Phase-Field Damage Model implementation for ductile fatigue, *5th International Conference on Computational Engineering ICCE 2024*, Darmstadt, Germany, 30 September-2 October 2024. (e-source)

[4] Dunić, V., Živković, J., Milovanović, V., Pavlović, A., Radovanović, A., Živković, M. Two-Intervals Hardening Function in a Phase-Field Damage Model for the Simulation of Aluminum Alloy Ductile Behavior, Metals, 2021, 11(11), 1685.

[5] Živković, J., Dunić, V., Milovanović, V., Pavlović, A., Živković, M. A Modified Phase-Field Damage Model for Metal Plasticity at Finite Strains: Numerical Development and Experimental Validation, Metals, 2021, 11(1), 47.

[6] Miehe, C., Welschinger, F., Hofacker, M. Thermodynamically consistent phase-field models of fracture: Variational principles and multi-field FE implementations. Int. J. Numer. Methods Eng. 2010, 83, 1273–1311.

[7] Živković, M., Dunić, V., Rakić, D., Grujović, N., Slavković, R., Kojić, M. PAK-DAM Software for Damage and Fracture Simulation; Faculty of Engineering, University of Kragujevac: Kragujevac, Serbia, 2025.

[8] Simo, J.C., Miehe, C. Associative coupled thermoplasticity at finite strains: Formulation, numerical analysis and implementation. *Comput. Methods Appl. Mech. Eng.* 1992, 98, 41–104.

[9] Kojić, M., Bathe, K.J. *Inelastic Analysis of Solids and Structures*, Springer: Berlin/Heidelberg, Germany, 2005.

41st Danubia-Adria Symposium Advances in Experimental Mechanics
September 23-26, 2025, Kragujevac, Serbia

Original scientific paper DOI: 10.46793/41DAS2025.143D

ANALYSIS OF DEEP DRAWING PROCESS USING FEA AND FLD

Marko DELIĆ[1], Vesna Mandić[2], Srbislav ALEKSANDROVIĆ[3], Dušan ARSIĆ[4], Đorđe IVKOVIĆ[5]

[1] 0000-0001-5493-7569, Faculty of Engineering, SestreJanjić 6, Kragujevac, Serbia,E-mail: marko.delic@kg.ac.rs;

[2] 0000-0003-1624-3536, Faculty of Engineering, SestreJanjić 6, Kragujevac, Serbia, E-mail: mandic@kg.ac.rs;

[3] 0000-0001-5068-5560, Faculty of Engineering, SestreJanjić 6, Kragujevac, Serbia, E-mail: srba@kg.ac.rs;

[4] 0000-0003-0326-0898, Faculty of Engineering, SestreJanjić 6, Kragujevac, Serbia, E-mail: dusan.arsic@fink.rs;

[5] 0000-0002-5747-7876, Faculty of Engineering, SestreJanjić 6, Kragujevac, Serbia, E-mail: djordje.ivkovic@fink.rs;

1. Introduction

The forming limit diagram (FLD) of sheets is determined experimentally. The diagram is often called the Keeler-Goodwin diagram named for the engineers who defined it. There are several ways to determine the diagram, but the most commonly used method is the fixed-edge tensile method. FLD is defined in the coordinate system of the principal strains in the plane of the sheet. The problem of the limit deformability of sheets is presented in the papers [1] and [2].

In this paper, first a review of the experimental determination of the FLD will be given and then it will be integrated into a numerical simulation. The FLD of DC04 steel was determined and the case of deep drawing of a non-standard box section was analyzed using the Simufact.forming software.

Two numerical experiments were performed, with two different lubrication conditions. Based on the results of the numerical simulation, it will be interpreted whether both cases satisfy, i.e. whether fracture occurs. The goal of the numerical experiment is to show how much using of FLD into the numerical simulation can improve the analysis of the sheet metal forming process.

2. Experimental determination of FLD

Based on the principle of the invariance of volume, the following relationship always holds:

$$\varphi_1 + \varphi_2 + \varphi_3 = 0, \qquad (1)$$

where φ_1, φ_2 and φ_3 in Eq. (1) are the principal strains and based on the two main strains, a third one can be calculated, which represents the thinning of the sheet.

In the experimental part, sheet metal test samples (Fig. 1) with one dimension of 120 mm, which does not change, were used. The second dimension starts from 20 mm and increases in steps of 10 mm. This results in 11 test tubes.

Fig. 1. Sheet metal samples made of DC04 material for FLD determination

Before cutting the test piece, it is necessary to apply a measuring grid consisting of circles with a nominal diameter of 3 mm to the surface of the sheet (Fig. 2).

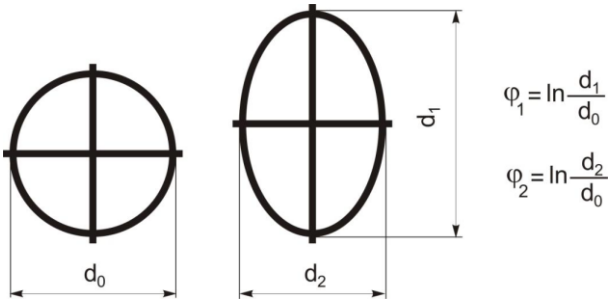

Fig. 2. Measuring grid element with equations for defining local strains

Each test sample is deformed in the tool under conditions of complete fixation of the peripheral zone (rim). In this way, the deformation zone is focused on the space under the punch cap and the so-called sheet stretching process is realized. Each deformed test piece corresponds to a specific stress-strain state. Narrower test pieces correspond to deformation states to the left of the ordinate axis, and wider ones (up to the largest square) to the right. In the right zone there is a biaxial tension region, and in the left zone there is a uniaxial tension region with negative strain φ_2 and biaxial deformation also with negative strain φ_2. The forming process is carefully monitored and interrupted at the moment of the appearance of a crack in the sheet. The position of the crack should be precisely located in relation to the pole of the punch cap. The symmetrical position on the other side of the pole determines the position of the measurement point of localization. Most often, both measurement points are easily visible visually.

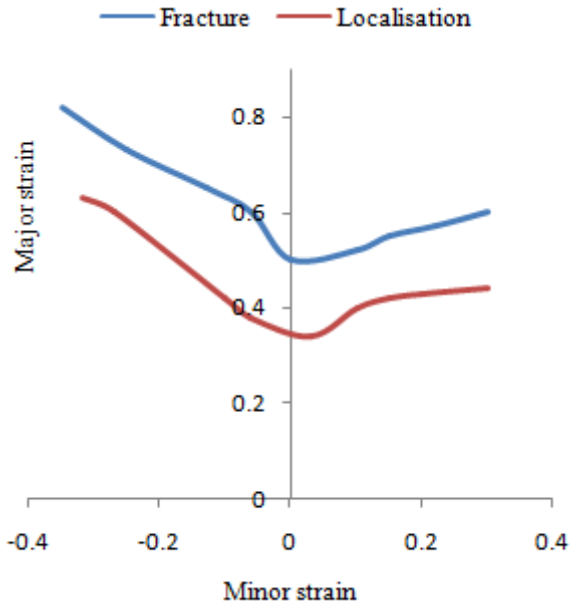

Fig. 3. Experimentally obtained FLD for material DC04

For both places, the dimensions d_1 and d_2 should be measured precisely (with a minimum measuring accuracy of 0,1 to 0,05 mm) and φ_1 and φ_2 should be calculated. In this way, the coordinates of two FLD points are obtained. One point corresponds to localization, and the other to fracture. Therefore, with 11 successfully deformed test samples, 11 pairs of points are obtained, which is sufficient to construct both the limit curve and the localization zone. All of the above experiments were performed in the metal forming laboratory of the Faculty of Engineering. The FLD for the DC04 material was determined. The experiment was performed on the ERICHSEN 142/12 machine.

Based on the results, the FLD curve is constructed, which is shown in Fig. 3.

3. Defining FLD in FEA

For numerical simulation the Simufact.forming software was used, which has the ability to define FLD for materials. Carbon steel DC04 was taken from the material database and then the properties were changed, data for the flow curve and FLD were added. The use of FLD is only possible for 3D simulations. The diagram is defined by an equation for two cases $\varepsilon_2<0$ and $\varepsilon_2>0$. In Simufact.forming software minor strain is marked as ε_2 and major as ε_1. In order to assess the risk of failure, a forming limit parameter was introduced, which has a value between 0 and 1. When this parameter has a value of 1, the material fracture occurs. This parameter [3] is calculated according to the formula given in Eq. (2):

$$F = \frac{\varepsilon_1}{\varepsilon_1^{crit}(\varepsilon_2)}, \qquad (2)$$

where ε_I^{crit} is the maximum major strain that can be reached. In addition to determining the value of the factor, the simulation result is a simplified representation of the zones on the material that are "critical", "at risk" and "uncritical". The flow curve was determined by a uniaxial tensile test and is defined by the Eq. (3):

$$K = 542{,}66 \cdot \varphi^{0{,}2259}. \qquad (3)$$

The froming limit diagram is defined in the Simufact.forming software by the equations of two lines. The DGD is shown in Fig. 4 and is defined by the Eq. (4) and Eq. (5):

$$FLD(\varepsilon_2) = C_0 + D_1\varepsilon_2 \quad \text{и} \qquad (4)$$

$$FLD(\varepsilon_2) = C_0 + C_1\varepsilon_2 \qquad (5)$$

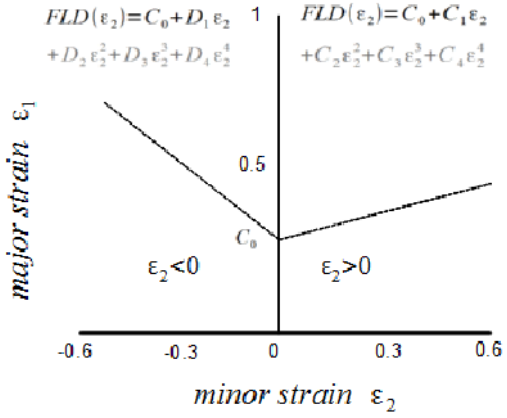

Fig. 4. Defining FLD in FEA software

Based on the experimental results, two equations of the line, Eq. (6) and Eq. (7), were defined:

$$FLD(\varepsilon_2) = 0{,}51 + (-0{,}85)\varepsilon_2 \text{ и} \quad (6)$$

$$FLD(\varepsilon_2) = 0{,}51 + 0{,}34\varepsilon_2. \quad (7)$$

4. Numerical simulation of the deep drawing process

Numerical simulation of deep drawing was performed in the Simufact.forming software as cold forming, the simulation type is 3D and the process type is stamping. The element type used is solid-shell and the mesher is sheetmesh. The element size is 2 mm.

Deep drawing was performed on a hydraulic press with a velocity of 10 mm/s. The tool consists of a die, a punch and a blankholder. The layout of the tool set up for numerical simulation is shown in Fig. 5.

It is possible to define the value of the blank holding force in the software, but in this case the blankholder is defined as a rigid body that completely prevents the appearance of wrinkles in the sheet metal. The stroke of the punch is defined as 20 mm.

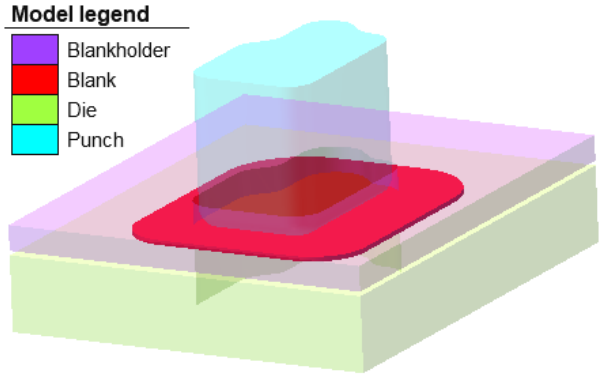

Fig. 5. Deep drawing tool set for simulation

In this numerical experiment, the deep drawing operation was analyzed for two cases of tribological conditions. For cold forming when lubrication is applied, the friction coefficient value is between 0,08 and 0,15, while in the case of no lubrication, the coefficient value increases to 0,2 – 0,3.

In this paper, a numerical simulation was performed for two cases of lubrication, the first with a friction coefficient of 0,08 and the second with a value of 0,15. The aim of the research is to determine whether friction conditions can endanger the stability of the deep drawing process.

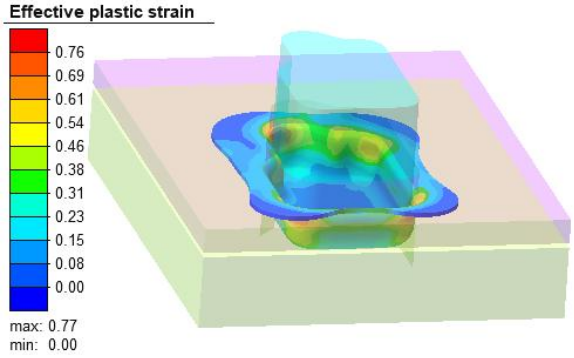

Fig. 6. Effective plastic strain (μ=0,08)

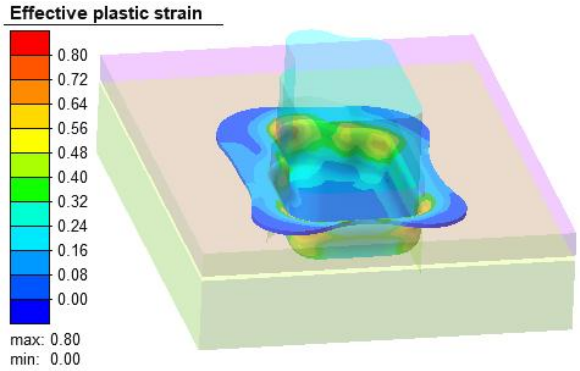

Fig. 7. Effective plastic strain (μ=0,15)

The results of the numerical simulations are shown in Fig. 6 and Fig. 7. In the first case, the value of the effective plastic strain is 0,77 and in the case of a higher friction coefficient value of strain is 0,8. After these values, it is necessary to review the simulation results related to fracture. Fig. 8 and Fig. 9 show the results of the forming limit parameter. In the first case, when lubrication is very good and the friction coefficient is 0,08, this parameter is 0,97, which means that fracture will not occur (Fig. 8).

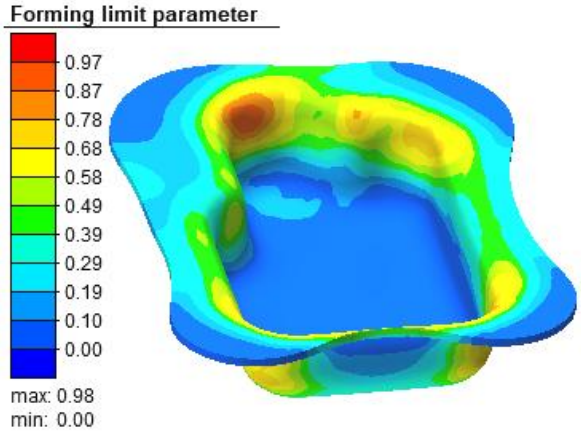

Fig. 8. Forming limit parameter for the first case (μ=0,08)

In the second case, when the lubrication conditions have deteriorated slightly and the friction coefficient has a value of 0,15, the parameter value

is 1, which means that fracture will occur at a certain point (Fig. 9).

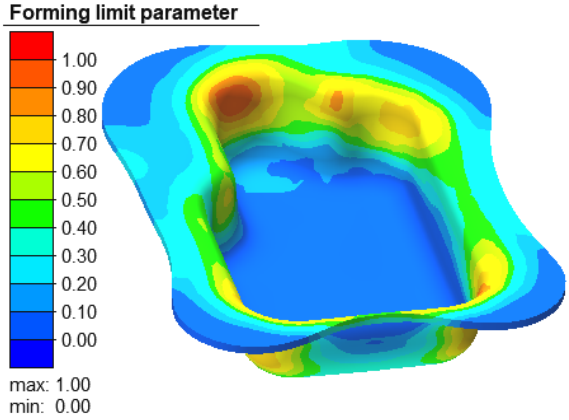

Fig. 9. Forming limit parameter for the second case (μ=0,15)

Based on the results of the forming limit parameter, the software provides the ability to show critical areas on the sheet. These areas are shown in Fig. 10 and Fig. 11. Fig. 10 shows the simulation result for the first case. Green indicates the area where there is no risk of failure, and yellow indicates the zone where there is thinning and the possibility of failure.

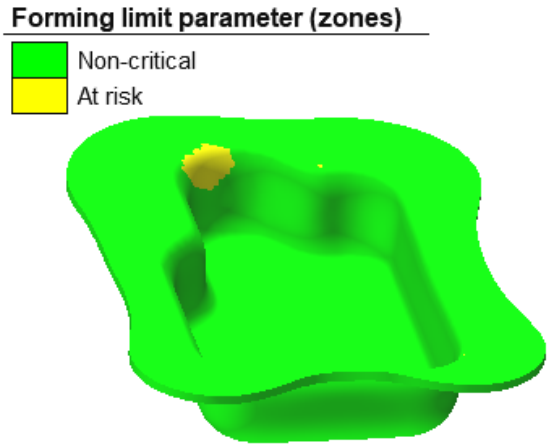

Fig. 10. Areas on the sheet metal (μ=0,08)

Fig. 11 shows the areas for the second case when the friction coefficient is 0,15. The figure shows the area that is significantly at risk and the area where the fracture will occur.

The results showed that friction has a great influence and importance on the success of the deep drawing operation. This way of using FLD can be extremely useful for checking the design of the tool.

By directly applying FLD, it is possible to detect zones that may be at risk and, based on the results, implement measures to reconstruct the sheet metal part or tool. It is also possible to detect the influence of production conditions such as lubrication conditions, as was done in this case.

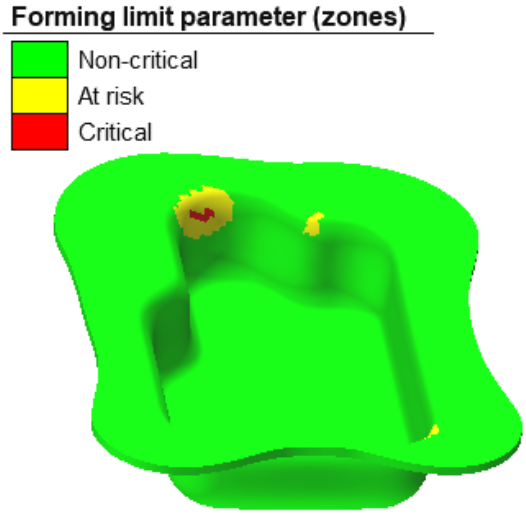

Fig. 11. Areas on the sheet metal (μ=0,08)

Based on the simulation results, it was concluded that the deep drawing process with existing tools can only be successfully performed if the lubrication is very good. Based on these results, the technologist can determine the appropriate lubricant and ensure the success of the process.

5. Conclusions

Using FLD in numerical simulations of sheet metal forming significantly improve the analysis of results. By defining FLD, a specific area that is critical is obtained as a result of the simulation, and based on this result, the design engineer can take certain actions and, after constructive changes, repeat the simulation and find out whether the problem of the endangered region has been overcome.

Acknowledgements

The present work was funded by the Ministry of Science and Technological Development of the Republic of Serbia under the project TR34002.

References

[1] Aleksandrovic, S., Stefanovic, M. Significance of strain path in conditions of variable blank holding force in deep drawing. *Advanced Technologies and Materials*, 2005, 30(1-2), 25-35.
[2] Aleksandrović, S., Stefanović, M., Vujinović, T., Samardžić, M. Formability of stainless sheet metals by deep drawing-integral approach. *Advanced Technologies and Materials*, 2007, 32(1-2), 67-75.
[3] Simufact forming manual.

Original scientific paper DOI: 10.46793/41DAS2025.147J

DEVELOPMENT AND EXPERIMENTAL TESTING OF A HYDRAULIC STAND WITH PUMPS INTENDED FOR A CENTRAL HEATING SYSTEM

Mladen JOSIJEVIĆ[1], Dušan GORDIĆ[2], Davor KONČALOVIĆ[3], Filip NASTIĆ[4]

[1] 0000-0001-9619-0897, Faculty of Engineering, University of Kragujevac, Kragujevac, Serbia, E-mail: mladen.josijevic@fink.rs

[2] 0000-0002-1058-5810, Faculty of Engineering, University of Kragujevac, Kragujevac, Serbia, E-mail: gordic@kg.ac.rs

[3] 0000-0003-1207-2653, Faculty of Engineering, University of Kragujevac, Kragujevac, Serbia, E-mail: davor.koncalovic@kg.ac.rs

[4] 0000-0002-2164-6658, Faculty of Engineering, University of Kragujevac, Kragujevac, Serbia, E-mail: fillip.nastic@uni.kg.ac.rs

1. Introduction

Contemporary engineering education increasingly relies on integrating theoretical knowledge with practical activities; laboratory stands play a key role in the experimental verification of models, the visualization of phenomena, and the development of relevant professional skills [1-3]. I In the fields of thermotechnics and hydraulics, experimental teaching plays a crucial role as it enables students to connect theoretical foundations with practical experience and real technical systems. For example, when testing pumps, measurements of flow rate, head, and power are conducted, allowing the determination of characteristic curves and comparison with nominal data. In the analysis of hydraulic systems, the pressure drop in pipelines and fittings is observed as a function of geometrical and hydraulic parameters. Regarding thermotechnical systems, the analysis is based on measuring temperature differences between the supply and return lines, as well as the flow rate in the system, which makes it possible to calculate the actual heat output, identify losses, and evaluate the energy efficiency of the heating system. In this way, students gain a comprehensive understanding of the functioning and optimization potential of complex energy systems [4], [5].

It is well known that there is a gap between theory and application. Laboratory work ensures a deeper understanding of abstract concepts and their application in real-life scenarios; this enhances the development of critical thinking in students [2], [6]. Although virtual and distant labs have certain benefits, such as wider accessibility and more flexibility, the educational experience of physical interaction with equipment is more memorable and effective [5], [7], [8].

Contemporary research has indicated the significance of open projects and active learning in a laboratory setting. For instance, a 2022 analysis in the field of chemical engineering has shown that project-based learning (PBL) focused on design can enrich students' experience and deepen their understanding [9].

A systematic review of PBL learning in engineering (2024) has demonstrated that PBL improves technical skills and soft skills while contributing to interdisciplinarity [10].

In addition, virtual learning has also been taken to the next level. A 2023 study has shown that immersive virtual learning activities (VLAs) rely on visual and haptic feedback to improve the understanding of complex mechanical concepts and increase knowledge retention [1]. Also, the adoption of VR simulations in education shows that virtual laboratories can effectively replace physical ones, especially in terms of accessibility and student engagement [11], [12].

Laboratory transformation through digital technologies and active learning has also been confirmed on the interdisciplinary level. A 2023 study reports positive reactions among physics teachers in Germany, Finland, and Croatia when it comes to the combinations of digital tools (smartphones, simulations) and laboratory work in developing digital competence in students [13]. Active learning practice in higher education improves conceptual thinking, motivation, and interpersonal skills [14].

In the context of contemporary education, the concept of Education 5.0 incorporates a holistic and humanistic approach, ethical awareness, international cooperation, and technology to support student-oriented learning [15]. This framework highlights the importance of technology, inclusivity, creativity, and ethical considerations – all components that can be effectively implemented through laboratory stands and immersive tools such as VR and digital twins.

The development and implementation of a laboratory stand with pumps for central heating systems is not only a technical instrument, but also a powerful pedagogical tool. It can be used to explore pump properties, determine operating points, draw pipeline curves, test valves, regulate flow through a bypass, and apply a frequency drive; this allows the direct application of theoretical knowledge in industrially relevant scenarios [9, 11, 15].

This paper aims to demonstrate the process of developing a hydraulic stand with pumps used in central heating systems and experimental testing. The emphasis is placed on the educational role of such a stand and preparing students for future professional challenges.

2. Laboratory Stand Description

The Fig. 1 presents the schematic overview of the laboratory stand.

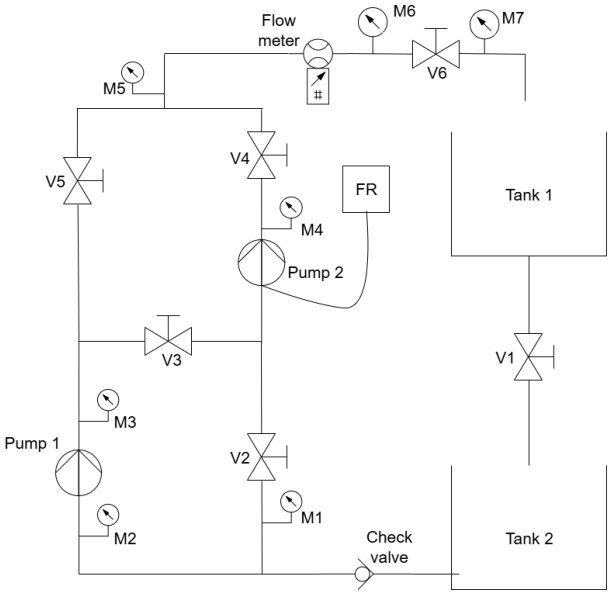

Fig. 1. Schematic overview of the laboratory stand

The most crucial components of the stand are shown in Fig. 2. Together, they enable a detailed exploration of how the pumps and the valves operate and how to regulate flow in central-heating systems.

Fig. 2. The laboratory stand

Two centrifugal pumps (Grundfos UPS 32/40 180) are the core components. In practice, they are used as circulation pumps for floor heating. One pump is connected to the electricity grid via a flow regulator. This allows a precise regulation of flow and thus the working pressure. In addition, it enables the investigation of system efficiency when the flow is regulated via the valve, bypass, or frequency drive.

The pipeline was made of water pipes certified for a maximum working pressure of 15 bars. This provides safety and reliability during experiments. The valves direct fluid so that the pumps can be connected in a series or in parallel, depending on the type of experiment to be conducted. The pumps push water from the tank through the pipeline. At the end of the system, just before the return to the tank, there is a valve that can be easily removed with two holders, and it can be replaced with a valve of a different kind. This allows students to explore the properties of different valve types.

Manometers are distributed along the entire system at several locations. Hence, it is possible to monitor pressure values precisely in different parts of the stand. A digital flowmeter is installed in the last branch of the pipeline. Flow can also be estimated by measuring volume in the upper tank. It is equipped with a level gauge with scaled divisions. This enables comparisons between the measures obtained for flow.

This stand configuration allows students and researchers to use practical training and experimental tests to deepen their understanding of

the complex hydraulics processes, draw pump and valve characteristics, determine the working points of the system, and analyze the efficiency of regulating flow with a valve, bypass, or frequency drive.

In the next section of the paper, we shall present the results obtained for this particular stand in order to illustrate its functionality and potential for educational and research purposes.

2.1 Experiments

A laboratory stand developed at the Department of Energy and Processing Engineering, Faculty of Engineering, University of Kragujevac, can be used to conduct different experiments in the field of water hydraulics and fluid mechanics. The laboratory can be used for the following experiments:

- Measuring flow and pressure to determine the reference points for drawing the curves for the pipelines and the curves for the pumps;
- Evaluating the pump efficiency (measuring electrical power and hydraulic power with different loads;
- Testing the system with different performance shares among two pumps connected in a series and/or in parallel;
- Testing the flow regulation in the system with different regulation systems (e.g., bypass, valves, a frequency drive);
- Comparing flow measuring with a direct or indirect method;
- Determining the properties of different types of valves.

2.1.1 Pump characteristics curve

One of the most basic and common experiments is drawing pump characteristics. The parameters of both pumps can be measured. To minimize the impact of measurement errors, it is recommended to draw the properties of Pump 1, as the manometers are installed immediately before and after the pump, thereby reducing the likelihood of errors due to local pressure losses at the measurement locations. The experiment procedure starts with starting the pump. The valves are positioned not to disturb fluid flow. The valves 2, 3, and 4 are closed, so the fluid runs through the pump branch 1, valve 5, and enters the outlet branch that contains the turbine flow gauge.

Flow is evaluated with the already mentioned digital gauge device or by measuring the volume of the fluid that fills the tank after some time. The manometer installed in the suction and discharge pump pipeline detects the pressure. The values change depending on system resistance.

The first measurement, which represents the first point on the pump curve diagram, is most commonly obtained by reading pressure values and determining their differences. This also includes the reading of the flow value from the digital gauge instrument. The next measurement is conducted by increasing local resistances in the system, recording pressures at the pump inlet and outlet, and recording flow.

Each difference in pressures before and after the pump (pump load) has a corresponding flow value in the pipeline. By plotting these values on the ordinate and abscissa of the Cartesian coordinate system, students can connect the dots and obtain the pump system curve. After a series of consecutive measurements, we have obtained the values presented in Table 1.

Table 1. The results of the pump measuring 1

Case no.	**Pressure in the pipeline** [bar]	**Pressure in the suction pipeline** [bar]	**Fluid flow** [m^3/h]
1	0.43	0.025	0.01
2	0.39	0.025	0.2
3	0.34	0.02	0.58
4	0.32	0.02	0.93
5	0.27	0.015	1.21
6	0.21	0.01	1.64
7	0.16	0.0075	2.36
8	0.1	0.005	2.8

The Fig. 4 shows the pump curve obtained by performing measurements for eight different valve 6 positions.

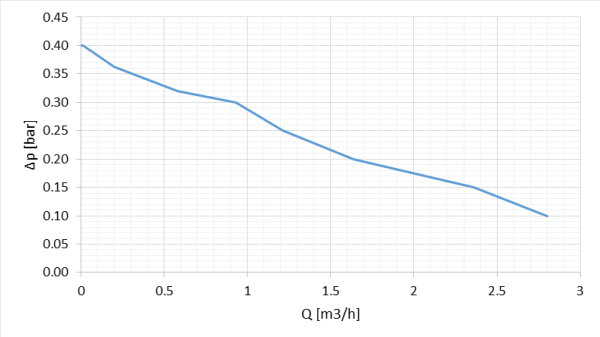

Fig. 4. The pump curve obtained based on performing measurements at the laboratory stand

As can be seen from the image, the curve is relatively flat. The shape of the curve stems from the fact that the pump is a component of the heating

system. In such systems, the curves are flat since the pumps used are centrifugal (*i.e.*, pressure changes gradually with flow). Such a shape ensures the stable system operation because changes in the resistance of the installation do not cause large oscillations in pressure and flow, which further contribute to quieter operation and better regulation.

3. Conclusions

The developed laboratory stand with the pumps for central heating systems can be a key tool in students' education. Such teaching methods enable the direct use of theoretical knowledge. Students can gain clear insight into how pumps work, valve properties, flow regulation, and system efficiency. This can contribute significantly to a deeper understanding of complex hydraulic processes and the development of practical professional skills.

The paper demonstrates the results obtained for some experiments. Due to length limitations, the paper does not include the results obtained for regulating flow via a drive frequency, comparing flow with a direct or indirect method, and the evaluations for different types of valves. In addition to standard experiments, the stand is flexible enough to enable, with certain modifications, other experiments. It is, hence, a valuable resource for research work. This approach to practical learning strengthens critical thinking, motivation, and independent problem-solving. Hence, theory and practice in modern engineering education are successfully blended.

Acknowledgments

The Ministry of Science, Technological Development and Innovation of the Republic of Serbia (No. 451-03-66/2024-03/ 200107)

The paper was translated and edited by Ph.D. Jelena M. Josijević Mitić, employed at the Faculty of Education, University of Kragujevac.

References

[1] R. Padilla Perez and Ö. Keleş, "Immersive Virtual Reality Environments for Embodied Learning of Engineering Students," *arXiv preprint*, Mar. 2025.

[2] K. Boettcher *et al.*, "Developing a real-world scenario to foster learning and working 4.0 – on using a digital twin of a jet pump experiment in process engineering laboratory education," *European Journal of Engineering Education*, vol. 48, no. 5, pp. 949–971, 2022.

[3] Ö. Keleş *et al.*, "Experiential Learning of Engineering Concepts in Immersive Virtual Learning Environments (VLEs)," *Journal of STEM Education: Innovations and Research*, vol. 24, no. 2, 2023.

[4] D. May *et al.*, "Rapid transition of traditionally hands-on labs to online instruction in engineering courses," *European Journal of Engineering Education*, vol. 48, no. 5, pp. 842–860, 2022.

[5] D. Basu and V. K. Lohani, "Learning and engagement with an online laboratory for environmental monitoring education," *European Journal of Engineering Education*, vol. 48, no. 5, pp. 861–879, 2023.

[6] S. Terkowsky *et al.*, "Digital transformation in physics lab courses: a tri-national survey," *arXiv preprint*, May 2023.

[7] S. Rogers, "Experiential and authentic learning in a Living Lab: the role of a campus-based Living Lab as a teaching and learning environment," *Journal of Learning Development in Higher Education*, no. 28, 2023.

[8] K. Frady, "Use of virtual labs to support demand-oriented engineering pedagogy…: a systematic review," *European Journal of Engineering Education*, 2022.

[9] "Constructivist-based experiential learning: A case study… distillation laboratory," *Education for Chemical Engineers*, vol. 41, 2022.

[10] "Project-Based Learning (PBL) as an Experiential Pedagogical Methodology in Engineering Education: A Review of the Literature," *Education Sciences (MDPI)*, 2024.

[11] "Immersive Learning: A Systematic Literature Review… Virtual Reality," *MDPI*, 2023.

[12] "A review on cultivating effective learning: synthesizing educational theories and virtual reality…" *PeerJ Computer Science*, 2023.

[13] S. Zacharias Lahme *et al.*, "Physics lab courses under digital transformation…," *arXiv preprint*, May 2023

[14] "Active learning"—Meta-analysis summary, *Wikipedia*, 2025.

[15] "Student 5.0: immersive learning in next-gen Automation… Industry 5.0 era," *Frontiers in Education*, 2025.

41st Danubia-Adria Symposium Advances in Experimental Mechanics
September 23-26, 2025, Kragujevac, Serbia

Original scientific paper DOI: 10.46793/41DAS2025.151S

FINITE ELEMENT ANALYSIS OF PLATELET ACTIVATION AND CELL MECHANICS IN CIRCULATING TUMOR CELL ARREST

Vladimir SIMIĆ[1], Aleksandar NIKOLIĆ[2], Miljan MILOŠEVIĆ[3], Shao NING[4], Fransisca LEONARD[2], Miloš KOJIĆ[3]

[1] 0000-0001-7842-8902, Institute for Information Technologies, University of Kragujevac, Jovana Cvijića bb, 34000 Kragujevac, Serbia, E-mail: vsimic@kg.ac.rs;

[2] 0000-0002-7052-7444, Institute for Information Technologies, University of Kragujevac, Jovana Cvijića bb, 34000 Kragujevac, Serbia, E-mail: dziga@kg.ac.rs;

[3] 0000-0003-3789-2404, Metropolitan University, Tadeuša Košćuška 63, 11158 Belgrade, Serbia, E-mail: miljan.m@kg.ac.rs;

[4] 0000-0003-2625-4546, The Department of Nanomedicine Houston Methodist Research Institute, 6670 Bertner Ave, 77030 Houston Texas, USA, E-mail: shaon@houstonmetrhodist.org;

[5] 0000-0003-1888-6279, The Department of Nanomedicine Houston Methodist Research Institute, 6670 Bertner Ave, 77030 Houston Texas, USA, E-mail: fleonard@houstonmethodist.org;

[6] 0000-0003-2199-5847, The Department of Nanomedicine Houston Methodist Research Institute, 6670 Bertner Ave, 77030 Houston Texas, USA, E-mail: mkojic42@gmail.com;

1. Introduction

The progression of cancer from a localized tumor to a widespread metastatic disease is a complex and multifaceted process, making it cancer patients' leading cause of death [1]. The driving force behind this process is the presence of the Circulating Tumor Cells (CTCs), which break from the primary tumor site and spread through the bloodstream to colonize other organs (Fig. 1). The presence of CTCs in the blood is a strong indicator of the metastatic potential of a tumor [2-4].

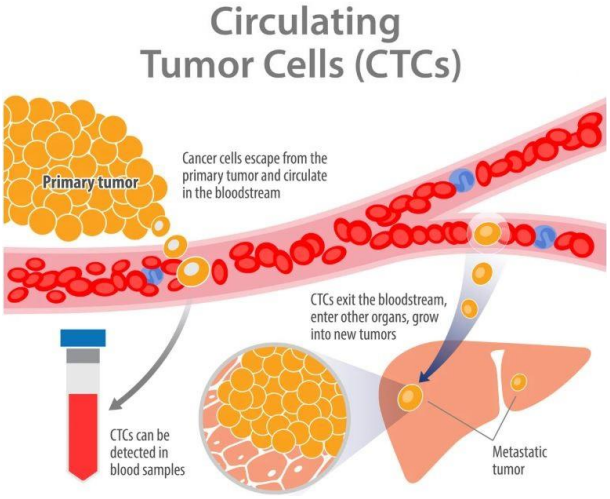

Fig. 1. Human metastasis disease progression process.

Despite their heterogeneity—since only a fraction can initiate secondary tumors—CTCs that persist in the bloodstream and evade immune surveillance are pivotal to metastatic progression. Metastasizing cancer cells can activate platelets at the primary site, increasing the local concentration of platelet microparticles (PMPs) [5], that consequently can target CTCs regarding their number or affecting their metastatic potential presents a promising strategy for managing and preventing metastatic disease. Over the past decades, extensive research has explored the interaction between CTCs and platelets in the context of metastasis. Activated platelets play a crucial role in protecting CTCs from immune surveillance and hemodynamic shear forces, thereby enhancing their survival during circulation [6].

Although the role of platelets in cancer metastasis is increasingly acknowledged, the exact mechanisms that initiate and sustain CTC–platelet interactions remain only partly understood. A deeper understanding of the molecular dynamics underlying CTC–platelet and CTC–vessel wall interactions is crucial for developing targeted strategies to disrupt these processes selectively, without compromising normal hemostasis or inflammatory responses and stiffness), the platelet size and stiffness, the ligand-receptor interaction intensity, on one side; and time in contact between

the CTCs and platelet, conditions for the cell arrest, on the other side.

This study applies a 2D computational model to investigate CTC dynamics in plasma flow through a parametric analysis of platelet adhesion, CTC size and stiffness, and ligand–receptor bond stiffness. Using a strong coupling method, solid–fluid interactions are solved simultaneously, supported by dynamic remeshing for stability. Ligand–receptor bonds are represented by 1D rope elements and experimentally measured adhesive forces with non-activated and thrombin-activated platelets are incorporated. This framework enables systematic evaluation of how geometrical and material properties, as well as platelet activation, influence CTC arrest and adhesion in circulation.

2. Materials and methods

In our previous work [7], we have considered the motion of cells and platelets within the systemic circulation as the motion of the deformable solid bodies within the fluid. Therefore, as it is mentioned above, we used a strong coupling concept with a remeshing procedure, and furthermore, introduced a simple concept for modeling the contact problems between the moving deformable solids, by using 1D solid elements that represent the contact conditions. Complete review of the basic and governing equations for modeling the fluid and solid part, as well as the solid-fluid interaction are given in [7].

2.1 Process of the experimentally determined CTC-platelets adhesion forces

This procedure is inspired by a method for measuring cell adhesion force [8]. To quantify CTC–platelet adhesion forces, mouse platelets were incubated in 96-well plates for 1 h to form a platelet-coated substrate, after which non-adherent platelets were removed by gentle washing. Fluorescently labeled 4T1 clone 17 cancer cells were then added, centrifuged at 10 × g for 5 min to ensure platelet contact, and overlaid with RPMI medium. Wells were sealed with microplate tape and centrifuged upside down at forces ranging from 10 × to 750 × g. Images of identical regions were acquired before and after each centrifugation step, and adherent cell counts were quantified using ImageJ.

2.2 Governing equations for the correction of platelet-cell adhesion forces

Here, we will focus on the explanation of the platelet-cell adhesion forces correction, according to previously mentioned experimental results and to describe the computational concept for the correction of platelet-cell adhesion forces according we use schematics shown in Fig. 2.

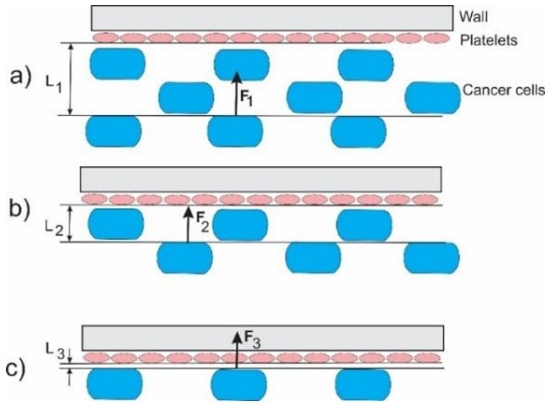

Fig. 2. Schematics of detachment of cells from the wall. a)-c) Cell distances L_1, L_2, L_3 from the wall covered by platelets, and the detachment adhesive forces F_1, F_2, and F_3, respectively. (According to [10])

As the brief explanation of the process is given above, the detachment begins when the smallest centrifugal force is acting on cells (smallest angular velocity of the device) and starts with cells at the largest distance from the wall. This is possible when the distance is L= L_{max} (L_{max} is essentially the size of the wall-cell interaction domain), the interaction force is equal to zero, so we can write for L= L_{max}:

$$L / L_{\max} = 1, \quad p_{\max} = 100, \quad F = 0. \tag{1}$$

p_{max} represents the maximum percentage of adhered cells, and F is the adhesion force. We can represent the p_{max} as

$$p_{\max} = \frac{\rho_A L_{\max}}{\rho_A H} = \frac{L_{\max}}{H} = 100 \tag{2}$$

where ρ_A is the area density of cells, and H is the device height. Regarding Fig. 2a, displayed are cells with the detachment distance L_1 so that the percentage p_1 of adhered cells is

$$p_1 = \frac{\rho_A L_1}{\rho_A H} = 100 \frac{L_1}{L_{\max}} \tag{3}$$

From the above equation (3), the percentage of the adhered cells is proportional to the distance L_1, which can be considered the thickness of the adhered cell layer. Further, the detachment continues with the cells corresponding to distances L_2 and L_3 (Fig. 2b, and 2c) with the percentages- p2 and p3, respectively. This leads to the conclusion that related to the distance L, we have a percentage p,

$$p = 100\frac{L}{L_{\max}} \qquad (4)$$

Considering our FE model, we can state that for a distance L between corresponding nodes at a platelet and a cell, cell and wall, or platelet and wall (length of our 1D element), we have that the value (modulus) of the adhesion force is

$$F = K\left(L_{\max} - L\right), \quad F_a = K_a\left(L_{\max} - L\right) \qquad (5)$$

3. Results and discussion

A simple benchmark example of the 2D axisymmetric capillary with a CTC and platelets attached is considered (Fig. 3). At first, we examine the CTC flow through a capillary without flowing platelets, leading to the cases with one up to four platelets. We have considered a case where adhesion is present in the case of non-activated platelets, as well as the adhesion forces between all the solid bodies (cells and platelets) and walls are always present.

As is described above, we consider a 2D problem of the motion of the cell and platelets caused by fluid flow within a capillary. Adhesion forces are present between cell and platelets, and cell and platelets with the wall (Fig.3a). Regarding the modeling process and generation of the computational model (Fig.3b), we have established a procedure for executing the FE simulations, which consists of three steps: pre-processing, execution of FE simulation, and post-processing. Pre-processing and model generation, ready to be executed using the FE code PAK, is achieved using our CAD FiS (Fields and Solids) software [9] (Figure 3).

The model generation process begins with the selection of appropriate options within the CAD environment, including the choice of the CAD module, definition of model geometry, specification of material models, and assignment of time-stepping parameters. Dedicated dialog interfaces are provided to define the geometrical characteristics of individual solid components (e.g., capillary channels, circulating tumor cells, and platelets), fluid flow parameters and their associated boundary conditions, mesh configuration, and the material properties of solid structures.

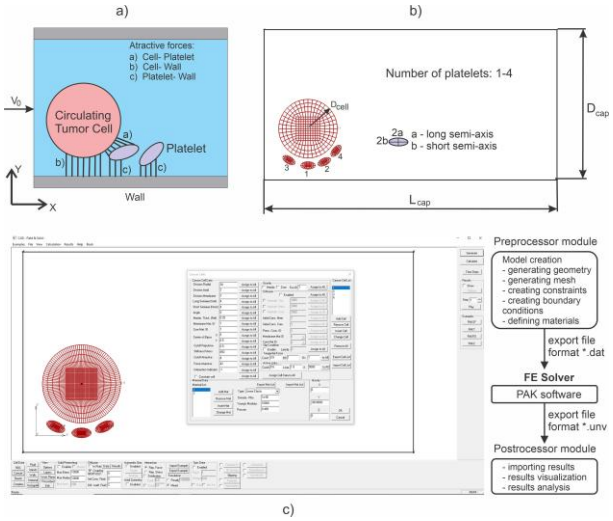

Fig. 3. Schematics of deformable cell motion in a capillary with platelet and wall interactions: a) adhesion forces between cell, platelets, and wall; b) initial platelet positions relative to the cell (1–4 platelets); c) CAD FiS pre-/post-processing interface showing CTC and platelet generation with data flow for input/output.

We examine the effects of the number of flowing platelets on the CTC stoppage time and axial position within the capillary channel. Solutions are shown in Figs. 4a and 4b, assuming cases: without platelets,1-4 platelets, and for cell diameters D=8 and 11 [μm]. The left panels represent the axial velocity Vx (of the cell center, normalized to the entering velocity V0) vs. Time; while on the right panels are the graphs of velocity Vx vs. axial position of the CTC center. Value for the ligand-receptor bond stiffness is constant- K=350 [kPa μm] as well as the Young modulus of the cell- E_{cell}= 30 [kPa].

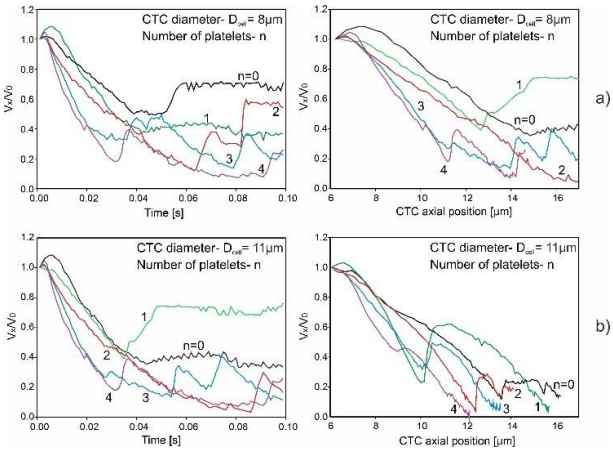

Fig. 4. Effects of number of platelets for 2 different cell diameters. Axial Velocity–Time graphs (left) and Velocity–Axial Position graphs

(right) of the cell center, for 2 cell diameters D[μm] of CTC: a) D=8, b) D=11 (According to [10])

It is notable, from Fig.4a, that only CTC without attached platelets (n=0 line on diagrams) can overcome the ligand-receptor bond forces of the capillary wall and continue its motion through the channel. Ultimately, for the cell diameter of 11 μm (Fig.5b), the cell continues its motion even for a maximum number of platelets. Hence, an increase in the number of attached platelets enhances the attachment to the wall (enhances metastasis, right panel of the Fig. 5b). This can be explained because of fluid flow changes and instabilities, but also due to an overall increase of adhesive bonds per unit surface of the cell.

4. Conclusion

This study analyzed CTC transport within capillaries, focusing on fluid flow, platelet interactions, and vessel wall adhesion. Using a finite element solid–fluid interaction framework, we showed that CTC arrest is strongly influenced by platelet activation and by key parameters including platelet number, CTC size, stiffness, and ligand–receptor bond properties. Experimental data further confirmed the role of platelet activation in enhancing CTC adhesion, underscoring its importance in metastasis.

Acknowledgments

This research was funded by the National Institutes of Health, U01CA244107. Research is also supported by the Ministry of Education, Science and Technological Development of the Republic of Serbia, contract number [451-03-68/2022-14/ 200378 (Institute of Information Technologies, University of Kragujevac)] and the University of Kragujevac [Project MODELETS] and grant number F-134 (Serbian Academy of Sciences and Arts)..

References

[1] Ganesh, K. & Massagué, J. Targeting metastatic cancer. Nat. Med. 27, 34–44 (2021).
[2] Chen J, Luo Y, Xi X, Li H, Li S, Zheng L, Yang D, Cai Z. Circulating tumor cell associated white blood cell cluster as a biomarker for metastasis and recurrence in hepatocellular carcinoma. Front Oncol. 2022 Nov 17;12:931140. https://doi.org/10.3389/fonc.2022.931140
[3] Ju S, Chen C, Zhang J, Xu L, Zhang X, Li Z, Chen Y, Zhou J, Ji F, Wang L. Detection of circulating tumor cells: opportunities and challenges. Biomark Res. 2022 Aug 13;10(1):58. https://doi.org/10.1186/s40364-022-00403-2
[4] Lin D, Shen L, Luo M, Zhang K, Li J, Yang Q, Zhu F, Zhou D, Zheng S, Chen Y, Zhou J. Circulating tumor cells: biology and clinical significance. Signal Transduct Target Ther. 2021 Nov 22;6(1):404. https://doi.org/10.1038/s41392-021-00817-8
[5] Lou XL, Sun J, Gong SQ, Yu XF, Gong R, Deng H. Interaction between circulating cancer cells and platelets: clinical implication. Chin J Cancer Res. 2015 Oct;27(5):450-60. https://doi.org/10.3978/j.issn.1000-9604.2015.04.10
[6] Yu L, Guo Y, Chang Z, Zhang D, Zhang S, Pei H, Pang J, Zhao ZJ, Chen Y. Bidirectional Interaction Between Cancer Cells and Platelets Provides Potential Strategies for Cancer Therapies. Front Oncol. 2021 Oct 14;11:764119. https://doi.org/10.3389/fonc.2021.764119
[7] Milosevic M, Simic V, Nikolic A, Shao N, Kawamura Hashimoto C, Godin B, Leonard F, Liu X, Kojic M. Modeling critical interaction for metastasis between circulating tumor cells (CTCs) and platelets adhered to the capillary wall. Comput Methods Programs Biomed. 2023 Dec;242:107810. https://doi.org/10.1016/j.cmpb.2023.107810
[8] McClay D R, Hertzler P L. Quantitative measurement of cell adhesion using centrifugal force[J]. Current Protocols in Cell Biology, 1998 (1): 9.2.1-9.2.10.
[9] Milosevic M. (2020). CAD Solid and Field - software for biomedical engineering research and accompanied software for the book: "Computational Models in Biomedical Engineering - Finite Element Models Based on Smeared Physical Fields: Theory, Solutions, and Software". https://github.com/miljanmilos/CAD-Solid-Field
[10] Simic V, Nikolic A, Ning S, Milosevic M, Leonard F, Liu X, Kojic M. A parametric study of motion and attachment to capillary walls of circulating tumor cells (CTCs) interacting with non-activated and activated platelets. Comput Methods Programs Biomed. 2025 Jun;264:108699. https://10.1016/j.cmpb.2025.108699

41st Danubia-Adria Symposium Advances in Experimental Mechanics
September 23-26, 2025, Kragujevac, Serbia

Original scientific paper DOI: 10.46793/41DAS2025.155M

CONDITIONS RELATED TO THE ROOF STRUCTURE STRENGTH OF BUSES POWERED BY NATURAL GAS AND FUEL CELLS

Saša MILOJEVIĆ[1], Snežana VULOVIĆ[2], Marija RAFAILOVIĆ[3], Slobodan SAVIĆ[4]

[1] 0000-0003-0569-047X , Faculty of Engineering University of Kragujevac, Sestre Janjić 6, Kragujevac, Serbia, E-mail: sasa.milojevic@kg.ac.rs

[2] 0000-0001-5784-0906 , Institute for Information Technologies Kragujevac, Jovana Cvijića bb, Kragujevac, Serbia, E-mail: vsneza@kg.ac.rs

[3] 0009-0001-2132-9249 , Faculty of Engineering University of Kragujevac, Sestre Janjić 6, Kragujevac, Serbia, E-mail: marija.rafailovic@kg.ac.rs

[4] 0000-0001-6609-4845 , Faculty of Engineering University of Kragujevac, Sestre Janjić 6, Kragujevac, Serbia, E-mail: ssavic@kg.ac.rs

1. Introduction

Modern public transport is increasingly turning to cleaner energy solutions such as compressed natural gas (CNG) or biomethane and hydrogen fuel cells. These technologies help reduce air pollution and greenhouse gas emissions, making buses more sustainable compared to traditional diesel vehicles. However, the use of alternative fuels also creates new engineering challenges, especially in relation to vehicle safety and structural design [1-3].

One important issue is the strength of the bus roof. In many CNG and fuel cell buses, heavy storage tanks or fuel cell systems are installed on the roof. This additional load changes how forces are distributed across the vehicle and may influence how the structure behaves during accidents, such as rollovers. Ensuring that the roof can safely carry these components while still protecting passengers is therefore a critical part of bus design.

This paper examines the conditions that affect roof structure strength in buses powered by CNG. It focuses on how roof-mounted components influence mechanical performance, safety compliance, and overall reliability. The regulations UN ECE 110R [4] and UN ECE 115R [5] more closely define the technical requirements for the installation and homologation of natural gas devices and equipment. The aim of presented researches is to contribute to the development of safer and more efficient bus designs that support sustainable public transport.

The presented calculation methods are also applicable to fuel cell and battery electric buses.

2. Methods for calculating the roof structure strength of the buses powered by CNG

From the perspective of safety and equipment installation rules for gas systems, the requirements that vehicles powered by natural gas must meet are defined by the ECE regulations [4, 5]:

- ✓ UN ECE 110R - Uniform provisions concerning the approval of specific equipment for motor vehicles using natural gas and vehicles equipped with specific natural gas equipment regarding installation.
- ✓ UN ECE 115R - Uniform provisions concerning the approval of vehicles originally approved for a primary fuel, which are subsequently equipped with specific equipment for natural gas propulsion, regarding the installation of such equipment.

CNG tanks are fastened to the bus structure according to the manufacturer's instructions, without direct contact with metal parts, and in accordance with the technical requirements of UN ECE 115R for volumes up to 150 liters.

CNG tanks with a volume greater than 150 liters, when full, must withstand the appropriate deceleration or acceleration without deformation of the tank, the supports, or the part of the bus structure where the tanks are mounted, Table 1.

Table 1. Accelerations that CNG tanks must absorb.

Categories of buses	M2	M3
The acceleration of a bus:		
- in the driving direction	20 × g	6.6 × g
- perpendicular to the driving direction	5 × g	
- g (gravitational acceleration)		

This requirement may also be verified by calculation, in accordance with the conditions defined by the aforementioned standards.

2.1 *Bus roof structure model*

The FEM model of the bus structure was created in Simcenter Femap program and includes the roof section with CNG tanks, see Figure 1. The beam-type finite elements are commonly utilized in the literature for modeling large tubular structures, similar to the upper structures of buses and coaches [7-9]. In this paper, general beam finite elements are used, with a total of 487 elements and 287 nodes.

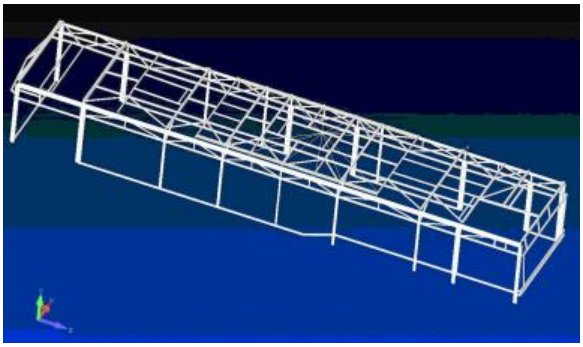

Fig. 1. Supporting roof structure for CNG tanks.

The beam finite elements of the chassis were divided into 22 groups. The chassis structure of the bus consists of four groups of box profiles with the following dimensions: 40×100 mm, 40×120 mm and 40×135 mm. The finite element computer code PAK (abbreviation for „Program for Structural Analysis" in Serbian) [6] was used for the analysis.

The bus roof structure loading conditions were defined following the Table 1, considering the CNG tanks weight and equipment that are installed on the bus roof (m = 733 kg or G = 720 daN).

Based on Table 1, the maximum values of the inertial forces in both directions can be calculated by applying equations (1) and (2):

$$F_a = 6.6 \cdot m \cdot g = 4750 \text{ daN}, \quad (1)$$

$$F_b = 5 \cdot m \cdot g = 3600 \text{ daN}. \quad (2)$$

Where are:

F_a - the intensity of the inertial forces in the driving direction and

F_b - the intensity of the inertial forces in the horizontal plane perpendicular to the driving direction.

The loading model, represented as a system of rigid bodies, was defined by a concentrated resultant force acting at the imaginary center of the CNG tank assembly located on the bus roof at the height of h = 200 mm.

2.2 *Stresses in the bus structure for the first loading case (longitudinal direction)*

The bus structure model for the first loading case, in accordance with equations (3) and (4), is shown in Figure 2.

$$Z=(-F_a) = (-4750) \text{ daN}, \quad (3)$$

$$Y = (-G) = (-720) \text{ daN}. \quad (4)$$

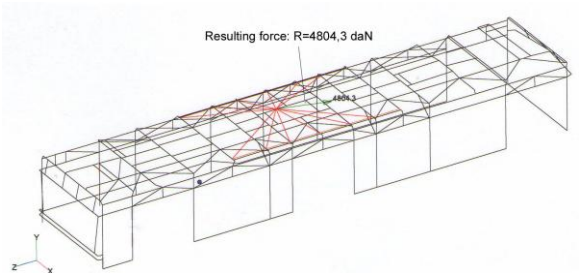

Fig. 2. Bus structure model (first loading case).

The deformed shape of the bus structure model for the first loading case is shown in Figure 3.

Fig. 3. Bus model in the deformed state (first loading case).

Figure 4 shows the stress distribution in the bus structure for the first loading case. The maximum stress $\sigma_{max} = 19.95 \text{ daN/mm}^2$ occurs in the box-section profiles of the structure.

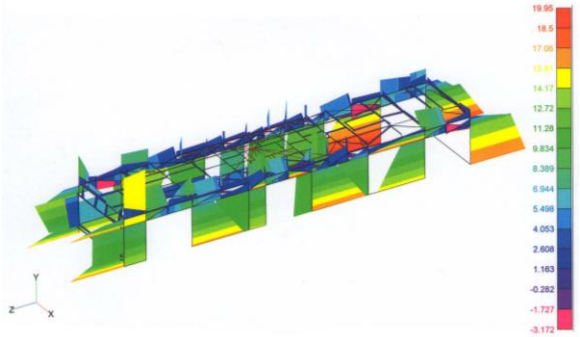

Fig. 4. Stresses distribution within the model (first loading case).

The maximum deflection of the structure obtained for the adopted loading case is Δu_{max}=5.95 mm.

2.3 *Stresses in the bus structure for the second loading case (normal to the driving direction)*

The bus structure model for the second loading case, in accordance with equations (5) and (6), is shown in Figure 5.

$$X=(-F_b) = (-3600)\ \text{daN}, \quad (5)$$

$$Y = (-G) = (-720)\ \text{daN}. \quad (6)$$

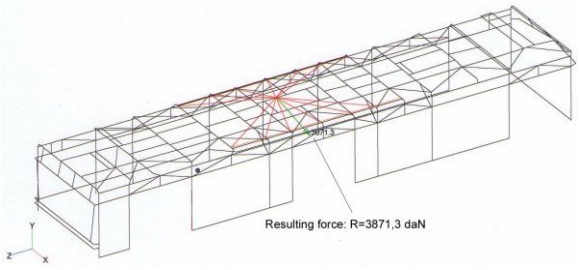

Fig. 5. Bus structure model (second loading case).

Figure 6 depicts the deformed shape of the bus structure under the second loading case.

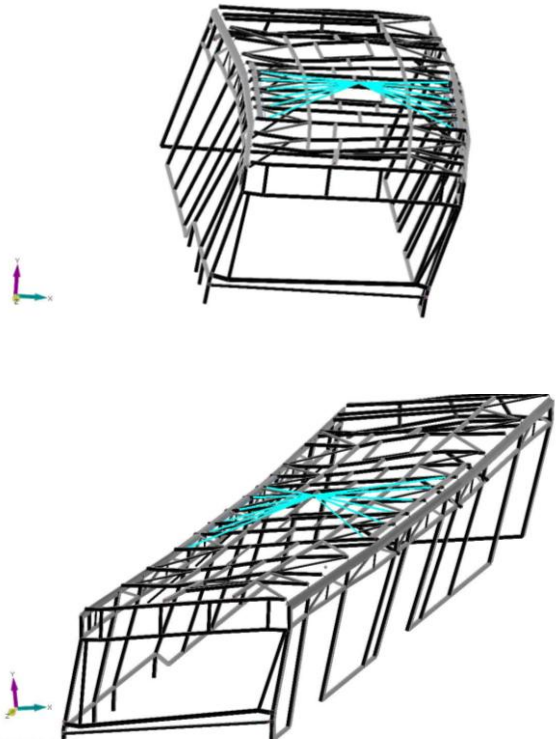

Fig. 6. Bus model in the deformed state (second loading case).

Figure 7 shows the stress distribution in the bus structure for the second loading case. The maximum stress $\sigma_{max} = 26.99\ \text{daN/mm}^2$ occurs in the box-section profiles of the structure with cross-section dimensions (40×40) mm.

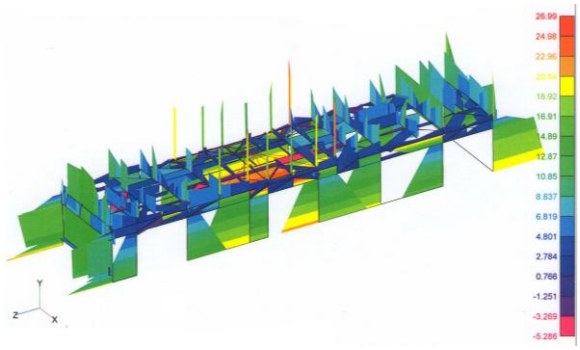

Fig. 7. Stresses distribution within the model (second loading case).

The maximum deflection of the structure obtained for the adopted second loading case is Δu_{max}=24.19 mm.

For the bus structure, the material tensile strength of $\sigma_m = 41.2\ \text{daN/mm}^2$ was adopted. For "U" profiles through which the battery with four CNG tanks is bolted to the bus roof structure, as shown within Figure 8, the tensile strength value of $\sigma_m = 36\ \text{daN/mm}^2$was adopted.

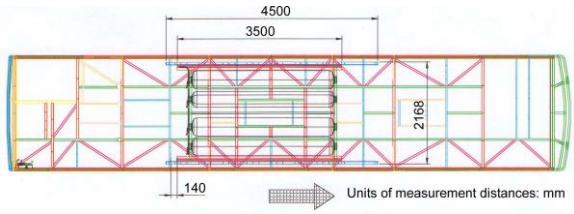

Fig. 8. Position of the CNG tanks with U-profile supports on the bus roof.

The values of the safety coefficients (SC), defined as the ratio between the tensile strength and the calculated stresses, were determined, based on FEM results for the following elements of the bus chassis:

- ✓ Roof base structure: SC = 1.53;
- ✓ U-profiles for connecting the CNG tanks to the bus roof: SC = 3.60;
- ✓ M12 bolts for the detachable connection of the CNG tank battery to the bus roof structure (the bolts are subjected to both tensile and compressive stresses): SC = 1.68.

In order to maintain the structural strength of the bus construction, the limiting value of SC = 1.5 was adopted. This value was selected based on available data from the relevant scientific literature.

Based on the FEM calculation results and the obtained SC values, it can generally be concluded that the proposed solution for connecting the CNG tank battery to the bus roof structure, using welded

U-profiles and bolts, meets the requirements of the UN ECE 110R standard.

In general, the goal of the proposed solution for installing CNG tanks was not only to ensure traffic safety but also to achieve better accessibility to the tanks during inspections and maintenance throughout the bus operation [1].

In this way, the connection with bolts through the U-profile also enables easier disassembly during inspection or replacement of devices and equipment, since in such cases it is necessary to dismantle the tanks and empty the natural gas.

The reliability of the structure, as well as the time between maintenance intervals of CNG buses in operation, can be determined on the basis of research data by applying appropriate distribution functions [10, 11].

3. Conclusions

The transition to buses powered by natural gas and fuel cells represents a significant step toward cleaner and more sustainable public transport. However, the integration of heavy roof-mounted components, such as pressurized storage tanks and fuel cell systems, introduces additional demands on vehicle structure and safety. The roof must not only bear increased static loads but also maintain its integrity under dynamic conditions, particularly during rollover scenarios.

The analysis of conditions affecting roof strength highlights the need for careful structural design and adherence to safety standards. By addressing these challenges, manufacturers can ensure that alternative fuel buses are both environmentally friendly and safe for passengers.

Future research should focus on advanced materials, innovative design methods, and simulations to optimize structural performance while reducing vehicle weight. Such efforts are key to advancing sustainable bus technologies without compromising safety or reliability.

The paper presents a technical solution for the installation of CNG tanks on the bus roof, in accordance with the requirements of relevant regulations and standards. The proposed solution has been implemented in practice and facilitates the maintenance of CNG tanks with their complete equipment during the operational service of buses in traffic.

By applying the proposed solution, in addition to traffic safety, contributions are also made to occupational safety as well as to the reduction of maintenance costs during the operational service of buses.

References

[1] Milojević, S., Stopka, O., Orynycz, O., Tucki, K., Šarkan, B., Savić, S. Exploitation and Maintenance of Biomethane-Powered Truck and Bus Fleets to Assure Safety and Mitigation of Greenhouse Gas Emissions. *Energies*, 2025, 18(9), 2218. https://doi.org/10.3390/en18092218

[2] Hora, T.S., Agarwal, A.K. Compressed Natural Gas and Hythane for On-road Passenger and Commercial Vehicles. In: Singh, A., Agarwal, R., Agarwal, A., Dhar, A., Shukla, M. (eds) *Prospects of Alternative Transportation Fuels. Energy, Environment, and Sustainability*; Springer: Singapore, 2018, pp. 79-106.

[3] Skrucany, T., Semanova, S., Milojević, S., Ašonja, A. New Technologies Improving Aerodynamic Properties of Freight Vehicles. *Applied Engineering Letters*, 2019, 4(2), 48–54.

[4] UN ECE Regulation No. 110 Rev.3—CNG and LNG Vehicles. Available online: http://www.unece.org/trans/main/wp29/wp29regs101-120.html. Accessed August 18, 2025.

[5] UN ECE Regulation No. 115 Rev.1—LPG and CNG Retrofit Systems. Available online http://www.unece.org/trans/main/wp29/wp29regs101-120.html. Accessed August 18, 2025.

[6] Kojić, M., Slavković, R., Živković, M., Grujović, N. THE FINITE ELEMENT METHOD I; University of Kragujevac, Faculty of Mechanical Engineering: Kragujevac, 2010.

[7] Alcalá, E., Badea, F., Martin, Á., Aparicio, F. Methodology for the accuracy improvement of FEM beam type T-junctions of buses and coaches structures. *Int J Auto Tech-Kor*, 2013, 14(5), 817–827.

[8] Romero, F.B., McWilliams, J.M., Fazio, E.A., Izquierdo, F.A. Bayesian kriging regression for the accuracy improvement of beam modeled T-junctions of buses and coaches structures with a methodology based on FEM behavioral analysis. *Int J Auto Tech-Kor*, 2014, 15(6), 1027–1041.

[9] Badea, F., Perez, J.A., Olazagoitia, J.L. Beam T-junction model accuracy improvement based on experimental modal analysis. *Int J Auto Tech-Kor,* 2022, 23(6), 1537–1545.

[10] Panic, S., Petrovic, V., Draskovic, S., Kontrec, N., Milojevic, S. Performance analysis of hybrid fso/rf communication system with receive diversity in the presence of chi-square/gamma turbulence and rician fading. *Bulletin of D. Serikbayev EKTU*, 2023, 4, 304–312.

[11] Marinković, D., Dezső, G., Milojević, S. Application of Machine Learning During Maintenance and Exploitation of Electric Vehicles. *Advanced Engineering Letters*, 2024, 3(3), 132–140.

41st Danubia-Adria Symposium Advances in Experimental Mechanics
September 23-26, 2025, Kragujevac, Serbia

Original scientific paper DOI: 10.46793/41DAS2025.159LJ

CFD INVESTIGATION OF TURBULENT WATER FLOW IN A PIPE ELBOW: ASSESSMENT OF CAVITATION RISK

Pavle LJUBOJEVIĆ[1], Saša STAŠEVIĆ[2]

[1] 0000-0002-5546-5046, Faculty of Mechanical Engineering, Kraljice Marije 16, Belgrade, Serbia, E-mail: pljubojevic@mas.bg.ac.rs

[2] Faculty of Mechanical Engineering, Kraljice Marije 16, Belgrade, Serbia, E-mail: d16-2024@studenti.mas.bg.ac.rs

Abstract: *In this study, turbulent water flow in a DN65 pipe elbow was analysed at high Reynolds numbers using the OpenFOAM software with a two-dimensional model. The research aims to determine the critical mean inlet velocity of the fluid—water that leads to a pressure drop below the saturation pressure and the onset of vapour phase formation, i.e., cavitation. Although such elbows in practice usually operate at lower flow rates, corresponding to fluid velocities that do not reach cavitation conditions, here the limiting conditions were examined for potential non-standard applications involving extremely high flow rates resulting in large velocities. After developing the turbulent flow model, the visualisation was performed in ParaView, and the data were subsequently processed in Python, where the cavitation zone areas were calculated.*

Keywords: *cavitation; turbulent flow; CFD; pipe-elbow flow*

1. Introduction

Cavitation represents the formation and subsequent collapse of vapor or gas bubbles in the vicinity of solid surfaces [1, 2]. Depending on the mechanism of initiation, cavitation can be classified as hydrodynamic, acoustic, optical, or particle cavitation. Broadly, these phenomena may be grouped into two categories: cavitation induced by stress in liquids (hydrodynamic and acoustic) and cavitation induced by localised energy deposition (optical and particle) [3].

In mechanical systems, particularly in fluid transport applications, hydrodynamic cavitation is the most common type and is associated with adverse effects such as noise, vibration, and a reduction in the load-carrying capacity and durability of machine elements (gears and bearings) [4, 5]. A combined mechanism, referred to as hydrodynamic–acoustic cavitation (HAC), arises when structural vibrations at specific natural frequencies, or other excitation sources, produce pressure fluctuations that promote bubble formation under the influence of ultrasound. In such cases, acoustic cavitation act synergistically with hydrodynamic cavitation, resulting in more severe material degradation within the system [6]. Both hydrodynamic and acoustic cavitation processes generally progress through four characteristic stages: incubation, acceleration, deceleration, and terminal stage. Potentially, a fifth phase may also appear, which refers to the complete degradation of the work and the consequences of which can be catastrophic [7].

In fluid transport piping systems, cavitation arises in regions where the local pressure decreases below the saturation pressure. Such conditions may occur along straight pipe sections due to frictional losses, at abrupt changes in flow direction (e.g., elbows), within various fittings, or in pump impellers. In addition, entrained gas molecules within the liquid often act as nucleation sites for vapour–gas bubble formation, thereby promoting the initiation of cavitation [8–10]. Therefore, one of the key parameters when sizing and determining the geometry of pipelines is protection against cavitation.

In this study, computational fluid dynamics (CFD) simulations using OpenFOAM were conducted to investigate water flow through a DN65 pipe elbow at five different average inlet velocities: 5, 10, 15, 20, and 25 m/s. Although such elbows are not typically subjected to these flow rates in practical applications, the primary objective of this research was to identify the threshold average inlet velocity at which the system pressure falls below the saturation pressure.

2. Model development and setup

The simulation setup, its workflow, and the post-processing of the obtained results are schematically shown in Fig. 1.

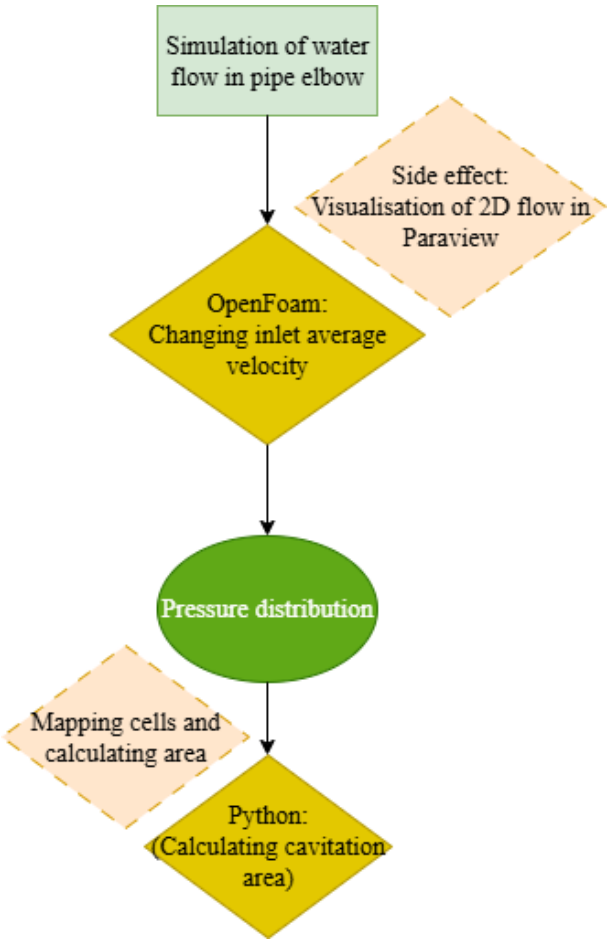

Fig. 1. Flow chart of simulation and results processing

The computational domain was defined by the inner pipe diameter (66.1mm), as it represents the fluid region. To reduce computational cost, the pipe was sectioned along the mid-plane, enabling a 2D flow analysis. The pipe geometry and mesh generation were carried out in Gmsh and are illustrated in Fig. 2.

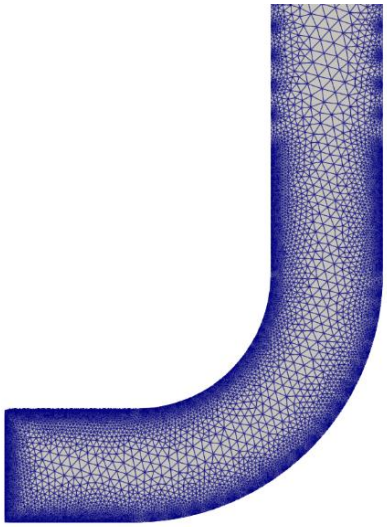

Fig. 2. Pipe elbow model mesh

The mesh consists of a total of 32 884 prismatic cells and one layer in depth to achieve a 2D simulation. The mesh parameters, with a maximum non-orthogonality of 28.82° and an average of 5.87°, indicate excellent mesh accuracy.

The simulation was carried out for water at 20 °C, with the flow considered isothermal. Under these conditions, the kinematic viscosity of water is $1\text{x}10^{-6}$ m^2/s, and the Reynolds numbers for the inlet velocities are given in Table 1.

Table 1. Reynolds number values

U_{avg} [m/s]	5	10	15	20	25
Re/10^5	3.3	6.6	9.9	13.2	16.5

These Reynolds number values indicate turbulent flow in the pipe elbow, which is why the RNG k–ε model was selected in the pimpleFoam solver. Since the flow at the inlet to the elbow itself is laminar, in order to avoid extending the pipe upstream of the elbow, following the approach in [11], the inlet velocity profile was prescribed using Equation (1).

$$\frac{\bar{u}}{U_c} = \left(\frac{R-r}{R}\right)^{1/n}, n = f^{-1/2} \quad (1)$$

Where U_c is velocity in pipe centre, and f is the friction coefficient calculated according following Swamee and Jain modification of Colebrook equation for our values of Reynolds number [12]:

$$f = \left[-2\log\left(\frac{\varepsilon}{3.7} + \frac{5.74}{Re^{0.9}}\right)\right]^{-2} \quad (2)$$

Where ε is relative pipe roughness (0.1mm).

For the validation of the velocity profile, the plot over line option in ParaView was used, and the velocities at the centre were compared with the velocity at the centre obtained according to the following expression (sdhadsh):

$$\frac{U_c}{U_{avg}} = \frac{(n+1)(2n+1)}{2n^2} \quad (3)$$

The plotted velocities at the center and the velocities calculated according to the expression have a relative error of less than 1%.

It is assumed that the fluid is thermally isolated and maintained at a constant temperature of 20 °C. The applied model refers to transient flow; however, by comparing the p and U files after a certain number of iterations, very small oscillations of these values were observed, indicating that the flow becomes steady after a certain time. The analysis of pressure distribution was therefore carried out for

these steady-state values. Since the model refers to an incompressible fluid, the pressure values were divided by the water density, meaning that the scales represent pressure per unit mass (m^2/s^2). At the outlet of the elbow, the pipe length was set to five diameters due to computational limitations and simulation time. A relative pressure of 200 m^2/s^2, corresponding to an overpressure of 2 bar, was imposed at the outlet. Since this model does not account for fluid compressibility or vapor phase formation, the critical values were taken as pressures in the field corresponding to a scale value of –70, which represents an absolute pressure of 30 kPa, because the saturation pressure of water at 70 °C is 30 kPa.

3. Results and discussion

Fig. 3. shows the velocity field for an average inlet velocity of 20 m/s at three different iterations for visualising the fluid flow.

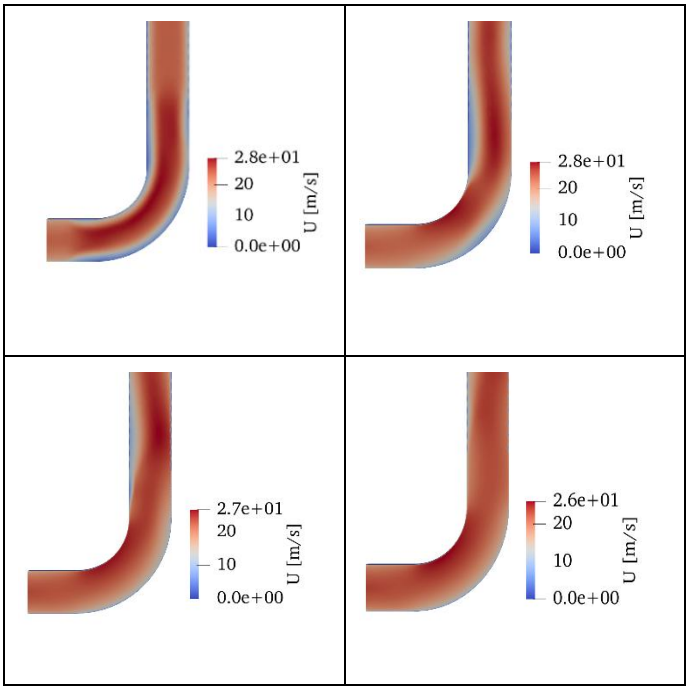

Fig. 4. Velocity profile for average U = 20 m/s

The figure shows the initial phase of the flow, followed by the flow development and the velocity profile when it begins to converge, but has not yet reached the steady-state regime.

The analysis of the model was performed for a steady-state flow regime, where the values of the quantities fluctuate negligibly.

The pressure distribution in the model at the final iteration, for the specified simulation duration and time steps that varied depending on the Courant number, is shown in the figure.

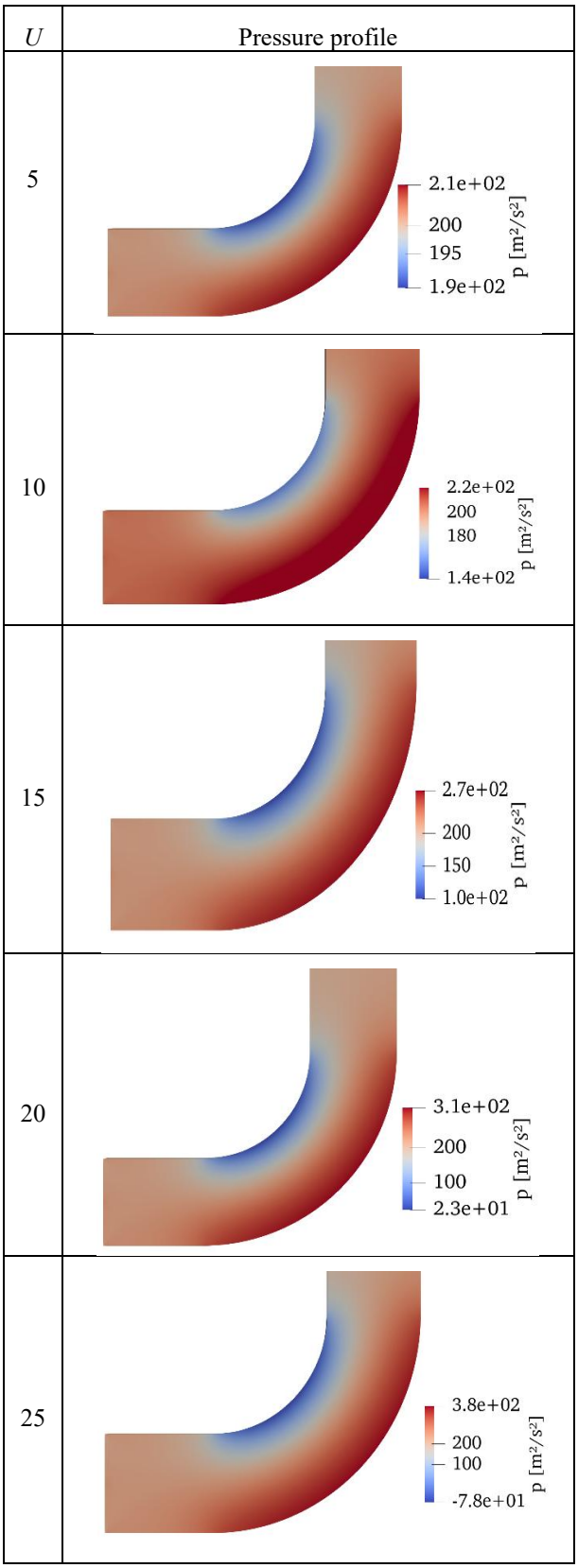

Fig. 3. Pressure profile for different average inlet velocities

The pressure scale shows that among the analysed velocities, only 25 m/s leads to a drop of the absolute pressure below the saturation pressure; that is, the critical inlet velocity is slightly below 25 m/s, due to the minimum absolute pressure on the scale being 22 kPa. For an inlet velocity of 20 m/s, the minimum pressure is 23 kPa, above atmospheric pressure, which means that for water at a temperature of 100 °C, a slightly higher velocity than 20 m/s would be critical.

For the final analysis and inspection of the cavitation zone surface, the results from the VTK file were imported into Python, where the cells with pressure below the critical value were mapped and their surface area determined. A total of 21 cells were mapped, with a total surface area of 0.000109 m², which is 0.81% of the total elbow surface area.

4. Conclusions

Based on the brief overview of cavitation in mechanical systems and the conducted simulation, the following conclusions can be drawn:

- Cavitation can represent a major issue in the operation of mechanical systems, primarily in fluid transport systems but also in power transmission systems.
- In pipelines, there is a significant risk of cavitation, which in its final stage can destroy the pipe wall.
- The simulation performed for different inlet velocities shows that the critical average velocity at the inlet of the DN65 elbow for cavitation onset in water at 70 °C is slightly below 25 m/s.
- Since this model does not account for temperature variation, it can also be applied to other water temperatures, but for that reason, it provides a somewhat rougher estimate.
- To validate these results, it is necessary to conduct an experiment and repeat the simulation in a model that supports two-phase flow, in order to possibly track the development of cavitation bubbles.

Acknowledgments

This work was supported by the Ministry of Science, Technological Development and Innovations of the Republic of Serbia (Contracts: 451-03-137/2025-03/ 200105) and CA23155 - A pan-European network of Ocean Tribology (OTC).

References

[1] Knapp, R.T. Cavitation Mechanics and its Relation to the Design of Hydraulic Equipment. *Proceedings of the Institution of Mechanical Engineers*, 1992 166, 150–163.

[2] Dojčinović, M. *Razaranje materijala pod dejstvom kavitacije*; Monograph, Tehnološko-metalurški fakultet, Beograd, 2013.

[3] Lauterborn, W. Cavitation and Inhomogeneities in Underwater Acoustics. In *Proceedings of the First International Conference*, Göttingen, Fed. Rep. of Germany, July 9–11, 1979; Springer Science & Business Media (2012)

[4] Dowson, D., Taylor, C.M. Cavitation in Bearings. *Annu. Rev. Fluid Mech*., 1979, 11, 35–65. https://doi.org/10.1146/annurev.fl.11.010179.000343

[5] Ouyang, T., Mo, X., Lu, Y., Wang, J. CFD-vibration coupled model for predicting cavitation in gear transmissions. *International Journal of Mechanical Sciences*, 2022, 225.

[6] Wu, P., Bai, L., Lin, W., Wang, X.: Mechanism and dynamics of hydrodynamic-acoustic cavitation (HAC). *Ultrasonics Sonochemistry*, 2018, 49, 89–96.

[7] G02 Committee: Test Method for Cavitation Erosion Using Vibratory Apparatus, http://www.astm.org/cgi-bin/resolver.cgi?G32-16

[8] Chang, H., Xie, X., Zheng, Y., Shu, S., Numerical study on the cavitating flow in liquid hydrogen through elbow pipes with a simplified cavitation model. *International Journal of Hydrogen Energy*, 2017, 42, 18325–18332.

[9] Jin, Z., Gao, Z., Qian, J., Wu, Z., Sunden, B., A Parametric Study of Hydrodynamic Cavitation Inside Globe Valves. *Journal of Fluids Engineering*, 2018, 140.

[10] Martin, C.S., Medlarz, H., Wiggert, D.C., Brennen, C., Cavitation Inception in Spool Valves. *Journal of Fluids Engineering*, 1981, 103, 564–575.

[11] Homicz, G.: Computational Fluid Dynamic simulations of pipe elbow flow, (2004)

[12] Genic, S., Aranđelović, I., Kolendić, P., Jarić, M., Budimir, N., Genić, V., A Review of Explicit Approximations of Colebrook's Equation. *FME Transaction*, 2011, 39(2), 67-71.

41st Danubia-Adria Symposium Advances in Experimental Mechanics
September 23-26, 2025, Kragujevac, Serbia

Original scientific paper DOI: 10.46793/41DAS2025.163C

KINEMATIC ANALYSIS OF THE COMPLEX PLANETARY GEAR TRAIN OVERVIEW

Stefan ČUKIĆ[1], Slavica MILADINOVIĆ[2], Anđela PEROVIĆ[3], Lozica IVANOVIĆ[4], Saša MILOJEVIĆ[5], Blaža STOJANOVIĆ[6]

[1] 0009-0002-5765-1712 , Faculty of Engineering University of Kragujevac, Sestre Janjić 6, Kragujevac, Serbia, E-mail: stefan.cukic@kg.ac.rs;

[2] 0000-0002-4408-0634 , Faculty of Engineering University of Kragujevac, Sestre Janjić 6, Kragujevac, Serbia, E-mail: slavicam@kg.ac.rs;

[3] 0009-0005-5637-9827 , Faculty of Engineering University of Kragujevac, Sestre Janjić 6, Kragujevac, Serbia, E-mail: andjela.perovic@kg.ac.rs;

[4] 0000-0002-9503-593X , Faculty of Engineering University of Kragujevac, Sestre Janjić 6, Kragujevac, Serbia, E-mail: lozica@kg.ac.rs;

[5] 0000-0003-0569-047X , Faculty of Engineering University of Kragujevac, Sestre Janjić 6, Kragujevac, Serbia, E-mail: sasa.milojevic@kg.ac.rs

[6] 0000-0003-4790-2856 , Faculty of Engineering University of Kragujevac, Sestre Janjić 6, Kragujevac, Serbia, E-mail: blaza@kg.ac.rs;

1. Introduction

Planetary gear trains represent a special type of gear transmission whose element motion resembles the movement of planets around the Sun. Thanks to their compact design and the ability to achieve high transmission ratios with a relatively low total mass, they have found application in various fields of mechanical engineering.

The basic planetary gear train (PGT) consists of two central gears (one with external teeth and the other with internal teeth), planet gears, and a carrier on which the planets are mounted. By connecting the appropriate elements to the input and output shafts, as well as by fixing certain components, different configurations or planetary gear train schemes can be obtained. This is described in the literature [1] and [2]. By adding gears and carriers to the structure of a simple planetary gear train, complex planetary gear trains are formed. Their advantage over simple ones lies in achieving a greater number of different transmission ratios. This has defined the wide application of PGT in automatic transmissions of various passenger and heavy-duty vehicles, as well as buses and construction machinery.

To determine the transmission ratios, or the speeds of a multi-stage planetary gear train, it is necessary to understand the kinematics of the coupling between its elements. Considering the complexity of the motion, this represents a very challenging task. In books [1, 2], the most commonly used methods for solving the kinematics of PGT are presented.

The applying of these methods for determining the transmission ratios of a complex PGT requires a great deal of time due to the increasing complexity of the motion equations and the difficulty in expressing the transmission ratios caused by the large number of degrees of freedom. Because of these shortcomings, an overview of research related to new methods for determining the speeds of the complex Ravigneaux planetary gear train (RPGT) model is presented, Figure 1-a.

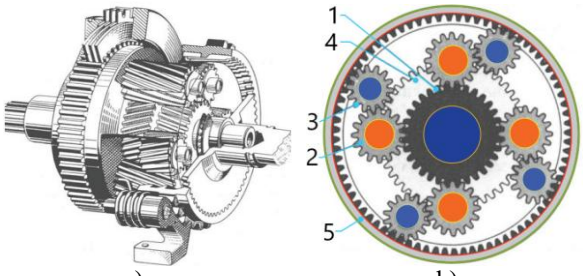

a) b)

Fig. 1. Ravigneaux planetary gear train [3]

The Ravigneaux model features a compact design with a single planet carrier, three central gears (1), (4), and (5), and two planet gears (2) and (3) that are meshed with each other, Figure 1-b. By connecting the central gear (5) to the output shaft and fixing or connecting the remaining three central elements, gears (1) and (4) and the carrier to the input shaft, it is possible to achieve the max. value of six different transmission ratios. In practice, however, due to the way the aforementioned elements are connected to the components of an automatic transmission, it is possible to achieve the max. of four forward speeds and one reverse speed.

Some of the commonly used transmissions with the RPGT are: Ford AOD, ZF 4HP14, ZF 6HP19/26, Mercedes-Benz 5G-Tronic, A5S310Z for BMW 530i, Mercedes-Benz 7G-Tronic, etc.

Taking into account the complexity of the motion regarding the elements of the mentioned multi-stage RPGT, this paper will provide a systematic review of methods, emphasizing their advantages, disadvantages, and areas of applying.

2. Kinematic Analysis

Among the standard methods, the most widely used are Willis's equation and the general motion equation in the form of a combined method. These methods are described in detail in books [1, 2]. Using the conditions given in [1], inside [4] analytically expressed the overall transmission ratio for one of the gears of the RPGT as a function of the number of teeth of the central gears. To determine the transmission ratio, two general equations were used due to the division of the RPGT into two simple planetary gear trains.

In the following text, the methods for determining kinematics of the RPGT are presented.

2.1 Lever Analogy Method

Benford and Leising [5] introduced this method as a new tool for analyzing automatic transmission systems. The method is based on drawing a vertical line with corresponding points. This line represents the lever, while the points define the central elements of the RPGT. The construction of the lever for the RPGT is shown in Figure 2.

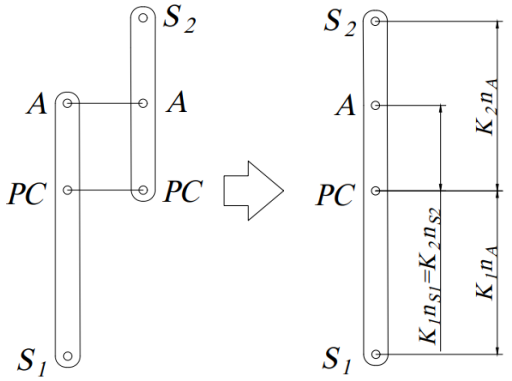

Fig. 2. Lever construction for the RPGT [8]

The RPGT represents a combination of two simple planetary gear trains in which the planet carrier (PC) and the central gear with internal teeth (A) are identical, while the central gears with external teeth (S1) and (S2) differ. By connecting their all levers, one lever for the analyzed RPGT is obtained, Figure 2.

On the obtained lever, the distances are then defined as $K \cdot n_A$ and $K \cdot n_S$ between the points, which represent the rotational speeds of the central gears multiplied by constants K_1 and K_2. By knowing the rotational speed of the input element and fixing the corresponding gear, the scale constants can be determined based on this relationship, and using them, the rotational speeds of all elements can be calculated. Based on the obtained values of the rotational speeds for the input and output elements, the overall transmission ratio for the corresponding speed of the RPGT can be easily determined.

Today the method applying allows determining the values of loads that occur at the gear contacts. The drawback of the method is that it does not take into account data related to the planet gears and their mutual relationships. This problem was addressed in [6] by adding nodal points that define the planet gears.

2.2 Matrix Method Based on Graph Theory

Kinematic relationships between the elements inside RPGT can be represented with graph theory. The graph construction for the RPGT, presented in literature [7], can be seen in Figure 3-a.

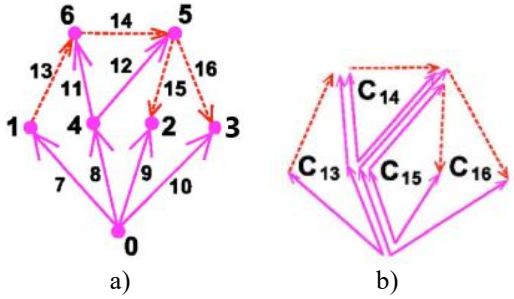

a) b)

Fig. 3. Construction a)-graph and b)-of the closed loop for RPGT [7]

Node of the input shaft (0) is connected to the nodes of the central gears (1) and (2) and the planet carrier (4). The carrier node (4) is connected to the nodes of the planet gears (5) and (6). The node of the central gear with internal teeth is connected to the output shaft node, which is labeled as (0). Solid connections (7, 8, 9, 10, 11, and 12) are defined with a solid line between the nodes, while transmission connections (13, 14, 15, and 16) are represented with a dashed line. Based on its construction, closed loops can be obtained (C_{13}), (C_{14}), (C_{15}) i (C_{16}) which are shown in Figure 3-b.

For the graph in Figure 3-a, the incidence matrix is determined $\Gamma^o = m \times k$ (m – nodes, k – edges) the incidence matrix, which can be reduced so that the node is not included (0). Reduced matrix Γ can be divided into two parts from which the path matrix

is determined Z oriented graph. From this matrix, the cycle metric can be determined as the function of closed loops, Figure 3-b, and through it, the linear equation of the absolute angular speed can be obtained in the following form [7]:

$$\begin{bmatrix} -i_{13} & 0 & 0 & i_{13}+1 & 0 & -1 \\ 0 & 0 & 0 & i_{13}+1 & -1 & -i_{14} \\ 0 & -i_{15} & 0 & i_{13}+1 & -1 & 0 \\ 0 & 0 & 1 & i_{13}+1 & -i_{16} & 0 \end{bmatrix} \cdot \begin{pmatrix} \omega_1 \\ \omega_2 \\ \omega_3 \\ \omega_4 \\ \omega_5 \\ \omega_6 \end{pmatrix} = \begin{pmatrix} 0 \\ 0 \\ 0 \\ 0 \\ 0 \\ 0 \end{pmatrix}, \quad (1)$$

Where are: i_{13}, i_{14}, i_{15} i i_{16} partial transmission ratios between the elements of the RPGT, and ω_i angular speeds of all elements. By knowing the input parameters, the matrix equation (1) is simplified. By connecting and fixing the appropriate elements of the complex PGT, the angular speeds can be expressed in matrix form ω_i, and through them, the overall transmission ratios for each of its speeds.

The procedure for determining transmission ratios using the linear equation of absolute angular speed is presented in [8]. Unlike the previous method, this study performs a structural decomposition, where the RPGT is divided into two parts, graphically represented using a rotation graph. The rotation graph is similar to the graph in Figure 3-a. The difference is that the nodal points are connected in the form of a closed polygon. Discretization of the rotation graph into two substructures, the node matrix is determined, from which the angular speed matrix is obtained. Based on the angular speed matrix, the linear equation of angular speeds in matrix form is derived, which is similar to equation (1). The difference lies in the definition of partial transmission ratios on the left side of the equation. Solving the resulting linear equation is similar to the procedure in [7].

2.3 Nomogram Method

A new method for analyzing kinematic quantities, as well as torques on the elements of PGT, was developed by [9, 10], where is RPGT presented graphically using a nomogram. The construction of the nomogram involves drawing vertical lines corresponding to the angular speeds of the PGT elements relative to the horizontal axis.

In [9, 10], a detailed procedure for obtaining speeds in an automatic transmission containing the RPGT is presented. The mentioned transmission represents a conceptual design and includes two drives. The nomogram for the RPGT is shown in Figure 4. Normal (3) corresponds to the planet carrier, the outer normals (5) and (6) to the planet gears, and normals (1), (3), and (4) to central gears.

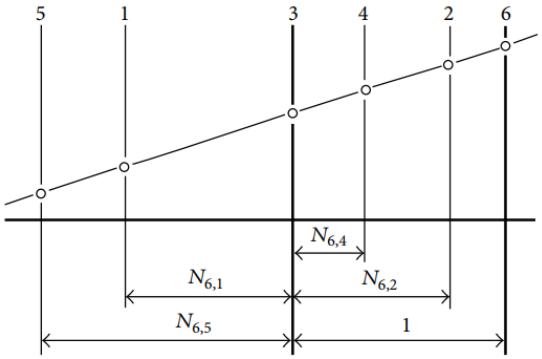

Fig. 4. Nomogram for RPGT [9]

The carrier normal (3) is placed at the zero position on the horizontal axis, and the outer planet gear (6) at a distance of 1 from normal (3), as shown in Figure 4. The distances of the other normal relative to the planet carrier normal represent the partial transmission ratios $N_{6,1}, N_{6,2}, N_{6,4}$ i $N_{6,5}$. Partial transmission ratios are defined using Willis's equation:

$$N_{gb,ga} = \frac{\omega_{ga} - \omega_c}{\omega_{gb} - \omega_c} = \frac{z_{gb}}{z_{ga}}, \quad (2)$$

where are: ω_{ga}, ω_{gb} and ω_c angular speeds of the input, output, and fixed elements, z_{gb} and z_{ga} the numbers of teeth of the output and input elements of the planetary gear train, respectively.

If a line is drawn at an angle across the normal, the distances of the intersected points on the normal relative to the horizontal define the angular speeds of the elements of the RPGT. Using the ratios of partial transmission on the horizontal axis and the differences in angular speeds on the vertical axis, the overall transmission ratios for each speed of the mentioned complex PGT are determined. Moreover, the advantage of the nomogram lies in drawing and determining the torque values on all elements of the RPGT, as well as listing all possible sequences of connecting the central elements with the clutches and brakes of the automatic transmission [10].

2.4 Discussion of Modern Methods

All three methods are based on graphical interpretation and analytical expression of transmission ratios. However, clear differences can be observed between them. The Lever Analogy Method provides precise results, provided that the distances between the nodal points on the lever are correctly defined. On the same lever, the values of peripheral speeds and torques of the elements of the RPGT can then be plotted in vector form, and their

relationships can be further analyzed in terms of dynamic analysis. The procedure is very simple, but it is not suitable for computer implementation.

According to the Lever Method, [9, 10] it is possible to graphically and analytically represent the relationships between the angular speeds of the elements inside RPGT for each gear ratio using a nomogram. On the nomogram and the lever, it is possible to plot the values of peripheral speeds and torques, which can be used for dynamic analysis. The procedure for determining the transmission ratios is more complex when using the nomogram due to the methodology required to determine the transmission ratio values for each gear. A drawback of this method is that it requires additional use of Willis's equation and is not suitable for computer implementation.

The matrix method is the most complex of the analyzed methods, as it requires knowledge of a mathematics. Although it is based on graphical interpretation, the entire procedure is analytical and time-consuming. It is suitable for computer implementation due to the use of matrices and provides the most accurate results. The method can be easily adapted to changes in the design of a complex PGT, provided that the input parameters are correctly defined. This is not the case for the other two groups of methods.

3. CONCLUSIONS

The analyzed methods for determining the transmission ratios, i.e., the speeds of a complex planetary gear train, are complex to execute. Unlike conventional procedures, they provide more accurate results and better insight into the relationships between the gears and the planet carrier.

By applying these methods, any complex PGT can be analyzed, provided its elements are correctly represented graphically. In addition to kinematics, the methods allow for dynamic analysis of the PGT, as well as solving the problem of connecting the central elements to the input and output shafts of the automatic transmission via clutches. This provides a better understanding of the methodology for changing speeds and the loading of the elements of the PGT.

Each method has its own advantages and disadvantages, and their practical application depends on the initial requirements set during the design of an automatic transmission.

Among the analyzed methods, the use of graphs and the incidence matrix stands out due to their accuracy, easy adaptation to changes in the PGT design, and suitability for computer implementation.

Future research will focus on applying these methods to more complex PGT with 8, 9, and 10 speeds. In addition, the conditions for proper assembly and meshing of the elements of complex PGT, which are not fully addressed by these methods, will be thoroughly investigated.

References

[1] Tanasijević, S., Vulić, A. *Mechanical transmissions: Planetary gear units and variators*; Faculty of Mechanical Engineering: University of Kragujevac, 2006.

[2] Arnaudov, K., Karaivanov, D.P. *Planetary gear trains*; CRC Press: Boca Raton 2019.

[3] Abderazek H., Sait S.M., Yildiz A.R. Optimal design of planetary gear train for automotive transmissions using advanced meta-heuristics. *International Journal of Vehicle Design,* 2019, 80(2-4), pp. 121–136.

[4] Novakovic, M., Stojanovic, B., Milisavljević, M., Miladinovic, S. The kinematic analysis of Ravigneaux planetary gear set. *Technical Diagnostic*, 2016, 15 (1), pp. 7-12.

[5] Benford, H.L., Leising, M.B. The lever analogy: A new tool in transmission analysis. *SAE Transactions* 1981, pp. 429–437.

[6] Yang, X., Yu, W., Shao, Y., Xu, Z., Zeng, Q., Nie, C., Peng, D. An Augmented Lever Analogy Method for Kinematic Analysis of Dual-Input Planetary/Epicyclic Gear Sets Involving Planet Gear. *IEEE Access*, 2022, *10*, 101137-101148.

[7] Talpasanu I., Yih T., Simionescu P. A general method of kinematic analysis of parallel axes epicyclic gear trains based on graph-cycle matroid theory. *International Design Engineering Technical Conferences and Computers and Information in Engineering Conference,* 2005, vol. 4742, pp. 647–656.

[8] Hussen, H.A., Esmail, E.L. Application of incidence matrix to topological structure and kinematic analysis of multi-planet gear trains. *Results in Engineering,* 2021, 12, 100305.

[9] Esmail, E.L., Hussen, H.A. Nomographs for kinematics, statics and power flow analysis of epicyclic gear trains. In *ASME International Mechanical Engineering Congress and Exposition,* 2009, vol. 43864, pp. 631–640.

[10] Esmail E.L. Nomographs for synthesis of epicyclic-type automatic transmissions. *Meccanica,* 2013, 48(8), 2037–2049.

Original scientific paper DOI: 10.46793/41DAS2025.167DZ

IMPROVEMENT OF THE TECHNICAL AND OPERATIONAL CHARACTERISTICS OF ZA-27 ALLOYS REINFORCED WITH SIC AND AL_2O_3

Dragan DZUNIC[1], Stefan MILETIC[2], Milan IVKOVIC[3], Slobodan MITROVIC[4]

[1] 0000-0002-1914-1298 , Faculty of Engineering University of Kragujevac, Sestre Janjić 6, Kragujevac, Serbia, E-mail: dzuna@kg.ac.rs;

[2] 0009-0007-0253-2819 , Faculty of Engineering University of Kragujevac, Sestre Janjić 6, Kragujevac, Serbia, E-mail: smiletic@kg.ac.rs,

[3] 0000-0001-5176-5837 , Faculty of Engineering University of Kragujevac, Sestre Janjić 6, Kragujevac, Serbia, E-mail: : milan.ivkovic@kg.ac.rs;

[4] 0000-0003-3290-7873 , Faculty of Engineering University of Kragujevac, Sestre Janjić 6, Kragujevac, Serbia, E-mail: milanivkovicfin@gmail.com;

1. Introduction

The ZA-27 alloy belongs to the group of zinc–aluminium alloys, which are well known for their high strength and wear resistance, good dimensional stability, and relatively low cost compared to other materials with similar technical and operational characteristics. Composites such as ZA-27+Al_2O_3+SiC are increasingly applied in technical and tribo-mechanical systems. These alloys have found wide application in mechanical engineering and transportation, particularly in the automotive industry for brake components, engine parts, and steering systems, as well as in aerospace applications and machine tools, where elements are exposed to increased friction and wear [1, 2].

By combining ZA-27 with reinforcements such as Al_2O_3 (aluminium oxide) and SiC (silicon carbide), composites with exceptional properties are obtained. Al_2O_3 is used as a reinforcement in composites due to its high hardness and wear resistance. This material significantly improves the mechanical properties of the composite, such as strength, impact resistance, and abrasion resistance. SiC is an extremely hard substance with high heat and wear resistance. When combined with ZA-27, SiC contributes to the composite's thermal stability and provides additional mechanical durability [1, 2].

Numerous studies and research papers highlight the advantages of these alloys in practical applications compared to many other materials. The focus of this study is not on comparing ZA-27 alloys with other materials, but rather on examining the ZA-27 alloy with reinforcements, specifically how SiC- and Al_2O_3-based reinforcements influence the coefficient of friction and penetration force during experiments.

The tribological properties of materials are influenced by several factors, including applied load, sliding speed, lubrication conditions and type of lubricant, as well as the surrounding environment in which the experiment is conducted. In the case of composites with reinforcements, the percentage of reinforcement also plays a key role. However, an increased reinforcement content does not necessarily guarantee improved properties; instead, the characteristics also depend on the fabrication method and the degree of homogeneity achieved. A more uniform microstructure ensures consistent performance across the entire surface. Research findings [3] have shown a significant reduction in the coefficient of friction for reinforced materials compared to the base alloy. Optimal results were obtained under a load of 20 N (load range: 20–80 N) and a sliding speed of 1 m/s (speed range: 1–2 m/s), where minimal wear and the lowest coefficient of friction were recorded. Notably, the best results were achieved with a 5% reinforcement content, with variations tested between 1% and 5% [3].

The fabrication method also significantly affects the properties of such composites. These materials are most commonly produced by either sintering or compo-casting. Increasing the sintering temperature has been found to reduce wear and improve friction resistance, highlighting the potential for application of these materials in

demanding industrial environments. The results confirm that high-temperature sintering substantially enhances the tribological properties of the material. These findings may be of great importance for the development of new materials in engineering and manufacturing, where wear resistance is critical [4, 5].

Several studies hypothesize that the addition of SiC and graphite enhances the wear resistance of composites under dry sliding conditions, since these solid particles can reduce friction and wear compared to unreinforced ZA27 alloy. Experimental results confirm that composites reinforced with SiC and graphite exhibit significantly reduced wear compared to the base ZA27 alloy, thereby supporting the hypothesis regarding improved tribological properties. This analysis highlights the potential of ZA27/SiC/Graphite composites for industrial applications in environments where wear resistance is critical. Another important finding is that composites containing graphite demonstrated much better results than those without, as graphite acted as a solid lubricant [6, 7].

In addition to dry sliding tests, investigations including lubrication with oil at the contact interface have also been carried out. These results confirm the positive influence of nano-graphite on the tribological performance of ZA27 alloys under lubricated conditions, opening new opportunities for industrial applications [6, 7].

Furthermore, results have shown that the strength and hardness of aluminium alloys increase with the addition of Al_2O_3, while the wear rate decreases. This emphasizes the role of Al_2O_3 as a reinforcement in aluminium-based composites, which may be highly relevant for the development of more efficient braking systems in the automotive industry [8].

2. Experiment

The experiment was carried out using a CSM+ Instruments nano-tribometer, as shown in Figure 1.

The tests were performed under dry sliding conditions, where the contact pairs consisted of the prepared composite samples obtained by the compo-casting method and a counter ball. The ball was made of Inox 440C stainless steel, with a hardness of 62–64 HRC and a diameter of 1.5 mm. In addition, an optical microscope, presented in Figure 2, was used as part of this investigation. The experimental plan is summarized in Table 1.

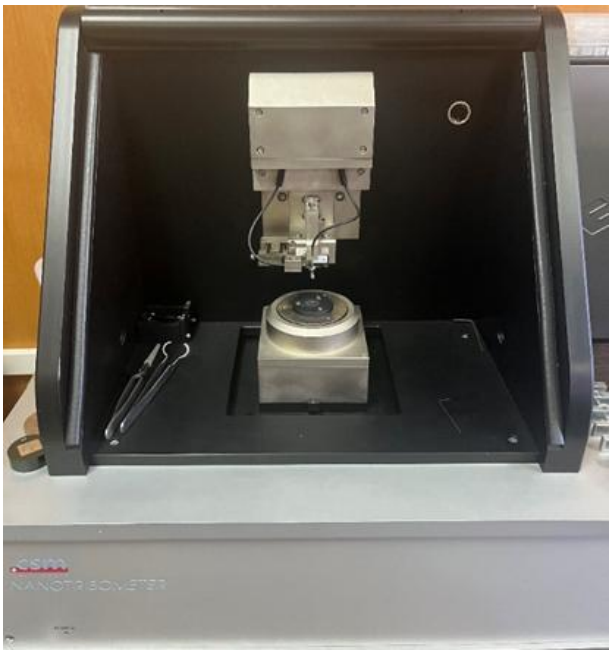

Fig. 1. Nanotribometer CSM + Instruments.

Fig. 2. Optical Microscope.

Table 1 presents the material composition in one column and the testing conditions in the other.

Table 1. Experimental Plan.

Materials	Conditions
ZA-27+0.5%Al_2O_3+5%SiC	Counter ball: Inox 440C, 62-64 HRC, diameter 1.5 mm. Experimental parameters: Sliding speed v=8 m/s, Load F= 200mN, Number of cycles n=500. Wear track radius: r=2 mm, r=3 mm, r=4 mm Reinforcement size: Al_2O_3 - 20-30 nm SiC - 40 µm

3. Results and discussion

After the completion of the experiment, which consisted of tribo-pairs made of a composite block and a steel ball, under constant load, sliding speed, and a fixed number of wear cycles, but with varying wear track radii (r = 2 mm, r = 3 mm, r = 4 mm), the results were obtained as shown in Figures 3, 4, and 5. Figure 6 presents the histogram of the coefficient of friction.

Figure 3 shows the diagram of the coefficient of friction and penetration force under the following experimental parameters: sliding speed v = 8 m/s, load F = 200 mN, number of cycles n = 500, and wear track radius r = 2 mm.

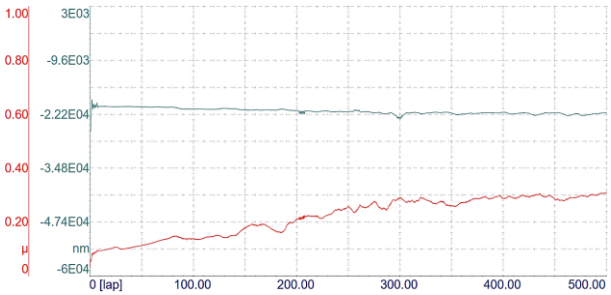

Fig. 3. Diagram of the coefficient of friction and penetration force under the experimental parameters: sliding speed v = 8 m/s, load F = 200 mN, number of cycles n = 500, and wear track radius r = 2 mm.

Figure 4 presents the diagram of the coefficient of friction and penetration force under the following experimental parameters: sliding speed v = 8 m/s, load F = 200 mN, number of cycles n = 500, and wear track radius r = 3 mm.

Figure 5 shows the diagram of the coefficient of friction and penetration force for the parameters: sliding speed v = 8 m/s, load F = 200 mN, number of cycles n = 500, and wear track radius r = 4 mm.

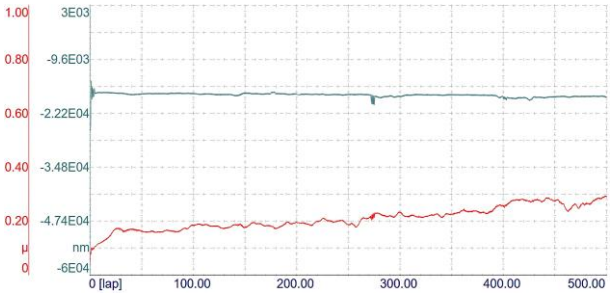

Fig. 4. Diagram of the coefficient of friction and penetration force under the experimental parameters: sliding speed v = 8 m/s, load F = 200 mN, number of cycles n = 500, and wear track radius r = 3 mm.

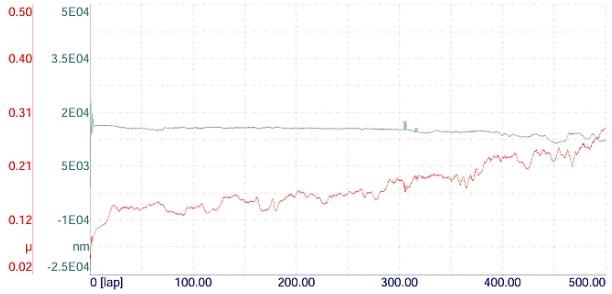

Fig. 5. Diagram of the coefficient of friction and penetration force under the experimental parameters: sliding speed v = 8 m/s, load F = 200 mN, number of cycles n = 500, and wear track radius r = 4 mm.

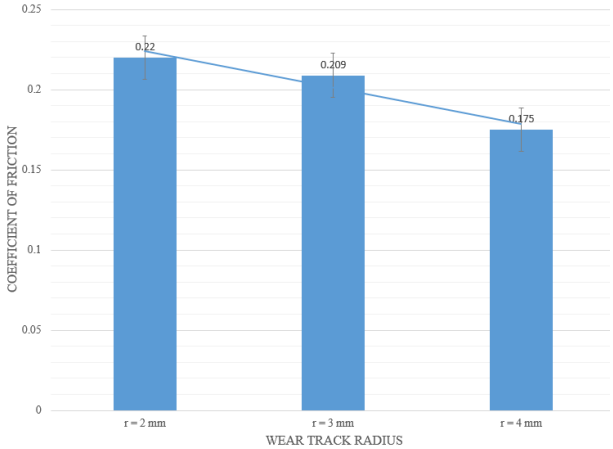

Fig. 6. Histogram of the coefficient of friction.

The specimens exhibited similar penetration depths across all three experiments, but their coefficients of friction showed slight variations. In all cases, the coefficient of friction increased slightly with the number of cycles. The sample with a wear track radius of 4 mm demonstrated the most irregular diagram of the coefficient of friction, most likely due to pronounced adhesion as one of the dominant wear mechanisms. However, this same sample also recorded the lowest average coefficient of friction.

Wear is governed by multiple interacting mechanisms, which makes its behavior highly complex. When the wear track radius was small, the primary process was two-body abrasion. With an increase in radius, the wear scars became wider and adhesion effects intensified, producing transfer films and micro-welded particles. The progression of wear was also strongly dependent on the number of cycles, since repeated loading promoted material fatigue and the gradual stabilization of transfer layers. For long-term service of engineering components, both of these factors must be taken into account. A clear understanding of such phenomena is key to improving material processing methods as well as ensuring reliable performance in industrial use [3, 5, 6, 8].

The diagrams show that penetration force remained nearly constant with minimal variation, while the coefficient of friction in the third case (r = 4 mm) was the lowest. In contrast, the first two samples exhibited similar but considerably higher coefficients of friction. For the first sample, the coefficient of friction was 0.220 (r = 2 mm); for the second, it was 0.209 (r = 3 mm); and for the third, it was 0.175 (r = 4 mm). As the wear track widened, the actual contact area increased. In materials capable of sustaining higher loads, this led to a redistribution of stress over a larger contact zone, thereby reducing local pressure. With lower local pressure, the tendency toward adhesion and micro-welding decreased, ultimately resulting in a reduced coefficient of friction.

4. Conclusion

The results highlight the complex nature of wear and its mechanisms. Two-body abrasion was dominant in samples with smaller wear track radii, while increasing the radius led to larger wear scars and more pronounced adhesion, resulting in the formation of transfer layers and micro-welded particles. The number of cycles had a significant influence on the stability of the wear process, suggesting that material fatigue and the formation of stable transfer layers must be considered in long-term operating conditions of technical systems. Understanding these factors is essential for optimizing both the manufacturing and exploitation of materials, as well as their application in industrial environments.

It is also important to account for surface imperfections resulting from the compo-casting method of sample preparation, as these imperfections significantly influence both penetration force and the coefficient of friction. Sudden jumps and drops in the diagrams of friction coefficient and penetration force may indicate that the ball encountered either a porous region of the material or a zone of higher hardness compared to the surrounding surface.

References

[1] Babić, M. Mitrović, S. Tribološke karakteristike kompozita na bazi ZnAl legura, Mašinski fakultet Univerziteta u Kragujevcu, 2007.

[2] Babić, M. Ninković, R. Tribološki potencijal ZnAl legura, Mašinski fakultet Univerziteta u Kragujevcu, 2007.

[3] Shivakumar, N., Vasu, V., Narasaiah, N., Kumar, S. Synthesis and characterization of nano-sized Al_2O_3 particle reinforced ZA-27 metal matrix composites, *Procedia Materials Science*, 2015,10, 159–167.

[4] Narayana, Y. N. R. K., Kaleemulla, M. K. Experimental study of tribological behavior of aluminum oxide(AL_2O_3) using pin-on-disc wear testing apparatus, *Journal of Manufacturing Engineering*, 2020, 15(4).

[5] Behera, V. R., Nallu, R., Chebolu R., Rao, M. S. S. S. Multi-Objective optimization of heat treatment criteria on the corrosion and wear behaviour of ZA27/SIC/TIB_2 hybrid Metal Matrix Composite, *Journal of Engineering Research*, 2024.

[6] Miloradović, N., Vujanac, R., Mitrović, S., Miloradović, D. Dry sliding wear performance of ZA27/SIC/GraphiteComposites, *Metals*, 2019, 9(7), 717.

[7] Murugaveni, S. P., Thyla, P. R. Assessing the performance of nano lubricant on zinc aluminium alloy, *Defence Science Journal*, 2019, 69(4), pp. 396–401.

[8] Dange, A. S., Jayakumar, J. Evaluation of Mechanical and Wear Properties of Aluminium-Al_2O_3 Composite Material, *International Research Journal of Engineering and Technology (IRJET)*, 2018, 5(8), pp. 1440-1447.

41st Danubia-Adria Symposium Advances in Experimental Mechanics
September 23-26, 2025, Kragujevac, Serbia

Original scientific paper DOI: 10.46793/41DAS2025.171S

CHALLENGES OF ADDITIVE MANUFACTURING IN MACHINE ELEMENT APPLICATIONS

Ivan SIMONOVIĆ[1], Aleksandar MARINKOVIĆ[2], Jovana ANTIĆ[3], Nenad KOLAREVIĆ[4]

[1] 0000-0002-5097-9486 , Faculty of Mechanical Engineering University of Belgrade, Kraljice Marije 16, Belgrade, Serbia, E-mail: isimonovic@mas.bg.ac.rs;

[2] 0000-0003-1657-4431 , Faculty of Mechanical Engineering University of Belgrade, Kraljice Marije 16, Belgrade, Serbia, E-mail: amarinkovic@mas.bg.ac.rs;

[3] 0009-0002-6452-0294 , Faculty of Mechanical Engineering University of Belgrade, Kraljice Marije 16, Belgrade, Serbia, E-mail: jrantic@mas.bg.ac.rs;

[4] 0000-0003-2836-7405 , Faculty of Mechanical Engineering University of Belgrade, Kraljice Marije 16, Belgrade, Serbia, E-mail: nkolarevic@mas.bg.ac.rs;

1. Introduction

Additive manufacturing, also known as 3D printing, has become increasingly relevant in science as well as industrial applications, thanks to its ability to produce complex geometries that are difficult to achieve with conventional methods. Sliding bearings are essential machine parts, characterized by great reliability, constant performance, and minimal noise [1]. In machine systems, sliding bearings allow shaft rotation with minimal friction and heat dissipation. The use of additive technologies to make machine parts, especially sliding bearings, allows for on-demand manufacturing without large series or expensive tools and the use of a variety of materials, from engineering polymers to metals. Industries that need customized solutions benefit from mass personalization and customized production enabled by these technologies [2]. Additive manufacturing contributes to environmentally friendly production by reducing material waste, lowering energy consumption, and minimizing the carbon footprint, thus supporting strategies of circular economy [3]. One of the disadvantages of additive technologies is the higher price per unit of the product compared to conventional methods, as well as the longer time for manufacturing the part. In addition, parts made with additive technologies often require additional machining using traditional methods, such as turning or grinding, in order to achieve the appropriate finish and surface quality. The need to evaluate tribological properties, primarily the coefficient of friction and wear of additively produced parts, arose from the increasing application of additive technologies in the production of sliding bearings. The aim of this paper is to provide an overview of additive manufacturing technologies that can be applied to the production of machine elements, with special reference to sliding bearings, as well as to analyse the tested tribological properties of the relevant materials.

2. Overview of additive manufacturing technologies

The additive manufacturing paradigm involves manufacturing a part based on a CAD model, whereby material is deposited layer by layer using controlled and automated tools [4]. Sheet lamination, material extrusion, powder bed fusion, direct energy deposition, binder jetting, material jetting, and vat photopolymerization are some of the most frequently used categories of AM technology. Each technology, thanks to its specific features, is adapted to specific applications [5]. The process of creating a part begins with the creation of a CAD model and the generation of an stereolithography (STL) file of the desired object, which is a standard procedure in almost all AM processes [6]. The 3D model is converted into a series of 2D slices, which are suitable for printing as they contain information about the lateral profiles of each layer. Based on those slices, the model is created layer by layer, following those slices. The STL format of the model consists of several triangular facets, which approximate the geometry of the object [7].

2.1 Fused Deposition Modeling (FDM)

In FDM technology shown on Fig.1., thermoplastic extrusion is done through a heated nozzle and the material is applied in layers to form a 3D object based on the STL file. The properties of the manufactured part can be influenced by several printing parameters, including layer thickness, infill shape and density, raster angle, build orientation,

number of contours, as well as other factors [8]. Process parameters influence the tribological characteristics of parts made by the FDM method. Wear rate can be reduced by reducing the thickness of the layer or by a certain orientation of the print, while increasing the roster angle and air gap can lead to the opposite effect. Road width and number of contours can also affect the wear rate [9].

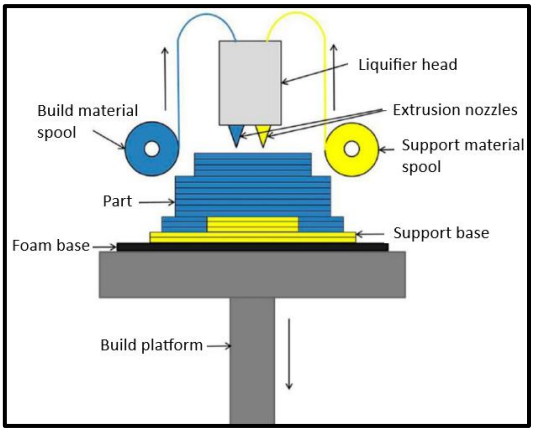

Fig. 1. Fusion Deposition Modeling method [5]

2.2 Selective Laser Sintering (SLS)

The selective laser sintering (SLS) method uses a directional laser beam to selectively irradiate and sinter powder layers, as illustrated in Fig.2., forming the desired three-dimensional product [10].

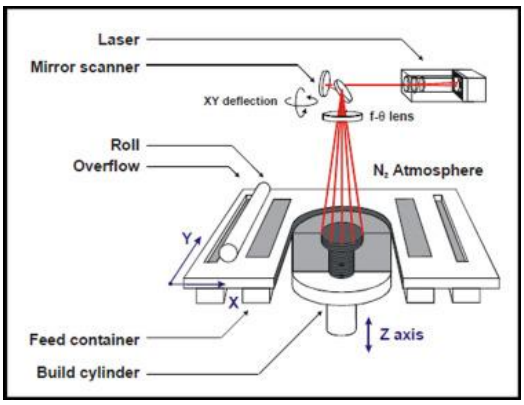

Fig. 2. Selective Laser Sintering method [12]

Before starting the laser beam, it is necessary to heat the powder to the appropriate temperature. This method fulfils the basic principle of additive technologies, adding material layer by layer to create a part directly based on the 3D model and the corresponding STL file. The recoating roller first uniformly applies a thin layer of powder to the working surface inside the chamber, which is later selectively sintered under the influence of a laser. After the formation of one layer, the working platform is restrained by a predefined layer height, and a new layer of powder is again applied to the surface. This process is repeated until the part is completely finished [11].

2.3 Stereolithography (SLA)

SLA is a vat polymerization technique in which layers of a liquid precursor in a vat are consecutively subjected to ultraviolet (UV) radiation, resulting in selective solidification, as shown in Fig.3. A photoinitiator (PI) molecule in the resin reacts to incoming light and, upon irradiation, locally initiates the chemical polymerization reaction, resulting in curing exclusively in the exposed regions. Subsequent to the formation of the initial layer, a new resin film is placed, irradiated, and cured [13].

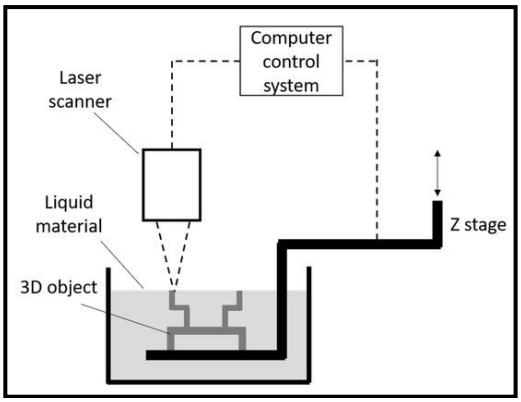

Fig. 3. Stereolithography method [7]

3. Tribological behavior of common 3D printing materials

Tribological properties and behaviour of 3D printed materials is important for optimizing materials and parts performance in applications where friction and wear are significant concerns. The most commonly used materials in additive manufacturing are engineering polymers, metals and ceramics. The most common polymers are Polylactic Acid (PLA), Acrylonitrile Butadiene Styrene (ABS), Polyethylene Terephthalate Glycol (PETG) and Polyamide (PA), as well as composites based on these polymers. Composites are mainly reinforced with fibers, such as carbon fibers or glass, which improves the mechanical, tribological and thermal properties of the manufactured parts [14]. PLA is characterized by greater mechanical strength and is environmentally more stable, while ABS is more flexible and more resistant to higher temperatures, although on average it has lower strength. The properties of these materials can be influenced by printing parameters, such as layer thickness, infill density and shape, as well as printing orientation [15]. In the paper [16] ABS and PLA materials were tested. Layer thickness, infill angle and orientation of deposition were chosen as the main printing parameters. Under identical printing conditions, PLA and ABS did not show significant differences in tribological properties. The materials

predominantly utilized in Selective Laser Sintering (SLS) include thermoplastics such as Polyamide 12 (PA12), Polyamide 11 (PA11), and their composite variants. Additional materials comprise Thermoplastic polyurethane (TPU), Polypropylene (PP), Polystyrene (PS), Polyethylene (PE), Polycaprolactone (PCL), and high-performance polymers such as Polyetheretherketone (PEEK) [11]. Polyamides are the most widely used materials in commercial systems. They can be found in the most famous form PA12 as well as in forms with particles like glass or carbon. Tribological properties of SLS-made PA12 depend on sintering orientation and additives. Parallel orientation reduces wear and friction [17,18], while reinforcements with graphite, MoS_2, carbon fibers and SiC significantly improve wear resistance and reduce the coefficient of friction [19–21].

Recent studies have increasingly examined the tribological properties and the possibility of using sliding bearings manufactured using additive technologies. In the work [22] authors investigated the effect of texture on plain bearings fabricated by FDM technology using ABS, PLA and nylon. The focus of testing was the effect of texture depth, rotation speed and load, with optimization using Gray Relational Analysis. The authors in [23] compared the performance of sliding bearings made by different methods, SLS and FDM, where SLS nylon bearings showed lower friction, but limited application at higher temperatures. In [24] investigated bearings were made with MultiJet technology, where the load and joint of the bearing showed significant influence.

4. Challenges and limitations of 3D-printed bearings

Bearings produced by additive technologies have their own advantages, which are primarily reflected in the design and economy of production. Compared to traditionally produced bearings, there are numerous challenges. Most often, the problems are due to anisotropy, layered structure effects, reduced dimensional accuracy and sensitivity to high temperatures or loads. Anisotropy of additively manufactured bearings affects strength, wear and friction characteristics depending on the direction of load or rotation. This property is a consequence of layer-by-layer manufacturing, which weakens the bonds between the layers and leads to unstable wear and friction performance depending on the working conditions [22,25]. Surface roughness, as a consequence of the printing process, can lead to increased friction and wear, especially at high loads and rotation speeds [26]. 3D-printed bearings frequently exhibit dimensional inaccuracies resulting from printer resolution constraints, material shrinkage, and variations in post-processing [27]. Despite all the challenges, 3D printed bearings offer significant benefits, such as design flexibility that allows testing hypotheses about design improvement, lightweight construction, and the ability to produce bearings with different surface textures to improve tribological properties. Materials such as PA12 and its composites reinforced with carbon fibers, glass beads or dry lubricants ensure a low coefficient of friction and less wear, which makes them suitable for industries where traditional lubrication with lubricants cannot be used, such as the food and paper industries, as well as for maintenance-free bearings. The process of additive technologies enables faster development cycles and more economical production of small batches of bearings, which is especially useful in cases where it is necessary to quickly replace the bearing.

5. Conclusion and future work

Additive technologies provide significant improvements for the manufacturing of machine elements, especially sliding bearings, due to their ability to produce complicated structures, reduce material waste, and allow modification. However, the widespread application of 3D-printed bearings faces problems related to anisotropy of material, effects of layered structures, increased surface roughness, dimensional inaccuracies, and reduced thermal and mechanical stability compared to traditionally manufactured components. Tribological properties of printed parts are highly dependent on material selection, printing parameters, and post-processing treatments.

Recent studies have demonstrated that reinforcements such as carbon fibers, glass fibers, graphite, and MoS_2 can significantly improve wear resistance and reduce friction in SLS-produced polymer bearings. Nevertheless, careful optimization of sintering orientation and control of printing parameters remain crucial for achieving consistent tribological performance.

Future work will focus on experimental testing of 3D-printed sliding bearings under simulated real-world conditions, with an emphasis on long-term durability. Further research will also explore new composite formulations, improvements in surface finishing techniques, and the development of predictive models to better understand and optimize tribological behaviour.

REFERENCES

[1] Du, F., Li, D., Sa, X., Li, C, Yu, Y, Li, C, Wang, J, Wang, W. Overview of Friction and Wear Performance of Sliding Bearings. *Coatings,* 2022, *12*, 1303.

[2] Qin, J., Hu, F., Liu, Y., Witherell, P., Wang, C.C.L., Rosen, D.W., Simpson, T.W., Lu, Y., Tang, Q. Research and Application of Machine Learning for Additive Manufacturing. *Additive Manufacturing,* 2022, *52*, 102691.

[3] Hegab, H., Khanna, N., Monib, N., Salem, A. Design for Sustainable Additive Manufacturing: A Review. *Sustainable Materials and Technologies,* 2023, *35*, e00576.

[4] Tofail, S.A.M., Koumoulos, E.P., Bandyopadhyay, A., Bose, S., O'Donoghue, L., Charitidis, C. Additive Manufacturing: Scientific and Technological Challenges, Market Uptake and Opportunities. *Materials Today,* 2018, *21*, 22–37.

[5] Rajan, K., Samykano, M., Kadirgama, K., Harun, W.S.W., Rahman, Md.M.. Fused Deposition Modeling: Process, Materials, Parameters, Properties, and Applications. *Int J Adv Manuf Technol,* 2022, *120*, 1531–1570.

[6] Wong, K.V., Hernandez, A. A Review of Additive Manufacturing. *ISRN Mechanical Engineering,* 2012, *2012*, 1–10.

[7] Huang, J., Qin, Q., Wang, J. A Review of Stereolithography: Processes and Systems. *Processes,* 2020, *8*, 1138.

[8] Mohamed, O.A., Masood, S.H., Bhowmik, J.L., Somers, A.E. Investigation on the Tribological Behavior and Wear Mechanism of Parts Processed by Fused Deposition Additive Manufacturing Process. *Journal of Manufacturing Processes,* 2017, *29*, 149–159.

[9] Batista, M., Blanco, D., Del Sol, I., Piñero, D., Vazquez, J.M. Tribological Characterization of Fused Deposition Modelling Parts. *IOP Conf. Ser.: Mater. Sci. Eng.,* 2021, *1193*, 012068.

[10] Kruth, J.P. Material Incress Manufacturing by Rapid Prototyping Techniques. *CIRP Annals,* 1991, *40*, 603–614.

[11] Han, W., Kong, L., Xu, M. Advances in Selective Laser Sintering of Polymers. *Int. J. Extrem. Manuf.,* 2022, *4*, 042002.

[12] Kruth, J., Mercelis, P., Van Vaerenbergh, J., Froyen, L., Rombouts, M. Binding Mechanisms in Selective Laser Sintering and Selective Laser Melting. *Rapid Prototyping Journal,* 2005, *11*, 26–36.

[13] Schmidleithner, C., Kalaskar, D.M. Stereolithography. In *3D Printing*; Cvetković, D., Ed, InTech, 2018

[14] Bhatia, A., Sehgal, A.K. Additive Manufacturing Materials, Methods and Applications: A Review. *Materials Today: Proceedings,* 2023, *81*, 1060–1067.

[15] Otieno, D.B, Bosire, G.O, Onyari, J.M, Mwabora, J.M. Comparative Analysis of 3D-Printed Polylactic Acid and Acrylonitrile Butadiene Styrene: Experimental and Materials-Studio-Based Theoretical Studies. *J Polym Res,* 2022, *29*, 291.

[16] Roy, R., Mukhopadhyay, A. Tribological Studies of 3D Printed ABS and PLA Plastic Parts. *Materials Today: Proceedings,* 2021, *41*, 856–862.

[17] Wörz, A., Drummer, D. Tribological Anisotropy of Selective Laser Sintered PA12 Parts. *Polymer Testing*, 2018, *70*, 117–126.

[18] Gadelmoula, A., Aldahash, S.A. Tribological Properties of Glass Bead-Filled Polyamide 12 Composite Manufactured by Selective Laser Sintering. *Polymers,* 2023, *15*, 1268.

[19] Gadelmoula, A, Aldahash, S.A. Dry Friction and Wear Behavior of Laser-Sintered Graphite/Carbon Fiber/Polyamide 12 Composite. *Polymers* 2023, *15*, 3916.

[20] Nar, K., Majewski, C., Lewis, R. Evaluating the Effect of Solid Lubricant Inclusion on the Friction and Wear Properties of Laser Sintered Polyamide-12 Components. *Wear,* 2023, *522*, 204873.

[21] Yu, G., Ma, J., Li, J., Wu, J., Yu, J., Wang, X. Mechanical and Tribological Properties of 3D Printed Polyamide 12 and SiC/PA12 Composite by Selective Laser Sintering. *Polymers,* 2022, *14*, 2167.

[22] Mourya, V., Bhore, S.P. Experimental Investigation of Tribological Performance of 3D Printed Textured Journal Bearings for Various Polymers. *Journal of Thermoplastic Composite Materials,* 2024, *37*, 1586–1618.

[23] Lee, Y.-J, Lee, K.-H, Lee, C.-H. Self-Lubricating and Friction Performance of a Three-Dimensional-Printed Journal Bearing. *Journal of Tribology,* 2018, *140*, 054501.

[24] Andrearczyk, A., Bagiński, P. THE USE OF ADDITIVE MANUFACTURING TECHNOLOGYTO MANUFACTURE SLIDE BEARING SLEEVES – A PRELIMINARYSTUDY. *Tribologia,* 2020, *291*, 7–14.

[25] Silvestri, A.T., Papa, I., Rubino, F., Squillace, A. On the Critical Technological Issues of CFF: Enhancing the Bearing Strength. *Materials and Manufacturing Processes,* 2022, *37*, 123–135.

[26] Lee, Y.-J, Lee, K.-H, Lee, C.-H. Friction Performance of 3D Printed Ball Bearing: Feasibility Study. *Results in Physics,* 2018, *10*, 721–726.

[27] Uzcategui, A.C., Muralidharan, A., Ferguson, V.L., Bryant, S.J., McLeod, R.R. Understanding and Improving Mechanical Properties in 3D Printed Parts Using a Dual-Cure Acrylate-Based Resin for Stereolithography. *Adv Eng Mater*, 2018, *20*, 1800876.

AUTHOR INDEX

Supported by

Republic of Serbia

MINISTRY OF SCIENCE, TECHNOLOGICAL DEVELOPMENT AND INNOVATION

Sponsors

IC INŽENJERING D.O.O.
PROIZVODNO INŽENJERING PREDUZEĆE
SKLADIŠNI I TRANSPORTNI SISTEMI
www.icinzenjering.com; office @icinzenjering.com
Gornjomilanovačka 209, 34204 Divostin Kragujevac

jbr ndt

KONTROL INSPEKT

LOTRIČ METROLOGY

AXIOM TECH

MIND GROUP

VERTEX STAR
design & engineering

CIP - Каталогизација у публикацији Народна библиотека Србије, Београд

621(082)
531(082)

DANUBIA-Adria Symposium Advances in Experimental Mechanics (41 ; 2025 ; Kragujevac)

Proceedings / 41st Danubia-Adria Symposium Advances in Experimental Mechanics, September 23-26, 2025 Kragujevac, Serbia ; edited by Miroslav Živković ... [et al.]. - Kragujevac : University, Faculty of Engineering, 2025 (Kragujevac : Inter Print). - [16], 177 str. : ilustr. ; 30 cm

Tiraž 100. - Str. [9-10]: Preface / Miroslav Živković, Vladimir P. Milovanović. - Bibliografija uz svaki rad. - Registar.

ISBN 978-86-6335-157-8

1. Živković, Miroslav, 1962- [urednik] [autor dodatnog teksta] 2. Milovanović, Vladimir, 1979- [urednik] [autor dodatnog teksta] 3. Dunić, Vladimir, 1983- [urednik] 4. Bodić, Aleksandar S., 1997- [urednik]

a) Механика -- Зборници b) Технички материјали -- Испитивање -- Зборници

COBISS.SR-ID 175480073

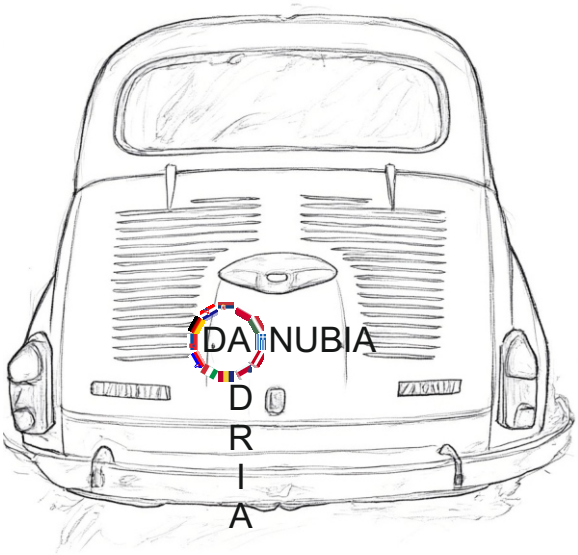

9 788663 351578